Improvement of the spatial quality of high energy lasers at high-repetition rate : development of stimulated Brillouin scattering phase conjugate mirrors for the correction of wavefront aberrations

Raphaël Humblot

université
PARIS-SACLAY

Improvement of the spatial quality of high-energy lasers at high repetition rate: development of stimulated Brillouin scattering phase conjugate mirrors for the correction of wavefront aberrations

Amélioration de la qualité spatiale des lasers multi-joules à haute cadence: développement de miroirs à conjugaison de phase par diffusion Brillouin stimulée pour la correction de front d'onde

Thèse de doctorat de l'université Paris-Saclay

École doctorale n°572: ondes et matière (EDOM)
Spécialité de doctorat: Physique
Graduate School : Physique. Référent : Institut d'Optique

Thèse préparée dans l' unité de recherche **Université Paris-Saclay, Institut d'Optique Graduate School, CNRS, Laboratoire Charles Fabry, 91127, Palaiseau, France**, sous la direction de **Frédéric Druon**, Directeur de recherche, la co-supervision de **Stéphane Branly**, Docteur et **Loïc Meignien**, Ingénieur de recherche

Thèse soutenue à Paris-Saclay, le 27 février 2025, par

Raphaël Humblot

Composition du jury

Membres du jury avec voix délibérative

Sophie Kazamias Prof. Dr. IJClab, Université Paris Saclay	Présidente
Christophe Dorrer Dist. Scientist, Dr., LLE Université de Rochester	Rapporteur & Examinateur
Olivier Utéza Directeur de recherche, Dr., CNRS-LP3, Marseille	Rapporteur & Examinateur
Vincent Bagnoud Prof. Dr., GSI - Darmstadt	Examinateur

Membres du jury sans voix délibérative

Frédéric Druon Directeur de recherche, Dr., Laboratoire Charles Fabry	Directeur
Stéphane Branly Dr., Amplitude laser	Invité
Loïc Meignien Ingénieur de recherche, Dr., LULI, École polytechnique	Invité

THESE DE DOCTORAT
NNT : 2025UPASP006

université PARIS-SACLAY

ÉCOLE DOCTORALE
Ondes et matière
(EDOM)

Title: Improvement of the spatial quality of high energy lasers at high-repetition rate: development of stimulated Brillouin scattering phase conjugate mirrors for the correction of wavefront aberrations

Keywords: Lasers, High-energy, High-repetition rate, Spatial phase, Stimulated Brillouin Scattering, Phase conjugation

Abstract: High-energy lasers are important tools in a large variety of scientific and industrial domains such as plasma physics, machining or energy sources for secondary lasers. Currently, the main drawback of such systems is their low repetition rate, limiting the number of shots provided. This limit rises from thermal energy accumulation shot after shot inside the amplifiers of the lasers systems during operation, generating laser beam wavefront distortion up to complete laser dysfunction. In this thesis, a collaboration between Amplitude laser, an industrial laser manufacturer, Laboratoire Charles Fabry, and Laboratoire pour l'Utilisation des Lasers Intenses (LULI), aim to develop a component capable of correcting those wavefront distortions. This component, called phase conjugated mirrors, uses a nonlinear effect called stimulated Brillouin scattering to invert the wavefront and allow self-correction of the laser wavefront aberration in a double pass amplifying scheme. In this work, the existing theoretical framework of the nonlinear effect is used for the development of numerical models simulating the reflection. Those models are applied to the design of experimental phase conjugate mirrors whose properties are investigated. The thesis places an emphasis on the fidelity of the mirror, that is to say, its capacity to conserve the spatial and temporal pulse properties while properly inverting the wavefront. In particular, the optical configuration used, and the input laser parameters are shown to have a large influence on the reflection quality. The capacity to be applied to arbitrary temporal shapes is demonstrated for the first time and paves the way to the usage of phase conjugate mirrors for broader applications requiring unusual temporal shapes. The phase conjugate mirror stability and reliability are considered for the usage in industrial commercial laser systems and no particular erratic behaviour is identified. The limits of the components are investigated up to unprecedented input energy and wavefront aberrations levels making this component compatible for laser sources up to the kilojoule energy level.

université PARIS-SACLAY

ÉCOLE DOCTORALE
Ondes et matière
(EDOM)

Titre: Amélioration de la qualité spatiale des lasers multi-joules à haute cadence: développement de miroirs à conjugaison de phase par diffusion Brillouin stimulée pour la correction de front d'onde

Mots clés: Lasers, Haute énergie, Haute cadence, Phase spatiale, Diffusion Brillouin Stimulée, conjugaison de phase

Résumé: Les lasers de forte énergie sont des outils d'importance croissante dans de nombreux domaines scientifiques et industriels tel que la physique des plasma, l'usinage ou encore en tant que source d'énergie pour d'autres types de lasers. A l'heure actuelle, une des problématique liées à ces lasers est leur cadence de tir, limitant le nombre total de tir pouvant être réalisés par les utilisateurs. Cette limite provient de l'accumulation de chaleur tirs après tirs au sein des amplificateurs et dégradant le front d'onde des impulsions lasers jusqu'à le rendre inutilisable. Cette thèse, issue de la collaboration entre un industriel du laser: Amplitude laser, le Laboratoire Charles Fabry et le Laboratoire pour l'Utilisation des Lasers Intenses (LULI), cherche à développer un composant optique permettant de corriger ces aberrations de front d'onde. Ce composant, appelé miroir à conjugaison de phase, permet la réflexion d'une impulsion laser en utilisant un effet non linéaire: la diffusion Brillouin stimulée. Lors de cette réflexion, le front d'onde et les aberrations optiques sont inversée et il est alors possible d'autocompenser tous les défauts introduit lors de l'amplification en réalisant un aller-retour dans les amplificateurs, avec inversion du front d'onde au milieu de cet aller-retour. Ce travail reprend la description physique de la diffusion Brillouin stimulée pour développer des modèles numériques permettant la simulation de la réflexion. Ces modèles numériques sont utilisés pour le design de miroirs à conjugaison de phase expérimentaux dont les propriétés sont caractérisées. Cette thèse cherche en particulier à optimiser la fidélité de la réflexion, c'est à dire la capacité à conserver les propriétés spatiales et temporelles de l'impulsion incidente tout en inversant le front d'onde. Les études numériques montrent que la configuration optique et les paramètres du laser ont une forte influence sur la qualité de la réflexion. Nous démontrons pour la première fois la capacité à conserver une forme temporelle arbitraire lors de la conjugaison de phase et rend possible l'utilisation du composant pour une nouvelle gamme d'application exigeant des formes temporelles diverses. La stabilité et fiabilité du miroir à conjugaison de phase est étudiée dans le but de l'introduire à terme dans des systèmes commerciaux, aucun comportement erratique n'est identifié lors de son utilisation sous les conditions d'utilisation nominales. Les limites d'utilisations du composant sont recherchées et son bon fonctionnement est démontré jusqu'à des niveaux d'énergie et d'aberration incidente record, rendant pour la première fois son utilisation possible sur des chaînes lasers de classe kilojoule.

Acknowledgements

Cela fait donc six ans que je travaille sur les lasers intenses… C'est beaucoup pour avoir le droit de mettre Dr. à côté de mon nom sur la boîte au lettre (Comment ça on a toujours pas le droit ?! Remboursez mes 6 ans !!) et à la fois très peu quand on regarde tout ce qu'il reste à apprendre et tout ce qu'il reste à faire. Mais quand je vois tout le beau monde qui travaille sur le sujet, je me dis que c'est pas si mal, finalement. On a encore un bon bout de chemin à faire ensemble.

C'est donc la fin de ma thèse, la fin de mes études et le début du prochain chapitre (pas en annexe, celui-là, il faudra se débrouiller avec Amplitude pour la PI). Après tout ce qu'on a réussi à faire durant ces trois ans, j'arrive à me dire "Bon travail". J'imagine donc que c'est une réussite. Et bien sûr, pour arriver à cette réussite, il a fallu du monde, et c'est dans ce petit chapitre que je vais m'atteler à les remercier. Si le volume d'écriture était proportionnel à l'importance pour les travaux, cette section ferait la moitié du manuscrit (voire plus) donc vous m'excuserez de la concision. Je me suis déjà assez étendu dans la suite, au grand dam de certains de mes encadrants.

Tout d'abord, je remercie Olivier Utéza et Christophe Dorrer d'avoir accepté de rapporter mon manuscrit, de s'être intéressés au sujet et pour la précision et la pertinence de leurs commentaires. Je remercie également Sophie Kazamias et Vincent Bagnoud pour leur participation au jury.

Je tiens évidemment à remercier mon équipe d'encadrement. Vous êtes la raison principale du succès de ces travaux, à la fois de par votre présence et votre suivi, mais aussi grâce à la variété de vos approches sur les problèmes rencontrés. J'ai eu la chance de baigner à la fois dans un cadre académique et industriel et je suis convaincu que ma thèse et moi-même en ont grandement profité.

Je remercie Loïc Meignien de m'avoir fait entrer dans le monde des lasers intenses, et ce trois ans avant le début de ma thèse, durant mon apprentissage au LULI. Et je suis heureux que les développements réalisés durant cet apprentissage aient pu servir à la fois au LULI et, plus tard, durant ma thèse. Merci également à Patrick Audebert, qui s'est impliqué, et a poussé pour que nous puissions finaliser nos expériences sur le laser HERA, malgré les contretemps expérimentaux.

Je tiens particulièrement à remercier Stéphane, qui a cru au sujet, l'a construit avant mon arrivée, et qui m'a ensuite fait confiance pour le réaliser. Je te remercie grandement pour ton suivi, ton engagement et ton

investissement pour la résolution des divers problèmes techniques rencontrés. C'est grâce à toi que l'on a pu avancer sans trop de remous, et atteindre les objectifs que l'on s'était fixés. Merci également pour ta droiture par rapport à tes engagements (qualité trop rare), ainsi que pour ton envie de mettre en avant de tirer vers le haut tes collaborateurs.

Merci également à mon directeur de thèse, Frédéric Druon pour son accompagnement tout au long de la thèse, ses relectures et commentaires avisés, sa présence et ses idées à la foi terriblement farfelues et fichtrement intéressantes (cf, l'épisode de la densité volante) durant les semaines d'expériences au LULI. Merci pour ta bonne humeur, ta pertinence scientifique, et ton encadrement en général (et ton matériel de plongée).

Il y a de nombreux avantages à travailler en collaborations entre plusieurs laboratoires et la concision de la section "Remerciements" n'en fait pas partie. Je vais essayer de m'y atteler de mon mieux.

Tout d'abord à Amplitude, où j'ai passé la majorité de mon temps. J'y ai croisé du monde ! Merci tout d'abord à toute l'équipe NAL (passée et présente): Florian Mollica, Nicolas Delmas qui étaient là dès le début ainsi que Hugo Delahaye, Pierrick Leroy, et Emmanuel Thoyer qui nous ont rejoints ensuite. Merci à tous ceux qui ont contribué de près ou de loin à mes travaux de thèse: Ivan Delgado pour le design mécanique de la cellule et sa fameuse stratégie de serrage ("Dès que ça grince, tu arrêtes"). Merci à Kevyn Mariette, actuellement à $10000\ \mathrm{km}$, qui a prit la relève; à Sebastien Jamet, Cyrille Bayart, Eric Audouard et Hugo Caherec. Et bien sur, un grand merci à Virginie Esteves, j'espère que ça boome et que ça continuera à boomer.

Je tiens à saluer les autres co-bureau entassés dans la mezzanine: Dr. Steven Calvez, Mohammed Zaoui, Olga Lozan, Christina Alexandridi (et les échanges de capybaras), Marceau Pintonato et Celia Fierobe. Merci d'avoir toléré les lancers de requins. Et ne vous inquiétez pas pour la suite, j'ai entendu dire que je changeais de bureau bientôt.

Merci également aux autres collègues avec qui j'ai eu l'occasion de travailler, ou de discuter: La cheffe de l'indus et comparse de sushi: Adeline Delmas, la best covoit' Solène Favier, Nour Daher - le petit soleil, Aura Gonzalez, Chems-Eddine Ouinten, Jinfeng Chen, Loïc Ramousse, Dr Alexis Guillemard, Seb Bonnet-Ligeon (qui m'a initié à l'escalade et fait découvrir la grimpe à Fontainebleau), Mon allié de code: Benoit Buissiere, Djamel-Dean Braham, Marco Rodrigues, le génial p'tit Fred, Ahmed Maghraoui, Georges-Eric Inglebert, l'autoproclamé "bébou" Samuel Poirier, Mon feu homonyme: Raphaël Raepsat, Nicolas Hainez, Léo Casinière et Nicolas Fierobe. Je laisse également un petit mot pour Anna Golinelli et Franck

Falcoz avec qui j'ai eu la chance de passer mon premier séjour outre-atlantique (Franck, je veux toujours ma revanche au mini-golf !), et pour l'équipe qui a prit la relève sur la présentation de mes travaux durant la rédaction, et qui font vivre (et qui j'espère continueront) la technologie SBS: Aurélia Durand, Antoine Courjaud et Gabriel Loata.

En plus de tous cette personnes formidables, j'aimerai remercier en particulier deux collègues et amies que j'ai eu la chance de rencontrer à Amplitude: Floriane Perrier, à qui je souhaite le meilleur pour la suite (et des F23, faudrait pas rester le ventre vide). Et Alyona Dotsenko ou "Dr. Gazouilli", ma camarade de tram-train. On en a vu, et on en reverra, des vertes et des pas mûres, mais j'ai été heureux de les voir avec vous.

Pour mes collègues du LULI, je n'ai malheureusement pas eu la chance de travailler avec beaucoup d'entre vous mais je tenais tout de même à remercier l'équipe des laséristes du LULI, Doina Badarau, et en particulier: Joanna De Sousa, et Cyril Rapeneau qui m'ont beaucoup aidé sur la chaîne HERA durant les expériences à haute énergie et dont la bonne humeur générale fût d'une grande aide à notre succès. Je salue également les collègues de bureau: Sophie Mennerat, Sylvain Savalle et Marie Froidevaux. Merci également à Sophie Baton pour nous avoir accordé du temps supplémentaire sur la chaîne laser, et à Sandra Dorard pour l'aide sur l'adaptation du montage mécanique.

Enfin, Je tenais à remercier le groupe laser de l'Institut d'Optique pour leur accueil et leur présence, en particulier durant la phase de rédaction. Les permanents: François Balembois, le très grand Patrick Georges (qui a très justement renommé mes travaux en "thèse laser grosse patate"), Marc Hanna, Gaëlle Lucas-Leclin, Xavier Délen, Sylvie Lebrun, Sylvie Janicot et Catherine Leblanc. Je salue également mes collaborateurs d'Amplitude y travaillant: Yoann Zaouter et sa collection de cartons ainsi que Michele Natile, seigneur du café. J'espère que la machine survivra encore longtemps (même si personnellement je parie sur un décès dans la semaine).

Je remercie les doctorants que j'ai pu rencontrer durant ma thèse. Les anciens: Lisa Lopez, Hussein Taleb, Maxime Nourry-Martin, Anahita Oumoumi, Qin Liu et Hippolyte Dupont. Et les nouveaux à qui je souhaite bon courage pour la suite: Elio Thellier, mon cher neveu Antoine Zheng, Alyona Dotsenko (encore elle… Sacré Gazouille), Gautier Parize dit "Le G.O.A.T.", mon compagnon d'escalade Joris Weinzaepflen, Matthieu Glasset, Marie-Céline Gathier-Danve (satané pluie) et Lisa Lallemand.

En particulier, j'aimerais tirer mon chapeau à Pierre Lebegue, camarade du LULI, collègue du LCF et autoproclamé "meilleure groupie" de l'Humblot-teur de cette thèse. C'est quand même fou de se dire qu'on est

allé visiter quatre pays différents ensemble, pour le boulot. Hâte de dépasser les 10 l'année prochaine (cette anecdote est fausse… Mais imagine !)

En sortant maintenant du cadre professionnel, j'aimerais remercier les personnes qui me supportent et me soutiennent au quotidien. Mes amis du passé, du présent et j'espère du futur: Arnaud Repain, Béatrice Chariar, Agnes, Lize Enn, Marie 25, Tituan Allain, Juliette Vlieghe, Cécile Le Gall, Noémie Marquet, Basile, Thomas Llauze, Léa Khater, Adrien Guitton, Arthur Soutenain et toutes les autres personnes fantastiques de ma vie.

Et bien sûr, merci à ma famille: Cédric, Sandrine, Anaïs, Pierre, Arthur et Isis.

C'est une page qui se tourne. Mais cela veut aussi dire, un nouveau chapitre, et de nouveaux objectifs. J'ai beaucoup appris, mais une thèse n'est pas une fin en soi. C'est un voyage, et non pas la destination.

Raphaël.

Contents

Acronyms and Symbols

We present here a list of the acronyms and symbols used in the following work grouped by type and ordered alphabetically. Every entry is associated with the page reference where it was first introduced. A single letter or symbol can in some cases be associated to multiple meaning. In this case, the interpretation should be based on the context. Such occurrences are supposed to be sparse enough so that the reader should not be troubled.

In the following developments, Vectorial quantities are noted using arrows $\overrightarrow{E}$ and their corresponding magnitude is denoted without it $E = ||\overrightarrow{E}||$. A physical quantity can either be written as a function of continuous parameters (that might sometime be implicit for the sake of readability) $E(z,t) = E$ or as sampled variables during the development of simulations, in which case the samples are noted as indices $E_{i,j}$.

Latin Letters

$\overrightarrow{B}$ Magnetic field, page 27

$\overrightarrow{D}$ Electronic displacement, page 27

$\overrightarrow{E}$ Electromagnetic field, page 26

$\overrightarrow{F}$ Force, page 29

$\overrightarrow{H}$ Auxiliaty magnetic field, page 27

$\overrightarrow{j}$ Current density, page 27

$\overrightarrow{k}$ Wave vector, page 25

$\overrightarrow{P_{NL}}$ Nonlinear part of the medium polarisation, page 27

$\overrightarrow{P}$ Medium polarisation, page 27

$\overrightarrow{p}$ Polarisation moment, page 29

$\overrightarrow{r} = (x, y, z)$ Cathesian coordinate system, page 26

A Cross-section/Area, page 33

A Envelope amplitude of the electromagnetic field, page 26

C Integration constant, page 37

C Medium compressibility, page 30

c Speed of light, page 28

D Insertion depth for a focusing geometry, page 36

G Linear SBS gain, page 35

g Medium Brillouin gain, page 34

$g^{(2)}$ Autocorrelation function, page 98

g_1 SBS coupling strength for Pump and Stokes waves, page 54

g_2 SBS coupling strength for the acoustic wave, page 54

h Height of the impact of the light ray on the aberrant optical component aperture in the Seidel wavefront decomposition, page 135

I Light intensity (Power per surface unit), page 34

$k_{Boltzmann}$ Boltzmann constant, page 33

L Length of a Brillouin cell, page 35

L_D Interaction length, page 36

n Medium index, page 28

P Laser power, page 47

p Pressure, page 29

R Reflectivity, page 37

T Temperature, page 33

t Time coordinate, page 26

U Electromagnetic energy, page 29

u Electromagnetic energy per unit volume, page 29

u Nomalised height of the impact of the light ray on the aberrant optical component aperture in the Seidel wavefront decomposition, page 135

V Volume, page 29

w Work of a force, page 29

w_0 Beam radius at beam waist, page 53

y Field variable in the Seidel wavefront decomposition, page 135

z_R Rayleigh length, page 53

AOM Acousto-optic modulators, page 107

DLS Dynamic Light Scattering, page 98

EOM Electro optic modulators, page 107

MOPA Master Oscillator Power Amplifier, page 107

OBT Optical Breakdown Threshold, page 96

OPD Optical path difference, page 137

PFC PerFluoro-Compounds, page 97

PV Peak-to-Valley amplitude of wavefront aberration, page 135

RMS Root-Mean-Square amplitude of wavefront aberration , page 136

S Spatial profile of a beam, page 77

SOA Semiconductor Optical Amplifiers, page 107

SVEA Slowly Varying Envelope Approximation, page 31

TEM Transmission Electron Microscope, page 103

w Beam radius, page 53

WFE WaveFront Error, page 188

Greek Letters

α Polarisability, page 29

χ Nonlinear susceptibility, page 27

Δn Difference for the variable n, page 29

Δ Wavefront of a beam, page 77

ϵ Medium permittivity, page 29

ϵ_0 Vacuum permittivity, page 27

γ Sampled variable of the space coordinate on the transverse dimension, page 78

Γ' Damping parameter of the sound wave in the medium, page 31

γ_ϵ Electrostrictive constant of a medium, page 29

Γ_B Brillouin decay parameter, page 32

λ Wavelength, page 31

$\langle u(t) \rangle_\tau$ average of time-dependent value $u(t)$ over time τ, page 30

μ_0 Vacuum permeability, page 27

ν conjugate transverse coordinate, page 78

Ω Phonon frequency, page 24

ω Electromagnetic wave frequency, page 24

$\partial \nabla \cdot \overrightarrow{u}$ Gradient of vectorial quantity $\overrightarrow{u}$, page 27

ρ Envelope amplitude of the acoustic field, page 26

ρ Medium density, page 29

ρ Medium charge density, page 27

Σ Wavefront, page 135

τ Duration, page 31

τ_B Phonon lifetime, page 44

θ Angle value, page 26

$\tilde{\rho}$ Acoustic field, page 26

φ Angle of azimut of the impact of the light ray on the aberratn optical component aperture in the Seidel wavefront decomposition, page 135

Superscripts

α Sampled time index, page 54

β Sampled space in propagation direction, page 54

(n) n-th order term of the expansion of a variable, page 27

Subscripts

B Relative to the acoustic wave, page 31

ES Relative to the electrostriction, page 29

in At Brillouin cell input, page 37

$medium$ relative to a nonlinear medium, page 43

P Relative to pump wave, page 24

$prop$ Relative to a propagation, page 43

$pulse$ Relative to a laser pulse, page 43

S Relative to Stokes wave, page 24

th At SBS threshold, page 37

Introduction

Soon after the experimental demonstration of lasers in 1960, the international community realised that intense lasers were an outstanding tool for a wide range of physical science experiments and industrial processes. Producing concentrated light pulses, they allow for high energy deposition on small surfaces (few hundreds of micro-meter squared) during short amount of time (nanosecond and below). This exceptional spatial and temporal concentration of energy enables the generation of extreme conditions of pressure and temperature and opens the door to otherwise unreachable physical effects. Nowadays, intense lasers are used to recreate on earth the matters of stars and study a wide range of astrophysical processes. They were also identified as one of the few ways to recreate in laboratory the process of nuclear fusion that might someday lead to unlimited clean energy production. More recently, intense lasers were used to accelerate charged particles in a more compact way than classical synchrotron accelerators. Laser-based particle accelerators may thus soon represent an interesting alternative extending the potential range of accelerators exploitation, such as in protontherapy, and therefore contribute to solve many cancer-related social issues. Intense lasers are also used in industrial manufacturing for precise micro-machining or for laser shock peening where the pressure of a laser-generated plasma induces mechanical stress in metal which improves its resistance to corrosion and overall hardness. High-energy lasers have also recently been used as a promising replacement of excimer lasers for annealing, improving the performances and efficiency of LCDs screens.

While the study of intense lasers is already a specialized subject in the field, the range of performances available in the literature and the market is significant. The typical pulse duration accessible varies from the attosecond duration and goes up to the nanosecond timescale spreading over 8 orders of magnitude. The same way, lasers defined as *intense* can present energy varying from few micro-joules up to the mega-joule level. In this work, we focus on the *high-energy* lasers, with relatively long pulses of typically few nanoseconds and high energy, from joule level and above. Those kinds of lasers are either used directly for plasma physics, nuclear fusion generation, industrial processes such as laser shock peening and are the main energy pumping energy source for shorter intense femtosecond laser chains.

In this field, the main drawback of the lasers is their repetition rate. A high-energy laser usually consists of a low-energy oscillator followed by a chain of amplifiers of increasing size with diameters larger and larger to avoid laser-induced damages due to high fluence. Moreover, during

amplification, the amplifiers accumulate heat which starts to impact the laser beam and distorts it. This deleterious process eventually makes the laser inoperable and the entire system deficient by introducing quantifiable spatial defects known as thermal aberrations. In the worst case, those can even lead to laser-induced damages in the amplifiers due to the apparition of hot spots in the propagating beam. In order to reduce optical aberrations, most of the high energy lasers are limited in repetition rate below few shots per second and down to few shots a day. For the laser users, this means fewer experimental results, fewer patients cured, or compromises on the energy production. This is currently one of the technical challenges preventing proliferation of lasers in all the aforementioned applications domains.

To solve this issue, four main work axes are currently being tackled by the international community. Firstly, more efficient energy sources are being developed. Classical flashlamps are being replaced by more efficient laser diodes to target specific absorption bands, improving pump absorption, quantum efficiency and quantum defect. Therefore, the laser amplifiers accumulate less thermal energy and higher repetition rates are subsequently accessible. Another work axis is the heat management architecture. Many mechanical designs aim at the optimisation of the sinking of thermal loads off the amplifiers by flowing a fluid next to the gain medium. The geometry, flow speed, and type of coolant define the heat drain efficiency of the system. In this context, several new cooling architectures are being developed to sink the heat in a more efficient manner. This can include replacing the first stages of the amplification by fibers amplifiers, with high surface to volume ratio and thus easily cooled down, or choosing different cooling geometries to sink the heat more efficiently. Third, different gain medium are being investigated. Crystalline lattices are known to present good thermomechanical properties compared to the usual doped glasses of high energy laser chains. On the other hand, large aperture crystals are often hard to manufacture which make their use difficult in very high energy laser chains. A compromise has been found in the form of large aperture crystalline ceramics that present good thermomechanical properties. Recent systems using those solutions conjointly have been demonstrated in cryogenics thin disc ceramics, at the expense of energy consumption to reach operating temperatures.

At last, it is also possible to compensate for thermal aberrations on the beam by introducing an optical correcting apparatus. This is usually done by measuring the beam distortion with a wavefront sensor and subsequently apply an opposite phase mask using a deformable mirror. While this solution is efficient up to a certain extent, it is limited to a low level of aberration, has limited spatial resolution and reaction speed. For instance,

such devices are at the moment not able to compensate for airflow perturbations. Those apparatus are overall complex and expensive solutions to put in place. Significant efforts have been made to improve the simplicity and the capability of those systems and excellent results are now accessible using these kinds of components.

In this work, an alternative to deformable mirrors is studied. This method, called phase-conjugation, is based on a passive component: a liquid in a cell. When a high energy laser pulse is focused inside the liquid, it triggers a nonlinear effect: Stimulated Brillouin Scattering which reflects the beam, inverting the wavefront in the process. Thus, all the phase aberrations are passively and automatically reversed during the reflection. It is then possible to design laser amplifiers in such a way that the beam performs a round trip in the amplifiers with aberration inversion occurring at the middle of the round trip. In this case, the amplifiers self-correct their defects during the second pass, no matter the distribution of thermal distortion. The on-shot self-correction makes this component compatible outside of a slow-varying steady state, e.g. before thermalisation, with laser operating in unusual, transient pulse train regime. It is then particularly adapted to reach maximal theoretical repetition rate, typically up to the kilohertz and beyond. While the component was already partially documented in the literature, very few scientific or industrial systems do make use of it due to its allegedly lack of reliability. The framework of the thesis then consisted in the demonstration of the capacity (or lack thereof) of those devices to be reliably used in a high energy laser system. This includes the study of its aberration compensation capacities, its stability, its reliability and the absence of degradation of spatial and temporal properties of the laser beam during the nonlinear reflection. A particular emphasis was placed on the conservation of the temporal profile of the input pulse to make accessible unusual energy distribution in time required for some of the applications described above.

This work takes place in a partnership between two laboratories, *Charles Fabry Laboratory* (LCF) and *Laboratoire pour l'Utilisation des Lasers Intenses* (LULI) as well as the *Amplitude laser group* company. The Ph.D. grant is provided by Amplitude laser group, a world leader for the development of femtosecond laser systems. Amplitude is looking, through this work, to develop a high energy laser product line operating at high repetition rate above the kilowatt regime. At amplitude, the development was supervised by Dr. Stéphane Branly, manager of the Nanosecond Advanced Lasers of the R&D department of Amplitude. The Charles Fabry laboratory (LCF), located in Institut d'Optique, is a long-time partner of Amplitude laser, hosting a common laboratory with Amplitude. In particular, Dr. Frédéric Druon, the supervisor of this thesis, is an experienced researcher in laser design. His former work included development of wavefront correction systems and

publications on thermal effects and their impacts on laser beams. The Laboratoire pour l'Utilisation des Lasers Intenses (LULI), located in École Polytechnique, being dedicated to the conception and use by the scientific community of high-intensity and high energy lasers was also interested in the prospects offered by such a technology. This laboratory is hosting several high energy laser beamlines including HERA ($200\ \mathrm{J}$, $1\ \mathrm{shot/20min}$), LULI2000 ($1\ \mathrm{kJ}$, $1\ \mathrm{shot/h}$) and APOLLON ($10\ \mathrm{PW}$) lasers facilities. Dr. Patrick Audebert and Dr. Loïc Meignien, co-supervisor of the thesis, allowed us to access the HERA laser chain to perform the high-energy experiments described in this thesis. This multi-laboratory partnership made possible experimental studies on the behaviour of SBS cells up to unprecedented energy level.

The current work and the manuscript is divided in five parts:

- Firstly, the formalism of the nonlinear effects is summarised. The Stimulated Brillouin scattering equations are derived and some important properties of the phase conjugation are presented under this formalism. This part aims to provide the reader all the theoretical tools needed to properly understand the physical process, the limits encountered and the key experimental design choices.

- In the second chapter, the aforementioned equations are solved using increasingly complex numerical simulations models. The numerical methods and their respective limits are detailed and the results they provide are then used to design the experimental test-bed of the phase conjugate mirror used afterwards.

- Subsequently, a state of the art of experimental Brillouin cells in the literature are presented. We also justify all the technical choices made to acquire a usable Brillouin cell and the experimental setups used during the thesis.

- We then present the experimental results regarding a first Brillouin cell and look to demonstrate the usability of the component for a laser system compatible with energy levels of $10\ \mathrm{J}$, at $5\ \mathrm{Hz}$ repetition rate. In this chapter, we experimentally explore the temporal and spatial fidelity, the cell behaviour at the Joule energy level and the long term stability of such a component.

- In a fifth chapter, we use a high energy laser chain from LULI to study the behaviour of a phase conjugate mirror under extremely high level of input energy. In this chapter, we aim to investigate the usability, or lack thereof, of an SBS mirror in kilojoule class lasers development perspective. The main goals are the demonstration of a good reflectivity, stability and spatial and temporal fidelity.

One highlight of this work concerns the record of energy reflected in a Brillouin cell, operating at energy level $> 100\ \mathrm{J}$, then compatible with multi-kilojoule round-trip architectures. The component is able to reflect input beams with extremely high efficiency (> 99%) while properly inverting the wavefront. More than twenty waves of spherical aberration were properly compensated for with near perfect accuracy. If properly designed, the apparatus is capable of doing so while conserving the temporal profile (power level along time) and the spatial profile (transverse distribution of energy) of the input beam. The innovative design choices allowing those results were the usage of a, relatively counter intuitive, very short focal length to limit at maximum the propagation of the acoustic wave, creating spatio-temporal coupling and disturbing the reflected pulse temporal profile. Another innovation was the usage of high contrast temporal shaping capabilities of the laser chain to generate initiation of the SBS effect with a tailored pedestal placed before the main pulse impulsion. This pedestal initiated the mirror effect before the main arrival of the energy and prevented ionization caused by the short focal length, as well as reducing compression effects to a maximum. Because of those two innovations, no fundamental limit on the input energy level is found. The two main drawbacks identified during this work are a limit on the maximal input aberration inside the cell to keep the spatial profile intact, and a slight degradation of the energy and wavefront stability during the reflection. Overall, thanks to our innovative approach, the component can be used in a wider range of systems: high energy and high repetition rate lasers, up to few tens of joules at hundreds of hertz and for extremely high energy lasers, up to the kilojoule and beyond with outstanding simplicity and adaptability. We show that SBS mirrors are compatible with temporal shaping, for generation of arbitrary energy deposition through time on target and thus make whole new applications accessible to SBS-mirror based systems.

1 - Phase conjugation by backward Stimulated Brillouin Scattering

1.1 . Introduction

While this work is mainly experimental, the formalism related to the Brillouin cell has to be studied to explain and understand most of the design choices since they are firstly derived based on either direct calculation or numerical simulations. In this first chapter, we aim to present a comprehensive study of the non-linear effect, allowing the reader to understand the origin of the process as well as several characteristics of Stimulated Brillouin Scattering (SBS) reflection. Firstly, a quick derivation of the fundamental equations of backward SBS is made based on non-linear optics formalism. While this derivation is largely based on several theoretical works [1, 2], this work focuses only on high-energy reflection in the backward direction. The orientation of this chapter is therefore adapted to integrate only the backward component, neglecting the other scattering directions. On the contrary, while SBS equations are generally derived assuming a steady-state regime and plane waves (or confined mode in fibres), we keep the spatial and temporal dependence in the derivation in order to simulate the spatio-temporal 4D (x, y, z, t) evolution in the following chapters.

Following the derivation of the fundamental equations, we largely simplify the problem to present to the reader simple yet quantitative process explanations. We exhibit the physical meaning of some key parameters such as the Brillouin gain and the phonon lifetime and put in evidence the intensity threshold behaviour of an SBS mirror. While this part cannot be used on its own to design a high-energy laser Brillouin cell, those behaviours will be met again in the simulation and experimental chapters.

At last, we use all the aforementioned approach to make an overview of different ways the SBS phenomenon can be used in the several fields in the literature. This last part completes the understanding of the phenomenon by broadening the view of the reader on the different conditions the process can appear and places the scope of this particular work inside the literature.

1.2 . Stimulated Brillouin Scattering

Scattering of light is a physical phenomenon defined as the deviation of electromagnetic waves away from their straight trajectory due to inhomogeneities encountered in the medium they propagate through. While scattering can have many different origins and effects, we separate in this

chapter *Spontaneous* scattering, that occurs from inhomogeneities naturally present in the medium at rest, from *Stimulated* scattering in which the inhomogeneities are created by an interaction between a radiation and the medium. In our case spontaneous scattering occurs on density inhomogeneities caused by thermal noise in the medium and the spontaneously scattered wave gives, in turn, birth to stimulated scattering. The theoretical spontaneous interaction between light and acoustic waves was originally described by Leon Brillouin in 1922 [3], whose name was given to the process.

Stimulated Brillouin Scattering (SBS) is a non-linear process experimentally demonstrated in 1964 [4]. It can occur in all the states of matter (solid, liquid, gas, plasma) and is characterized by a strong scattering in one direction with a shift of the initial wavelength. While spontaneous Brillouin scattering can be observed for many different input spectra, SBS is mostly present for narrow linewidth radiations (below GHz) of high intensity. Those two characteristics obviously make lasers the light source most adapted to SBS observation.

SBS originates from the interaction between two optical fields and an acoustic field. An initial electromagnetic radiation (in our case, a focused laser beam called pump beam) of frequency ω_P initially gets scattered spontaneously by the matter. This initial scattering occurs on thermal-noise-induced index inhomogeneity in the medium. At the quantum level, this inhomogeneity is described by an acoustic phonon of frequency Ω. The scattered light (Stokes beam) gets Doppler shifted and thus oscillates at the frequency $\omega_S = \omega_P - \Omega$. Interferences between pump and Stokes beam subsequently create a beating at frequency Ω. Stimulated scattering occurs when, under proper circumstances, this beating acts as a source term for the original acoustic wave and thus creates positive feedback for the scattering. In those conditions, an exponential feedback loop occurs and most of the input light can be scattered into the Stokes beam.

While different physical phenomena can trigger the positive feedback, the stronger term is usually electrostriction. This defines the inclination of matter to get attracted and displaced toward the maxima of an electromagnetic field. During SBS, the interference pattern between the pump and Stokes beam acts as a quasi-standing wave of frequency Ω. The particles of the medium thus gets pulled by the average maxima of this resultant standing wave and create in turn a density wave of frequency Ω. This density wave being formally equal to the original phonon wave that produced the initial scattering, a positive feedback loop is triggered and Stimulated emission starts. This whole effect is summarized in Fig.1.1.

SBS can also be initiated not by a standing wave but by an initial contra-propagative wave of frequency $\omega_s = \omega_p - \Omega_B$. In this case, the

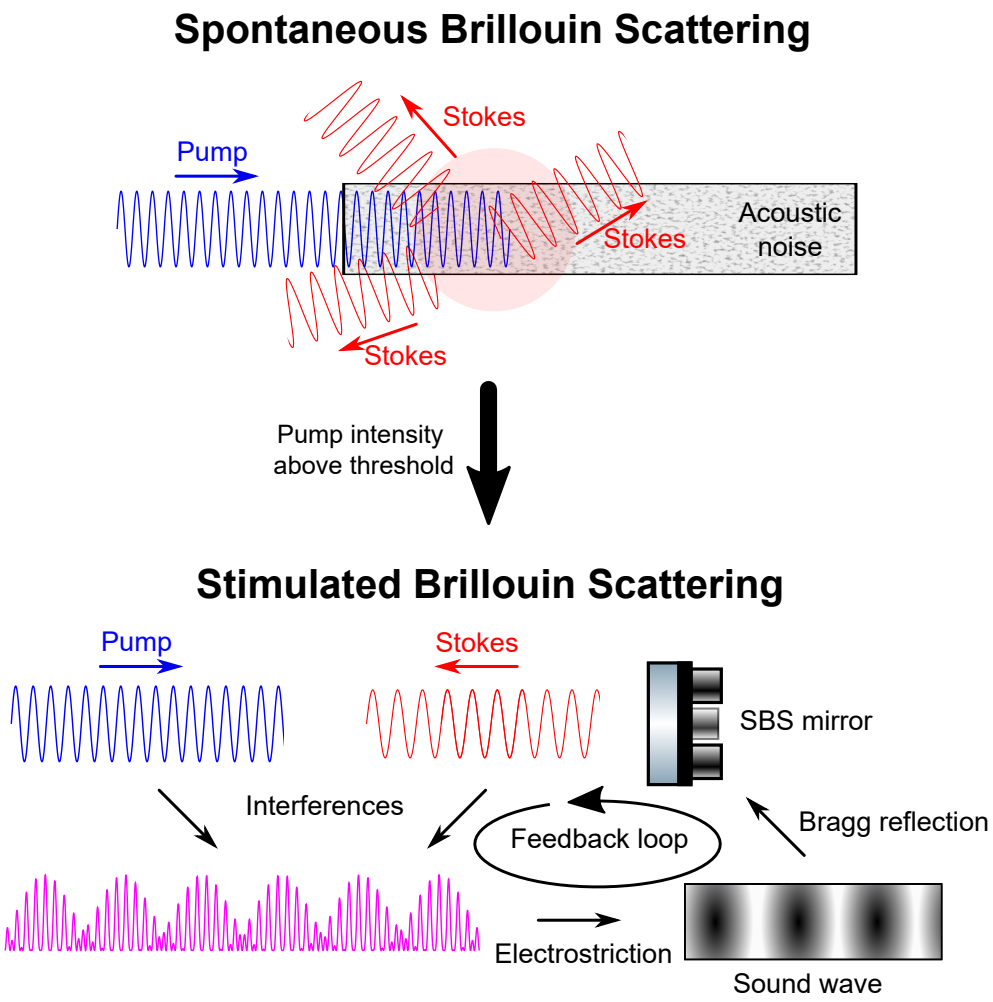

Figure 1.1: Representation of Stimulated Brillouin Scattering effect.

acoustic wave is generated by the beating and the process does not start from noise. Under those conditions, the sound wave frequency is imposed by the electromagnetic waves. This configuration is called *Amplifier configuration* in opposition to the *Generator configuration* described above. While the amplifier configuration is generally more efficient, all the experimental part of this work is experimentally achieved using the generator configuration. This approach allowed us to neglect, in the following, a possible mismatch between the Stokes frequency and the preferential acoustic wave frequency. We will now formally describe the geometry of SBS process:

Since the interaction has to respect momentum conservation, the respective wave vectors $\overrightarrow{k_P}$, $\overrightarrow{k_S}$ and $\overrightarrow{k_B}$ of the pump, stokes and acoustic waves follow the equation

$$\overrightarrow{k_S} = \overrightarrow{k_P} - \overrightarrow{k_B} \tag{1.1}$$

As the acoustic wave frequency is well below optical frequencies, we have

$$k_P \approx k_S \tag{1.2}$$

and thus

$$k_B \approx 2 \cdot k_P \sin(\theta/2) \tag{1.3}$$

with θ the angle between the pump and stokes beam.

This is the Bragg condition diffraction of light by an acoustic wave. SBS can then theoretically happen in all directions. Yet SBS usually happens for backward-propagating stokes wave as this direction presents the highest gain and can be stimulated over long distances [5]. For this particular kind of interaction, we have $\theta = \pi$ the conservation of momentum thus simply writes:

$$\overrightarrow{k_B} = 2\overrightarrow{k_P} \tag{1.4}$$

At this point we have already simplified the formalism of SBS by restricting the geometry of the system to 3 collinear waves travelling along the z axis of the coordinate system (x, y, z):

- The pump wave, E_P, forward travelling electromagnetic field of frequency ω_P and wave vector $\overrightarrow{k}_P$.

$$E_P(\overrightarrow{r}, t) = A_P(\overrightarrow{r}, t) \exp^{i(k_P z - \omega_P t)} + \text{c.c.} \tag{1.5}$$

- The Stokes wave, E_S backward travelling electromagnetic field of frequency ω_S and wave vector $\overrightarrow{k_S}$.

$$E_S(\overrightarrow{r}, t) = A_S(\overrightarrow{r}, t) \exp^{i(-k_S z - \omega_S t)} + \text{c.c.} \tag{1.6}$$

- The Acoustic wave, $\rho(\overrightarrow{r}, t)$ forward travelling sound wave of frequency Ω and wave vector $\overrightarrow{k_B}$. Physically, $\rho(\overrightarrow{r}, t)$ represents the local density of the nonlinear medium, and ρ_0 its average value.

$$\tilde{\rho}(\overrightarrow{r}, t) = \rho_0 + \left(\rho(\overrightarrow{r}, t) \exp^{i(k_B z - \Omega t)} + \text{c.c.}\right) \tag{1.7}$$

In the following, we write the equations describing both electromagnetic waves and the acoustic wave evolution in space and time as well as the coupling terms, and derive the fundamental equations of Stimulated Brillouin Scattering.

1.2.1 . Nonlinear optics

To derive the electromagnetic part of the fundamental formulas, we start from the classical Maxwell equations describing the propagation of electromagnetic waves in matter. They are given by Eq.1.8-1.11.

$$\nabla \overrightarrow{D} = \rho \tag{1.8}$$

$$\overrightarrow{\nabla} \times \overrightarrow{H} = \overrightarrow{j} + \frac{\partial \overrightarrow{D}}{\partial t} \tag{1.9}$$

$$\nabla \overrightarrow{B} = 0 \tag{1.10}$$

$$\overrightarrow{\nabla} \times \overrightarrow{E} = -\frac{\partial \overrightarrow{B}}{\partial t} \tag{1.11}$$

With $\overrightarrow{E}$ the electric field, $\overrightarrow{D}$ the electronic displacement, $\overrightarrow{B}$ the magnetic field and $\overrightarrow{H}$ the auxiliary magnetic field.

We place ourselves in a non-magnetic medium, with no current, and no free charges. The constitutive equations can then be reduced to:

$$\overrightarrow{B} = \mu_0 \overrightarrow{H} \tag{1.12}$$

$$\overrightarrow{D} = \epsilon_0 \overrightarrow{E} + \overrightarrow{P} \tag{1.13}$$

with $\overrightarrow{P}$ the polarisation of the medium. This polarisation is, in the general case, dependent on the input field and is described by the relation:

$$\overrightarrow{P} = \epsilon_0 \chi(\overrightarrow{E}) \overrightarrow{E} \tag{1.14}$$

In most media, χ, the nonlinear susceptibility, is only weakly dependent on the electric field and can thus be expanded in several terms, linear and nonlinear.

$$\overrightarrow{P} = \epsilon_0 \left(\chi^{(1)} + \chi^{(2)} \overrightarrow{E} + \chi^{(3)} \overrightarrow{E}^2 \right) \overrightarrow{E} = \epsilon_0 \chi^{(1)} \overrightarrow{E} + \overrightarrow{P_{NL}} \tag{1.15}$$

While the terms relative influences usually decrease with their order, the $\chi^{(2)}$ term only exists for centrosymmetric systems. In our case, since the media used are fluids, no symmetry exists and only the $\chi^{(3)}$ term is considered. However, even in centrosymmetric systems, the SBS process

can reach considerable magnitude since phase matching is automatically reached.

This $\chi^{(3)}$ is in itself composed of 3 main terms each describing a different non-linear effect:

- The Stimulated Brillouin Scattering.
- The Stimulated Raman Scattering effect, similar to SBS but involving optical phonons.
- The Kerr effect, or self phase modulation.

While all of those effects are known and observable, SBS has a larger linear gain and is therefore dominant for narrow-linewidth, high intensity laser radiations [1]. In the following, both Kerr effect and Raman scattering will be neglected and the nonlinear polarisation term will be reduced to its SBS contribution.

To get the propagation equations of an electromagnetic radiation inside the medium, we combine Eq.1.9, Eq.1.10 and Eq.1.11 to find the classical propagation equation:

$$\Delta\overrightarrow{E} - \frac{n^2}{c^2}\frac{\partial^2\overrightarrow{E}}{\partial t^2} = \mu_0\frac{\partial^2\overrightarrow{P_{NL}}}{\partial t^2} \tag{1.16}$$

with c the speed of light in vacuum and n the linear optical index of the medium. In this case, the term representing absorption of light by the medium has been removed. While this term can in some cases be of significant importance, we will see later in this chapter that the characteristic propagation distance of the light in the medium is too small for the absorption to represent a large amount of losses. For Brillouin mirrors with long length (for example in fibres) or for unconventional high-absorption media, this term should be added for accurate description of the effect.

It is clear that the final equations will describe the evolutions in time ($\frac{\partial\overrightarrow{E}}{\partial t}$) and space ($\Delta\overrightarrow{E}$) of both the pump and stokes wave. The feedback loop on matter is described by the $\overrightarrow{P_{NL}}$ term and should include both the amplitude of the acoustic wave and the electromagnetic feedback. In the following, we derive the electrostrictive term, component of $\overrightarrow{P_{NL}}$ by equating the electromagnetic energy stored locally by the particles in the standing wave field and to the work of a force introducing a pressure gradient in the medium.

1.2.2 . Electrostriction

To derive the feedback of the electromagnetic waves on the medium, we first consider the influence of a standing field $\overrightarrow{E}$ on a particle. In the presence

of the field, the molecule develops a moment $\overrightarrow{p} = \epsilon_0 \alpha \overrightarrow{E}$. The total energy U stored in the polarisation is then

$$U = \int_0^{\overrightarrow{E}} \overrightarrow{p}\, d\overrightarrow{E} = \frac{1}{2}\epsilon_0 \alpha E^2 \tag{1.17}$$

and the electrostrictive force $\overrightarrow{F_{es}}$ associated to this potential energy is thus

$$\overrightarrow{F_{es}} = \nabla U = \frac{1}{2}\alpha\epsilon_0 \nabla(E^2) \tag{1.18}$$

The particle is therefore pulled toward the field maxima.

We now place ourselves at the macroscopic scale. The overall energy contained per unit volume is:

$$u = \frac{1}{2}\epsilon\epsilon_0 E^2 \tag{1.19}$$

If we consider an ensemble of particles (i.e. a material medium), we can describe the macroscopic displacement of the particles by studying the local density ρ of the medium. The local variation of the density due to the electromagnetic field $\Delta\rho$ induces a change $\Delta\epsilon$ in the susceptibility given by:

$$\Delta\epsilon = \left(\frac{\partial\epsilon}{\partial\rho}\right)\Delta\rho \tag{1.20}$$

This, in itself, changes the stored electromagnetic potential energy by a value

$$\Delta u = \frac{1}{2}\epsilon_0 E^2 \Delta\epsilon = \frac{1}{2}\epsilon_0 E^2 \left(\frac{\partial\epsilon}{\partial\rho}\right)\Delta\rho \tag{1.21}$$

and this energy is equal to the work per unit volume Δw performed to compress the medium

$$\Delta w = -p_{es}\frac{\Delta V}{V} = -p_{es}\frac{\Delta\rho}{\rho} \tag{1.22}$$

With p_{es} the contribution to the pressure due to electrostriction. By equating the work Δw and the variation of the stored potential energy $\Delta\rho$, we can write

$$p_{es} = -\frac{1}{2}\epsilon_0 \gamma_e E^2 \tag{1.23}$$

where we introduced the electrostrictive constant $\gamma_e = \rho(\partial\epsilon/\partial\rho)$. Eq.1.23 describes the pressure as being negatively proportional to the field: even macroscopically, the particles tend to get pulled toward field maxima.

While this is an interesting result on its own, we still need to describe the actual susceptibility change. For that, we calculate the density change:

$$\Delta\rho = -\rho\left(\frac{1}{\rho}\frac{\partial\rho}{\partial p}\right)p_{es} = \frac{1}{2}\epsilon_0\gamma_e\rho C E^2 \tag{1.24}$$

With C the material compressibility.

This derivation implied the presence of a static electric field. For actual electromagnetic waves, the static field term is replaced by the dynamic field averaged over a certain time. In this case, the value of γ_e and C depends on the integration time. They represent the capacity of the medium to respond to specific frequency components. In particular, the macroscopic displacement of molecules requires a certain amount of time usually in the nanosecond range and acts as a low-pass filter on the integration time.

In the case of SBS, two waves of slightly different frequencies interact which leads to the apparition of slowly varying field as well as optical frequencies. The medium response is in this case, only for the slowly-oscillating field at Ω frequency.

$$\Delta\rho = \frac{1}{2}\epsilon_0\gamma_e\rho\langle\overrightarrow{E}\cdot\overrightarrow{E}\rangle_{1/\Omega} \tag{1.25}$$

Finally, this electrostriction phenomenon can be related to the standard susceptibility formalism by writing:

$$\Delta\chi = \Delta\epsilon = \left(\frac{\partial\epsilon}{\partial\rho}\right)\Delta\rho = \frac{1}{2}\epsilon_0 C\gamma_e^2\langle\overrightarrow{E}\cdot\overrightarrow{E}\rangle_{1/\Omega} \tag{1.26}$$

by identifying the terms in 1.15, and by considering the Ω frequency as very low compared to the other frequencies $\Omega \approx 0$, we find:

$$\overrightarrow{P_{NL}} = \Delta\chi\overrightarrow{E} = 3\epsilon_0\chi^{(3)}|\overrightarrow{E}|^2\overrightarrow{E} \tag{1.27}$$

using Eq.1.26 and Eq.1.27 subsequently gives

$$\chi^{(3)} = \frac{1}{3}C\gamma_e^2 \tag{1.28}$$

The electrostriction is thus a third-order nonlinearity. While numerical evaluation of $\chi^{(3)}$ does not lead to a high amplitude, it can lead to extremely strong process through propagation and with the influence of the feedback mechanism.

1.2.3 . Coupled equations

We previously calculated the nonlinear polarisation source term. We can now introduce it in the nonlinear equation propagation for the electromagnetic waves to derive the fundamental equations of the SBS

phenomenon coupling pump, stokes and acoustic waves. In this part, we aim to reach the 3 coupled differential equations needed for further investigation of the phenomenon.

Slowly varying envelope approximation While we have currently derived the electromagnetic equations in the general case, the scope of this work targets high energy lasers of wavelength in the near-infrared, with limited frequency bandwidth and timescale above nanosecond. To derive the fundamentals equations of SBS further, we use a classical approximation called *Slowly Varying Envelope Approximation* or SVEA. This reduces the study to laser pulses whose temporal amplitude varies slowly compared to an oscillation period.

$$\frac{\partial A}{\partial t} \ll \omega A \tag{1.29}$$

and spatial variation are small over a distance of one wavelength

$$\frac{\partial A}{\partial z} \ll kA \tag{1.30}$$

Those two conditions are almost always valid for temporal variation of the nanosecond timescale and for optical frequencies, as well as reasonable focusing conditions. In our case, the validity can be checked by considering a monochromatic beam of wavelength $\lambda = 1\ \mu\mathrm{m}$, with a FWHM temporal width of $\tau = 10\ \mathrm{ns}$.

$$\frac{\partial A}{\partial t}/A \approx 1/\tau = 10^8\ \mathrm{s}^{-1} \ll 2.10^{15}\ \mathrm{s}^{-1} = 2\pi c/\lambda$$

The same way, if the characteristic damping length of the pump beam in the medium is above the micrometre, the second order derivative of the spatial part of the propagation equation can be neglected. Quantitative characterisation of this damping length will be given later in this chapter and usually are on the millimetre range.

Sound-wave equation The acoustic wave propagation is written as [6]:

$$\frac{\partial^2 \tilde{\rho}}{\partial t^2} - \Gamma' \nabla^2 \frac{\partial \tilde{\rho}}{\partial t} - v^2 \nabla^2 \tilde{\rho} = \overrightarrow{\nabla} \cdot \overrightarrow{f} \tag{1.31}$$

with Γ' the damping parameter of the sound wave, v the velocity of sound in the medium and $\overrightarrow{f}$ the driving force per unit volume being $\overrightarrow{f} = \overrightarrow{\nabla} p_{es}$. Calculating this force using Eq.1.23 gives

$$\overrightarrow{\nabla} \cdot \overrightarrow{f} = \epsilon_0 \gamma_e k_B^2 \left(A_P A_S^* \exp^{i(k_B z - \Omega t)} + \text{c.c.} \right) \tag{1.32}$$

Where only the cross terms corresponding to slow oscillations were kept to take into account the frequency dependence of γ_e mentioned in Sec.1.2.2.

Comparing the phonon damping time (≈ 1 ns) to its velocity (≈ 500 m/s), the sound wave is almost static during the duration of the SBS interaction. The spatial propagation factor can therefore be neglected. SVEA further reduces Eq.4.10 to:

$$\left(\frac{\partial}{\partial t} + \Gamma_B/2\right)\rho = \frac{i\epsilon_0\gamma_e k_B^2}{\Omega} A_P A_S^* \tag{1.33}$$

With $\Gamma_B = k_B^2\Gamma'$ the decay parameter. This characterises the damping time of the stimulated sound wave and will prove in the following to be one of the most important parameters.

Electromagnetic waves equations We previously derived the nonlinear propagation equations for electromagnetic waves (Eq.1.16). When injecting the value for the nonlinear polarisation given Eq.1.27, and using the SVEA, the equation becomes:

$$\begin{aligned}\left(\frac{n}{c}\frac{\partial}{\partial t}A_P - ik_P\frac{\partial A_P}{\partial z} + \frac{1}{2}\nabla_\perp^2 A_P\right)\exp^{i(k_P z-\omega_P t)} + \text{c.c.}& \\ = -\mu_0\frac{\partial^2}{\partial t^2}(\frac{1}{2}\epsilon_0 C\gamma_e^2\langle E\cdot E^*\rangle E)& \\ = -\mu_0\frac{\partial^2}{\partial t^2}\left(\frac{\epsilon_0\gamma_e}{\rho_0}\tilde{\rho}E\right)&\end{aligned} \tag{1.34}$$

Where we have separated the spatial dependence of the longitudinal axis and the transverse direction ($\Delta = \nabla_\perp^2 + \partial^2/\partial z^2$). The polarisation dependence of the electromagnetic equations can be removed by simply projecting on the transverse axis for non-birefringent media [7]. By considering only the phased matched terms (meaning, only the components of P_{NL} oscillating at ω_P for the pump wave and at ω_S for the stokes wave) the coupled equations for the optical waves become:

$$\left(\frac{n}{c}\frac{\partial}{\partial t} + \frac{\partial}{\partial z} + \frac{i}{2k}\nabla_\perp^2\right)A_P = \frac{i\omega\gamma_e}{2nc\rho_0}\rho A_S \tag{1.35}$$

$$\left(\frac{n}{c}\frac{\partial}{\partial t} - \frac{\partial}{\partial z} + \frac{i}{2k}\nabla_\perp^2\right)A_S = \frac{i\omega\gamma_e}{2nc\rho_0}\rho^* A_P \tag{1.36}$$

With the approximations $\omega_P \approx \omega_S = \omega$ and $k_P = k_S = k$

With equations 1.33, 1.35 and 1.36, one can see that if we start with only the pump wave, both Stokes and sound wave stay at zero amplitude. As stated before, the initiation of the effect starts on thermal noise which is not represented in the previous equations. To introduce this noise term, we add

a Langevin noise source of amplitude $f(t)$ in the phonon equation. This noise term is a Gaussian random variable, with zero mean [8], and of strength Q:

$$Q = \frac{2k_{Boltzmann}T\rho_0\Gamma_B}{v^2 A} \tag{1.37}$$

With A the area of the considered section, $k_{Boltzmann}$ the Boltzmann constant and T the temperature of the medium. This source term acts as the initial sound wave the pump beam will scatter on. The fundamental equation for the sound wave is then

$$\left(\frac{\partial}{\partial t} + \Gamma_B/2\right)\rho = \frac{i\epsilon_0\gamma_e k_B^2}{\Omega} A_P A_S^* + f \tag{1.38}$$

The triplet of coupled equations 1.38, 1.35 and 1.36 represents the fundamental equations of the SBS interaction and will be used as a basis for the numerical simulations. In the following, we simplify those equations in order to explain the physical meaning of some of the parameters. We will place ourselves in the cw regime to describe the threshold effect of the SBS interaction as well as explicitly calculate the reflectivity and the damping length for simplified configurations.

1.3 . CW regime

Because the fundamental equations cannot be solved formally in the general case, most of the design choices will be made using numerical simulations. The results and phenomena observed by using the simulations being sometime hard to understand, we start by presenting some of the effects characteristic of SBS reflection. In this section, we first define the meaning of the *Brillouin gain*, characteristic of the efficiency of the interaction. Then, we explicitly calculate the reflectivity of a Brillouin cell and identify the threshold effect of the interaction. At last, we study the influence of the propagation depth of the laser in a cell. The relative importance of the parameters of the cell can also be intuited even if the description is simplified

1.3.1 . Brillouin gain

To find the expression of the Brillouin gain, we assume a steady state of the interaction for plane waves. Under those approximations, all the derivatives beside the one along z vanish. Using Eq.1.38, the expression of ρ is then

$$\rho = \frac{2i\epsilon_0\gamma_e k_B^2}{\Omega\Gamma_B} A_P A_S^* + \frac{2f}{\Gamma_B} \tag{1.39}$$

In the case where no SBS interaction exists, the first term of the right-hand side vanishes since the Stokes wave amplitude is 0. On the other hand, if the stimulated process exists, this first term usually dominates and the noise term can be neglected.

By directly injecting this value in the pump and stokes amplitude, assuming SBS interaction, we find:

$$\frac{dA_P}{dz} = -\frac{\epsilon_0 \omega k_B^2 \gamma_e^2}{2nc\rho_0 \Gamma_B \Omega} |A_S|^2 A_P \tag{1.40}$$

and

$$\frac{dA_S}{dz} = -\frac{\epsilon_0 \omega k_B^2 \gamma_e^2}{2nc\rho_0 \Gamma_B \Omega} |A_P|^2 A_S \tag{1.41}$$

which are the equations of perfect energy transfer between stokes and pump waves. In particular, the interaction is perfectly phased matched. Assuming no depletion of the pump, the intensity of the Stokes wave grows exponentially with linear gain

$$gI_P = \frac{\gamma_e^2 \omega^2}{nvc^3 \rho_0 \Gamma_B} I_P \tag{1.42}$$

In this equation, g is the medium Brillouin gain, tabulated for usual materials, which describes the strength of the coupling. Usually, this value is given in centimetre per gigawatt and is on the order of unity for dense matter (for gas, it is highly dependent on the pressure and can range from $1 \cdot 10^{-3}$ $\mathrm{cm/GW}$ to few tens of $\mathrm{cm/GW}$). Experimental values taken from the literature are given in Tab.1.1. The liquids selected in this table are CFCs liquid, widely used as SBS nonlinear medium for their low absorption in the infrared, maximizing reflection, and their high ionization potential, reducing plasma generation and SBS breakdown.

Medium	State	Brillouin gain ($\mathrm{cm/GW}$)
HT-70	Liquid	5.7
FC770	Liquid	3.5
FC3283	Liquid	4.2
SF6	Gas (22 atm)	35
CH4	Gas (100 atm)	65
Silica	Solid	2.9

Table 1.1: Tabulated values of medium Brillouin gain taken from [9, 10] (Values for laser radiation at 1064 nm).

A gain of $1\,\mathrm{cm/GW}$ means that, for a pump beam with $1\,\mathrm{GW/cm^2}$ intensity, the Stokes beam intensity gets multiplied by a factor of e over $1\,\mathrm{cm}$. We already see that the SBS threshold (i.e. the input power at which the Stokes output intensity becomes comparable to the Pump input), depends on both the input intensity and the length of interaction. Fibers are obviously candidates of choice for SBS generation at low energy due to the high concentration of light in their core as well as long propagation distances. For typical phase conjugation mirrors in high energy lasers, the interaction length is on the order of few tens of centimetres up to the meter. In this case, we can already estimate the value of the intensity required to trigger the process to be on the order of $\mathrm{GW/cm^2}$. For a pulsed input beam of $10\,\mathrm{ns}$ duration, focused down to $10\,\mu\mathrm{m}$ at waist, this corresponds to an input energy of the millijoule level.

While exponential gain is valid under the approximation of the non-depleted pump, we can't use this to estimate the characteristic insertion depth of the beam inside the medium since this parameter characterises the distance at which all the pump energy will be transferred into the Stokes wave. As stated in Eq.1.42 during its propagation over a distance L, for small Stokes amplification, the Stokes beam is amplified by a magnitude of:

$$\exp^{gIp\cdot L} = \exp^{G} \tag{1.43}$$

Where G, the linear SBS gain, includes the Brillouin gain, input intensity and interaction length. Because a low medium Brillouin gain can be compensated by higher propagation distance and, more importantly, higher input power, it is not a critical parameter for high-energy SBS conjugation.

1.3.2 . SBS initiation

In Eq.1.41, no mention of the initiation process was made. As stated before if no Stokes wave is injected in the system, no feedback loop is generated. In order to produce the initial Stokes wave, a noise term is introduced in the acoustic wave in Eq.1.38. This noise term is not localised in the medium and can in principle generate backward Stokes wave anywhere in the medium. Yet Stokes waves generated at long propagation depth will travel though longer distances and experience more total gain, in the case of a collimated beam. High energy Brillouin cells for phase conjugation yet present a slightly different geometry: since the input pump beam is expanded to avoid nonlinear effects, or optical damages in the amplifying chain, it has to be focused inside the cell to reach SBS threshold intensities. In this particular case, only the spatial region around focus point reaches the required intensities and the Stokes wave always originates from near focus areas. For this reason in the following, the origin of the z axis is placed at the

focus point and we define:

- The *Insertion Depth* is the distance D between cell entrance (at position $z = -D$) and focus.
- The *Interaction Depth* L_d is the characteristic attenuation distance of the pump beam in steady state regime. It depends on the geometry of the system as well as on the physical parameters.

The configuration is presented in Fig.1.2.

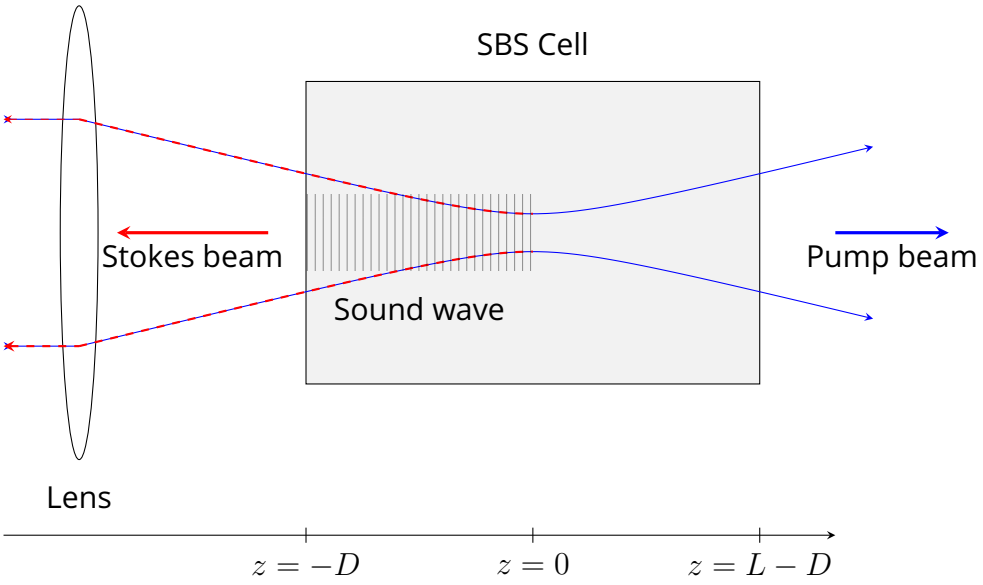

Figure 1.2: SBS cell geometry for high-energy phase conjugate mirrors.

By introducing a focusing geometry, we have implicitly added a dependence of the propagation axis on the intensity. While this dependence does exist in practice and will be extensively discussed in the simulation part, we, for now, assume the beam cross section to be constant in the insertion depth region. This approximation allows for direct solving of the cell reflectivity, and interaction depth for a configuration albeit a lack of accuracy.

Under this configuration, the initial Stokes source term due to thermal noise is written as:

$$I_S(0) = f \cdot I_P(0) \tag{1.44}$$

Where f is a constant of proportionality describing the relative amplitude of the scattered part of a wave on noise in the backward direction.

In the following development, $I_P(-D)$ will be written as I_{Pin} for readability. Using Eq.1.43, the Stokes intensity at the cell output is then

$$I_S(-D) = f \cdot I_{Pin} \exp^{gI_P D} \tag{1.45}$$

And in the small-signal-gain regime, the gain is exponential.

We remind the reader that this small-signal-gain regime assumes low pump depletion (without which the exponential gain is invalid) and also allows to replace $I_P(0)$ the pump intensity at the waist by I_{Pin}, the pump intensity at the cell entrance. Experimental values of f are demonstrated to be around 10^{-11} in the literature [11]. We can now estimate the initial power needed to initiate the effect and introduce a quantitative SBS initiation threshold defined as the minimal pump intensity to reach $R_{th} = 0.01$ reflectivity. In this case, the pump is almost completely transmitted and the non-depletion approximation is valid. For typical values $\mathrm{g} = 6\ \mathrm{cm/GW}$ and an input pulse of $10\ \mathrm{ns}$ duration focused to a $200\ \mu\mathrm{m}$ radius with an insertion depth of $20\ \mathrm{cm}$, SBS initiation is reached for a total pump energy of $\approx 2.7\ \mathrm{mJ}$. Experimental values are slightly higher due to the divergence of the laser beams between focus and entrance and are usually on the order of $\approx 5\ \mathrm{mJ}$ even for smaller spots at focus.

1.3.3 . Reflectivity

We now estimate the reflectivity of the system in steady state in the general case. Using Eq.1.40 and Eq.1.41, the evolution of the pump and Stokes intensities can be written

$$\frac{dI_P}{dz} = \frac{dI_S}{dz} = -gI_P I_S \tag{1.46}$$

Leading to:

$$I_P(z) = I_S(z) + C \tag{1.47}$$

Where $C = I_{Pin} - I_S(-D)$ is a constant that represents the energy not reflected by the cell.

Introducing this relation in Eq.1.46 gives the equation for Stokes intensity along the z axis:

$$\frac{dI_S}{I_S(I_S + C)} = -gdz \tag{1.48}$$

That can be integrated between cell entrance ($z = -D$) and any point before focus ($z = 0$) to give:

$$\ln\left(\frac{I_S(z)(I_S(-D) + C)}{I_S(-D)(I_S(z) + C)}\right) = -gC(z + D) \tag{1.49}$$

Solving this equation for $C = I_{Pin} - I_S(-D)$ gives the value of the amplitude of the Stokes wave anywhere in the medium as a function of the input intensity and the reflectivity $R = I_S(-D)/I_{Pin}$:

$$I_S(z) = \frac{I_{Pin}R(1-R)}{\exp^{gI_{Pin}(z+D)(1-R)} - R} \tag{1.50}$$

This description is what we call in the following the *general case* of SBS reflectivity. The second term of the denominator is always almost negligible, even for high reflectivity. The validity of this approximation is studied in Fig.1.3-1.4.

To retrieve all the parameters as a function of only the input intensity, we use once again Eq.1.47

$$I_P(0) - I_S(0) = I_{Pin} - I_S(-D) \tag{1.51}$$

Where we express $I_P(0)$ as a function of $I_S(0)$ using the threshold condition given by Eq.1.44

$$\frac{1}{f}I_S(0) = I_{Pin} - I_S(-D) \tag{1.52}$$

by multiplying both side of the equation by a factor of f/I_{Pin}, this gives the result:

$$\frac{I_S(0)}{I_{Pin}} = f(1-R) \tag{1.53}$$

and thus, using Eq.1.50

$$f(1-R) = \frac{R(1-R)}{\exp[gI_{Pin}D(1-R)] - R} \tag{1.54}$$

Solving the equation gives the relation between the small signal SBS gain $G = gI_{Pin}D$ and the small signal gain at threshold $G_{th} = \ln(R_{th}/f) \approx 25$:

$$\frac{G}{G_{th}} = \frac{G_{th}^{-1}\ln(R/R_{th})}{1-R} + \frac{1}{1-R} \tag{1.55}$$

This model is presented in Fig.1.3 and Fig.1.4 as *Model 1* and is completely indistinguishable from the general case (where the $-R$ term of the denominator of Eq.1.50 isn't neglected) over the whole reflectivity range. Subsequently, all the calculations in the following will be made with this model.

Eq.1.55 present two terms, each corresponding to an operation regime:

- the first term is dominant for $|ln(R/R_{th})| \gg G_{th}$ that is to say very low reflectivity value. In this case the denominator is close to 1 and the reflectivity grows exponentially with G (and thus with I_{Pin}). We find once again the formula for reflectivity with no pump depletion.

- The second term becomes significant at high reflectivity and describes the actual energy exchange between pump and stokes wave with pump depletion taken into account. For SBS reflection well above threshold and reflectivity above few percent, the term $G_{th}^{-1} \ln R$ can be neglected. The reflectivity is then simply written as

$$R = 1 - \frac{1 - G_{th}^{-1} \ln(R_{th})}{G/G_{th}} \tag{1.56}$$

  and the steady state reflectivity tends to 1 for high G.

The plot of the reflectivity as a function of input energy for a typical pump pulse of duration $10\ \mathrm{ns}$, beam radius of $400\ \mu\mathrm{m}$ and propagation length of $20\ \mathrm{cm}$ in liquid HT70 is shown in Fig.1.3

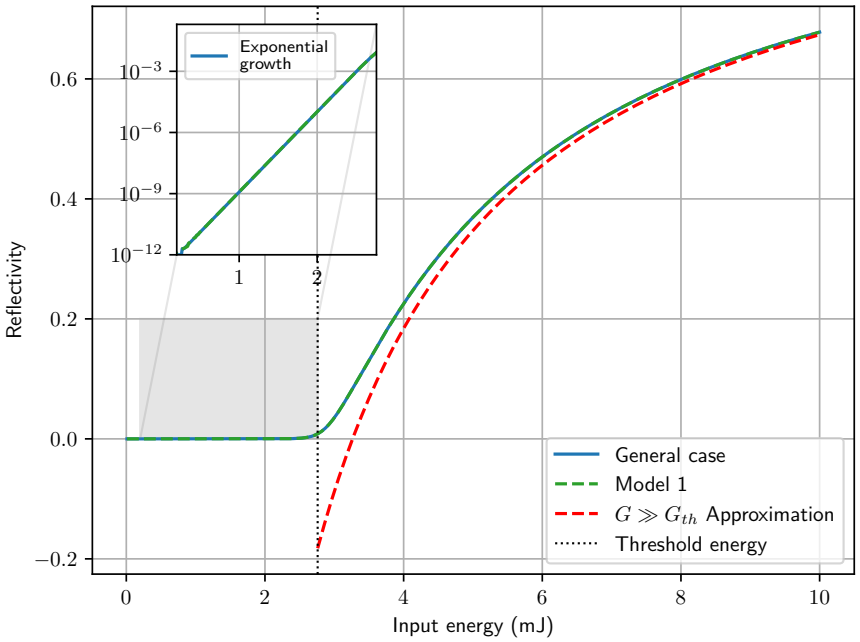

Figure 1.3: Reflectivity as a function of input energy near SBS threshold for a typical pulse from of a Q-switched system with duration $10\ \mathrm{ns}$, interaction distance $20\ \mathrm{cm}$ and beam radius $200\ \mu\mathrm{m}$, assumed constant over the propagation distance.

Theoretically, almost all the pump energy can be transferred into the Stokes wave if sufficient input power is sent into the medium. Since the scope of this work is the use of Brillouin mirrors for high energy lasers, we can expect extremely high reflectivity. This is a very important result: **While**

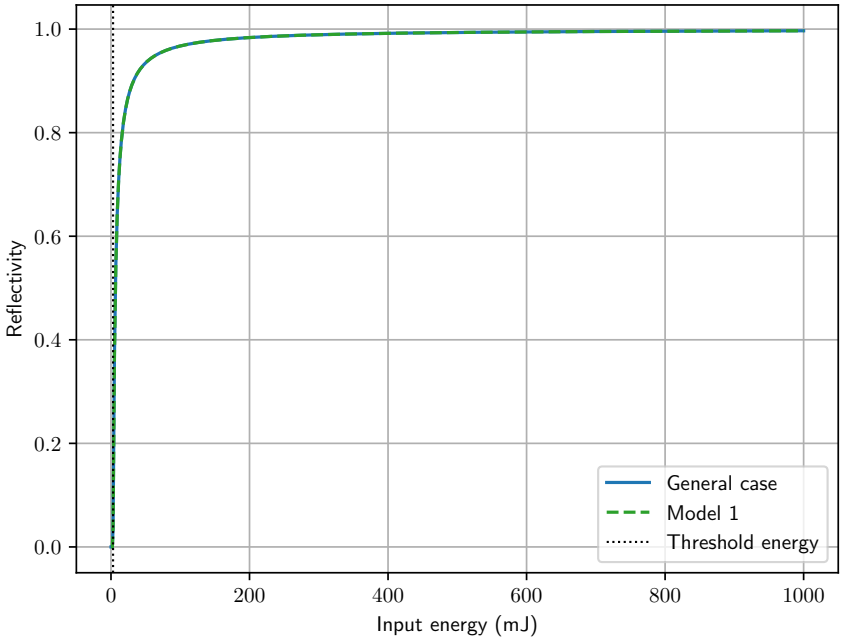

Figure 1.4: Reflectivity as a function of input energy near SBS threshold for a typical pulse from of a Q-switched system with duration $10\ \mathrm{ns}$, interaction distance $20\ \mathrm{cm}$ and beam radius $200\ \mu\mathrm{m}$, assumed constant over the propagation distance.

the phase conjugate mirror corrects aberrations, almost no energy is lost in the process.

1.3.4 . Interaction length

Using Eq.1.56, we can also estimate the insertion depth by calculating the reflectivity of the interaction if the medium had a reduced length $L < D$. In this case, the SBS process does not start from $z = 0$ but from $z = L - D$. The reflectivity is thus:

$$\frac{I_s(-D)}{I_{Pin}} = 1 - \frac{1 - G_{th}^{-1}\ln(R_{th})}{GI_{Pin}L/G_{th}} \tag{1.57}$$

by using the energy conservation during the interaction:

$$I_S(-D) = I_{Pin} - I_p(L - D) \tag{1.58}$$

The output intensity is:

$$I_P(L - D) = I_{Pin}\frac{G_{th} - \ln(R_{th})}{gLI_{Pin}} = \frac{L_d}{L} \tag{1.59}$$

The residual pump power is inversely proportional to the propagation distance in the medium. The characteristic attenuation length called *interaction length* is $L_D = \frac{G_{th}-\ln(R_{th})}{gI_{Pin}}$ and depends on the threshold parameters as well as the input power. Examples of typical attenuation in HT70 are shown in Fig.1.5

The calculation for a high-energy beam of 1 J input energy gives a typical interaction length below 0.7 mm. This is an important result of SBS phase conjugation at high energy: **In steady state, almost all the energy is reflected at the cell entrance**. This experimentally demonstrated fact [12] justifies the removal of the absorption in the propagation equation. Furthermore, since almost no propagation is allowed in the medium, all the other nonlinear effects can be neglected.

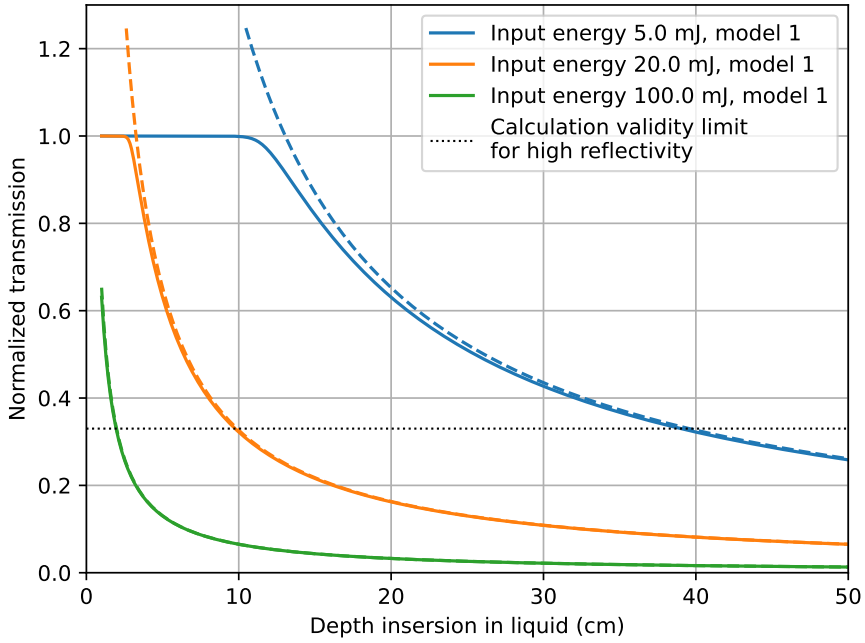

Figure 1.5: Transmission of characteristic input beams of durations 10 ns, with radius 200 µm propagating in HT70. Dashed lines indicate the results given by Eq.1.59, in the strong interaction approximation.

1.3.5 . Limits of the model

Albeit interesting insights on the behaviour of an SBS cell, all the obtained results present significant discrepancies with experimental results. This is due to two invalid hypotheses for phase conjugation in high energy lasers: steady state regime and plane wave approximation.

- By assuming a steady state regime, we removed the losses caused by the response time of the system. Before the acoustic wave creation, the medium is transparent, and the pump wave is not reflected. We thus have to take into account the response time of the system that can be limited by either the acoustic lifetime $\tau_{medium} = 1/\Gamma$ or the typical propagation time of the optical waves D/c.

- By removing the transverse dependence evolution, we simplified the problem. In particular the focusing of the wave is not described in the simplified equations which lead to an overall overestimation of the pump intensity in the medium. To compensate this, we chose to consider a collimated flat-top beam of intermediate size as a compromise between the area near focal spot and the large beam

diameter near the entrance.

- Furthermore, since we assumed a flat-top beam, the spatial profile (local intensity pattern $I(\overrightarrow{r})$) is not described. Subsequently, the spatial defects introduced during SBS reflection are not described. To quickly describe the limitations of the model brought about by this hypothesis, we can imagine the effect on a Gaussian beam. Since the intensity at the edge of the beam is lower than at the centre, the total reflectivity is decreased around the beam edge: we observe a beam narrowing. For the case of an aberrated input beam, the spatial phase is not flat. Therefore, the focal spot size will be increases and the process efficiency drops. In the worst case, the SBS threshold might not be reached at all.

In this section, we have only considered the steady-state regime. In the following, we aim to qualitatively describe the physical effects associated with the transient regime. While the equations are not resolved formally in the general case, no order of magnitude are given. More quantitative results will be thoroughly presented, with the support of numerical simulations, in Chap.2.

1.4 . An introduction to the transient regime

In the previous part, we described the SBS interaction in the steady state regime. For high energy laser phase conjugation, the input laser beam is usually in the nanosecond timescale or below. Under this operating regime we can define three characteristic timescales for the interaction:

- The characteristic amplitude variation of the light waves $A_P(t)$ and $A_S(t)$ and in particular, the input pulse duration τ_{pulse}.
- The characteristic travel time of the waves in the medium. Although we defined an interaction depth in steady state L_D, the actual propagation depth scale in transient regime is taken between cell entrance and focus. It is evaluated at $\tau_{prop} = 2|D|/c$
- The characteristic response time of the acoustic wave to electromagnetic stimulation can be taken directly from Eq.1.38 and is a parameter of the medium. It is noted $\tau_{medium} = 1/\Gamma_B$. Typical values for solids and liquids are $1\,\mathrm{ns}$ and can exceed $10\,\mathrm{ns}$ for gases. Numerical values for typical media are given in Tab.1.2.

Coupled equations with three different dynamic time-scales are known to exhibit complex dynamics if all time scales are close to each others. In the

Medium	State	Response time (ns)
HT70	Liquid	0.9
FC770	Liquid	0.57
FC3283	Liquid	0.6
SF6	Gas (22 atm)	17
CH4	Gas (100 atm)	17
Silica	Solid	0.98

Table 1.2: Tabulated values of typical medium response time. Taken from [9]

case of an SBS cell for phase conjugation, this implies that the output temporal pulse shape of the Stokes wave is not necessarily the same as the input one. While analytical solutions of SBS interaction in the transient regime are available in the literature [7], they always assume weak interaction under the low reflectivity regime using a perturbative approach. Since in the following, only high efficiency interaction will be considered, the explicit description of space-time-resolved wave will be based on numerical simulations. Despite the lack of analytical results, several considerations can still be made. In particular, the theoretical and experimental literature describe the establishment of the Brillouin gain over timescale of τ_{medium} (also referred to as τ_B in this work) [13]. This leads to several remarks about the efficiency of a real phase conjugate mirror.

1.4.1 . Losses by transmission

Since the nonlinear effect needs to be initiated before Stokes amplification is active, the medium is effectively transparent before the pulse and during a few τ_{medium} at the start of the interaction, when pump intensity exceeds threshold. This is usually the main limitation of the reflectivity for phase conjugation at high energy. For this reason **the response time of the medium should be chosen as short as possible to maximize reflectivity.** In particular, gaseous media usually present a response time above the pulse duration and would therefore induce high losses. In the present work, all the considered Brillouin media are liquid, simultaneously presenting short reaction time, low absorption and high resistance to optical damages.

On the one hand, since pre- and post-pulses do not typically have enough intensity to be reflected, they are transmitted through the medium and temporally filtered. An SBS cell can thus act as a pulse cleaner with nanosecond reaction time.

On the other hand, this initiation time also distorts the reflected temporal profile: the leading edge of the pump temporal shape is transmitted and the rise time of the stokes pulse is always above τ_{medium}. This means that sharp leading edges of the order of few hundreds of picoseconds are not conserved. In this case, most of the laser energy contained in this rise time is transmitted as shown in Fig.1.6. For high-energy lasers, this is the main effect preventing perfect reflectivity. Furthermore, for high energy lasers, the transmitted part of the temporal profile is focused down to few tens of micro has can in some case, present enough intensity for generating detrimental nonlinear effects and in the worst case, ionizing the medium. This last phenomenon is known in the literature to deteriorate the quality of the reflection (reflectivity drop and near field spatial modulations) [14].

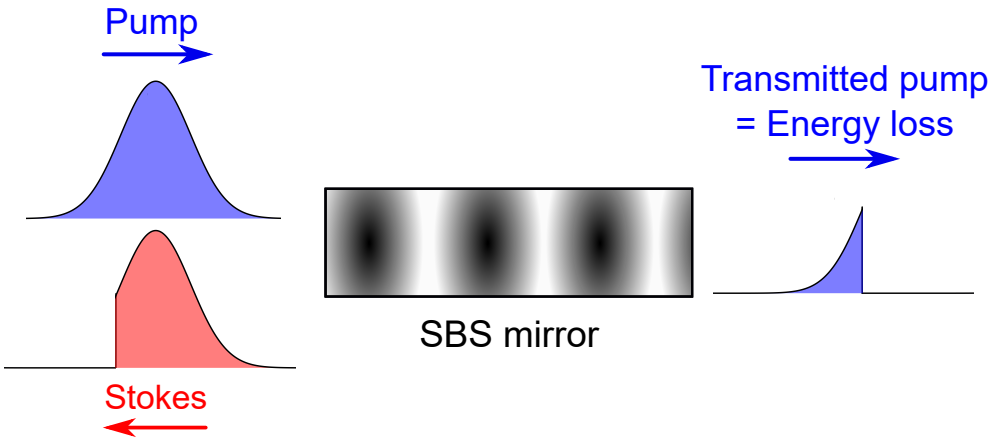

Figure 1.6: Representation of energy loss by transmission. The initiation time of SBS interaction in the pulsed regime implies losses of the first τ_{medium} ns.

1.4.2 . Temporal modulation bandwidth

The same way, the typical temporal modulation bandwidth accessible to an SBS mirror are in the nanosecond timescale. Arbitrary temporal shapes with fast modulations of frequency Γ will be filtered above the cut-off frequency Γ_B. One might also remember that Γ_B is the Brillouin linewidth and thus the frequency domain is also limited to pulses of linewidth below the gigahertz. Phase conjugate mirror are thus limited to single longitudinal modes lasers with nanosecond temporal modulation.

1.4.3 . Compression

A particular case of transient SBS interaction happens when the characteristic propagation time is of the order of the pulse width and longer than the response time of the medium $\tau_{pulse}, \tau_{prop} > \tau_{medium}$. In this case, a pulse compression process can occur:

- When the leading edge of the pump starts initiate the effect and creates a Stokes wave, the sound wave amplitude grows
- The envelope of the sound wave follows the leading edge of the Stokes wave, propagating toward the cell entrance acting as a mirror moving at relativistic speed.
- This mirror following the Stokes pulse, this leading edge picks up all the pump energy it encounters, and this energy gets compressed down to few hundreds of picoseconds.

This process has been theoretically and experimentally demonstrated [15] and allows for peak power increase of more than one order of magnitude. Further emphasis on this particular aspect (and in our case, how to avoid it) will be presented with the help of numerical simulations in Chap.2.

1.5 . Phase conjugation

All the previously derived equations obviously describe a coupling between two optical waves and an acoustic wave. Yet, no mention of the property of interest was made: the phase conjugation capabilities of the component.

On the contrary to a classical mirror, a phase conjugate mirror is able to reverse the sign of the wave vectors at any point in space while conserving the wavefronts. A Stokes beam always retraces the path of the input beam, including its propagation direction, its divergence and all the higher-order aberrations. A comparison of a phase conjugate mirror and a traditional mirror is given in Fig.1.7.

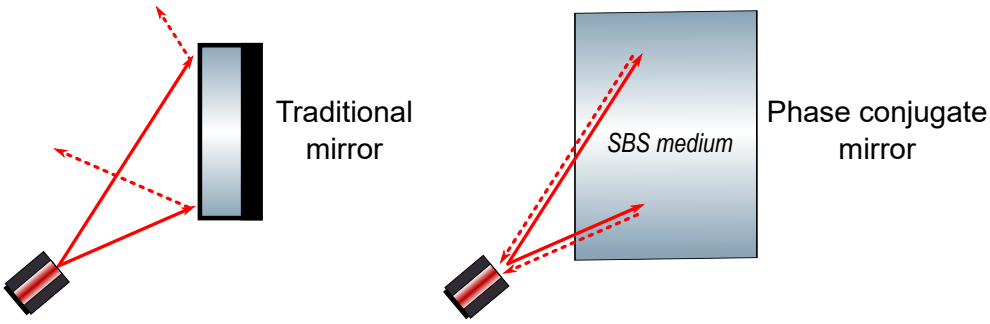

Figure 1.7: Comparison of ray tracing during reflection between traditionnal mirror and phase conjugate mirror.

The phase conjugating part of the fundamental equation is not obvious: even when solving in the CW regime, the gain for the Stokes wave is proportional to the intensity of the pump and no mention of its phase is

made. The entire phase information of the Stokes wave thus comes from the thermal noise phonon it originated from. Thermal noise being purely random, the Stokes wave could in principle contain all possible phase values. The actual phase of the Stokes beam at cell output is therefore the phase component that experiences the highest gain throughout its backward propagation in the medium. Since the total gain can reach 10^{12}, even slight improvements in the small-signal gain can cause extreme differences in total gain for the full propagation.

By doing the gain calculation for every point $\overrightarrow{r}$ in the transverse direction, for a single longitudinal value z, using Eq.1.46, we find:

$$\left\langle \frac{dI_S}{dz} \right\rangle_{\overrightarrow{r}} = \frac{g \int_{\overrightarrow{r}} I_P(\overrightarrow{r}, z) I_S(\overrightarrow{r}, z) d^2\overrightarrow{r}}{\int_{\overrightarrow{r}} d^2\overrightarrow{r}} \tag{1.60}$$

By defining P the total power of the pulse over the transverse direction, $P_i = \langle I_i \rangle = \int I_i(\overrightarrow{r}) d^2\overrightarrow{r}/A$, one gets:

$$\frac{dP_S}{dz} = -g \frac{P_P P_S}{A} \frac{\langle I_P I_S \rangle}{\langle I_P \rangle \langle I_S \rangle} \tag{1.61}$$

and the local gain is maximum for high correlation between the pump and stokes intensity profile (the rightmost term). Since the distribution of pump and Stokes beams intensity will vary during propagation due to the diffraction process, the overall maximum gain is reached for the phase conjugated Stokes wave that maximizes correlation for any given position z, that is to say, the phase conjugate beam. It is counter-intuitive to think that phase conjugation is best achieved for very aberrated input beams that present strong intensity modulation with propagation. On the contrary, near Gaussian input beams are susceptible to excite several Stokes modes with significant spatial correlation and thus degrade the overall phase conjugation. To the best of our knowledge, no experimental confirmation of the increase of phase conjugation with aberration level was observed since it simultaneously tends to deteriorate the intensity at focus point. However, it is possible to observe the excitation of several spatial modes by strongly driving the SBS process [14, 16]. With high pump intensity and relatively clean phase, several stokes modes are amplified, and a mode competition process starts and the overall spatial fidelity of the reflection is decreased. A quantitative definition of this spatial fidelity will be introduced during the analysis of the experimental results.

It is important to consider that the development introduced in this section only holds if no major influence of the propagating media (besides the SBS effect itself) takes place during the propagation. In particular, an absorbing element such as a speck of dust or a plasma might absorb so much incident (and Stokes) wave that the dominant backscattered beam is

not the phase conjugate one [17]. Furthermore, this gain selection principle is only possible during the initiation of the nonlinear effect. Subsequently, there is no guaranty that the phase conjugation will be perfect during the entire duration of the pulse, especially if the spatial properties of the pump vary in time.

1.6 . SBS in the literature

Now that the process has been fully described, we aim to make a modest overview of the different manners it is encountered in diverse fields of the literature. We briefly introduce the conditions for SBS to appear and outline the specific condition for backward SBS to appear and the implications

SBS in high confinement propagation medium Optical fibers are media of choice for SBS generation. Associating high field confinement and thus high light intensity with long propagation distances makes SBS happen "naturally". It is actually mostly referred to as a parasitic effect limiting transmission in high power narrow linewidth fiber amplifiers. Besides that, the process has been used in fibers to generate narrow-linewidth radiation on the order of the Brillouin linewidth (typically $100\ \mathrm{MHz}$). Those are themselves commonly used in microwave generation and for rotation sensing in gyroscopes [18]. The SBS effect itself is used for spatially resolved temperature sensing by measuring the Doppler shift of the Stokes wave [19]. Another high confinement propagation medium are the photonic circuits. Several uses of SBS including SBS resonators and microwave generation [20].

SBS in plasma Inertial confinement fusion is currently a topic of growing interest in the laser community. Following experimental ignition demonstration at the National Ignition Facility [21], this process could potentially lead to unlimited clean energy production. Internal confinement fusion (ICF) initiates ignition with a high energy input light impulsion which creates a hot plasma. In this context of high intensity radiation on small surface, SBS can appear inside the plasma and reflect a part of the input beam [22, 23]. This process significantly reduces the useful part of the input laser energy and is therefore greatly detrimental to fusion process efficiency. Furthermore, Stimulated Forward Brillouin Scattering can also happen in laser induced plasmas and is known to produce light filaments. The resultant spatial inhomogeneities are detrimental to target compression and overall fusion efficiency [24, 25].

Transverse SBS in high-energy lasers chains Although backward SBS is usually the dominant process, in large diameter optical components,

the width of the component is significantly larger than its length. In this case, the propagation distance on the transverse direction is so much greater that transverse SBS becomes dominant. This process induces transmission losses, temporal deformation [26, 27] (since only the trailing end of the pulse is scattered) and, in some case, optical damages [28].

Both the SBS in plasma at the chain output and the transverse SBS in the laser chain make of SBS a parasitic effect in kilojoule class lasers and have led to numerous SBS-suppression architectures such as frequency modulations to broaden the beam spectrum outside SBS amplification bandwidth [29]. This is still an active research field.

We can therefore see that Stimulated Brillouin Scattering appears in several different nonlinear media as either a positive or detrimental effect depending on the application chosen. In all cases, the narrow linewidth, power density, and propagation length are the parameters that can make SBS appear. In the following, we present the numerical simulation describing the SBS interaction in a phase conjugate mirror.

Bibliography

The following bibliography contains all the references cited in this chapter. A full bibliography of the thesis is given after the general conclusion. In addition, every bibliography entry is associated with every paragraph it has been referenced in. The corresponding section numbers are indicated at the very end of the entry.

[1] Govind P. Agrawal. *Nonlinear Fiber Optics*. Academic Press, 2013. 1.1, 1.2.1

[2] Robert W. Boyd. *Nonlinear Optics, Third Edition*. Academic Press, Inc., USA, 3rd edition, 2008. 1.1

[3] Léon Brillouin. Diffusion de la lumière et des rayons X par un corps transparent homogène - Influence de l'agitation thermique. *Annales de Physique*, 9(17):88–122, 1922. Number: 17 Publisher: EDP Sciences. 1.2

[4] R. Y. Chiao, C. H. Townes, and B. P. Stoicheff. Stimulated Brillouin Scattering and Coherent Generation of Intense Hypersonic Waves. *Physical Review Letters*, 12(21):592–595, May 1964. Publisher: American Physical Society. 1.2, 3.1

[5] Amnon Yariv. *Quantum electronics*. Wiley, New York, 1989. 1.2

[6] Immanuil L. Fabelinskii. *Molecular Scattering of Light*. Springer New York, Boston, MA, 1968. 1.2.3

[7] Norman M. Kroll. Excitation of Hypersonic Vibrations by Means of Photoelastic Coupling of High-Intensity Light Waves to Elastic Waves. *Journal of Applied Physics*, 36(1):34–43, January 1965. 1.2.3, 1.4

[8] Robert W. Boyd, Kazimierz Rzaewski, and Paul Narum. Noise initiation of stimulated Brillouin scattering. *Physical Review A*, 42(9):5514–5521, November 1990. Publisher: American Physical Society. 1.2.3

[9] Zhenxu Bai, Hang Yuan, Zhaohong Liu, Pengbai Xu, Qilin Gao, Robert J. Williams, Ondrej Kitzler, Richard P. Mildren, Yulei Wang, and Zhiwei Lu. Stimulated Brillouin scattering materials, experimental design and applications: A review. *Optical Materials*, 75:626–645, January 2018. 1.1, 1.2

[10] W. L. J. Hasi, Z. W. Lu, S. Gong, S. J. Liu, Q. Li, and W. M. He. Investigation of stimulated Brillouin scattering media perfluoro-compound and perfluoropolyether with a low absorption coefficient and high power-load ability. *Applied Optics*, 47(7):1010–1014, March 2008. Publisher: Optica Publishing Group. 1.1

[11] Boris Ya. Zel'dovich, Nikolai F. Pilipetsky, and Vladimir V. Shkunov. Introduction to Optical Phase Conjugation. In Boris Ya. Zel'dovich, Nikolai F. Pilipetsky, and Vladimir V. Shkunov, editors, *Principles of Phase Conjugation*, pages 1–24. Springer, Berlin, Heidelberg, 1985. 1.3.2

[12] M. Maier, W. Rother, and W. Kaiser. Time-resolved measurements of Stimulated Brillouin Scattering. *Applied Physics Letters*, 10(3):80–82, February 1967. 1.3.4

[13] D. Pohl and W. Kaiser. Time-Resolved Investigations of Stimulated Brillouin Scattering in Transparent and Absorbing Media: Determination of Phonon Lifetimes. *Physical Review B*, 1(1):31–43, January 1970. Publisher: American Physical Society. 1.4

[14] C. Brent Dane, William A. Neuman, and Lloyd A. Hackel. Pulse-shape dependence of stimulated-Brillouin-scattering phase-conjugation fidelity for high input energies. *Optics Letters*, 17(18):1271–1273, September 1992. Publisher: Optica Publishing Group. 1.4.1, 1.5

[15] David T. Hon. Pulse compression by stimulated Brillouin scattering. *Optics Letters*, 5(12):516–518, December 1980. Publisher: Optica Publishing Group. 1.4.3

[16] John J. Ottusch and David A. Rockwell. Stimulated Brillouin scattering phase conjugation fidelity fluctuations. In *Conference on Lasers and Electro-Optics (1991), paper CTuW23*, page CTuW23. Optica Publishing Group, May 1991. 1.5

[17] E. Wolf and W. H. Carter. Comments on the theory of phase-conjugated waves. *Optics Communications*, 40(6):397–400, February 1982. 1.5

[18] S. P. Smith, F. Zarinetchi, and S. Ezekiel. Narrow-linewidth stimulated Brillouin fiber laser and applications. *Optics Letters*, 16(6):393–395, March 1991. Publisher: Optica Publishing Group. 1.6

[19] Toshio Kurashima, Tsuneo Horiguchi, and Mitsuhiro Tateda. Distributed-temperature sensing using stimulated Brillouin scattering in optical silica fibers. *Optics Letters*, 15(18):1038–1040, September 1990. Publisher: Optica Publishing Group. 1.6

[20] Benjamin J. Eggleton, Christopher G. Poulton, and Ravi Pant. Inducing and harnessing stimulated Brillouin scattering in photonic integrated circuits. *Advances in Optics and Photonics*, 5(4):536–587, December 2013. Publisher: Optica Publishing Group. 1.6

[21] Indirect Drive ICF Collaboration. Lawson Criterion for Ignition Exceeded in an Inertial Fusion Experiment. *Physical Review Letters*, 129(7):075001, August 2022. Publisher: American Physical Society. 1.6

[22] D. W. Forslund, J. M. Kindel, and E. L. Lindman. Theory of stimulated scattering processes in laser irradiated-plasmas. *The Physics of Fluids*, 18(8):1002–1016, August 1975. 1.6

[23] Qingsong Feng, Lihua Cao, Zhanjun Liu, Chunyang Zheng, and Xiantu He. Stimulated Brillouin scattering of backward stimulated Raman scattering. *Scientific Reports*, 10(1):3492, February 2020. Publisher: Nature Publishing Group. 1.6

[24] Andrew J. Schmitt and Bedros B. Afeyan. Time-dependent filamentation and stimulated Brillouin forward scattering in inertial confinement fusion plasmas. *Physics of Plasmas*, 5(2):503–517, February 1998. 1.6

[25] S. Depierreux, D. Pesme, R. Wrobel, D. T. Michel, P.-E. Masson-Laborde, G. Riazuelo, E. Alozy, N. Borisenko, A. Orekhov, M. Casanova, A. Casner, M. Grech, A. Heron, S. Huller, P. Loiseau, C. Meyer, P. Nicolaï, C. Riconda, V. Tikhonchuk, and C. Labaune. Experimental investigation of the interplay between optical and plasma smoothing induced on a laser megajoule beamline. *Physical Review Research*, 5(4):043060, October 2023. Publisher: American Physical Society. 1.6

[26] J. M. Eggleston and M. J. Kushner. Stimulated Brillouin scattering parasitics in large optical windows. *Optics Letters*, 12(6):410–412, June 1987. Publisher: Optica Publishing Group. 1.6

[27] J. R. Murray, J. Ray Smith, R. B. Ehrlich, D. T. Kyrazis, C. E. Thompson, T. L. Weiland, and R. B. Wilcox. Experimental observation and suppression of transverse stimulated Brillouin scattering in large optical components. *JOSA B*, 6(12):2402–2411, December 1989. Publisher: Optica Publishing Group. 1.6

[28] J. R. Smith, J. R. Murray, D. T. Kyrazis, R. B. Wilcox, T. L. Weiland, R. B. Ehrlich, C. E. Thompson, R. B. Engle, and A. E. Brown. Acoustic Damage To Large-Aperture Optics. In *Mirrors and Windows for High Power/High Energy Laser Systems*, volume 1047, pages 219–225. SPIE, July 1989. 1.6

[29] Christophe Dorrer, Richard Roides, Robert Cuffney, Andrey V. Okishev, Wade A. Bittle, Gregory Balonek, Albert Consentino, Elizabeth Hill, and Jonathan D. Zuegel. Fiber Front End With Multiple Phase Modulations and High-Bandwidth Pulse Shaping for High-Energy Laser-Beam Smoothing. *IEEE Journal of Selected Topics in Quantum Electronics*, 19(6):219–230,

November 2013. Conference Name: IEEE Journal of Selected Topics in Quantum Electronics. 1.6

2 - Numerical simulations

2.1 . Introduction

In the previous chapter, a theoretical description of the SBS effect was introduced and observations on the behaviour of a typical SBS interaction were made. A comprehensive guide of the effects taking place during the reflection of a high energy pulse was presented, and the reader was given some keys to understand the physical processes in action behind the mirror behaviour. However, several approximations were made to solve the SBS coupled equations. In particular, the transient regime of an SBS mirror was deemed too complicated to be solved by hand.

In the scope of this work, we aim to study an SBS cell placed in a pulsed high-energy laser, used to reflect nanosecond pulses and correct their wavefront. This SBS cell is therefore operating in this very transient regime. To properly understand what can be expected of such a system, precise calculations are developed to properly design the cell configuration.

In this chapter, we develop several simulation models allowing to numerically solve the SBS reflection from the set of differential equations developed in Eq.1.35-Eq.1.38. The main complexity lies in the numerical description of the spatial distribution of the laser pulse in the transverse direction. This can be understood as follows:

- If the spatial description is ignored in the numerical model, the transverse distribution of energy will not be calculated. The diffraction effects and focusing will not be implemented. This leads to limited results but correct approximation of the rise time of the reflectivity. A simple extension of the spatial description can be implemented to simulate focusing, without any diffraction effect by simply adjusting the intensity of the optical waves according to the longitudinal position, assuming a perfectly focused, unaberrated beam. This allows a good description of the SBS effect with limited accuracy on the temporal profile conservation.

- The more accurately spatial description is implemented, the finer the effects of diffraction and wavefront aberrations will be simulated. In particular the spatial profile is here of prime importance: a Gaussian spatial shape will lead to less efficient reflectivity on the edges of the pulse since those edges present lower intensity. The wavefront can also play a part: significant aberration level will increase the focal spot size and therefore decrease the maximum intensity inside the cell. We can

expect lower efficiency and high energy threshold in the case of a highly aberrated beam.

In the following, different simulation models of increasing complexity are described and compared here. Those simulations helped design the experimental cells and the setup developed in the next chapters. Most of the quantitative predictive studies are presented in this chapter while the next ones are mostly experimental.

Nevertheless, in this chapter, we still try to keep a strong link with experimental studies. To this aim, all the simulations in the following use tabulated data from existing nonlinear media used in the state of the art. The validity of the simulations are also confirmed using published experimental results. This theoretical study aims to increase the performance of the state of the art and will also allow us to understand some of the limitations encountered by previous experiments. The work presented in this chapter was done at the very start of the thesis and was limited in duration, most of the available time being allocated to experiments. Perfect agreement between simulations and experiments has yet to be reached and several prospects to further improve the numerical model have yet to be explored. In particular, the developed simulation codes still have a significant margin of improvement in terms of calculation speed and memory allocation.

Three models will be developed in the current chapter and will be called respectively 2D, modal-decomposition and Split-step. The *2D* model doesn't take into account the spatial distribution of energy or aberration. The focusing is implemented directly in the Brillouin coupling strength and the input beam is assimilated to a plane wave. The *modal-decomposition* model takes into account the spatial profile and approximates the transverse distribution of energy of the beam by a decomposition on Laguerre-Gauss modes. The modes propagate independently and are coupled through the SBS interaction. Although this theoretically could lead to perfect approximation of the pulse, the computation time is highly dependent on the number of modes used in the simulation and is thus limited. The limit makes the *modal-decomposition* model inadequate to reach fine spatial profile description, especially in our cases, where the spatial profiles of interest are top-hat, presenting sharp edges and requiring a high number of mode for fitting. Yet, accurate temporal profiles have been simulated with this model. This model is currently the finest numerical simulation model available in the state of the art for SBS interaction [1, 2].

The Split-Step model is an attempt to include a full spatial and wavefront description which have previously been assumed unachievable. To this aim, a classical numerical model for beam propagation with nonlinear interaction is implemented and adapted for the first time to free-space SBS. This model

is theoretically capable of simulating arbitrary spatial profile, wavefront and calculating the diffraction for every step. The main difficulty lies in the computation time and memory allocation issues when trying to simulate real beams. Encouraging results have been obtained in the simplest cases studied.

All the algorithms presented in the following were developed in Python 3, and several optimisation schemes were put into place to make the simulations run in a reasonable amount of time. Some are presented, but the description of numerical optimisations is kept to minimum.

Sections 2.2,2.4 and 2.5 of this chapter describes the different simulation models. For each model, a description of the algorithm used is presented, the results of the simulations obtained are then compared with experimental results from [1]. Furthermore, an extension of description of the behaviour of SBS cells for high energy interaction given Sec.1.3-1.4 is presented in Sec.2.3 using the 2D model as a basis.

2.2 . 2D model

2.2.1 . Strategy

The first numerical model developed is a classical finite difference model. To simplify the calculation, we fully neglect the spatial transverse dependence of the Pump, Stokes and Acoustic beams in the nonlinear equations. We therefore make the approximation:

$$E(x, y, z, t) = E(z, t) \tag{2.1}$$

This approximation obviously introduces a certain amount of inaccuracy in the calculated results. Maximum accuracy is reached for almost collimated beams with flat-top spatial profile and deteriorates when significant spatial profile distortions appear through propagation. In particular, this model is unable to simulate focusing effects. Yet, it is possible to replicate a simplified focusing by introducing a correcting factor on the amplitude of the optical waves in the equations:

$$A(z, t) = \langle E(z, t) \rangle / (w(z = 0)/w(z))^2 \tag{2.2}$$

where $w(z)$ is the beam radius at longitudinal position z. In the following, this beam radius is calculated with the classical formula for gaussian beams radius:

$$w(z) = w_0 \sqrt{1 + (z/r_R)^2} \tag{2.3}$$

Because the transverse components of the waves have been neglected, the equations of the SBS (Eq.1.35-1.38) effect become:

$$\left(\frac{n}{c}\frac{\partial}{\partial t}+\frac{\partial}{\partial z}\right)A_P = g_2\rho A_S \tag{2.4}$$

$$\left(\frac{n}{c}\frac{\partial}{\partial t}-\frac{\partial}{\partial z}\right)A_S = g_2\rho^* A_P \tag{2.5}$$

$$\left(\frac{\partial}{\partial t}+\Gamma_B/2\right)\rho = g_1 A_P A_S^* + f \tag{2.6}$$

where g_1 and g_2 are the coupling strength of the nonlinear equations.

$$g_1 = \frac{i\epsilon_0\gamma_e k_B^2}{\Omega} \tag{2.7}$$

and

$$g_2 = \frac{i\omega\gamma_e}{2nc\rho_0} \tag{2.8}$$

with the Brillouin gain g being

$$g = 2g_1 g_2/\Gamma_B \tag{2.9}$$

To numerically solve those equations, we sample the space and time variables. The corresponding sampled variables are noted thereafter α and β, the corresponding continuous variables t_α and z_β can be written $t_\alpha = t_{\alpha=0} + \alpha dt$ and $z_\beta = z_{\beta=0} + \beta dz$

Spatial and temporal derivatives can therefore be calculated using the classical growth rate formula:

$$\left(\frac{\partial A}{\partial t}\right)_{\alpha+1} = \frac{A_{\alpha+1} - A_\alpha}{dt} \tag{2.10}$$

And our aim is then to calculate $A^\alpha_{P\beta}$, $A^\alpha_{S\beta}$ and ρ^α_β for all α and β.

2.2.2 . Calculation

Initial condition SBS interaction starts with a pump beam incident inside a material medium in which only thermal noise is present. For this reason, the initial conditions are:

- $A^\alpha_{P,0}$ is known for every α (initial pump temporal profile). Before the start of the calculation, no pump signal is present in the cell for $\beta > 0$: $\forall\beta > 0, A^0_{S,\beta} = 0$
- $\forall\beta, A^0_{S,\beta} = 0$: There is no Stokes signal in the cell before the start of the interaction.
- The acoustic wave inside the cell is only noise and can be added directly using a white noise term with strength Q given by Eq.1.37.

the initial conditions can then be represented by a 2D graph presented Fig.2.1 where a coloured tile represents a known value (either initial condition or calculated value) for the wave considered.

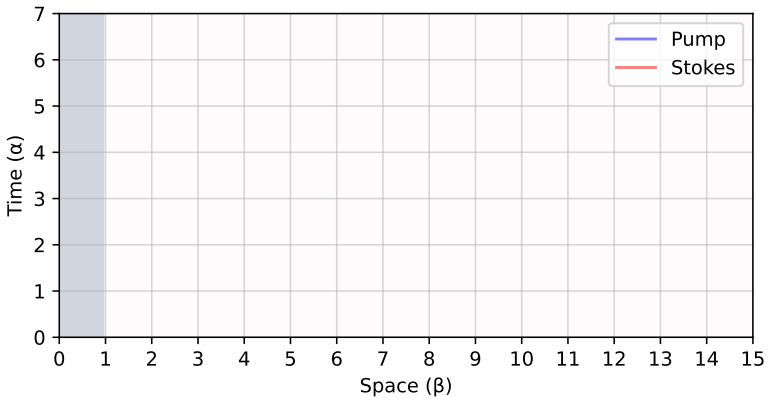

Figure 2.1: Initial condition at the start of the SBS simulation. A coloured tile indicates the presence of a calculated value.

Progression of the calculation To properly simulate the propagation of the optical waves as well as the build-ups from the acoustic wave, the calculation is performed for increasing time, starting for $\alpha = 0$ then $\alpha = 1$ and so on.

We first start by propagating the pump wave in ascending β. Starting from the initial condition at $\alpha+1, \beta = 0$ and using the recursive formula taken from Eq.2.4:

$$A_{P,\beta+1}^{\alpha+1} = A_{P,\beta}^{\alpha+1} + dz \cdot \left(g_2 \rho_{\beta+1}^{\alpha+1} A_{S,\beta+1}^{\alpha+1} - \frac{n}{c \cdot dt} (A_{P,\beta}^{\alpha+1} - A_{P,\beta}^{\alpha}) \right) \tag{2.11}$$

To calculate $A_{P,\beta+1}^{\alpha+1}$, we require the following:

1. $A_{P,\beta}^{\alpha+1}$ that we know since we perform the calculation for ascending β.
2. $A_{P,\beta}^{\alpha}$ that we know since we perform the calculation for ascending α
3. $\rho_{\beta+1}^{\alpha+1}$ and $A_{S,\beta+1}^{\alpha+1}$ that we don't have at this stage. Those two values are then approximated using their value at time α.

This method is represented Fig.2.2

After the calculation of all the $A_{P,\beta+1}$ for fixed time $\alpha + 1$, we then perform the same calculation for Stokes wave in *decreasing* β this time (since this wave is counter-propagative) -as displayed Fig.2.3- and finish by calculating the acoustic wave. At this point we got an approximation of the

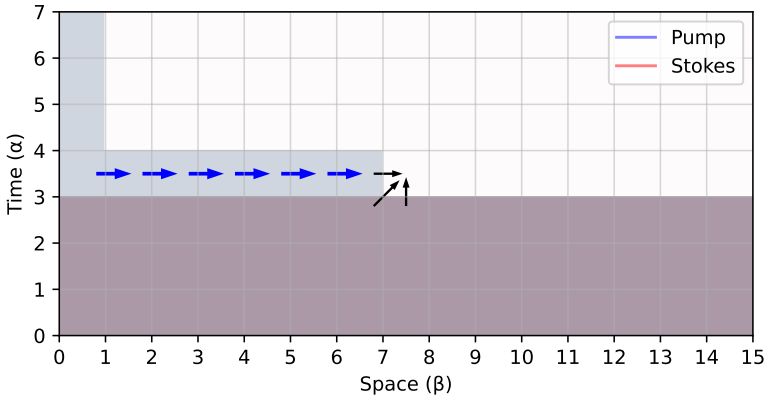

Figure 2.2: Representation of the calculation for all spatial components for a given time. Here, the propagation of the pump beam is represented in blue and the black arrows represent the necessary data to proceed to the calculation of the next step.

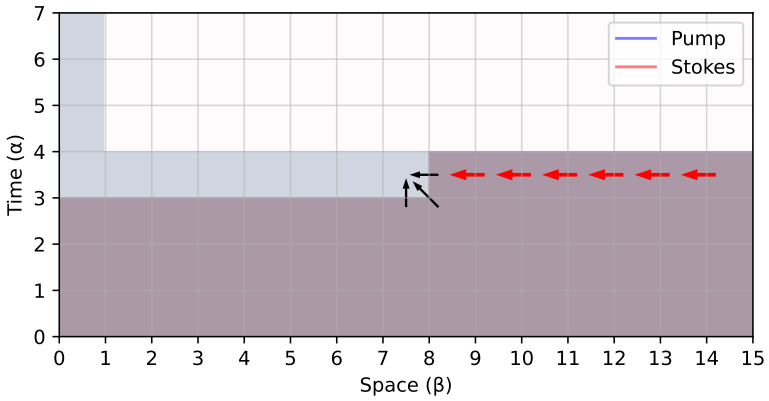

Figure 2.3: Representation of the calculation for all spatial components for a given time for the Stokes beam. The propagation of the Stokes beam is represented in red and the black arrows represent the necessary data to proceed to the calculation of the next step.

true values of all Pump, Stokes and acoustic wave for all β at time $\alpha + 1$. The calculation is performed using a recursive similar to the one given in Eq.2.11.

After an approximation of every value for every wave at time $\alpha + 1$ has been obtained, we can perform the calculation again, using this time the approximated values of the $\rho_{\beta+1}^{\alpha+1}$ and $A_{S,\beta+1}^{\alpha+1}$ as replacement of their true value. This loop can be performed any number of times until convergence of the successively calculated values to their true values. Depending on the sampling chosen, this sometimes proved to be unnecessary. A study on the accuracy of the simulation against this *number of loops* will be presented in

Sec.2.3.2.

Simulation output When the calculation is complete and all the pump, Stokes and acoustic wave complex amplitude have been calculated for all α and β, we obtain the complete description of the interaction for the given parameters. The amplitude of the 2D table obtained can be displayed directly or interpreted to obtain exploitable data such as temporal profiles. Because we used the same set of functions to plot the output of the 2D, 3D modal and 3D split-step, an additional step is added where we reconstruct the spatial profile for every (z, t) to obtain a (r, z, t) description of the beam. In the case of the 2D simulation, this reconstruction is just a Gaussian beam for every (z, t) where the diameter of the Gaussian beam is given by Eq.2.3. This homogenises the display functions but cause some slightly aberrant reconstructed data near waist as the spatial profile at this longitudinal position is often under-sampled. This error in graphic representation does not correspond to an error in calculation as the full calculation is done under the modal approach. In particular, the Pump values for propagation depth after waist is valid and the Stokes values is valid. Examples of such aberrant display can be seen in Fig.2.4 near $z = 0$. We use this opportunity to introduce the 2D-spatio-temporal representation for SBS interaction that will be used to present some of the spatiotemporal effects. It consists of 3 graphs representing the 3 interacting waves, each representing the normalised amplitude of the waves along time and space. It is the exact same representation as presented in Fig.2.1, Fig.2.2 and Fig.2.3 where the binary *full or empty* parameter has been replaced by the actual amplitude of the wave. An example of such a result is shown in Fig.2.4. In those graphs, for proper visibility, the Pump and Stokes graph are plotted with linear dynamic when the acoustic wave is plotted in logarithmic scale.

On this graph, one can directly see the amplitude of the 3 waves along time and space. It is then possible to see the temporal profile for every wave at any depth in the liquid by looking at a cut along the x-axis for a given position. In particular, it is possible to identify the input pump temporal profile and output Stokes pulse after reflection by looking at the cut close to cell entrance. This is presented Fig.2.5.

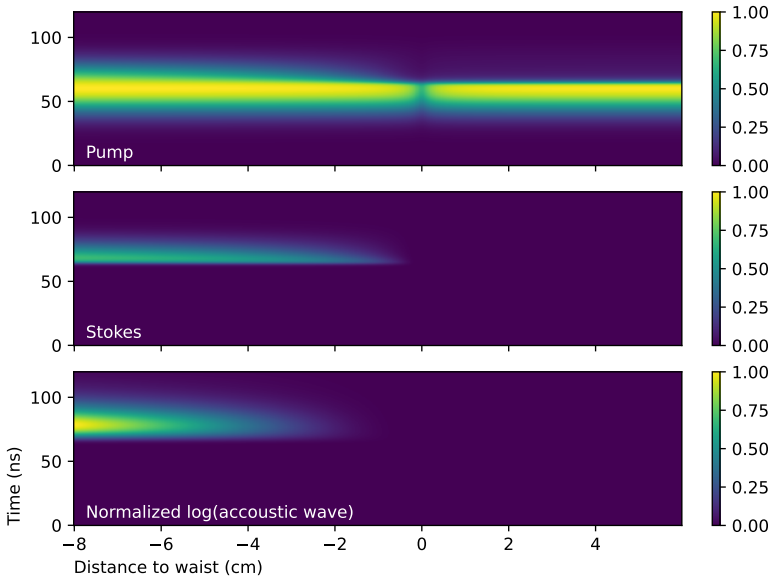

Figure 2.4: 2D spatiotemporal representation of an SBS interaction. Simulation parameters: interaction in SF6 at 20 bar, input wavelength: 1064 nm, input energy 41 mJ, beam focused down at 8 cm inside the 14 cm cell with a beam radius at waist of 20 µm.

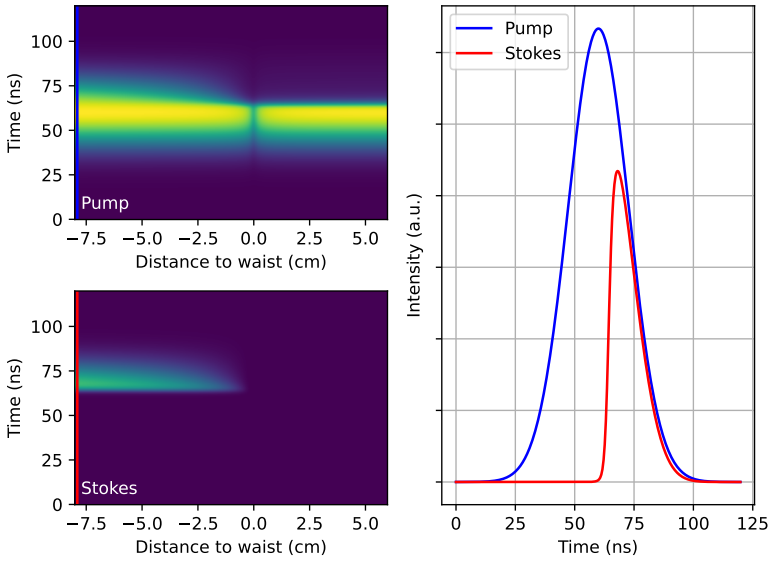

Figure 2.5: 2D spatiotemporal representation of an SBS interaction and the corresponding temporal profile of the input pump pulse and output Stokes pulse.

2.3 . Results

In the previous chapter, we only introduced qualitatively the behaviour of the SBS cell under a transient regime. In this section, we use the developed numerical model to quantify and visualize this behaviour.

2.3.1 . Propagation of optical waves

Firstly, we can directly observe the propagation effects in the cell. For a spatiotemporal graph representing a cell of length L during a time t_{max}, a forward propagating optical wave signal entering the cell at $t = 0$ will arrive at the cell output at $t = Ln/c$ and will therefore present an angle on the graph of θ with

$$\theta = \arctan\left(\frac{a}{b} \times \frac{L \cdot n}{c \cdot t_{max}}\right) \tag{2.12}$$

with a and b respectively the vertical and horizontal sizes of the graph. This is shown Fig.2.6

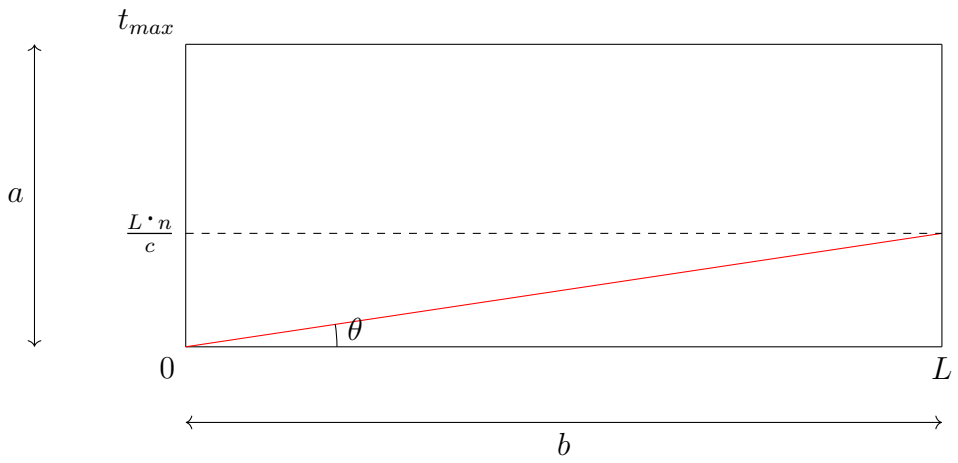

Figure 2.6: Representation of the angle corresponding to the propagation in cell of a forward-propagating optical wave.

This explains why the propagation is hardly noticeable on Fig.2.4. If we calculate the angle θ for the given parameters, we find an angle of $0.007°$. On the contrary, if we represent an SBS interaction in a 1 m cell during 10 ns, the angle is then about $4.9°$ and can be noticed on the graph. In the following, we describe some of the phenomenon observed on the simulations.

2.3.2 . Result accuracy

To evaluate the accuracy of our numerical simulations, we used experimental and theoretical results accessible in the literature [1]. This reference contains several simulation models as well as comparisons between experimental data and simulations. A noticeable difference in their

simulation model is the simulation of the noise term. In our model, we used the thermodynamic expression of the phonon noise term as given in Eq.1.37 when the models described in [1] used the noise term as a fitting parameter to best fit the experiments.

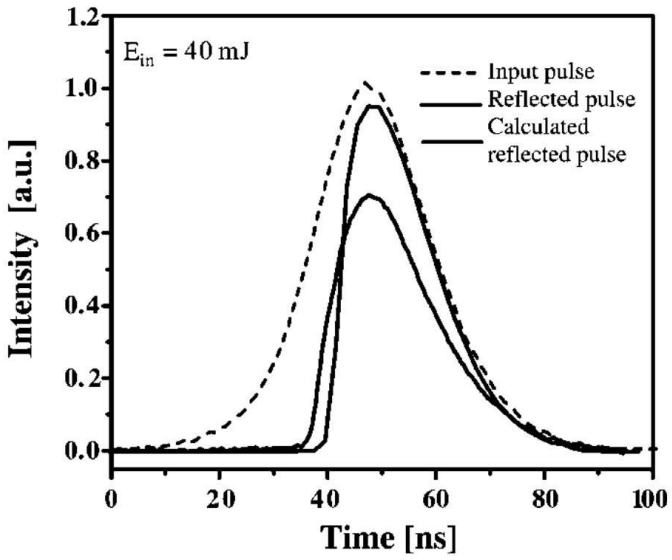

Figure 2.7: Pulse shapes of incident pump pulse and reflected Stokes pulse from SBS in SF6 for a $40\ \mathrm{mJ}$ pulse focused down to $40\ \mu\mathrm{m}$ radius at $8\ \mathrm{cm}$ depth inside the cell. Result obtained from [1].

We present in Fig.2.8 the results of our custom python simulation based on the 2D model presented above. Different simulation results are given for different number of loops. As we can see, the general shape of our simulation corresponds well to the simulated curve of the state of the art: a sharp increase from a low-reflectivity to a high reflectivity in a time close to the response time of the medium. Although the temporal profile of our simulations start about $20\ \mathrm{ns}$ after, probably due to the difference in the noise term description. For all the simulated curves, and in particular even in the state-of-the-art simulation model, the sharpness of the reflected temporal profile leading edge is higher than the experimental one. Furthermore, the reflectivity in steady state is also higher in the 2D model. This can be attributed to the complete lack of spatial description in this numerical model: the experimental spatial profile being Gaussian, the effect is stronger for the beam centre than on the edges. The peak power is increased, and the effect starts for lower pump power (experimental initiation is quicker) but the edges are not properly reflected (steady state reflectivity is lower experimentally).

In the description of the simulation model, we mentioned the need to

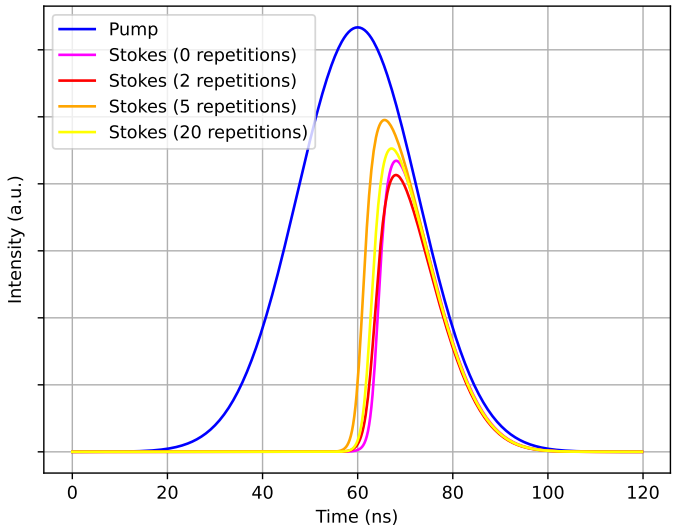

Figure 2.8: 2D simulation performed for the same input parameter as in Fig.2.7 with number of loops increasing from 0 to 20.

have a number of loops to the calculation to reduce the errors at every time step and to reach best simulated temporal shapes. Experimentally, this parameter has very low influence as shown in Fig.2.8. Hence, in the following all simulations will be performed in a single straightforward step to reduce calculation time.

2.3.3 . Response time of the nonlinear medium

As we can see on Fig.2.5, the Stokes wave reflection does not start immediately once the pump intensity at waist reaches SBS threshold (the reflection starts after the pump peak power has already passed). The start of the reflection is delayed by a time proportional to the response time of the medium in which the interaction is taking place. This leads to several consequences on the SBS reflection.

Maximising reflectivity Because the nonlinear medium is effectively transparent before the build-up of the acoustic wave in the medium that takes a time τ_{medium}, all the energy present in the first τ_{medium} in the pump pulse will be transmitted. In a laser system, this means that this energy is lost, and the mirror loses reflectivity. This is one of the reason we chose a dense medium such as liquids: maximizing reflectivity. Although since the small signal gain g is proportional to the response time of the liquid (Eq.2.9 the reflectivity is larger for gas once steady state is reached. In the case of high energy SBS reflection, we saturate the gain so much that this difference in steady state gain doesn't affect the overall efficiency, $> 90\%$ in our typical

operation cases.

In Fig.2.9, we demonstrate this effect with the example of a $15\ \mathrm{ns}$ FWHM Gaussian input pulse of energy $250\ \mathrm{mJ}$. As described, the delay for the SBS effect activation is shorter for the liquid (here, FC770 with response time $\tau_{\mathrm{liquid}} = 0.57\ \mathrm{ns}$) compared to the gas (here SF6 with response time $\tau_{\mathrm{SF6}} = 17\ \mathrm{ns}$). In steady state, the reflectivity for the gas is slightly higher, but the faster initiation time for the liquid clearly compensates for the slight steady state losses.

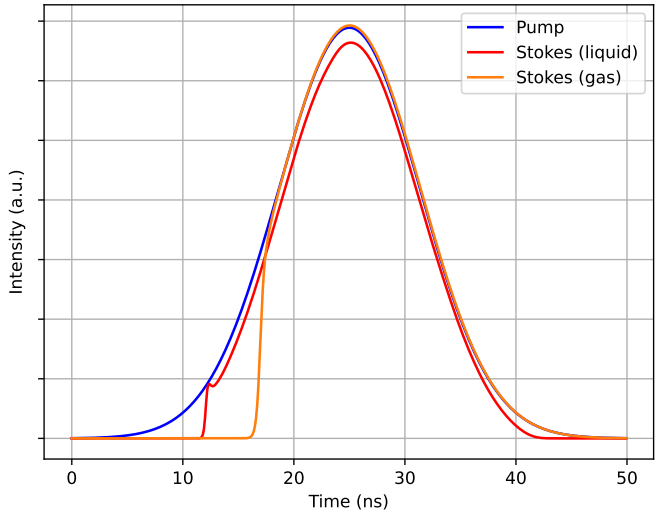

Figure 2.9: Comparison of the output temporal shapes for SBS reflectivity with FC770 liquid and SF6 gas. $15\ \mathrm{ns}$ FWHM Gaussian input pulse of energy $250\ \mathrm{mJ}$. Pump beam focused down to $20\ \mu\mathrm{m}$ beam radius at waist at $8\ \mathrm{cm}$ inside a $14\ \mathrm{cm}$ long cell.

Despite presenting a lower SBS threshold, the gas higher reaction time makes the effective threshold increase for lower pump pulse duration as shown in Fig.2.10. The reflectivity for the gas is then lower for the whole range of energy. Furthermore, although the asymptotic reflectivity might look similar, the spatiotemporal graphs comparison presented in Fig.2.11 shows that the gas reaction time makes most of the reflection happen deeper inside the cell, closer to the waist, making it more susceptible to ionization during high energy operation.

For high-energy SBS interaction, and *especially for short pulses*, the response time should therefore be minimized. This is one of the reasons the interaction medium are mainly liquids.

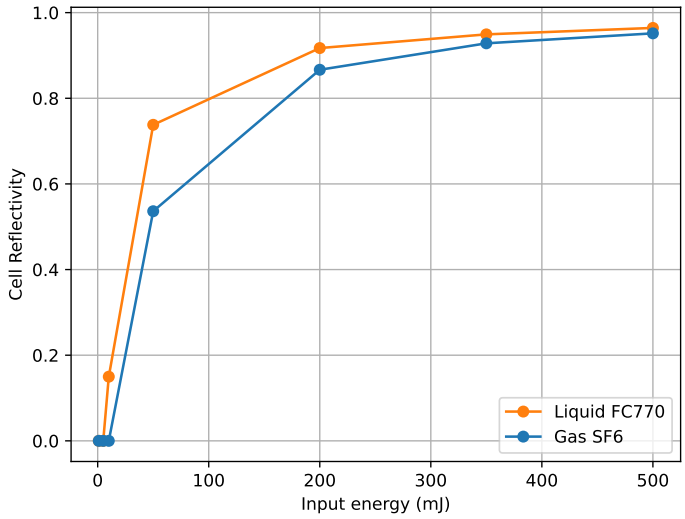

Figure 2.10: Comparison of the reflectivity curves for an SBS mirror filled with FC770 liquid and SF6 gas. $10\ \mathrm{ns}$ FWHM Gaussian input pulse. Pump beam focused down to $20\ \mu\mathrm{m}$ beam radius with waist depth of $8\ \mathrm{cm}$ inside the $14\ \mathrm{cm}$ cell.

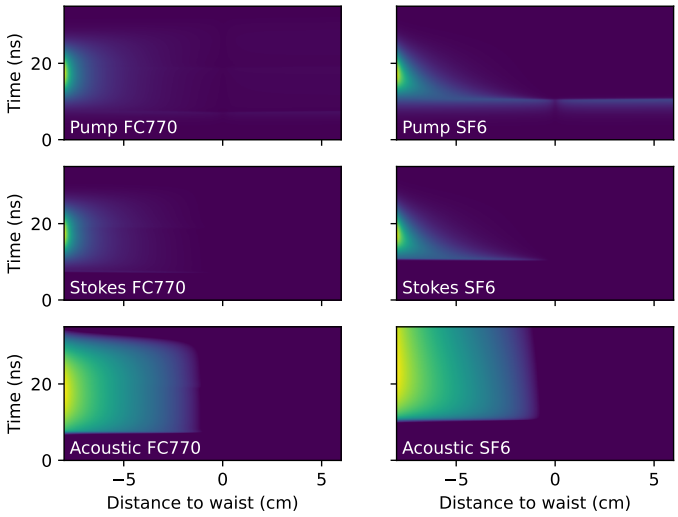

Figure 2.11: Comparison of the spatiotemporal graphs for SBS mirror filled with FC770 liquid and SF6 gas. $10\ \mathrm{ns}$ FWHM Gaussian input pulse of energy $500\ \mathrm{mJ}$. Pump beam focused down to $20\ \mu\mathrm{m}$ beam radius with waist depth of $8\ \mathrm{cm}$ inside the $14\ \mathrm{cm}$ cell.

2.3.4 . Compression

As presented in Sec.1.4.3, SBS interaction is capable in some cases to compress the input pulse. This happens when the propagation time in the cell (between cell entrance window and waist) is larger than the response time of the medium, and on the same order of magnitude than the pump pulse duration. This effect is easily simulated by our numerical model. An example of the input and output temporal profile in a compression configuration is given Fig.2.12

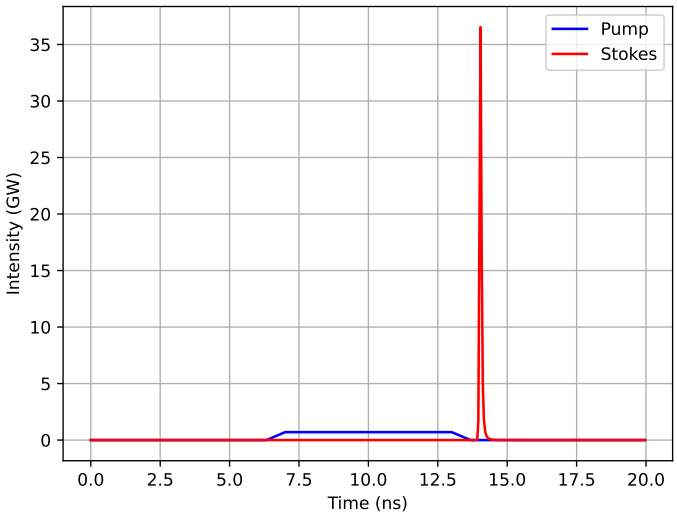

Figure 2.12: Comparison of the input and output temporal shapes in a compression experiment. Input pulse: square pulse, 7 ns duration, with input energy of 5 J. Input beam focused at 90 cm inside a 110 cm cell filled with FC770 ($\tau_{\mathrm{FC770}} = 0.57$ ns. Output pulse duration is simulated to be ≈ 200 ps.)

In this case, it is interesting to look at the spatio-temporal figure and observe the coupling between the 3 characteristic times of the interaction: the pump pulse duration τ_{pulse}, the propagation time τ_{prop} and the response time of the liquid τ_{liquid}. This spatiotemporal representation is given in Fig.2.13

Several observations can be made from this figure:

- Since the input temporal pulse shape is square, the cut of the pump plot along the y-axis at $x = -90$ cm (i.e. at cell entrance) is a square.
- Since, this time, the propagation time is non-negligible before the duration of the pump pulse, we can see the propagation effect: the pump pulse moves on a diagonal: the leading edge of the pulse

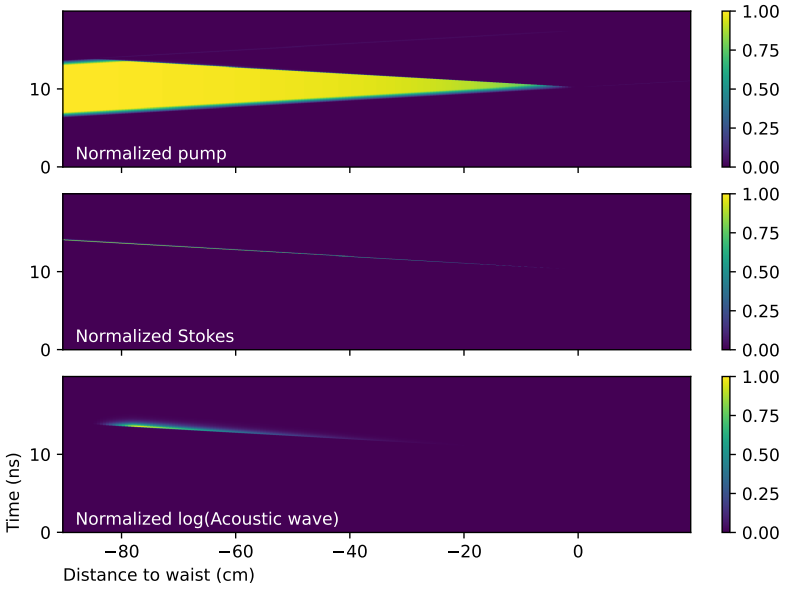

Figure 2.13: Spatiotemporal representation of a compression SBS interaction experiment.

arrives at increased depth in the cell later in time: it propagates in the positive direction.

- Conversely, the Stokes pulse moves on a symmetric diagonal: it propagates in the backward direction.
- Now, when looking at the Acoustic wave graph, we can see that it also propagates in the backward direction, approximately at the same position as the Stokes pulse.

We can in this graph, see the exact scheme explained in section 1.4.3.

1. The Pump beam reaches the focal point and SBS effect is initiated there
2. Backward propagating Stokes pulse propagates backward and stimulates the acoustic wave (mirror effect) before the waist position.
3. The mirror effectively moves from focal point to cell entrance at a speed close to the speed of light.
4. The Stokes pulse leading edge acquires all the energy it crosses with high efficiency.
5. The more intense this leading edge is, the more reflective the acoustic wave is and it triggers a positive feedback loop, most of the pump energy is depleted by the leading edge and leading edge only, and

compressed down to a time that is proportional to the response time of the nonlinear medium, necessary to *activate* the mirror effect, that is to say τ_{medium}.

This depletion effect can be seen on the *Normalised pump* graph on Fig.2.13: the trace of the acoustic beam is visible very clearly as basically no pump signal is allowed to be transmitted through this backward propagating mirror.

This effect is widely known and used in the literature [3–5], although to actually generate efficient compression, different cell architectures (2 cells configuration) are typically used [6].

Relaxation oscillations In the configuration presented in Fig.2.12, compression was achieved in a single spike as the duration of the pump pulse was shorter than (but almost equal to) the time of a round trip from cell entrance to focal point (about $6\ \mathrm{ns}$ in the configuration presented). In Fig.2.14, the same optical configuration is used for the simulation of a pump pulse thrice as long.

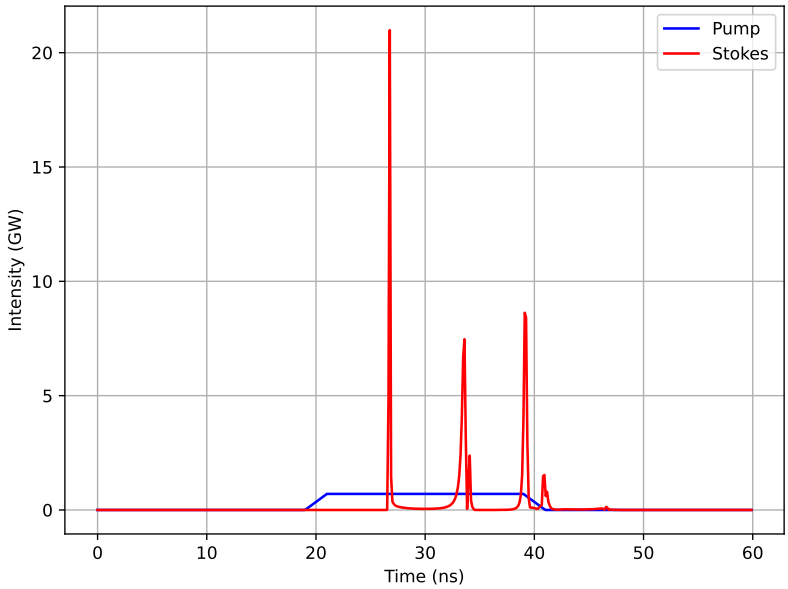

Figure 2.14: Comparison of the input and output temporal shapes in a relaxation experiment. Input pulse: square pulse, $21\ \mathrm{ns}$ duration, with input energy of $15\ \mathrm{J}$. Input beam focused at $90\ \mathrm{cm}$ inside a $110\ \mathrm{cm}$ cell filled with FC770 ($\tau_{\mathrm{FC770}} = 0.57\ \mathrm{ns}$.)

This time, we can still see compression appear, but several spikes are visible in the Stokes pulse temporal profile. This can be explained as follows:

1. The first spike is perfectly equivalent to single spike compression.

2. Because all the pump pulse is reflected by the propagating acoustic wave, the transmitted power reaching the focal point decreases and can go under threshold power. At this point, the acoustic wave at focal point vanishes in a time equal to a few τ_{medium}.

3. This vanishing of the acoustic wave at focal point triggers a vanishing of the generated Stokes wave from focal point and therefore of the stimulated acoustic wave just before.

4. The dissipation of this acoustic wave also propagates toward the cell entrance, following the initial compression spike.

5. When the first Stokes compression spike leaves the cell, the pump pulse still being sent inside the cell do not encounter acoustic wave, is not reflected and can therefore propagate to focus point once again, triggering a new compression spike.

The spatiotemporal graph confirms this interpretation by showing a series of mirrors appearing at focus, moving toward cell entrance and disappearing there(Fig.2.15).

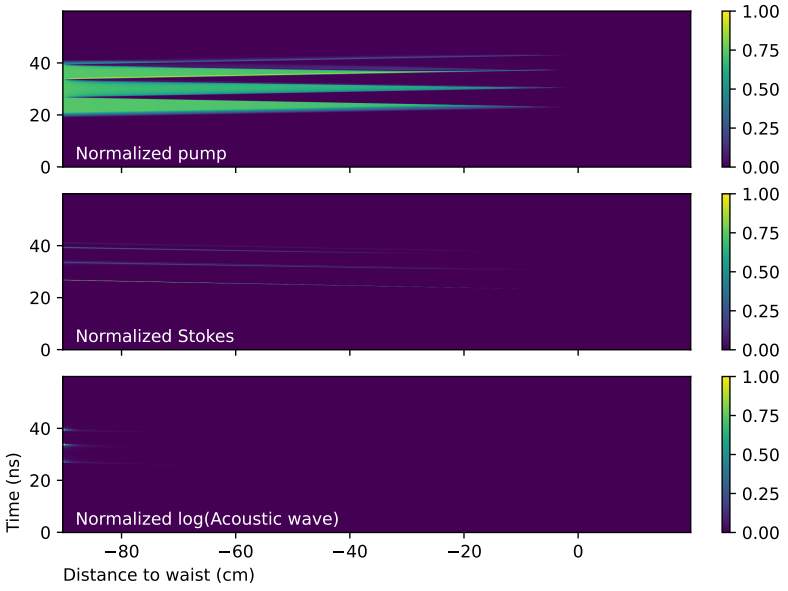

Figure 2.15: Spatiotemporal representation of a relaxation SBS interaction experiment.

Those oscillations have been observed in other simulation models [7] but proper fitting with experimental results has yet to be reached. This can be explained by the poor simulation model capacities to accurately represent the exact spatial beam profile in the cell near focus and therefore simulating

stronger simulation of the acoustic grating, stronger reflectivity near the waist and therefore underestimating the power density reaching the waist during the compression spike displacement toward cell entrance.

2.3.5 . Suppressing compression

We've seen some of the ways SBS interaction can distort the pump pulse temporal profile during reflection due to the displacement of the acoustic wave inside the cell during the interaction. In the scope of this work, we aim to design and demonstrate the proper operation of an SBS cell that can properly conserve any temporal shape sent inside it. Or at least, to get the temporal shape required at cell output. In this part, we investigate a cell design that minimizes the deformation of the pump pulse during the SBS interaction. Firstly, as stated in Sec.2.3.4, the compression spike intensity depends on the amount of energy acquired by the backward propagating Stokes pulse between focal point and cell entrance that is directly dependent on the pump energy present inside the cell during this time.

Hence, reducing compression can be done by limiting this pump energy present in the cell. This can be done in two ways:

- The distance between cell entrance and waist can be minimized.
- The temporal profile of the input pulse can be shaped to minimize energy sent before the first compression spikes exits the cell.

Focal length selection A study of the influence of focal length in a given configuration can be done using the 2D simulations and is presented Fig.2.16. The simulations show that the compression ratio is directly dependent on the focal length. Using shorter focal length leads to a reduction of the compression spike relative intensity. Conversely, using short focal length means tighter focusing and can experimentally lead to nonlinear effects or plasma generation in the medium if the intensity near focus exceeds a certain threshold.

Temporal profile shaping Minimizing the pump energy sent in cell SBS initiation can be done by shaping the temporal profile of the pump pulse to manipulate the acoustic wave dynamics. This allows SBS initiation with power close to threshold and reduction of the compression spike by displacing the grating close to cell entrance without shielding the waist from further pump signal (as the pump power is low, the reflectivity is limited and some energy continues to reach the waist). This solution can be used conjointly with the short focal length selection and solves its main issue. We can indeed use the temporal shaping to limit the power of the pump pulse and therefore avoid parasitic nonlinear effects and ionization of the

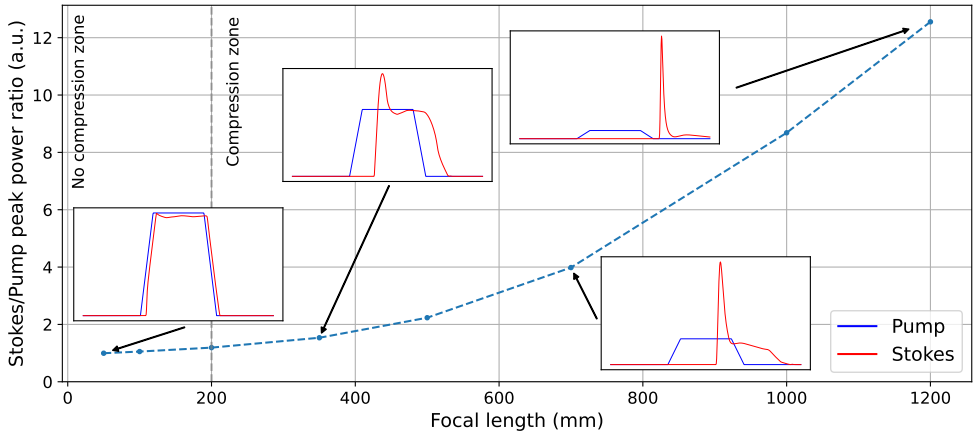

Figure 2.16: Stoke/pump peak power ratio as a function of the focal length used. Simulations made for an input pump pulse of energy $10\ \mathrm{J}$ with a diameter of $93\ \mathrm{mm}$ at cell entrance. Input temporal profile is a $10\ \mathrm{ns}$ square temporal shape with $1\ \mathrm{ns}$ rise time.

nonlinear medium. This becomes practical especially for high energy and sharp rise time. In the scope of this work, this solution was implemented during the high energy experiments in Chap.5.

In this section, we have obtained a way to solve the SBS transient equations by neglecting the transverse description of the three interacting waves. This allowed to introduce quantitatively some behaviour known experimentally in SBS literature. In the following, we introduce a more complex model describing the spatial description as a sum of modes invariant by propagation.

2.4 . Modal decomposition model

2.4.1 . Description of the transverse dimension

An arbitrary laser pulse can be described by a complex function of spatial and temporal variables (x, y, z, t). To simplify this description, we consider only the radial direction $r = \sqrt{x^2 + y^2}$ and the optical waves can therefore be written with amplitude $A(r, z, t)$. To further simplify, this amplitude will be written as a sum of orthogonal modes A_m invariant by propagation. We can therefore write:

$$A_P(r, z, t) = \sum_m a_m(z, t) A_m(r, z) \tag{2.13}$$

$$A_S(r, z, t) = \sum_m b_m(z, t) B_m(r, z) \tag{2.14}$$

In those equations A_m and B_m represent the mode number m on the basis for pump and Stokes waves respectively and depend on z only for the beam diameter (since we introduce focusing as in the 2D model) and a_m and b_m the amplitude of this mode. This amplitude can vary along space and time. The modes themselves are the classical modes of Laguerre-Gauss, and only the modes with radial symmetry are chosen. The modes themselves are given by the formula:

$$A_n(r,z) = \left(\frac{2}{\pi}\right)^{1/2} \frac{1}{\omega(z)} e^{i(n+1/2)\psi(z)} L_n\left(\frac{2r^2}{\omega(z)^2}\right) \times \exp\left[-i\frac{kr^2}{2R(z)} - \frac{r^2}{\omega(z)^2}\right] \tag{2.15}$$

with L_n is the n-th Laguerre polynomial, ω the beam radius as calculated by Eq.2.3, $R(z) = z + \frac{z_R^2}{z}$ the curvature radius and $\psi(z) = \tan^{-1}(z/z_R)$ the angular phase. The first modes of the basis are represented Fig.2.17

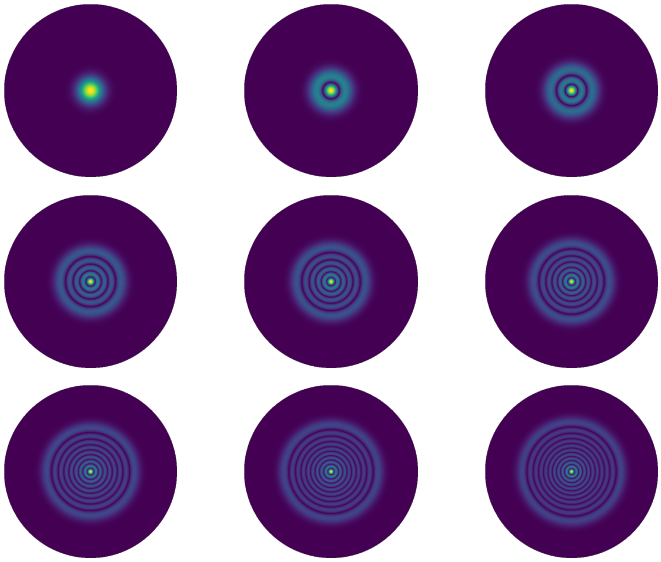

Figure 2.17: First few radial-symmetry modes of the Laguerre-Gauss basis.

As stated above, the modal description implemented by this model limits the accuracy of the numerical representation of the spatial profile. A typical high energy beam used in the industrial lasers is top-hat (or rather a high order supergaussian) and the modal decomposition has a hard time representing this kind of steep-edge energy distribution. This is presented in Fig.2.18. In this figure, we can already see the limitations of the model. Even using a high number of modes, the top-hat behaviour of our beam is poorly reproduced. In particular, in the low mode number top-hat approximation, the spatial extension of the approximated beam on the basis is large

compared to the true spatial profile. Actual simulation performed in this thesis use less than ten modes due to computation time. This simulation model, albeit better resolved than the 2D model, still lacks spatial representation accuracy.

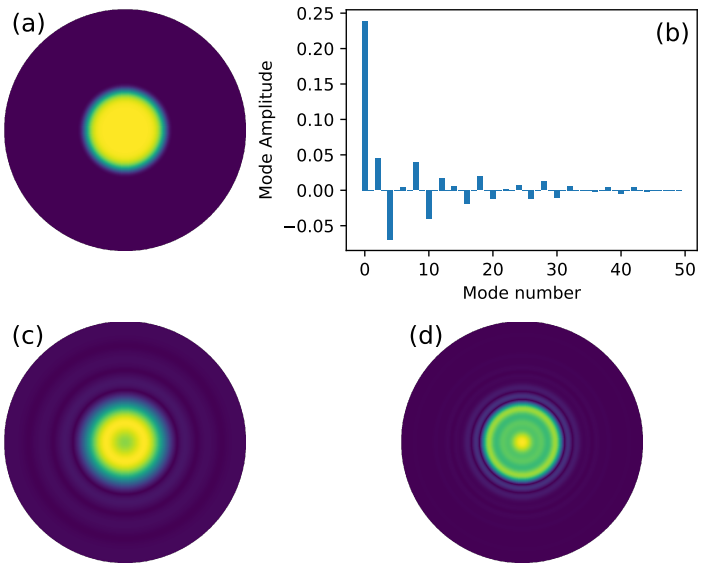

Figure 2.18: Representation of the decomposition of a supergaussian beam on the Laguerre-Gauss mode basis. a) Supergaussian beam of order 5. b) Decomposition of the supergaussian beam on the 50 first modes of the Laguerre Gauss basis. c) Reconstruction of the supergaussian beam using only the 5 first modes d) Reconstruction of the supergaussian beam using the 50 first modes.

2.4.2 . Calculation

In this description, the acoustic wave is not represented on a basis but every couple (i, j) of pump i-th mode and Stokes j-th mode stimulates an acoustic wave of amplitude $c_{i,j}(z, t)$. Those can be calculated using

$$c_{i,j}(z,t) = \int_0^t \left[a_i(z,\tau)b_j^*(z,\tau) + f_{ij}(z,\tau)\right] \exp^{-\Gamma_B(t-\tau)}\, d\tau \tag{2.16}$$

The reflection of a pump beam on mode k can happen on every c_{ij} and can amplify every Stokes mode n. This is schematically represented in Fig.2.16. The probability of the amplification of B_n by reflection of mode A_k on c_{ij} is proportional to the mode overlap g_{ijkn} given by the formula:

$$g_{ijkn} = \int_{-\infty}^{\infty} A_i^* A_k B_j B_n^* d^2 r \tag{2.17}$$

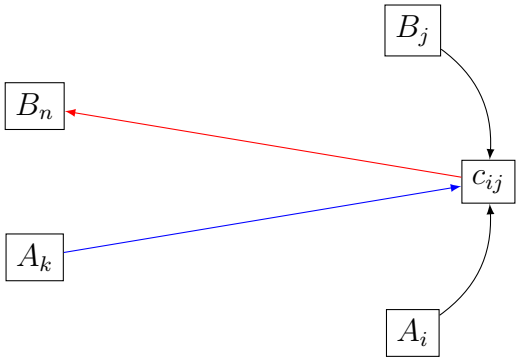

Figure 2.19: schematics of the representation of the energy transfer between mode A_k and mode B_n on acoustic wave c_{ij}.

By inserting the new expression of A_P and A_S as given Eq.2.13-2.14 in the differential equations and then projecting those equations on the Laguerre-Gauss modes, we can obtain a new differential equation for every pump and Stokes mode amplitude:

$$\left(\frac{n}{c}\frac{\partial}{\partial t}+\frac{\partial}{\partial z}\right)a_k = g_1 g_2 \sum_{i,j,k} c_{ij} b_n g^*_{knij} \tag{2.18}$$

$$\left(\frac{n}{c}\frac{\partial}{\partial t}-\frac{\partial}{\partial z}\right)b_n = g_1 g_2 \sum_{i,j,k} c^*_{ij} a_k g_{knij} \tag{2.19}$$

and we then have a system of $2n$ differential equations with n the number of modes used that we can once again sample along time α and space β.

Because the quantities g_{knij} depends on space only, they can be calculated directly using the formula:

$$g_{knij\beta} = \frac{2}{\pi}\frac{\exp(i(k+n-i-j)\cdot\phi_\beta)}{\omega^2_\beta}\int_0^\infty L_k(r)L_n(r)L_i(r)L_j(r)dr \tag{2.20}$$

We set $c^\alpha_{ij\beta} = 0$ for $\alpha = 0$, and they can then be calculated for increasing time steps using a sampled version of formula Eq.2.16:

$$c^{\alpha+1}_{ij\beta} = c^\alpha_{ij\beta}\cdot\exp(-\Gamma_B dt) + dt \times (a^{\alpha+1}_{i\beta}\cdot b^{\alpha+1}_{j\beta} + f) \tag{2.21}$$

and the values of $a^{\alpha+1}_{k\beta+1}$ and $b^{\alpha+1}_{n\beta}$ are then calculable using Eq.2.18-**??** with the sampled variables $a^\alpha_{k,\beta}$ and $b^\alpha_{n,\beta}$:

$$a^{\alpha+1}_{k,\beta+1} = a^{\alpha+1}_{k,\beta} + dz\cdot\left(\frac{\Gamma_B\cdot g}{2}\sum_{i,j,n} c^{\alpha+1}_{i,j,\beta+1}\cdot b^{\alpha+1}_{n,\beta+1}\cdot g^*_{k,n,i,j,\beta}\right) - \frac{dz\cdot n}{c\cdot dt}(a^{\alpha+1}_{k,\beta} - a^\alpha_{k,\beta}) \tag{2.22}$$

$$b_{n,\beta}^{\alpha+1} = b_{n,\beta+1}^{\alpha+1} + dz \cdot \left(\frac{\Gamma_B \cdot g}{2} \sum_{i,j,k} c_{ij\beta}^{*\alpha+1} \cdot a_{k,\beta}^{\alpha+1} \cdot g_{knij\beta} \right) - \frac{n \cdot dz}{c \cdot dt} (b_{n,\beta+1}^{\alpha+1} - b_{n,\beta+1}^{\alpha}) \tag{2.23}$$

Once again, we find that we need the values of a_i and b_j at time $\alpha + 1$ before their calculations. Following the method developed Sec.2.2.2, we first replace those values by the values at time α and then repeat the calculation several time using the approximated solution at time $\alpha+1$ until convergence.

Although those equations might look significantly more complex, they are perfectly analogous to the 2D equations Eq.2.11 where the coupling term, originally just the product of two waves and the coupling strength, has been replaced by the sum of the contribution of every mode. A modal calculation with 1 mode is then rigorously equivalent to a 2D simulation. A schematic of the *modal* method is represented Fig.2.20.

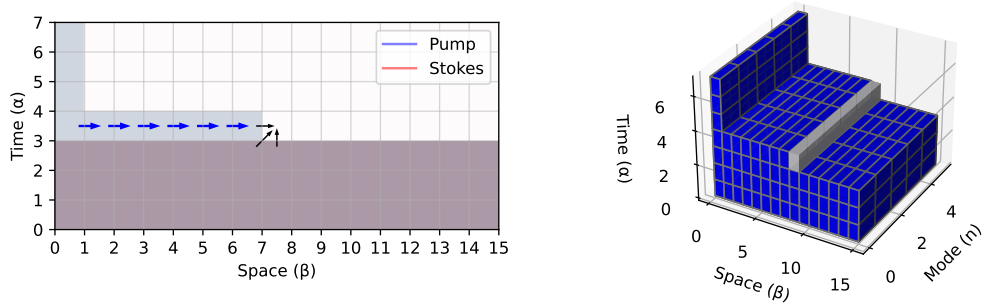

Figure 2.20: Representation of the modal calculation process for the pump wave. All red cubes represent a calculated value for a coordinate (α, β, n). All modes are calculated simultaneously for a given α, β. Stokes calculation is performed after pump calculation for a given alpha.

As one can see on this figure, the number of values to calculate is n time more important than in the 2D model (with n being the number of modes). But the real bottleneck lies in the equations. Indeed, since we split the calculation of A_P and A_S, we have n times more terms to calculate, but the mode coupling makes a sum over every combination of i, j, k appear in the Eq.2.22-2.23. This means that the calculation has a complexity of $\rho(n^4)$. A calculation on a basis of 10 modes then represent a calculation time over 10000 times longer than a 2D calculation. This limited the actual number of modes used in the following to less than 10. Even for this low amount of mode used, some optimisation schemes had to be implemented to reach an acceptable simulation time. In particular, the simulation code in python was converted into *C* for increased speed using the cython module [8].

2.4.3 . Results

Temporal profile By using the *modal* simulation model, we can reach a higher spatial and temporal resolution than achieved with the previously described *2D model*. Simulation results for an increasing number of modes and input condition similar with Fig.2.5-2.7 is given in Fig.2.21

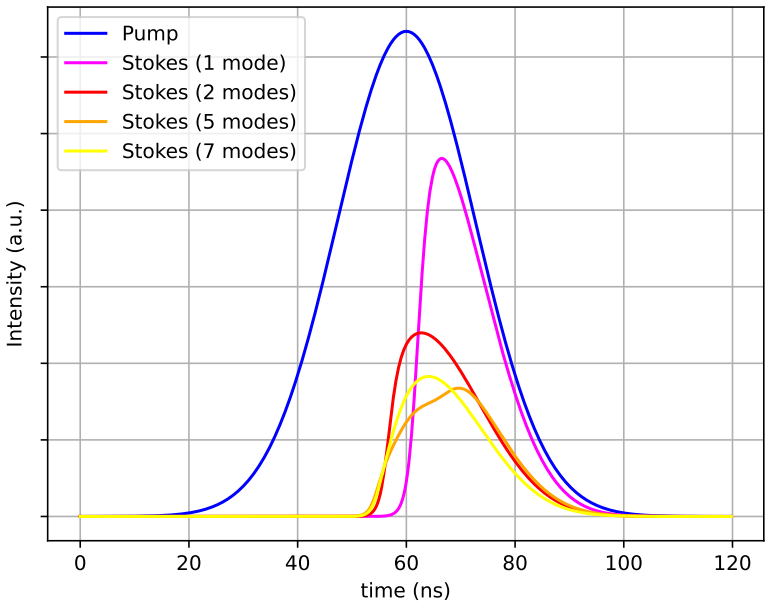

Figure 2.21: Comparison of the output temporal shapes of a modal SBS simulation compared with the number of modes used. Interaction in SF6 for a $40\ \mathrm{mJ}$ pulse focused down to $40\ \mu\mathrm{m}$ radius at $8\ \mathrm{cm}$ depth inside the cell.

The output temporal shape predicted by this newly implemented simulation model manages to properly reproduce the experimental behaviour presented Fig.2.7. As we stated, in Sec.2.3.2, the 2D model overestimate the reflectivity, predicts later initiation, higher reflectivity once initiation is achieved and sharper transition. Increasing the number of modes helps addresses all those issues. Comparing the results of the simulations with the experimental results presented in Fig.2.7, we can see that the shape of the high mode number used well reproduces the shapes of the experimental data, also the reflectivity is still below experimental. This could be solved as stated in the literature by changing the noise level to best fit the experimental curve. This new simulation model seems to be extremely accurate compared to the 2D model, at the cost of an increased simulation time (the 7 mode simulations take about $10\ \mathrm{h}$ to compute).

Spatial profile The new simulation model also allows to simulate the effect of SBS reflection on simple (i.e. close to TEM00) spatial profiles.

Simulated input and output spatial profiles with diverse number of modes used are represented Fig.2.22.

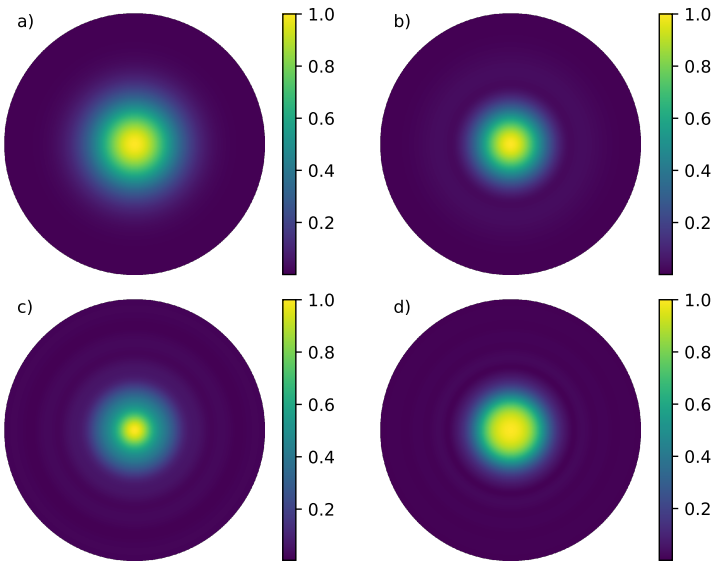

Figure 2.22: Comparison of the input and output spatial profiles of a modal SBS simulation compared with the number of modes used. Interaction in SF6 for a 40 mJ pulse focused down to 40 µm radius at 8 cm depth inside the cell. a) Input spatial profile (TEM00) b) Output spatial profile for a simulation on 2 modes c) Output spatial profile for a simulation on 5 modes d) Output spatial profile for a simulation on 7 modes.

The modal simulation allows to represent a behaviour described qualitatively in Sec.2.3.2. The SBS reflection is less efficient on the edge of the Gaussian spatial profile. This leads to a kurtosis of the Gaussian pump pulse through the reflection and a cut-off of the edges of the pulse: the beam becomes more leptokurtic. This phenomenon is represented in Fig.2.23.

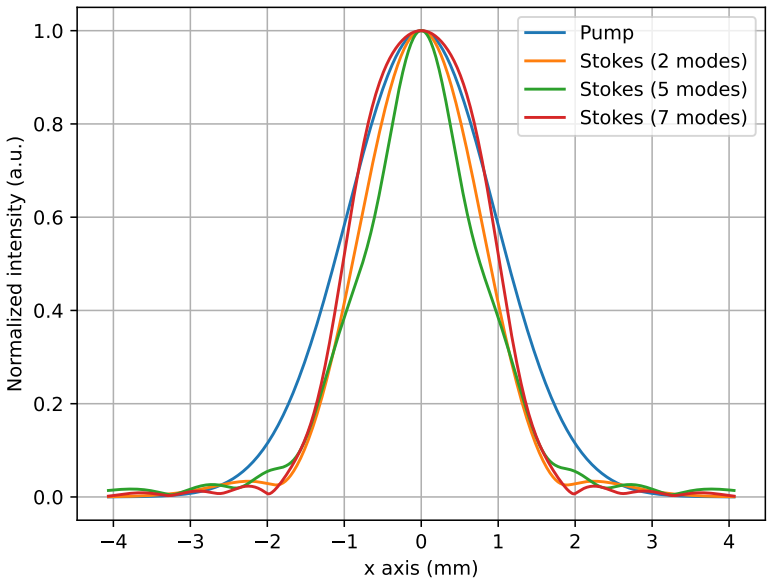

Figure 2.23: Comparison of the input and output spatial profiles of a modal SBS simulation compared with the number of modes used. Cut along the x axis. Interaction in SF6 for a $40\ \mathrm{mJ}$ pulse focused down to $40\ \mu\mathrm{m}$ radius at $8\ \mathrm{cm}$ depth inside the cell. a) Input spatial profile (TEMoo) b) Output spatial profile for a simulation on 2 modes c) Output spatial profile for a simulation on 5 modes d) Output spatial profile for a simulation on 7 modes.

2.4.4 . Conclusion for the modal simulation

The modal simulation model developed in the present chapter gives a more precise approximation of the actual temporal profile reflected by the cell at the cost of increased complexity, memory usage and calculation time. This simulation model gives precise approximation for unaberrated input beams but is unable to properly simulate the beam diameter expansion close to waist due to aberrations in the pump beam.

2.5 . Split step model

In the previous models described, we managed to reach a compromise between calculation time and result accuracy for the temporal profile of the simulated Stokes pulse. Yet, the *modal decomposition* numerical model is still limited in its spatial profile description and doesn't take into account the aberrations present in the input beam. This leads to stronger interaction near focus and this effect tends to favour relaxation oscillations appearance in the numerical simulations.

In this section, a new model is implemented to solve this last inaccuracy and reach a proper description of the spatial and wavefront description. This

model integrates the full description along the transverse axis (with radial symmetry approximation) and integrates an arbitrary wavefront. The simulation of the propagation is performed in the conjugated space in a half step and the nonlinear effect is added as a separate contribution in a second half step. Together, those two contributions form a *split-step* calculation scheme [9].

2.5.1 . Description of the transverse dimension

In this new numerical model, we can keep the complete description on the transverse dimensions of the beams with both intensity and phase. The beam can be described by:

$$A_P(x,y,z,t) = A_{PR}(x,y,z,t)\exp(j(\Phi(x,y,z,t)) \tag{2.24}$$

With spatial profile at position z defined by:

$$S_P(x,y,z) = \int_0^{\tau_{pulse}} |A_{PR}(x,y,z,t)|^2 dt \tag{2.25}$$

And wavefront

$$\Delta_P(x,y,z) = \int_0^{\tau_{pulse}} \Phi(x,y,z,t) dt \tag{2.26}$$

And if we can calculate $A_P(x,y,z,t)$ and $A_S(x,y,z,t)$ for all (x,y,z,t) we can have access to spatial profile and wavefront information of every beam at any position and in particular at cell output. This already presents a new challenge for numerical simulation: memory allocation. In the *2D model*, we only had three variables to store for every spatiotemporal coordinates (α,β). In the *modal model*, we split the pump and Stokes spatial profiles on the Laguerre-Gauss modes that constituted a basis. For n modes, the memory allocation had to be multiplied by n compared to the *2D model*. Because the number of modes was limited (< 10), the memory allocation stayed reasonable.

Here, if we keep both x and y dimension, the memory allocation required will be increased by a factor $nx \times ny$. For a sampling grid of 200 (which as we will see later, isn't remotely enough for a proper high energy SBS simulation), this means an increase of memory usage of 40 000. For this reason, we once again will assume radial symmetry. Although the method described below could perfectly be applied to an arbitrary (x,y) transverse description. This approximation reduces the capabilities of the model to simulations of beam with radial symmetry and to aberrations presenting radial symmetry meaning defocus and spherical aberrations. While this limits the capabilities of the model, the *split-step* SBS simulation model was developed in an attempt to study the effects of aberrations on the reflection. The full 4D model could

be implemented following the method presented hereafter given that several optimisations to the calculation are introduced to reduce the calculation time.

The deformation of the beam with propagation is described by the classical method of Fourier transform. Propagation over a distance dz is described by a sequence of:

1. Fourier transform of A_P to $\tilde{A_P}$ in the conjugated space.
2. Propagation in the conjugated space by multiplication by the propagation constant $\exp(i\pi\lambda dz\nu^2)$ with ν the conjugate transverse coordinate.
3. Inverse Fourier transform to return to the real space.

Since we assumed radial symmetry, we can use a simplification of the Fourier transform for laser beams with radial symmetry, the *Hankel transform*.

2.5.2 . Calculation

To compute all the values for A_P and A_S for all (r, z, t), we continue to follow the same scheme of calculation. The only difference is that this time, the spatial profile evolution has to be calculated. To this aim, we split a step $\beta \to \beta + 1$ into three sub-steps:

1. Calculation of the longitudinal propagation (the same way we did for the *2D model* and *modal model*)
2. Calculation of the diffraction term: the change in the amplitude and phase repartition on the transverse direction.
3. Calculation of the nonlinear contribution (the same way we did in the *2D model*), for every transverse component.

The real difficulty lies in the second sub-step. In particular, since a high number of transverse components will need to be calculated, we looked for a way to compute them in parallel rather than sequentially. In the following, we describe the full method for computing all the $A_{P\beta}^{\alpha\gamma}$ and $A_{S\beta}^{\alpha\gamma}$ with γ representing the sampled transverse variable ($\gamma = 0$ for $r = 0$ and $\gamma = n$ for $r = r_{max}$ with n the number of sampled along the transverse direction).

Hankel Transform To perform the calculation of the diffraction (second sub-step), we need to perform the Fourier transform of the beam to conjugated space. For a beam of transverse coordinate (x, y), this Fourier transform is given by:

$$\tilde{f}(\nu_x, \nu_y) = \int \exp(-2j\pi(\nu_x x + \nu_y y)) f(x, y) dx dy \tag{2.27}$$

which, in polar coordinates is:

$$\tilde{f}(\nu_r, \nu_\theta) = \int_0^{2\pi} \int_0^{\infty} f(r,\theta) \exp(-2i\pi r \nu_r cos(\theta - \nu_\theta)) r dr d\theta \tag{2.28}$$

Since in our case, we assumed radial symmetry, the spatial profile doesn't depend on θ and the transform can therefore be written as

$$\tilde{f}(\nu_r) = 2\pi \int_0^{\infty} f(r) J_0(2\pi r \nu_r) r dr \tag{2.29}$$

where J_0 is the 0-order Bessel function. This expression is called *Hankel transform*. This form is particularly convenient since it allows to approximate the transfer from real space to conjugated space as a matrix product. The diffraction step can therefore be performed by two simple matrix products, in parallel at the cost of a particular sampling along the radial direction and slight computation errors. This method has been developed in [10] and is applied for the first time here to SBS conjugation. In the following, we develop the formalism used in the simulation for diffraction simulation.

Discrete Hankel transform When we want to perform the diffraction sub-step, the longitudinal position z and time t are fixed. We can then write the amplitude as a function of r only. This amplitude has a limited spatial extension R and a limited frequency extension V. In the general case, this function can be decomposed under a sum of a Bessel series:

$$A_P(r) = \sum_{k=1}^{\infty} c_k J_0(\mu_k \frac{r}{R}) \tag{2.30}$$

where the μ_k are the k-th root of the Bessel function and the c_k the corresponding amplitude coefficients.

Utilising the method developed in [10], the sampling along r was made for every $r_{\gamma=k} = \mu_k / 2\pi R$ and $\nu_{\gamma=k} = \mu_k / 2\pi V$. Using this, the values of $A_P(r)$ and $\tilde{A_P}(\nu_r)$ can be approximated by:

$$A_p(r_\gamma) = \frac{1}{\pi V^2} \sum_{k=1}^{N} \frac{\tilde{A_P}(\nu_k)}{J_1^2(\mu_k)} J_0(\frac{\mu_\gamma \mu_k}{S}) \tag{2.31}$$

and

$$\tilde{A_P}(\nu_\gamma) = \frac{1}{\pi R^2} \sum_{k=1}^{N} \frac{A_P(r_k)}{J_1^2(\mu_k)} J_0(\frac{\mu_\gamma \mu_k}{S}) \tag{2.32}$$

if N is large enough. In those equations, we have introduced $S = 2\pi RV$.
It is possible to make those equations symmetric by introducing:

$$A_P^{'}(\gamma) = A_P(r_\gamma) \times \frac{R}{J_1(\mu_\gamma)} \tag{2.33}$$

$$\tilde{A_P^{'}}(\gamma) = \tilde{A_P}(\nu_\gamma) \times \frac{V}{J_1(\mu_\gamma)} \tag{2.34}$$

And the transfer from $A_P^{'}$ to $\tilde{A_P^{'}}$ can then be simplified to a simple transfer matrix multiplication T:

$$\forall (n,m) \subset \{1,2,...,N\}^2 \quad T_{mn} = \frac{2J_0(\mu_n \mu_m / S)}{|J_1(\mu_n)||J_1(\mu_m)|S} \tag{2.35}$$

And then

$$A_P^{'} = T\tilde{A_P^{'}} \tag{2.36}$$

$$\tilde{A_P^{'}} = TA_P^{'} \tag{2.37}$$

In Eq.2.35, the parameter S is chosen such that $T^2 = I_N$ so that the beam is unchanged by a transform followed by its inverse transform. We can then calculate the propagation using the propagation vector in the conjugated space:

$$\overline{prop} = \exp(2i\pi \cdot dz \cdot \sqrt{\lambda^{-2} - \nu^2}) \tag{2.38}$$

And we can then describe the full diffraction sub-step (getting all the $A_P(r_\gamma, z+dz)$ from $A_P(r_\gamma, z)$) by the following:

1. Multiplication term by term of vector $(A_P(r_\gamma))\gamma$ by the vector $(R/J_1(\mu_\gamma))_\gamma$. To get $(A_P^{'}(\gamma))_\gamma$
2. Hankel transform to switch to conjugated space with the matrix product $T \times A_P$
3. Term by term multiplication by vector $(\overline{prop})\gamma$
4. Inverse Hankel transform to go back to real space with the matrix product $T \times \tilde{A_P^{'}}$
5. Multiplication term by term by the vector $(J_1(\mu_\gamma)/R)_\gamma$.

In this calculation, the vectors $(R/J_1(\mu_\gamma))_\gamma$ and the matrix T can be computed in advance since they only depend on the edges of the transverse space grid and not on the loop variables (α, β, γ). Every single of this diffraction step is then constituted of only two matrix product and two vector products. The computation of term by term vector products is easily done in parallel and the associated calculation speed depends inversely on

the number of threads available. All the further code optimisation are therefore reduced to matrix product optimisation. The only constraint we have is that the sampling in the transverse (r) direction has to be the roots of the 0-order Bessel function.

This model was implemented in Python 3. Matrix product optimisation was not properly implemented but represent a nice prospect for computational speed increase. This model seems especially adapted to calculation on large number of cores, in particular GPU calculations. All the other sub-steps are not described here but are basically just a vectorized version of the 2D longitudinal propagation and nonlinear effects term given in Sec.2.2.2 and are also easily calculated in parallel. A schematic of the calculation steps is given Fig.2.24.

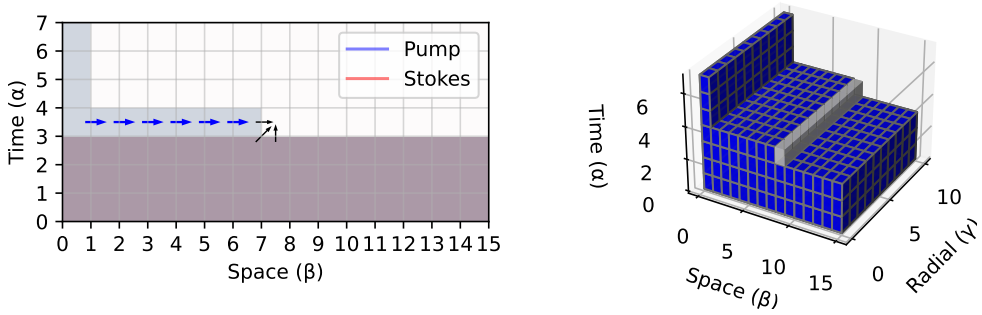

Figure 2.24: Representation of the split-step calculation process for the pump wave. All blue cubes represent a calculated value for a coordinate $(\alpha, \beta\gamma)$. All values γ for a given (α, β) are calculated in parallel simultaneously. Stokes calculation for a given α is performed after pump calculation for this same α.

2.5.3 . Results

Limits of the calculation As stated before, the Hankel transform requires the transverse sampling to be made at transverse position

$$r_k = \mu_k / 2\pi R \tag{2.39}$$

and the T matrix is computed before the start of the calculation for increased speed during the (α, β) loop. This means that the sampling grid has to stay constant during the loop. In particular, both the spatial extension and the dr parameter stays constant during the whole propagation. This is an issue in focused geometry: because the beam radius changes during the propagation, the parameter R has to be chosen as large enough that the full beam is sampled and the number of point large enough that the beam is well sampled even near the waist. In this case, the resultant number of point rises quickly as the focusing geometry is chosen as having large aperture

(and this physical configuration is exactly the one we found as being relevant to high energy SBS in Sec.2.3.5). For instance, a beam with $10\ \mathrm{mm}$ radius at cell input, focused to $10\ \mu\mathrm{m}$ inside the cell requires 10000 points over the full aperture for only 10 sample points near the beam waist. This means a matrix T of size 100 000 000, and calculation time for the matrix product rising accordingly.

For this reason, the results presented hereafter are limited to small input beam size with limited focusing. The introduction of an adaptive transverse sampling grid seems to be a required prospect for further study on high aperture SBS conjugation [11–13].

Temporal profile Once again, we present simulation result for a low-energy SBS conjugation in gas. The resulting temporal profiles are shown in Fig.2.25.

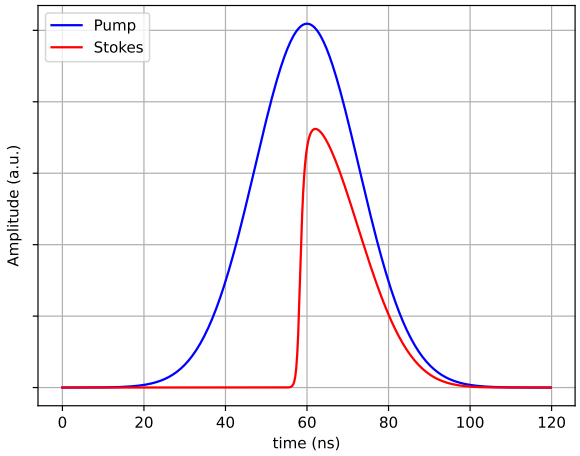

Figure 2.25: Temporal shapes of the input and output pulses in an SBS cell. Interaction in SF6 for a $40\ \mathrm{mJ}$ input pulse focused down to $100\ \mu\mathrm{m}$.

The behaviour of experimental SBS experiments is once again respected and the fitting with the simulation can be done by tuning the noise term.

Spatial profile The true advantage of this new model is the introduction of an arbitrary spatial profile in amplitude and phase and complete spatial description at all point during the interaction. We show in Fig.2.26 typical output spatial profiles from SBS reflection obtained with the developed split-step model.

Once again, the simulation confirms the lower reflectivity on the edges of the pulse. The accuracy of this simulation is not limited by the number of modes and confirms the behaviour predicted by the *modal* simulation. By plotting the cut along the beam (shown in Fig.2.27), the reflectivity drop

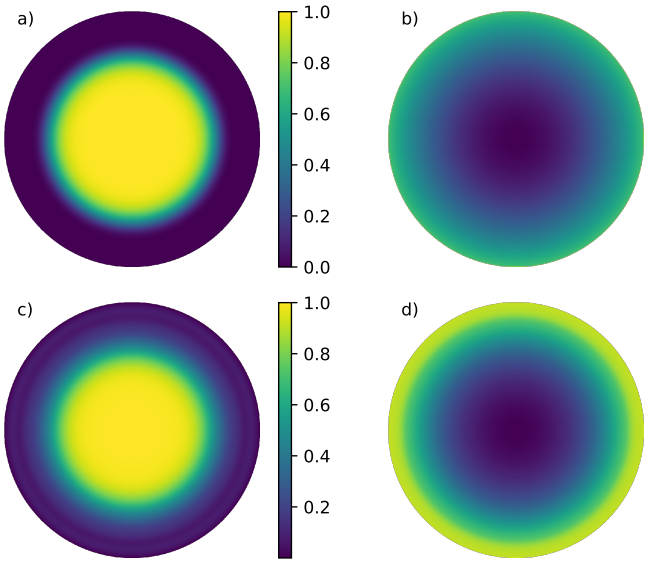

Figure 2.26: Input and output spatial profile and wavefront of pump and Stokes beams. Interaction in SF6 for a $45\ \mathrm{mJ}$, 5th order supergaussian beam, focused down at $8\ \mathrm{cm}$ inside the cell to $100\ \mu\mathrm{m}$ diameter. a) Input spatial profile b) Input wavefront c) Output spatial profile d) Output wavefront.

around beam edges is once again demonstrated. Some boundary effects caused by the sampling grid are still present on the very edges of the Stokes beam.

Aberration introduction A fully resolved *split-step* simulation model would theoretically allow to study the influence of spherical aberrations on the SBS reflection. In the scope of this work, the limited sampling caused by limited memory allocation made fine study on aberration impossible. In particular, the simulated beams were so lowly focused that no clear increase of the focal spot size were simulated. The main part of the aberration studies were then performed experimentally in Chap.4 and Chap.5.

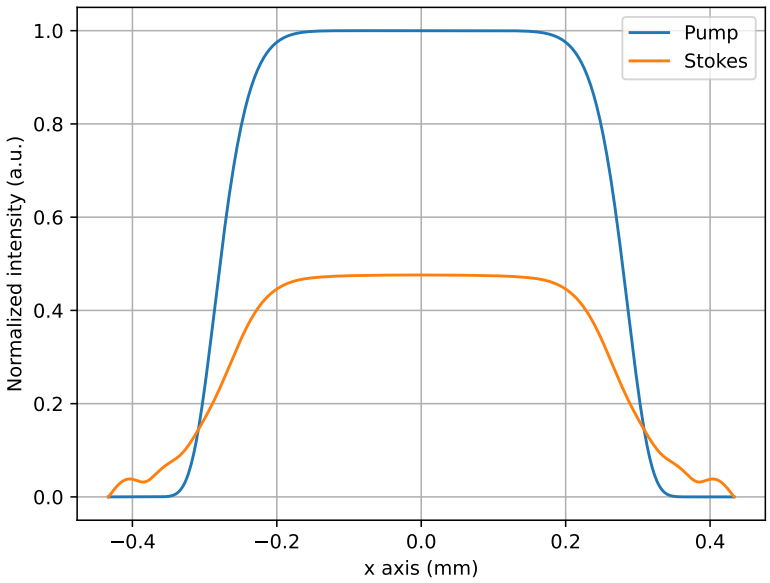

Figure 2.27: Cut of the input and output spatial profile of pump and Stokes beams. Interaction in SF6 for a $45\ \mathrm{mJ}$, 5th order supergaussian beam, focused down at $8\ \mathrm{cm}$ inside the cell to $100\ \mu\mathrm{m}$ diameter.

2.5.4 . Conclusion on the split-step model

Although split-step SBS simulation could become a powerful simulation tool to study in fine details the limits of the SBS aberration correction, and the potential near field spatial effects introduced by SBS, the model developed is for now limited to very specific operation conditions.

It presents the highest temporal accuracy and is the only model to date able to simulate fine spatial profiles and wavefront. In the scope of this thesis, the model has yet to be perfected to properly simulate high energy SBS reflection in the high aperture geometry. Several prospects are identified to solve those issues.

- Implementation of calculation on GPU could greatly increase the parallelisation of the calculations. As stated in Sec.2.5.2, all the half-steps are designed to be calculated in parallel and increasing the number of cores available could make the calculation significantly faster.

- Implementation of an adapting grid [11–13] could help reduce the sampling resolution issue by reducing the number of sampling points used without loosing resolution near focal point.

- The full study of the 2D transverse spatial dimension can easily be reached by replacing the Hankel transform by the usual 2D Fourier

transform. This could then be used to simulate all the effects of the different wavefront aberration types and precisely evaluate the SBS maximum capabilities for every configuration.

In the following, the limitation of the splitstep model on the current form, with its performance limitations, made us considered it not adapted for proper high energy SBS simulations. Most of the simulations used for the actual cell design were made using the 2D model first and then validating the results with the *modal decomposition* model. The development of this model still represent the best attempt, to the best of our knowledge, of simulation SBS reflection with a fully-resolved spatial description and hence the comprehension of the spatial fidelity drops that can happen during SBS reflection.

2.6 . Conclusion on the simulations

In this chapter, 3 distinct model are developed, implemented and compared for SBS simulations. The 2D model is the first one developed and is used to complete the theoretical chapter Chap.1 in the saturated transient regime. Several observations are made using this model. In particular, we demonstrate quantitatively how the propagation length in the cell can deform the temporal shape of the input pulse during reflection. The SBS mirror can then be used in different configurations, for example, as a compression component to compress pulses of a few nanosecond downs to few hundreds of picoseconds.

Conversely, we demonstrate how the SBS mirror can be designed to limit temporal deformation at maximum by shortening the focal length. This high aperture configuration helps reduce compression at the cost of higher aberration level introduced (since short focal lenses, high aperture are used) or smaller focal point. The *Split-step model* was developed to study the influence of strong aberrations during the reflection but is found to be limited in use and not yet adapted to high energy SBS with high aperture, at least until further optimisation. This PhD being mostly experimental, the time required for the full implementation of a functional Split-step model is deemed too high in the scope of the thesis. This last model still represents an interesting prospect for fundamental studies of SBS limitations in extreme regimes.

All the different models described in this chapter are summarised in Fig.2.28. In Tab.2.1 a summary of all the simulation models performances developed, and their limitations is also given.

With this chapter, we presented the numerical solving of the nonlinear equations. We not only gained an in-depth understanding of the spatiotemporal dynamics but also described the way temporal compression

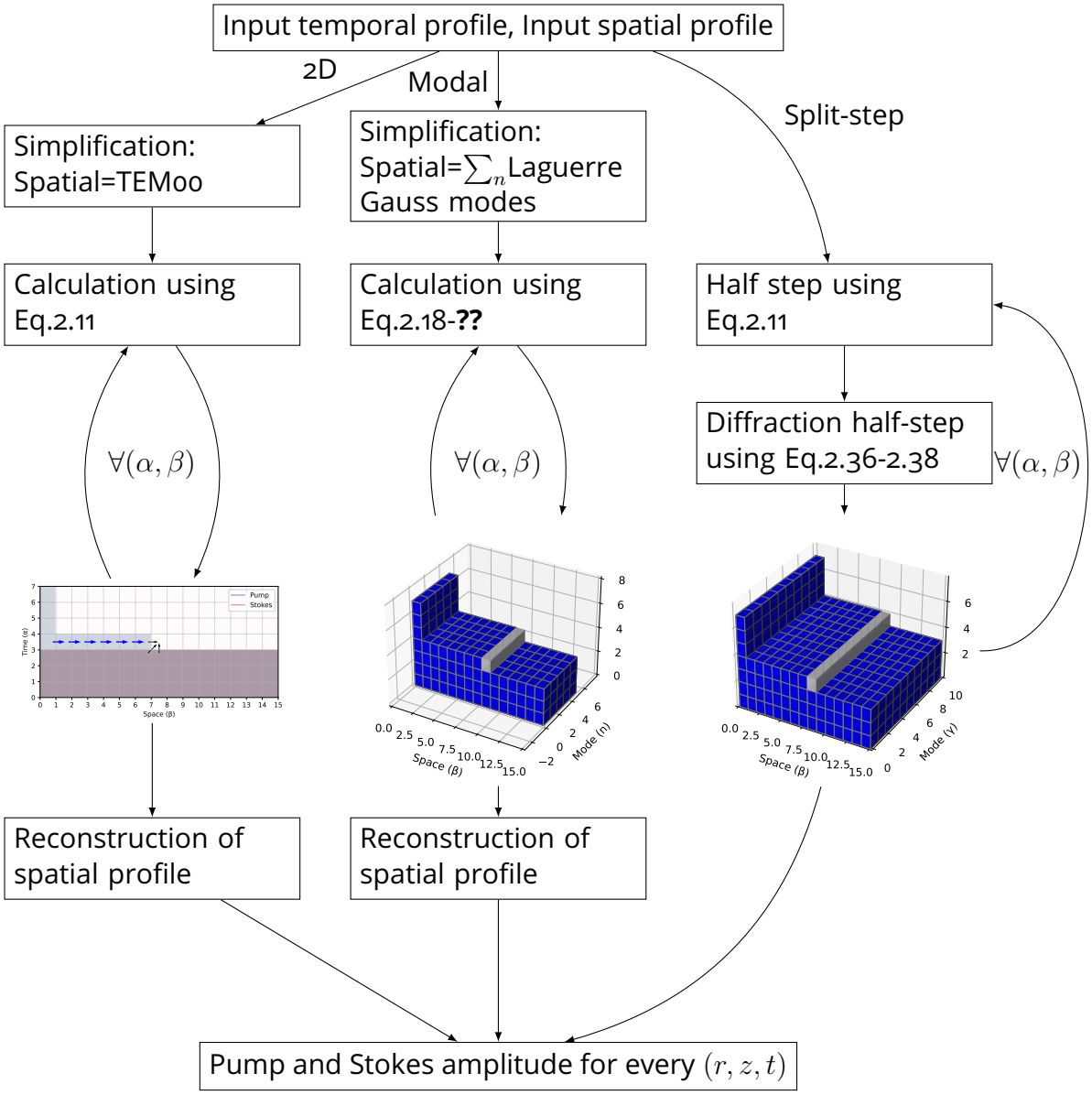

Figure 2.28: Summary of the simulation methods developed in this chapter

can happen during SBS reflection. Furthermore, we demonstrated the limits of the numerical model introduced. In particular, it was shown difficult to numerically study the effects of aberrations and other transverse spatial characteristics on the pump beam.

This chapter leads to a conclusion for the following chapter: any effect happening on the transverse dimension (spatial profile deformation or wavefront effects) will have to heavily rely on experimental studies. The numerical simulations are unable to provide a suitable theoretical support

Simulation model	2D	Modal	Split-step
Transient behaviour	Yes	Yes	Yes
Temporal profile	Approximate	Precise	Precise
Spatial profile	No	Approximate	Fine
Wavefront	No	No	Radial symmetry
Calculation time	Fast (1 min)	Slow ($\Theta(n^4)$)	Slow (10 hours)

Table 2.1: Summary of the performances of the simulation models developed in this chapter.

for those kinds of effects.

In the following chapter, we introduce experimental studies. In a first part, we study the state of the art of SBS mirrors for phase conjugation. Then, we use this state of the art in parallel with our simulation models to design laser sources and optical configurations suitable to the development of an experimental phase conjugate mirror.

Bibliography

The following bibliography contains all the references cited in this chapter. A full bibliography of the thesis is given after the general conclusion. In addition, every bibliography entry is associated with every paragraph it has been referenced in. The corresponding section numbers are indicated at the very end of the entry.

[1] Axel Heuer and Ralf Menzel. Principles of Phase Conjugating Brillouin Mirrors. In *Phase Conjugate Laser Optics*, pages 19–62. John Wiley & Sons, Ltd, john wiley & sons, ltd edition, 2003. 2.1, 2.3.2, 2.7

[2] Shahraam Afshaarvahid and Jesper Munch. A transient, three-dimensional model of stimulated brillouin scattering. *Journal of Nonlinear Optical Physics & Materials*, 10(01):1–27, March 2001. Publisher: World Scientific Publishing Co. 2.1

[3] Viliam Kmetik, Henryk Fiedorowicz, Alexander A. Andreev, Klaus J. Witte, Hiroyuki Daido, Hisanori Fujita, Masahiro Nakatsuka, and Tatsuhiko Yamanaka. Reliable stimulated Brillouin scattering compression of Nd:YAG laser pulses with liquid fluorocarbon for long-time operation at 10 Hz. *Applied Optics*, 37(30):7085–7090, October 1998. Publisher: Optica Publishing Group. 2.3.4

[4] Hidetsugu Yoshida, Takaki Hatae, Hisanori Fujita, Masahiro Nakatsuka, and Shigeru Kitamura. A high-energy 160-ps pulse generation by stimulated Brillouin scattering from heavy fluorocarbon liquid at 1064 nm wavelength. *Optics Express*, 17(16):13654–13662, August 2009. Publisher: Optica Publishing Group. 2.3.4

[5] W. L. J. Hasi, Z. Qiao, S. X. Cheng, X. Y. Wang, Z. M. Zhong, Z. X. Zheng, D. Y. Lin, W. M. He, and Z. W. Lu. Characteristics of SBS hundreds picosecond pulse compression and influence of energy on pulse stability in FC-770. *Optics Communications*, 311:375–379, January 2013. 2.3.4

[6] M. Ostermeyer, H. J. Kong, V. I. Kovalev, R. G. Harrison, A. A. Fotiadi, P. Mégret, M. Kalal, O. Slezak, J. W. Yoon, J. S. Shin, D. H. Beak, S. K. Lee, Z. Lü, S. Wang, D. Lin, J. C. Knight, N. E. Kotova, A. Sträßer, A. Scheikh-Obeid, T. Riesbeck, S. Meister, H. J. Eichler, Y. Wang, W. He, H. Yoshida, H. Fujita, M. Nakatsuka, T. Hatae, H. Park, C. Lim, T. Omatsu, K. Nawata, N. Shiba, O. L. Antipov, M. S. Kuznetsov, and N. G. Zakharov. Trends in stimulated Brillouin scattering and optical phase conjugation. *Laser and Particle Beams*, 26(3):297–362, September 2008. 2.3.4

[7] Shahraam Afshaarvahid, Vladimyros Devrelis, and Jesper Munch. Nature of intensity and phase modulations in stimulated Brillouin scattering. *Physical Review A*, 57(5):3961–3971, May 1998. Publisher: American Physical Society. 2.3.4

[8] Stefan Behnel, Robert Bradshaw, Craig Citro, Lisandro Dalcin, Dag Sverre Seljebotn, and Kurt Smith. Cython: The Best of Both Worlds. *Computing in Science & Engineering*, 13(2):31–39, March 2011. Conference Name: Computing in Science & Engineering. 2.4.2

[9] A. Couairon, E. Brambilla, T. Corti, D. Majus, O. de J. Ramírez-Góngora, and M. Kolesik. Practitioner's guide to laser pulse propagation models and simulation. *The European Physical Journal Special Topics*, 199(1):5–76, November 2011. 2.5

[10] Manuel Guizar-Sicairos and Julio C. Gutiérrez-Vega. Computation of quasi-discrete Hankel transforms of integer order for propagating optical wave fields. *JOSA A*, 21(1):53–58, January 2004. Publisher: Optica Publishing Group. 2.5.2, 2.5.2

[11] V. I. Talanov. Focusing of Light in Cubic Media. *JETP Letters*, 11(6):303, 1970. 2.5.3, 2.5.4

[12] W. Simmons, J. Hunt, and W. Warren. Light propagation through large laser systems. *IEEE Journal of Quantum Electronics*, 17(9):1727–1744, September 1981. Conference Name: IEEE Journal of Quantum Electronics. 2.5.3, 2.5.4

[13] Eyal Feigenbaum, Richard A. Sacks, Kathleen P. McCandless, and Brian J. MacGowan. Algorithm for Fourier propagation through the near-focal region. *Applied Optics*, 52(20):5030–5035, July 2013. Publisher: Optica Publishing Group. 2.5.3, 2.5.4

3 - Design and realisation of an SBS-PCM

In the previous chapters, we introduced the nonlinear effect *Stimulated Brillouin Scattering* and presented its phase conjugating behaviour. Although this effect is usually considered as a detrimental effect in the literature (especially in fibers), it is possible to harness it to reverse the wavefront of a high energy input beam, and hence, to self correct all the wavefront perturbations occurring in the middle of a round trip amplifying scheme.

Using this information, we first decided to dive into the dynamics of the nonlinear effect. To this aim, we developed the theoretical formalism as well as several numerical simulation models and studied the different optical configurations available for an SBS mirror to be used in a laser system. The simulation models were compared to published low-energy experimental results and the accuracy of the models was confirmed. Hence, we had access to a numerical tool for the design of our future experimental setups. Yet, the numerical simulations were shown to be limited in their resolution and capacity to take into account the transverse spatial dimension. The related effects will then have to be studied directly on an experimental setup.

In this chapter, we take a first step towards this experimental approach: we first study the state of the art of high energy SBS PCM. We then use this literature to confirm some of the results previously made in the simulation chapters and design our own SBS mirror. In particular the selection of a nonlinear medium is based not only on the physical properties relative to SBS but also has to take into account more down to earth parameters such as purity, or availability. Other parasitical physical processes neglected in the theoretical part (such as optical breakdown) are also introduced and taken into account for the design of our experimental setups. The purity of the liquid is found to be a crucial property for good operation of an SBS mirror. In this chapter is detailed the filtration process used as well as the purity analysis put in place to experimentally confirm the quality of our medium.

The state-of-the-art literature is then used to assert the feasibility of our own objectives. We establish the properties and ideal parameters an SBS PCM should present to be used in an experimental laser system. To this aim, existing solutions are studied to identify in advance some of the limitations frequently encountered by the communities working on similar topics. We then present the laser designs used in the following experimental chapters of this thesis as well as their implementations. The performances of the laser sources were specifically selected to properly address the objectives presented in the preceding sections. Conversely, the laser design developed in this section will explain some of the experimental limitation met in the

experiments.

3.1 . Existing Brillouin cells in the state of the art

The first experimental demonstration of SBS was performed in 1964 in solid [1] and in liquid [2]. Its wavefront reversal capacities have been firstly noted in [3]. Since then, several systems have implemented SBS cells, either for compression purposes (Sec.1.4.3) or for wavefront correction (Sec.1.5). In the scope of this work, only this second axis was approached.

Because the aim for the community is to develop high-energy, phase-corrected lasers at high repetition rate, the SBS-PCM have to simultaneously present a high energy load capacity (the capacity to reflect a single high energy pulse) and a high power load capacity (the capacity to reflect a large amount of average optical power). The energy load of the cell in a phase correction scheme is the energy at the middle of the round trip and therefore is directly linked to the maximum output energy of the laser. Whereas the power load for a fixed amount of energy is linked to the maximum repetition rate of the laser.

One other key parameter of interest for the community is the reflectivity. A high reflectivity of the cell means reduced losses originating from the reflection. Low reflectivity can also mean detrimental effects occurring in the cell. For example, a high transmission means higher energy density at focus point and hence increase the risk of ionisation and fluid degradation [4]. It also deposits more heat from the residual absorption of the medium and limits the power load in the cell.

In this section, we have compiled some of the results from the state of the art addressing SBS cell operating in phase correction regime [5–21]. In particular, cells placed in compression configuration were removed from the literature study. In the following, some key properties of interest are analysed and some of the trends in the performances are highlighted.

3.1.1 . Average power

The configurations presented in the following address SBS cells operating in widely varying range of energy and repetition rate, over 3 orders of magnitude for both parameters. SBS cells being used for compensating thermally induced aberrations means that the input average power inside the cells is one of the key parameters studied. A graph of the input energy inside the cell plotted against repetition rate of the laser is show in Fig.3.1.

As we can see, an increase of the repetition rate is generally linked to a decrease of input energy, although several works present cells operating over $100\ \mathrm{W}$ of average power incident on the cell [19, 20]. This indicates a

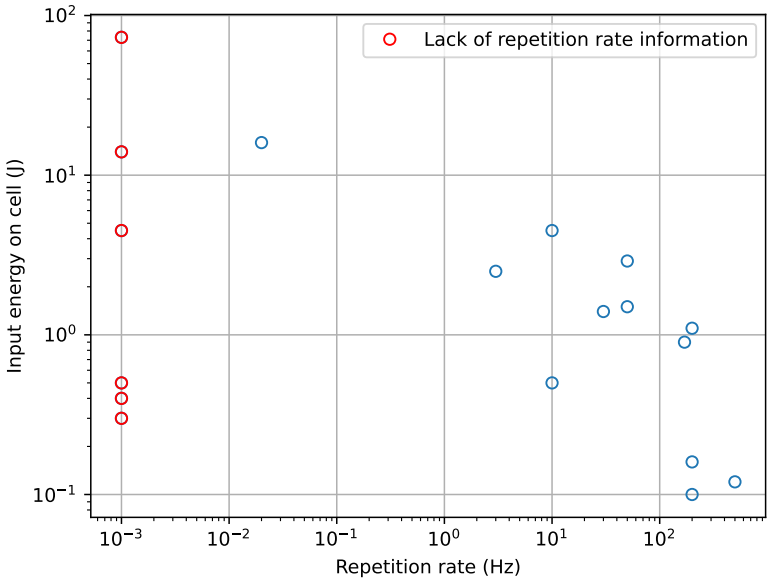

Figure 3.1: Input energy incident on the cell against repetition rate of the laser used. Source: [5–21].

technological limitation limiting the power load of SBS usage to the range of $100\ \mathrm{W}$. Conversely, no significant detrimental effects should appear for power loads way below this value. The experiments on SBS cell were therefore conducted with power load $< 30\ \mathrm{W}$ to better understand the physical process without having to manage an additional constraint.

3.1.2 . Efficiency

We then analyse the efficiency of the different SBS mirrors available. The literature describes very efficient SBS cells with several reflectivity value above 90% for all energy range and as high as 98% for energy above the joule level (Fig.3.2).

Because all the cells presented in this graph operate in saturated regime $E > 10 \cdot E_{th} \approx 100\ \mathrm{mJ}$, the threshold behaviour cannot be seen on this graph directly. Theoretical steady state prediction for this energy range (Fig.1.4) predicts reflectivity of over 95% for all the energy range and for all optical configurations. The reflectivity dispersion is then caused by the transient behaviour of the SBS effect as described in Chap.2. This can be confirmed by plotting the reflectivity against the duration of the input pulse as shown in Fig.3.3.

Although the drop of reflectivity due to the transient behaviour is multi-parametric (pump pulse temporal shape, focusing condition,...). The influence of the input pulse duration on the reflectivity is clearly shown, and a reflectivity drop is observed for pulse duration comparable with medium

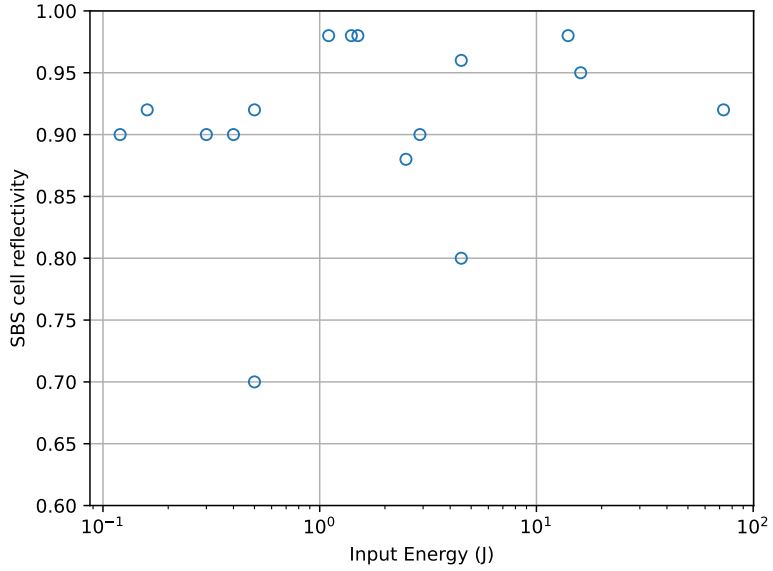

Figure 3.2: Experimental SBS cells reflectivity against input energy. Source: [5–21].

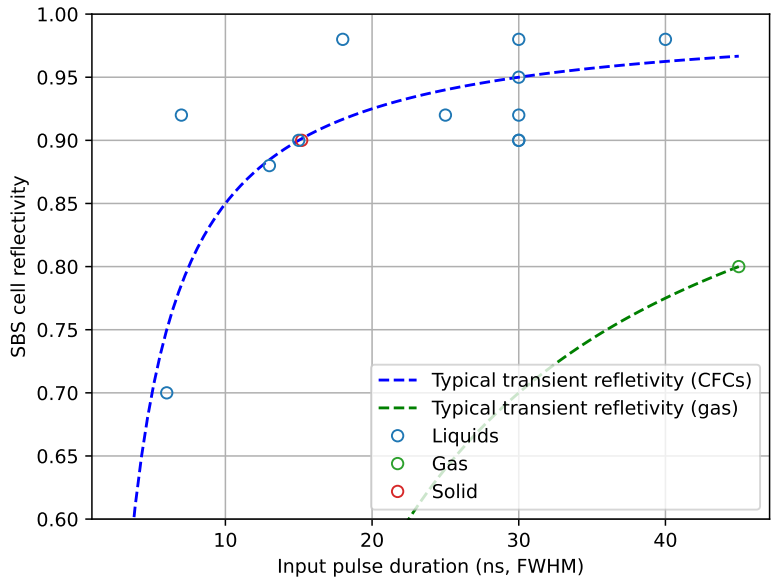

Figure 3.3: Experimental SBS cells reflectivity against input pulse duration. Typical transient reflectivity curves are calculated using SBS steady state reflectivity and removing the first $1.5\tau_{medium}$ of the pulse from the reflected energy to account for the initiation time. The actual reflectivity also varies depending on the input pulse temporal shape and on the optical configuration used. Source: [5–21].

lifetime ($\tau_{\text{liquid}} \approx 1$ ns, $\tau_{\text{gas}} \approx 15$ ns). The surprising performances of the point (7 ns, 92% reflectivity) [15] comes from a particular SBS scheme where the nonlinear effect is initiated before the arrival of the main pulse through a geometric separation of the beam and redirection of a small part of the energy into the cell, hence limiting the initiation losses to a minimum.

The curve Fig.3.3 once again confirms that liquids are the medium of choice for high energy SBS phase conjugation, linking fast reaction time, and fluid phase for optical breakdown mitigation. Furthermore, this analysis shows that to reach high reflectivity, it is required to operate with long pulses compared to the medium reaction time.

A second detrimental effect mentioned in the literature when the energy density at the waist is too strong before proper initiation of the SBS effect is the excitation of higher order modes and a dramatic drop in spatial fidelity [6,22]. In particular, short pulses and pulses with sharp rise time are shown to be hard to properly conjugate without disturbing the near-field and far-field distribution. This study indicates that the input temporal profile has a strong impact on the cell performances and should be managed accordingly.

To be able to control this in our studies, temporal profile shaping capabilities were for the first time introduced in the laser sources used in this thesis.

3.1.3 . Focusing condition

When increasing the energy, an issue that has for the moment not been introduced arises: If too much power density is present inside the medium, parasitic nonlinear effects, and in the worst case ionisation of the medium, can occur. For this reason, the SBS cells operating at very high energy tend to use longer focal length as shown in Fig.3.4.

The system presented in [17] operates above 10 J and uses a focal length above 1 m but places the focusing length at some distance away from the cell input window to mitigate the spatiotemporal and compression effects while no information of the reflected temporal profile is given in [7].

In both cases, increasing the energy further seems to be difficult, either due to the fluence on the cell input windows exceeding breakdown or due to temporal distortion of the reflected pulse. Those deformations have been experimentally confirmed and can be observed in the highest energy experiment [10]. In this article, a cell with the highest input energy is operated in single shot with input energy of 73 J, avoiding the aspect of reliability and reproducibility. And significant degradation of both the spatial and temporal fidelity was observed in the only high energy shot performed. The “good quality” operation of an SBS cell, preserving the spatial and temporal shape of the input pulse, is therefore currently limited to ≈ 15 J for long pulse operation ($\tau_{pulse} > 10\tau_{medium}$).

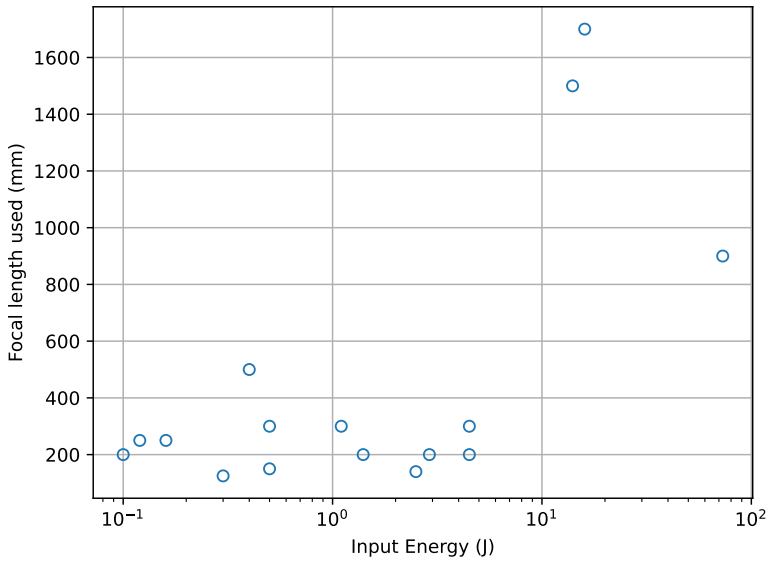

Figure 3.4: Focal length used against input energy. Source: [5–21].

3.2 . Experiment motivations

In this context, we try to develop and characterize our own SBS cells. In particular, two main applications domains are targeted.

In a first phase, we want to acquire an SBS cell compatible with high-energy, high-repetition-rate laser operation, typically $15\ \mathrm{J}$, $200\ \mathrm{Hz}$. Because this cell will be placed in the middle of a round trip amplification scheme, the actual input energy on the cell depends on the optical configuration of the amplifiers. A high number of amplifiers getting saturated only during the second pass of the round trip could lead to input power incident on the cell of a few joules. To reach those performances, several technological bottlenecks have yet to be explored:

- The wavefront correction capacities are mostly unexplored. Some experiments were performed with random aberration plates [16] and shows that an SBS mirror is capable of correcting several waves of optical aberrations. This study showed that wavefronts with high RMS can be properly compensated for up to $4\ \lambda$ RMS. The information of more specific aberrations is still mostly unknown. In particular, the spherical aberration, usually hard to compensate for: exhibiting highly concentrated wavefront distortion on the edges of the beam. This particular aberration presents high PV corresponding to a large strain value on the deformable mirror when trying to compensate for it. The correction capacities of the cell for this specific aberration is largely unexplored in the state of the art.

- The possibility to efficiently reflect shorter pulses (with τ_{pulse} comparable to τ_{medium}, in our case $\tau_{\mathrm{pulse}} \approx 3\ \mathrm{ns}$) is to be investigated. In particular, the solution of pre-initiation developed in [15] could be further developed and would help to reduce the drop of reflectivity observed for short pulses.
- Going even further, the capacity for the SBS cell to become compatible with temporal shaping solutions would be of very high interest for the community. In the general case, the temporal shape at laser output depends on the input temporal shape and on the deformation due to saturation in the amplifiers [23]. An arbitrary temporal shape at laser output thus requires the SBS cell to be able to reflect any temporal shape, including the one pre-compensating saturation. This approach is, to the best of our knowledge, completely unexplored as all the input pulse shape studied up to now on SBS cells were Gaussian.
- The stability of all the parameters of the SBS cells over a long period of time has to be characterized. In particular, it is mandatory for the component to not generate occasionally a *highly aberrated shot* (*rogue wave*) that could then damage the laser chain optical components during the round trip.
- Furthermore, the power load of the SBS cell starts becoming an issue. The residual absorption of the nonlinear medium at those power levels can create thermal inhomogeneities in the medium itself. In this case, the available literature shows that the spatial fidelity of the cell can be impacted [21, 24–26]. In this work, it was chosen to perform the experiments with lower repetition rate to separate the thermal issues from the other parasitic effects encountered during SBS reflection. However, some of the results obtained let us foresee possible improvement to the power load accessible in future experiments.

In a second phase, we aim to acquire an SBS-PCM compatible with high energy (up to kilojoule class) lasers. The requirements for this particular cell are unchanged, but the energy load should be greatly increased. Some configuration studied requires energy load on the cell above $100\ \mathrm{J}$, maintaining temporal and spatial fidelity.

In the following, we present the preliminary design and experimental realisation of the SBS cells and laser sources dedicated for these experiments. Those studies will be performed conjointly with the support of the numerical models at the start of the PhD and on the data available in the literature.

3.3 . Nonlinear medium

We detail in this section, the selection and realisation of the nonlinear SBS medium. We first consider the parameters of the available SBS media, and we then detail the experimental realisation of the cell.

3.3.1 . Medium choice

As we largely developed in the previous sections (2.3.3,3.1), the nonlinear medium used in the cell is of major importance. Several media have been studied in the literature [27, 28] and the identified parameters of interest are the following:

- The Brillouin gain coefficient g (Eq.1.42) characterizes the linear gain of the media as well as the steady state reflectivity. In the scope of this work, the high-energy lasers in focused regime provide largely enough power density for saturating the gain in almost any configuration. Thus, this parameter is not particularly critical in our case.

- The phonon lifetime τ_{medium} has been identified as a key parameter in the previous section. A fast phonon lifetime allows the build-up of the acoustic wave in short amount of time and therefore reduces the losses due to transparency before initiation, mitigates the amount of energy reaching focus point, and allows to reflect shorter pulse duration and sharper rise time. Although short phonon lifetime can potentially enhance compression, fast initiation was identified as one of the most critical parameter for our applications.

- The medium absorption characterizes the residual absorption of the pump and Stokes waves and thus, the heating of the medium. This value should be minimized to reduce losses and avoid the thermal blooming effects.

- The *Optical Breakdown Threshold* (OBT) characterizes the maximum power density allowed in the medium before breakdown. All kinds of physical effects (chemical reactions by bonds breaking, ionisation, heating induced electron avalanche) are described by this single value. The state of the art describes this OBT as the power density threshold before the SBS breakdown (reflectivity loss, stability loss, fidelity loss, medium damage, ...). This value should be chosen as high as possible to minimize the risks of breakdown during cell operation.

The phonon lifetime has been identified as being the key parameter for efficient SBS reflection. As such, the initial selection of medium includes only relatively low lifetime medium. Those include liquids and solids (≈ 1 ns). Solids do not present convective heat flow, that has been proven to reduce the quality of the SBS reflection under high power load, and are currently

being investigated by the community [29–31]. Using solid state SBS media is deemed too dangerous for initial experiments due to irreversibility in case of breakdown. For this reason, a liquid medium is chosen as in most cases of the literature.

The choice among liquids is made by comparing the residual absorption and the optical breakdown of the fluids available [27]. Among them, the perfluoro-compounds (PFCs) are known in the community for presenting both characteristics. They consist of hydrocarbon chains where the H atoms are replaced by F atoms. This leads to a high number of C-F atomic bonds with high bond energy (5.6 ev) and exhibiting high chemical stability and durability, in particular, high OBT ($> 100\ \mathrm{GW/cm^2}$). Furthermore, the absorption of those compounds is extremely low ($< 0.001\ \mathrm{cm^{-1}}$) making it compatible with our applications. Most of the articles from the literature actually use those liquids, and a large part of the state-of-the-art performances were obtained with PFCs from the manufacturer *3M* (FC75 [10, 11], FC770 [18], FC72 [26]...). When trying to acquire some of those liquids, we learned that most of them are being discontinued due to new environmental regulations. Hence, most of the experiments have to be performed using PFPE instead (also mostly composed of C-F bonds) produced by *Solvay Solexis*. Those liquids have also largely been documented, especially in recent years [26, 32].

In the following experiments, several liquids are acquired. The lower-energy experiments are performed using PFPE HT-70 and the high-energy experiments are performed using residual PFC FC770 available at LULI.

3.3.2 . Filtration

Once the liquid is chosen, we perform a purification step to remove all its residual impurities. This step has been demonstrated to greatly increase OBT and thus the reliability of the cell [7]. If the liquid is not purified and filtered, some impurities indeed stay in suspension inside the liquid. If during a shot, the laser hits a highly absorbent dust speck, this particle can act as a spark and initiate breakdown inside the liquid. This phenomenon is known to trigger large scale instabilities of the SBS mirror and in some cases fidelity losses, including hot spot apparitions and optical damages during the round trip into the laser. This is one of the likely reason SBS cells are not often used in commercial laser sources.

Several filtration schemes are present in the literature [4, 21, 33]. In our experiments, we replicated the filtration scheme presented in [7]: a two-step filtration scheme with a first filter of pore size $220\ \mathrm{nm}$ followed by a second stage of filtration through pore size $25\ \mathrm{nm}$. Furthermore, the cell was cleaned in an ultrasound bath to prevent any residual impurities from

Figure 3.5: Filtration station. Picture taken in LULI2000 class-100 clean room.

staying attached to the cell edges and being released during operation. The cell was then assembled in a class-100 clean room, and several fillings and drains of the cell were successively performed to ensure the purity of the fluid. Then, the cell was filled one last time and sealed. A picture of the filtration station is presented in Fig.3.5.

3.3.3 . Purity analysis

To guarantee the purity of the liquid used in the SBS cell, the filtration protocol was first used on tap water. We analysed the purity of the water before filtration and after filtration. At first, we used a technique called *Dynamic Light Scattering* (DLS) to confirm the purity of the liquid. This method consists of sending a monochromatic laser beam inside a liquid sample and analysing the scattering intensity in a particular direction (Fig.3.6). Because the scattering particles move, the scattering intensity varies along time. Smaller particles typically move faster and thus fast variation of the scattered light intensity indicates their presence.

This *speed of variation* is quantified rigorously by the *autocorrelation* $g^{(2)}(q,\tau)$ of the scattered signal, where $q = 4\pi/\lambda \sin(\theta/2)$ the norm of the vectorial subtraction of the scattered wave compared to the incoming wave and τ the delay time used for the autocorrelation. DLS theory [34] gives the expression

$$g^{(2)}(q,\tau) = 1 + \exp(-2q^2 D_0 \tau) \tag{3.1}$$

with D_0 the scattering coefficient that can be linked with the particle size (assumed spherical) by the *Stokes-Einstein formula* [35]

$$D_0 = \frac{k_{Boltzmann} T}{6\pi\eta R_H} \tag{3.2}$$

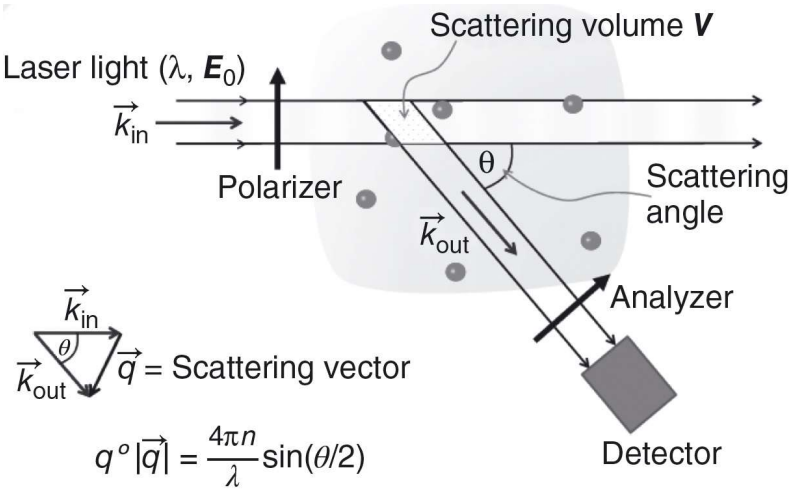

Figure 3.6: Dynamic light scattering schematics. Source: [34].

with η the viscosity and R_H the radius of the sphere considered. Typical autocorrelation figures for different diameters are given in Fig.3.7

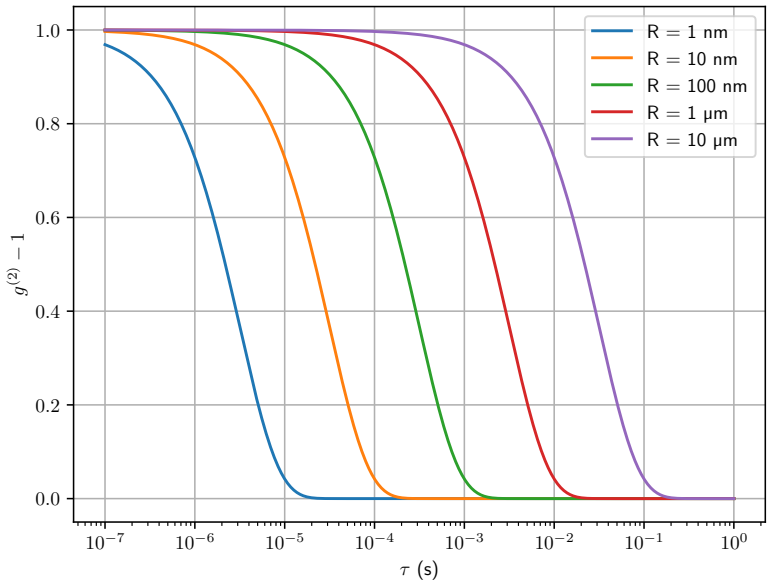

Figure 3.7: Examples of DLS autocorrelation figures for populations consisting of a single particle size. Angle of scattering: $90°$.

This model was experimentally confirmed using a DLS measurement tool at *Laboratoire de Physique de la Matière Condensée* at *École Polytechnique*. To confirm the accuracy of our model and the validity of our protocol, we were given a sample of one of their solution consisting of a population of 1 nm gold particles. The autocorrelation measurements were performed using a

Zetasizer nano from *Malvern*. The resulting curve was fitted to our model by varying the R_H parameter (in this case, the angle of scattering was $173°$). The autocorrelation result and the fitted curve are given Fig.3.8.

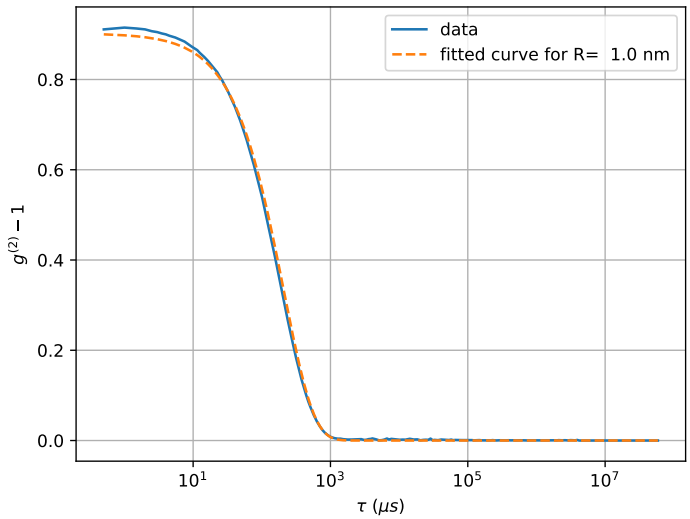

Figure 3.8: DLS autocorrelation measurements and corresponding fitted curve using our model. Sample: 1 nm gold particles, Zetasizer output value for measurement: 1 ± 0.1 nm.

As we can see, the retrieved diameter matches well with the theoretical diameter of the gold particles.

This means we can easily acquire the size of the particles present in the medium as long as

- They scatter enough light. For example, the autocorrelation value for $\tau = 0$ s observed on Fig.3.8 is below 1, corresponding to a loss of signal-to-noise ratio. When this value becomes close to 0, the measurements become unusable.

- Only one population is present. In our first example case, the gold particles were the dominant population, but in the case of impurities in suspension in the liquid, the population might be diverse.

To attempt to solve this issue, we extend the model by considering several independent populations with varying scattering intensities. The formula for the curve fitting then becomes:

$$g^{(2)}(q,\tau) - 1 = \sum_n I_n \exp(-2q^2 D_{0,n}\tau) \tag{3.3}$$

with $\sum_n I_n = 1$. (or < 1 when scattered signal is weak). Note that Eq.3.3 is not necessarily rigorously derived from DLS theory but seems like a reasonable extension. Furthermore, all results presented in the following using this model have been checked with the measurement tool results and give particle diameter with same order of magnitude. The remaining errors noticed can be explained by the simplicity of the model used and the assumption of spherical particles, incorrect for the case of dust-like particles in suspension in a liquid.

Pre-tests with water measurements Firstly, the filtration system was used on water. Tap water was analysed before and after filtration with the first filter stage. The results are given in Fig.3.9-3.10.

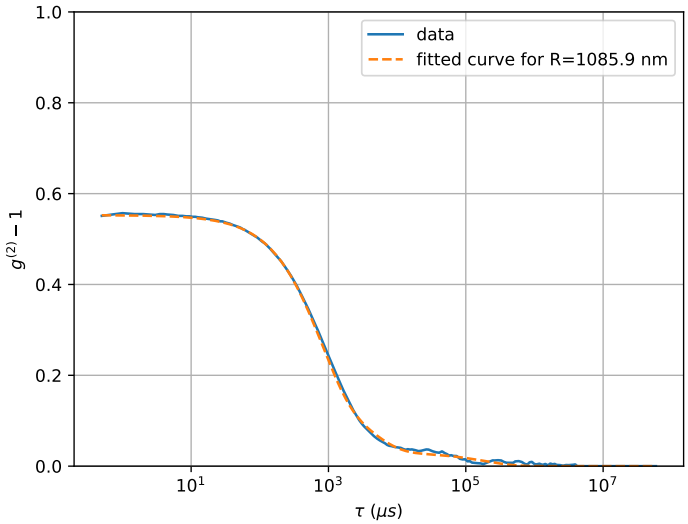

Figure 3.9: DLS autocorrelation measurements and corresponding fitted curve for a sample of unfiltered tap water. Zetasizer measurement gives 500 ± 100 nm.

Two information can be gained from this figure: firstly, although several populations are present in the medium, the maximum intensity detected is below 1, even for $\tau = 0$ µs. This means the signal received by the detector is low and a drop of signal to noise ratio is observed. The identification of the real particle size might therefore be arduous, especially once the water have been filtered. Secondly, even though the signal received is low, the autocorrelation figure still manages to fit the theoretical curve. Therefore, a certain level of trust can still be placed in those results.

In the following, we take this same tap water and pass it through the first stage of filtration only. The corresponding autocorrelation curve is given in

Fig.3.10.

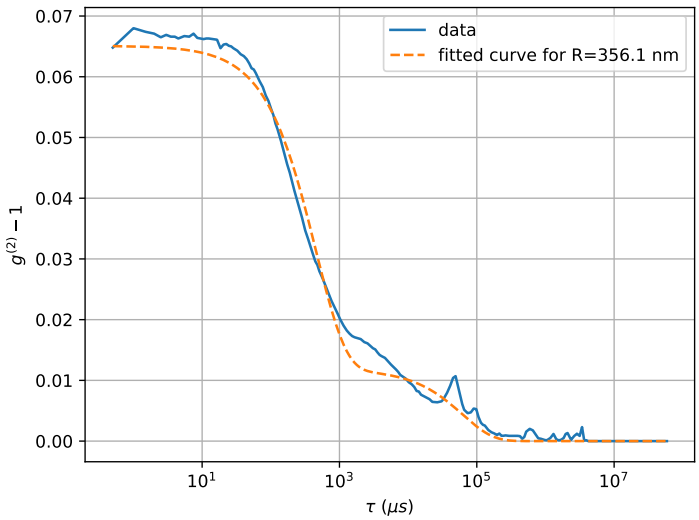

Figure 3.10: DLS autocorrelation measurements and corresponding fitting curve for a sample of filtered tap water. Zetasizer measurements gives 236 ± 40 nm.

By comparing the two curves Fig.3.9 and Fig.3.10, we directly observe the effects of filtration. The maximum particle size in the liquid is reduced and the overall scattered signal also greatly decreases. This last point in particular makes the measurement extremely noisy (and the fitting quality with the model starts to deteriorate). This does confirm that the liquid purity increases, but the quantitative study of the residual impurities becomes challenging.

This is even worse in the case of the analysis after filtration through the second stage filter, with pore size of 25 nm. In this case, the analysis fails most of the time (no signal detected). One of the few autocorrelation curves obtained is presented in Fig.3.11.

At this last stage of filtration, the measure becomes unreliable. The curve is extremely close to 0 for all delays τ and no particular shape can be identified.

This analysis procedure therefore brings a limited amount of information:

- The filtration system clearly improves the quality of the liquid.
- The results for the first stage of filtration gives results close to the expected values (≈ 350 nm for the water filtered with 220 nm pores)

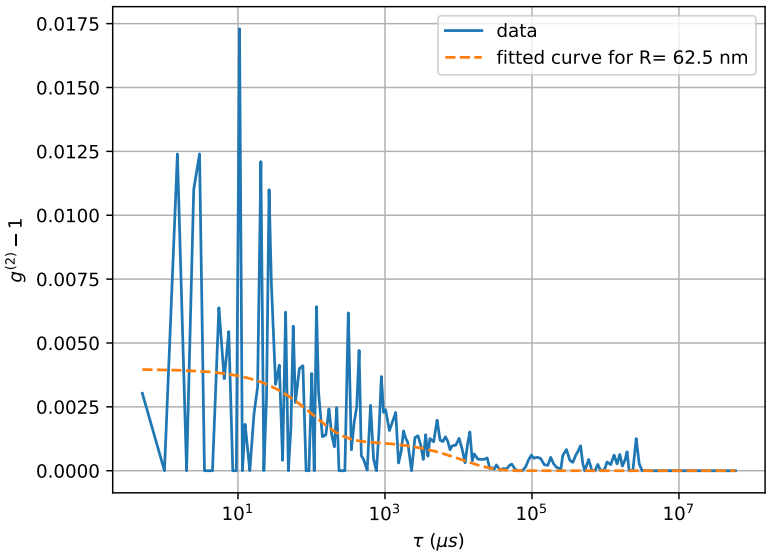

Figure 3.11: DLS autocorrelation measurement and corresponding fitting curve for a sample of filtered tap water through the two stages of filtration. Zetasizer measurements unavailable.

- The measurement finds its limit when the scattered signal goes below detector noise. In the case of our ultra-filtered water, this limit is reached, and we can't properly analyse the liquid.

To go beyond this measurement, state-of-the-art filtration system use a particle counter [21]. Because we didn't have access to those kinds of measurement tools, we analysed the ultrapure water with a *Transmission Electron Microscope* (TEM) available at the *Laboratoire de Physique de la Matière Condensée*.

Transmission electron microscope measurements Measurements performed with the TEM were used as a confirmation of the measurements with the DLS system. Because the TEM was not in a clean room and the liquid had to be transferred in the air before measurement, some impurities might be added to the liquid, degrading its actual purity before measurement. The goal of this measurement was to find the typical size of residual particles present in the medium. Single large-sized particles presence were then attributed to the transfer between clean room and TEM chamber.

Before being analysed, a drop of the liquid was taken out from the output of the filtration cell and was placed on the TEM measurement target. This measurement target is constituted of copper grids of two scales. The first scale has square holes of edges $\approx 50\ \mu\mathrm{m}$ separated by copper lines. In

those holes is placed the second sized grid: a layer of copper in which holes or diameter $2\ \mu\mathrm{m}$ and separated by $1\ \mu\mathrm{m}$ have been pierced. Those two grids are covered by a carbon layer of size $3\ \mathrm{nm}$. During the measurement, we observe the transmitted signal through the target. The grids (copper + carbon) then appear as darker than the holes (only carbon layer). The presence of a particle is indicated by a darker spot inside the holes of the grid. A view of the full grid is shown Fig.3.12.

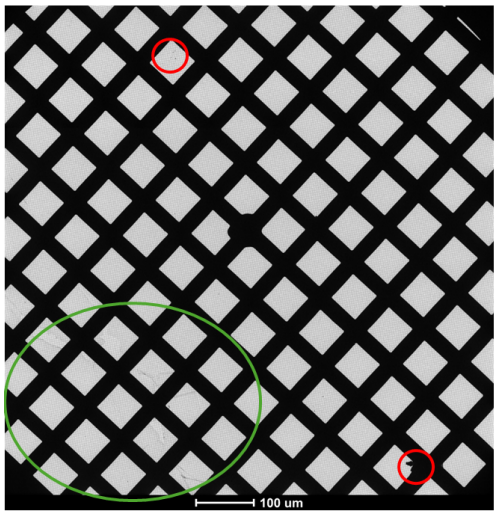

Figure 3.12: View of the full TEM target for a water measurement, red circles indicate the presence of particle clusters (attributed to the deposition of air particle during the transfer of the liquid on target) and the green circle indicates a defect in the carbon layer.

On this grid, besides the few particles cluster probably caused by the deposition of an air dust particle during the transfer, we can highly zoom on a hole of the grid and analyse the composition and presence of actual particles inside the liquid. Different scales of TEM analysis are presented in Fig.3.13.

Those images do not permit an absolute measurement of the number of particles still present inside the medium after filtration. Yet, they allow one to observe that the number of particles with size several times above pore diameter have almost completely been eliminated though the filtration process. The residual particles present in the medium are indeterminately either due to small defects still present during the filtration process (cell or tubes cleaning, filter nonconformity, air contamination,...) or due to the transfer to TEM target. And the typical particles size observed on a average hole in the copper grid do not exceed $\approx 20\ \mathrm{nm}$. Although those results are imperfect, they allow to confirm a certain level of purity and the resources needed for deeper analysis were considered out of reach.

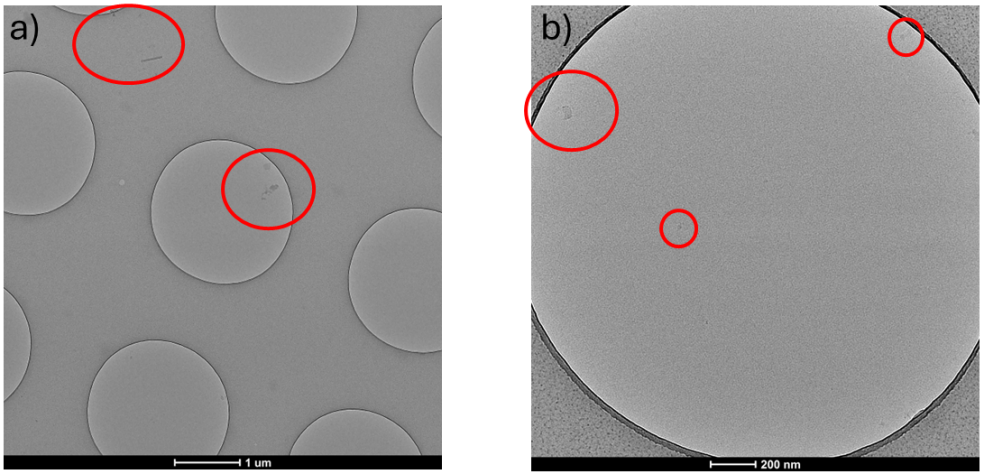

Figure 3.13: View of TEM analysis for water filtered at $25\ \mathrm{nm}$ level. a) zoom on a particle cluster, particle of size $\approx 100\ \mathrm{nm}$ are visible (circled in red). b) Zoom on a typical hole of the grid. Some particles of size $\approx 20\ \mathrm{nm}$ are visible (circled in red).

PFC and PFPE analysis The measurements are then performed again using this time PFC (FC770) and PFPE (HT70) analysis. Because we don't want to contaminate the tubes placed after the lowest pore size filtration, only the ultra-filtrated measurements are performed. The zetasizer measurement are once again below noise level, guaranteeing a good filtration level. However, on the contrary to the water case, the TEM analysis is compromised by the chemical composition of the liquid, composed of long carbon chains. In this second case, the electrons sent by the TEM are heavily absorbed, and no particles diluted inside the liquid can be seen. An example of a TEM measurement on FC770 is given in Fig.3.14.

The conclusion of the purity measurements was mitigated. We could confirm that the filtration had an effect and that the purity of the fluid obtained was good (no scattering signal and low number of particles observed by TEM) but no quantitative values of the absolute purity of the fluid could be obtained. In particular, TEM measurements were impossible for the fluids of interest.

Even given this slight uncertainty on the fluid quality, the filtration output was redirected inside the cells and once filled, those cells were sealed and operated on the available laser sources. In the following, we describe the architectures of the two available laser systems.

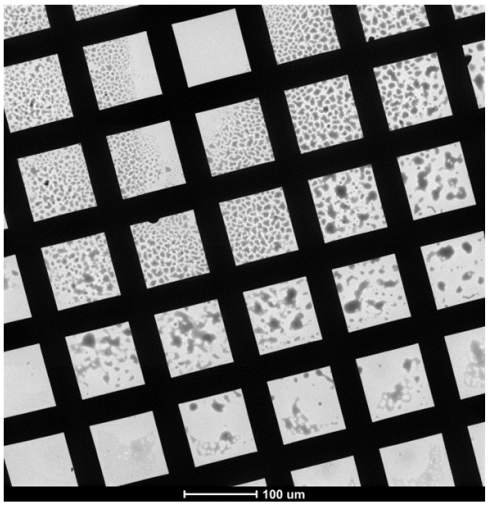

Figure 3.14: View of the TEM analysis for an ultra-filtered FC770. The visible dark drops correspond to residual molecules from the FC770 during evaporation. The evaporation front is clearly visible: the dark spots get smaller the closer to the centre of the evaporation zone. No residual particles could be observed under those conditions.

3.4 . Experimental setups

In Sec.3.2, we detailed our goal for the experiments. Several technological bottlenecks were presented (wavefront correction capacities, short pulse reflection, temporal shaping conservation, stability, energy load...) and represent numerous parameters to study.

To this aim, two laser sources were used in the experiments. Firstly, a custom-made laser was designed and built at *Amplitude* facility in *Lisses* to provide a suitable basis for parametric study. This laser architecture could be changed at will to best fit the requirements for a particular study. It was designed energetic enough, stable enough and with high enough repetition rate to perform the required cell stability measurements.

The second laser source was used to study the behaviour of the cell at very high energy. This laser source was a high-energy laser source of LULI: HERA, and 6 weeks of beam time (3 for preparation, 3 for experiments) were allocated for our studies. Because of the architecture of the laser, the repetition rate was limited. Hence, the studies on this laser were performed after the initial studies on the custom laser at *Amplitude*.

3.4.1 . Requirements

The results of the numerical simulations of the SBS effect (Chap.2) as well as the study of the state-of-the-art source (Sec.3.1) were used as a basis for the design of the laser chains usable for the experiments. In this section, we

present the quantitative requirements of the laser chains needed to answer the objectives developed previously.

Firstly, since we study SBS dynamics, we need to be able to trigger efficient SBS effect. To this aim, the laser sources need to be narrow-linewidth, typically, a few times below the Brillouin linewidth ($359\ \mathrm{MHz}$ for HT70 [28]). To this aim, we can either use a self-injection locked Q-switched laser or a Master Oscillator Power Amplifier (MOPA) with a seeder having narrow wavelength. In the scope of our work, the temporal profile has already been identified as a key parameter on the efficiency of SBS reflection. Furthermore, our requirements include the operation of SBS mirrors with arbitrary input pulse shape. Therefore, the MOPA architecture was selected as the seeder of choice for our experiments.

The MOPA consists of an oscillator having tailored properties (spectrum, temporal shape, polarisation, ...) subsequently amplified by a series of amplifiers to reach the desired energy. In our case, since we simultaneously require narrow linewidth spectrum and arbitrary temporal shape, we used a narrow linewidth cw diode (DFB with spectrum $< 1\ \mathrm{MHz}$) followed by a temporal pulse shaper that attenuates the laser diode emission to a very low input power (temporal gating) or alternatively transmit, or even amplify, the cw power, those two behaviours and all the in-betweens being controlled electronically. Several components are available in the literature to perform this operation such as Electro-Optic Modulators (EOM) [36, 37], Acousto optic modulators (AOM), Semiconductor Optical amplifiers (SOA) [38], or any combination of those systems. In the case of a seeder for SBS conjugation, we do not necessarily need fast modulation rise and fall time as the reaction time of the medium is limited to $\tau_{\mathrm{medium}} \approx 1\ \mathrm{ns}$ (which also corresponds to the spectral broadening caused by the modulation approaching the Brillouin linewidth of $\approx 500\ \mathrm{MHz}$ for the liquids considered). Hence, the SOA modulators, having higher contrast and lower cost compared to state-of-the-art EOM systems were chosen.

Subsequently, the seed signal of low energy ($\approx 1\ \mathrm{nJ}$ at SOA output) has to be amplified to the desired energy. Although several amplification geometries exist, the one commonly used is the combination of a single amplifier in a regenerative amplification scheme -or regen- (pulse trapping inside a cavity) to achieve large gain with minimal number of active components (typically 10^6 of gain up to millijoule energy level) followed by single or double pass amplification in amplifying heads of increasing diameter. This amplification scheme allows to increase the energy to the desired level with limited amount of active components and relative simplicity. It is to note that the amplification can influence some of the properties of the amplified pulse (in particular, the spatial and temporal profile through Frantz-Nodvik gain saturation [23]). Furthermore, several

beam spatial shaping schemes (serrated aperture, spatial filtering, imaging, ...) can be placed inside the amplification section to optimize the spatial properties of the output pulse after amplification.

In this work, the two lasers have this MOPA architecture with SOA seeding. Yet, some of the other properties such as wavelength, active medium, saturation level and spatial properties are dependent on the laser source used.

In both cases, the SBS mirror is not placed inside the laser, at the middle of a double pass but is instead placed directly at the laser output. This particular configuration, uncommon in the recent work in the literature, allows us to maximize the input energy on the mirror and separate the individual contribution of the SBS mirror from the contribution of the second pass inside the laser. Our aim is the understanding of the individual contribution of the SBS mirrors, their characteristics and their potential when subsequently integrated in a laser. This came at the cost of an isolation setup that had to be placed between laser output and the metrology experimental layout to prevent backward energy injection from the return of the Stokes wave from the SBS mirror into the laser.

In the following section, we detail the sources as initially designed. Any further modifications to those sources will be presented directly in the experimental part.

3.4.2 . Medium repetition rate source for parametric experiments

The first experiments are conducted on a custom laser source designed, built and aligned on-site at *Amplitude*. The design choices were made at the very start of the thesis, simultaneously with the simulations. The laser optical layout is largely derived from *Amplitude*'s standard regenerative amplifiers of the *Nanosecond Advanced Lasers* product line. In this case, the targeted wavelength is $1064\ \mathrm{nm}$ and the active medium is Nd:YAG. A simplified optical layout of the regenerative part of the amplifier is shown in Fig.3.15.

In this laser, the fibered DFB laser diode and SOA pulse shaper are firstly injected in free space by a commercial free space injector with linear polarisation. Feedbacks from the regen are prevented by the use of two subsequently placed Faraday isolators. The pulse is then injected inside the regen cavity and its polarisation is switched by a pockels cell. Once the entire pulse has passed, the tension of the pockels is switched on so that the pulse stay trapped inside the cavity. The amplifier of the cavity is a flash-pumped Nd:YAG head of diameter $7\ \mathrm{mm}$. The cavity mode is determined by a hard aperture of diameter $4\ \mathrm{mm}$ and the selected mode is TEMoo of radius $1.3\ \mathrm{mm}$ at cavity output. Once the amplifier energy is extracted and the seed energy starts to decrease pass after pass, the Pockels cell is switched off,

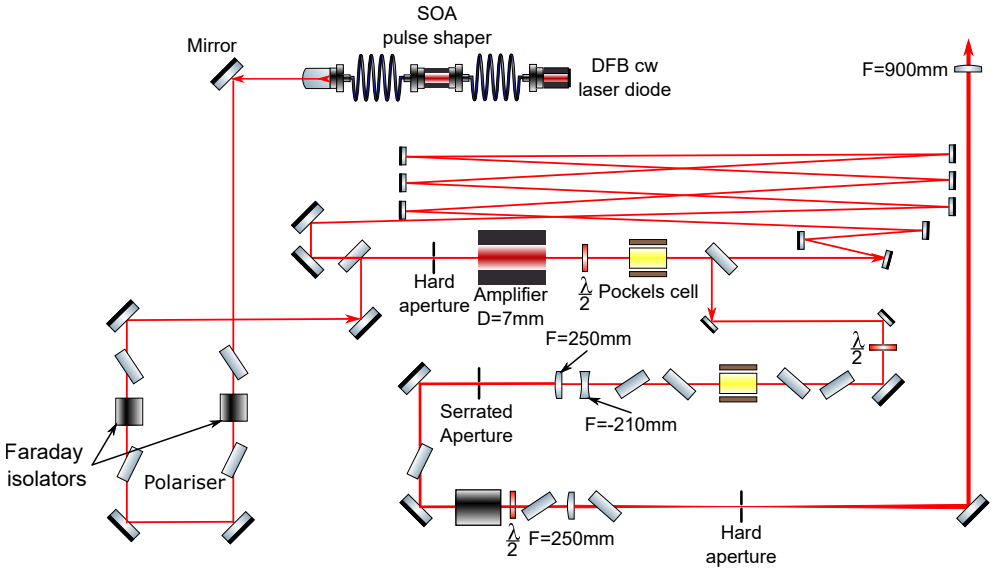

Figure 3.15: Schematics of the regen section of the custom laser source built at Amplitude for SBS experiments.

and the pulse is extracted. It then passes through a second *pulse cleaner* Pockels cell switched on only during a $20\ \mathrm{ns}$ gate corresponding to the maximum pulse width sustainable by the regen cavity, therefore filtering all pre- and post-pulses leaking from the cavity. The pulse is then magnified using a divergent-convergent imaging system and sent on a beam spatial shaper: a serrated aperture [39] that allows to cut the edges of the TEMoo Gaussian beam and thus efficient amplification without amplitudes modulations at the edges of the beam after propagation. The high spatial frequencies introduced by this serrated aperture are then spatially filtered using another magnification convergent-convergent imaging system, with a beam output full diameter of $10\ \mathrm{mm}$.

During the alignment of this system, the Nd:YAG amplifier head of the regenerative cavity had so much gain that several optical components of the regenerative section were damaged. The flashlamps power supply were thus tuned down in input power. This lead to operation of the power supply well below its typical operation regime and thus to a substantial decrease of the shot-to-shot stability of the module compared to expected behaviour. Furthermore, due to this low-level operation regime, the flashlamps sometimes didn't flash at all, resulting in a missed shot. This behaviour will lead to some aberrant points in the results curves presented in the following chapters. Even under those conditions, the pulse energy at cavity output is about $30\ \mathrm{mJ}$. After the spatial and temporal filtering, this energy is reduced to $15\ \mathrm{mJ}$ with energy stability of about 1%.

The beam then goes through a direct amplification section that consists

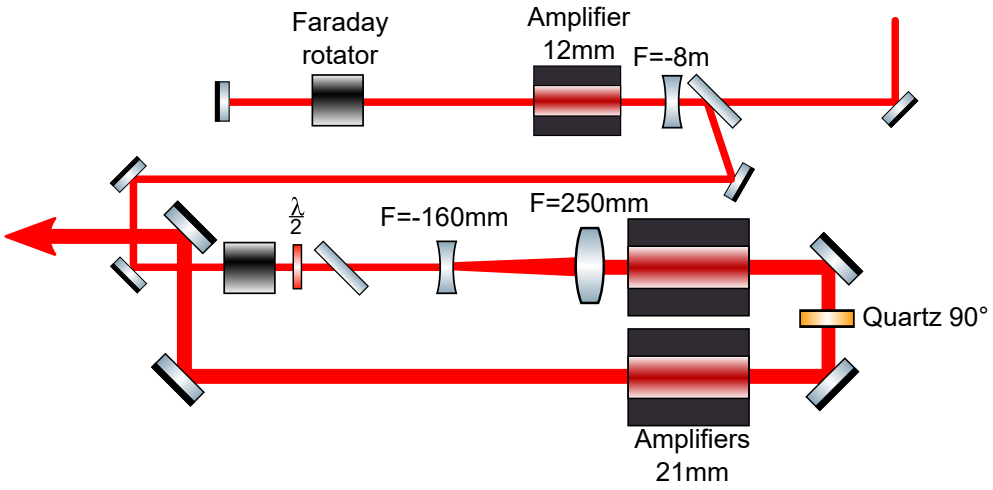

Figure 3.16: Schematics of the amplifier section of the custom laser source built at Amplitude for SBS experiments.

of 3 amplifying heads of diameter $12\ \mathrm{mm}$ and $21\ \mathrm{mm}$ as shown in fig.3.16. The pulse firstly goes through a double pass in the $12\ \mathrm{mm}$ to reach an energy level of $1\ \mathrm{J}$. Then, the laser beam is magnified one last time in a divergent convergent lens system to reach a diameter of $20\ \mathrm{mm}$ and is amplified in two single passes $21\ \mathrm{mm}$ Nd:YAG rod amplifiers.

The gain saturation in the amplifier tends to make the beam perceive higher gain on the edges of the beam than on the beam centre, therefore transforming the quasi-gaussian beam into a highly supergaussian beam. This is possible considering the fluence level in the amplifiers ($1.3\ \mathrm{J/cm^2}$ at the output of the $10\ \mathrm{mm}$ head and $2\ \mathrm{J/cm^2}$ at the output of the $21\ \mathrm{mm}$ heads) is several times higher than the saturation fluence of the Nd:YAG ($\approx 0.6\ \mathrm{J/cm^2}$). This strong gain saturation inside the amplifiers have several effects on the beams properties.

- The beam is turned into a high order supergaussian beam
- The temporal profile of the beam is modified. In particular, the pulse duration can be shortened by the gain saturation.
- The energy stability of the pulse is largely improved. Since almost all the energy available deposited by the amplifiers power supply is used by the beam, the energy stability of the amplifiers flashlamps, operating at nominal value, is dominant.

The output pulse from the amplifier was highly supergaussian of diameter $20\ \mathrm{mm}$ and output energy $6.9\ \mathrm{J}$ with $0.2\%\ \mathrm{RMS}$ energy stability at $5\ \mathrm{Hz}$. A measurement of the energy stability over 1000 shots is shown Fig.3.17.

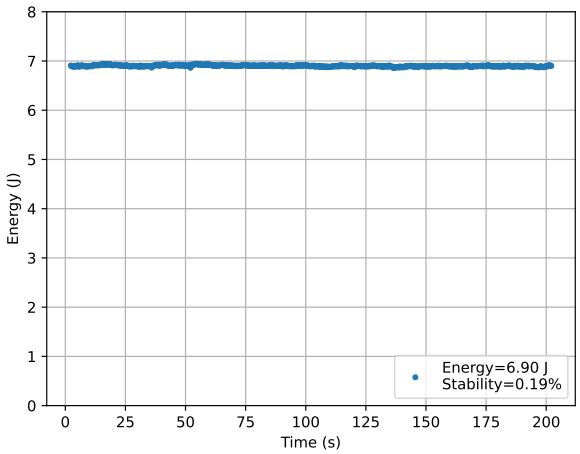

Figure 3.17: Pulse energy as a function of time at the output of the laser amplifier.

Because of the divergent convergent imaging systems, the image of the reference plane (serrated aperture - Fig.3.15) could not be placed after the last amplifiers. The near field profile (as seen by cameras), thus presented some amplitude modulation near the edges. Because of laser compactness requirements, a proper convergent-convergent imaging system could not fit inside the laser and replace the divergent-convergent system.

This experimental setup provides repetitive pulses with good stability and significant energy. Because this laser is custom-made, it was possible to change its optical configuration to change the input parameters. Most of the initial experiments were performed on this particular laser source and will be presented in Chap.4.

3.4.3 . High-energy source

The high energy laser source used for the qualification of high energy SBS cell was a laser chain of *Laboratoire LULI*: the HERA laser chain [40][1]. This laser provides pulses of arbitrary temporal shape with energy as high as $200\ \mathrm{J}$. It is once again built following the MOPA architecture and uses a DFB laser diode at $1053\ \mathrm{nm}$ temporally shaped by an SOA pulse shaper and subsequently amplified by a Diode pumped Nd:YLF regenerative amplifier and by several flash-pumped Nd:Glass amplifiers. The last stage of amplification being performed in Nd:Glass discs amplifiers at Brewster angle. An optical layout of the laser chain is presented in Fig.3.18.

This laser chain present the advantage of having active medium with

[1]The participation to the development of this laser source were performed during the thesis. In particular, the temporal shaping scheme has been described in an article given In Appendix.A

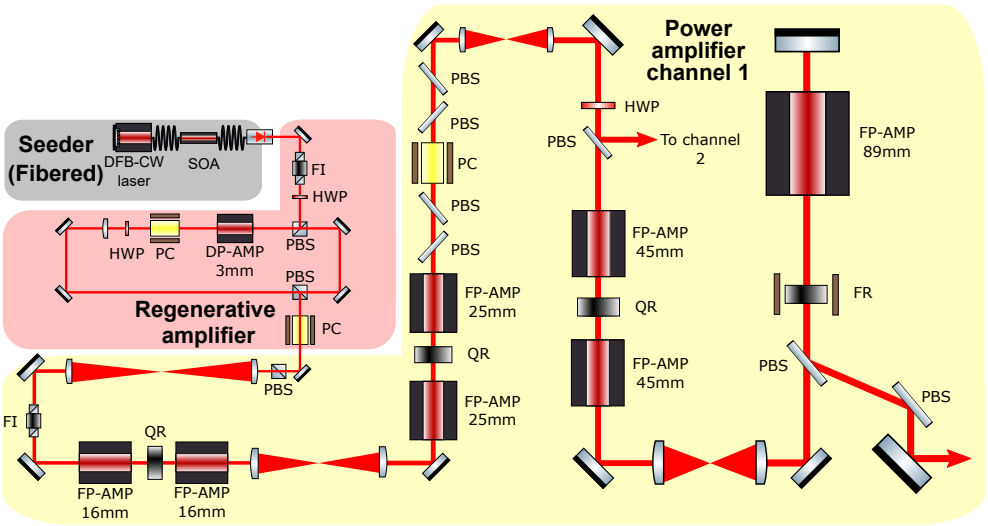

Figure 3.18: Schematics of the HERA laser. AWG: Arbitrary current Waveform Generator, DFB-CW laser: DFB laser diode, SOA: Semiconductor Optical Amplifier, FI: Faraday Isolator, HWP: Half-waveplate, PBS: Polarizing Beam Splitter, DP-AMP: Diode-pumped Amplifier, PC: Pockels cell, FP-AMP: Flash-pumped Amplifier, QR: Quartz Rotator, FR: Faraday Rotator.

extremely high saturation fluence ($> 5\ \mathrm{J/cm^2}$ for Nd:Glass) compared to the low fluence the laser chain operates at ($< 1\ \mathrm{J/cm^2}$). Therefore, the temporal profile deformation is low during amplification. This leads to far easier shaping than on the *Amplitude* laser chain. However, this chain has lower repetition rate (1 shot per 20 minutes) and its shot-to-shot stability is over 10%. Furthermore, this chain was accessible for short period of times during beam time campaigns. This limited the amount of modification that we could bring to the laser chain. Hence, this laser was used to confirm the proper conservation of the properties demonstrated on the smaller scale laser during the energy scale up. Those experiments at high energy are presented in Chap.5.

3.4.4 . Metrology experimental layout

In both systems, the SBS cell is placed at the laser output for the purpose of precise, isolated, parametric studies. Because the PCM reflects the input pulse backward, no geometrical configuration was possible to prevent Stokes pulse signal returning into the laser chain. To prevent damage to the laser source, the isolation between laser source and the cell was polarisation based. The cells themselves were designed after the results from the simulations and the state of the art analysis. An insertion depth of the waist inside the cell below $300\ \mathrm{mm}$ was chosen in both cases. For the high-energy laser, since the laser beam is $93\ \mathrm{mm}$ wide, this represents an aperture of $F/3$ and introduces

other challenges. This particular aspect is developed in Chap.5.

The measurements were performed before and after reflection to properly compare the properties of the pump beam and Stokes beam. Because the metrology was modified greatly during the experiments, the full metrology setup will be presented directly during the chapters corresponding to the experiments (Chap.4 for the *Amplitude* laser chain and Chap.5 for the high energy experiments). Yet, several observations can be made to compare the difficulties and challenges encountered.

Firstly, because the *Amplitude* laser chain had great stability, it was possible to perform the measurements of the pump beam properties *before* the measurements of the stokes beam and compare the two while assuming the pump beam almost constant. For the *HERA* laser chain, peak-to-peak stability is around 10% which makes the pump/stokes comparison possible on the same shot only. Therefore imposing all the data acquisition to be performed in parallel, on symmetric optical lines. The metrology components (spatial profile, energy, temporal profile) then have to be split.

Second, the stability measurements performed on the *Amplitude* laser chain had as an objective to identify eventual erratic behaviour of the PCM. On this particular experiment, about a million shots on the SBS cell were recorded and analysed, and special procedural data treatment had to be introduced.

3.5 . Conclusion

In this chapter, we started by studying the literature on high energy SBS for phase conjugation. This gave us insights on the experiments performed and the current limitations. In particular, we identified a challenge on the reflection of pulses with moderate or short pulse duration compared to the phonon lifetime of the nonlinear medium used. This study confirmed the simulation results of Chap.2 by showing that the temporal profile is a key parameter for SBS reflection.

This study of the state of the art also gave us insights on the feasibility of our own experimental objectives. Experimental reflectivity can be extremely high and efficiency of 95% are achievable with relative ease. Reflection of short pulse represent a challenge but some existing solutions [15] seem to offer interesting prospects. The reflection of arbitrary temporal profile, required for some applications has never been introduced and seems like a challenging but achievable result using the numerical tools previously developed. Long-term stability measurements have yet to be properly explored for industrialisation of such a component in commercial systems.

Only a few high-energy experiments were conducted with moderate or unknown success and low energy studies were required before attempting

our own design. Overall, the thesis objectives are challenging, and their realisation would bring a tool of interest for industrial laser manufacturers. The parametric study at high energy and the temporal profile conservation are also a largely unexplored topic of interest for both the academic and industrial community.

In the following part of this chapter, the experimental realisation of an SBS cell was presented. As demonstrated by the literature, this component requires precise filtration of the liquid to reach stable operation. Here, this liquid purification is reached by the development of a custom filtration system. The use of this developed system allowed us to obtain an ultrapure liquid for SBS nonlinear interaction and this purity was quantified using two distinct methods. The purity quantification was limited by measurement tools available.

At the end of the chapter, we identified the requirements for laser sources compatible with our experimental goals for SBS experiments and presented the general architecture used. In the following chapter, the first experiments at *Amplitude* on the custom, medium energy, medium repetition rate, laser system for initial SBS characterization and long-term stability measurements, are presented.

Bibliography

The following bibliography contains all the references cited in this chapter. A full bibliography of the thesis is given after the general conclusion. In addition, every bibliography entry is associated with every paragraph it has been referenced in. The corresponding section numbers are indicated at the very end of the entry.

[1] R. Y. Chiao, C. H. Townes, and B. P. Stoicheff. Stimulated Brillouin Scattering and Coherent Generation of Intense Hypersonic Waves. *Physical Review Letters*, 12(21):592–595, May 1964. Publisher: American Physical Society. 1.2, 3.1

[2] E. Garmire and C. H. Townes. Stimulated Brillouin Scattering in liquids. *Applied Physics Letters*, 5(4):84–86, August 1964. 3.1

[3] B. Zel'Dovich, V.I. Popovichev, and V.V. Ragul'skii. Connection Between the Wave Fronts of the Reflected and Exciting Light in Stimulated Mandel'shtem-Brillouin Scattering. *JETP Letters*, 15:109–112, January 1972. 3.1

[4] Nikolay Andreev, Oleg P. Kulagin, Oleg V. Palashov, Guerman A. Pasmanik, and Vladimir Rodchenkov. SBS of repetitively pulsed radiation and possibility of increasing the pump average power. In *Solid State Lasers for Application to Inertial Confinement Fusion (ICF)*, volume 2633, pages 476–493. SPIE, December 1995. 3.1, 3.3.2, 4.3.1

[5] Metin S. Mangir and David A. Rockwell. 4.5-J Brillouin phase-conjugate mirror producing excellent near- and far-field fidelity. *JOSA B*, 10(8):1396–1400, August 1993. Publisher: Optica Publishing Group. 3.1, 3.1, 3.2, 3.3, 3.4

[6] C.B. Dane, L.E. Zapata, W.A. Neuman, M.A. Norton, and L.A. Hackel. Design and operation of a 150 W near diffraction-limited laser amplifier with SBS wavefront correction. *IEEE Journal of Quantum Electronics*, 31(1):148–163, January 1995. Conference Name: IEEE Journal of Quantum Electronics. 3.1, 3.1, 3.2, 3.3, 3.1.2, 3.4

[7] H. Yoshida, V. Kmetik, H. Fujita, K. Yoshida, T. Yamanaka, and S. Nakai. High performance of phase conjugated stimulated Brillouin scattering mirror based on high purity liquid heavy fluorocarbons. *AIP Conference Proceedings*, 369(1):1004–1008, May 1996. 3.1, 3.1, 3.2, 3.3, 3.1.3, 3.4, 3.3.2, 3.3.2, 4.3.1

[8] R.J. St. Pierre, D.W. Mordaunt, H. Injeyan, J.G. Berg, R.C. Hilyard, M.E. Weber, M.G. Wickham, G.M. Harpole, and R. Senn. Diode array pumped kilowatt laser. *IEEE Journal of Selected Topics in Quantum Electronics*, 3(1):53–58, February 1997. Conference Name: IEEE Journal of Selected Topics in Quantum Electronics. 3.1, 3.1, 3.2, 3.3, 3.4

[9] Masahiro Nakatsuka and Hidetugu Yoshida. Wavefront compensator by SBS-PCM in power photonics. *Journal of the Communications Reasearch Laboratory*, 46(3):471–478, 1999. 3.1, 3.1, 3.2, 3.3, 3.4

[10] Viliam Kmetik, Hidetsugu Yoshida, Hisanori Fujita, Masahiro Nakatsuka, and Tatsuhiko Yamanaka. Very high energy SBS phase conjugation and pulse compression in fluorocarbon liquids. In *Advanced High-Power Lasers*, volume 3889, pages 818–826. SPIE, April 2000. 3.1, 3.1, 3.2, 3.3, 3.1.3, 3.4, 3.3.1, 5.4.1

[11] Takaki Hatae, Masahiro Nakatsuka, and Hidetsugu Yoshida. Improvement of Thomson Scattering Diagnostics Using Stimulated-Brillouin-Scattering-Based Phase Conjugate Mirrors. *Journal of Plasma and Fusion Research*, 80(10):870–882, 2004. 3.1, 3.1, 3.2, 3.3, 3.4, 3.3.1

[12] T. Hatae, O. Naito, M. Nakatsuka, and H. Yoshida. Applications of phase conjugate mirror to Thomson scattering diagnostics (invited). *Review of Scientific Instruments*, 77(10):10E508, September 2006. 3.1, 3.1, 3.2, 3.3, 3.4

[13] Tadashi Ikegawa, Takashi Sekine, and Ryo Yasuhara. Upgrade of Nd:glass zigzag slab laser by a wavefront compensation and second harmonic generation. *Annual progress report*, 2007, February 2008. 3.1, 3.1, 3.2, 3.3, 3.4

[14] Frank Wu, Anatoliy Khizhnyak, and Vladimir Markov. High-reflectivity SBS phase conjugate mirror. In *Nonlinear Frequency Generation and Conversion: Materials, Devices, and Applications VIII*, volume 7197, pages 317–323. SPIE, February 2009. 3.1, 3.1, 3.2, 3.3, 3.4

[15] Hong Jin Kong, Seong Ku Lee, Jin Woo Yoon, Jae Sung Shin, Sangwoo Park, Hong Jin Kong, Seong Ku Lee, Jin Woo Yoon, Jae Sung Shin, and Sangwoo Park. Stimulated Brillouin Scattering Phase Conjugate Mirror and its Application to Coherent Beam Combined Laser System Producing a High Energy, High Power, High Beam Quality, and High Repetition Rate Output. In *Advances in Lasers and Electro Optics*. IntechOpen, intechopen edition, April 2010. 3.1, 3.1, 3.2, 3.3, 3.1.2, 3.4, 3.2, 3.5

[16] Y. L. Wang, Z. W. Lu, Y. Li, P. Wu, X. M. Fan, Z. X. Zheng, and W. M. He. Investigation on high power phase compensation of strong aberrations

via stimulated Brillouin scattering. *Applied Physics B*, 99(1):257–261, April 2010. 3.1, 3.1, 3.2, 3.3, 3.4, 3.2

[17] A. A. Kuzmin, E. A. Khazanov, O. V. Kulagin, and A. A. Shaykin. Neodymium glass laser with a phase conjugate mirror producing 220 J pulses at 0.02 Hz repetition rate. *Optics Express*, 22(17):20842–20855, August 2014. Publisher: Optica Publishing Group. 3.1, 3.1, 3.2, 3.3, 3.1.3, 3.4

[18] Jisi Qiu, Xiongxin Tang, Zhongwei Fan, and Haocheng Wang. 200 Hz repetition frequency joule-level high beam quality Nd:YAG nanosecond laser. *Optics Communications*, 368:68–72, June 2016. 3.1, 3.1, 3.2, 3.3, 3.4, 3.3.1

[19] Yue Gao, Yanjie Wang, Amy Chan, Murray Dawson, and Ben Greene. High average power diode pumped solid state laser. *Laser Physics Letters*, 14(3):035803, February 2017. Publisher: IOP Publishing. 3.1, 3.1, 3.1.1, 3.2, 3.3, 3.4

[20] Xiongxin Tang, Jisi Qiu, Zhongwei Fan, Haocheng Wang, Hao Liu, Yueliang Liu, and Zhijun Kang. Experimental study on SBS-PCM at 200 Hz repetition rate pumped with joule-level energy. *Optical Materials*, 67:64–69, May 2017. 3.1, 3.1, 3.1.1, 3.2, 3.3, 3.4

[21] Zhijun Kang, Zhongwei Fan, Yutao Huang, Hongbo Zhang, Wenqi Ge, Mingshan Li, Xiaochao Yan, and Guoxin Zhang. High-repetition-rate, high-pulse-energy, and high-beam-quality laser system using an ultraclean closed-type SBS-PCM. *Optics Express*, 26(6):6560–6571, March 2018. Publisher: Optica Publishing Group. 3.1, 3.1, 3.2, 3.3, 3.4, 3.2, 3.3.2, 3.3.3

[22] C. Brent Dane, William A. Neuman, and Lloyd A. Hackel. Pulse-shape dependence of stimulated-Brillouin-scattering phase-conjugation fidelity for high input energies. *Optics Letters*, 17(18):1271–1273, September 1992. Publisher: Optica Publishing Group. 3.1.2, 4.4, 5.4.2

[23] Lee M. Frantz and John S. Nodvik. Theory of Pulse Propagation in a Laser Amplifier. *Journal of Applied Physics*, 34(8):2346–2349, August 1963. 3.2, 3.4.1, 4.2, 4.4.2

[24] Xiaozhen Xu, Chengyong Feng, and Jean-Claude Diels. Optimizing sub-ns pulse compression for high energy application. *Optics Express*, 22(11):13904–13915, June 2014. Publisher: Optica Publishing Group. 3.2

[25] Hongli Wang, Seongwoo Cha, Hong Jin Kong, Yulei Wang, and Zhiwei Lu. Rotating off-centered lens in SBS phase conjugation mirror for high-repetition-rate operation. *Optics Express*, 27(7):9895–9905, April 2019. Publisher: Optica Publishing Group. 3.2

[26] Yifu Chen, Bowen Tan, Duo Jin, Bin Chen, Zhenxu Bai, Kun Wang, Yulei Wang, and Zhiwei Lü. Characteristics and suppression of beam distortion in a high repetition rate nanosecond stimulated Brillouin scattering phase conjugation mirror. *High Power Laser Science and Engineering*, 12:e20, January 2024. 3.2, 3.3.1, 4.4

[27] W. L. J. Hasi, Z. W. Lu, S. Gong, S. J. Liu, Q. Li, and W. M. He. Investigation of stimulated Brillouin scattering media perfluoro-compound and perfluoropolyether with a low absorption coefficient and high power-load ability. *Applied Optics*, 47(7):1010–1014, March 2008. Publisher: Optica Publishing Group. 3.3.1

[28] Zhenxu Bai, Hang Yuan, Zhaohong Liu, Pengbai Xu, Qilin Gao, Robert J. Williams, Ondrej Kitzler, Richard P. Mildren, Yulei Wang, and Zhiwei Lu. Stimulated Brillouin scattering materials, experimental design and applications: A review. *Optical Materials*, 75:626–645, January 2018. 3.3.1, 3.4.1

[29] Hidetsugu Yoshida, Hisanori Fujita, Masahiro Nakatsuka, Tetsuji Ueda, and Akira Fujinoki. Compact Temporal-Pulse-Compressor Used in Fused-Silica Glass at 1064 nm Wavelength. *Japanese Journal of Applied Physics*, 46(1L):L80, January 2007. Publisher: IOP Publishing. 3.3.1

[30] Bin Chen, Zhenxu Bai, Yifu Chen, Kun Wang, Can Cui, Yaoyao Qi, Jie Ding, Bingzheng Yan, Yulei Wang, and Zhiwei Lu. Influence of a longitudinal-mode on stimulated Brillouin scattering characteristics in fused silica. *Optics Express*, 31(19):30030–30039, September 2023. Publisher: Optica Publishing Group. 3.3.1

[31] Bin Chen, Zhenxu Bai, Xuanning Hun, Jianping Wang, Can Cui, Yaoyao Qi, Bingzheng Yan, Jie Ding, Kun Wang, Yulei Wang, and Zhiwei Lu. Gain characteristics of stimulated Brillouin scattering in fused silica. *Optics Express*, 31(4):5699–5707, February 2023. Publisher: Optica Publishing Group. 3.3.1

[32] Hongli Wang, Seongwoo Cha, Hong Jin Kong, Yulei Wang, and Zhiwei Lu. Sub-nanosecond stimulated Brillouin scattering pulse compression using HT270 for kHz repetition rate operation. *Optics Express*, 27(21):29789–29802, October 2019. Publisher: Optica Publishing Group. 3.3.1

[33] Zhenxu Bai, Yulei Wang, Zhiwei Lu, Hang Yuan, Zhenxing Zheng, Sensen Li, Yi Chen, Zhaohong Liu, Can Cui, Hongli Wang, and Rui Liu. High Compact, High Quality Single Longitudinal Mode Hundred Picoseconds Laser Based on Stimulated Brillouin Scattering Pulse Compression. *Applied Sciences*, 6(1):29, January 2016. Number: 1 Publisher: Multidisciplinary Digital Publishing Institute. 3.3.2

[34] Erika Eiser. Dynamic Light Scattering. In *Multi Length-Scale Characterisation*, pages 233–282. John Wiley & Sons, Ltd, john wiley & sons, ltd edition, 2014. 3.6, 3.3.3

[35] A. Einstein. Zur Elektrodynamik bewegter Körper [AdP 17, 891 (1905)]. *Annalen der Physik*, 517(S1):194–224, 2005. 3.3.3

[36] Christophe Dorrer, Richard Roides, Robert Cuffney, Andrey V. Okishev, Wade A. Bittle, Gregory Balonek, Albert Consentino, Elizabeth Hill, and Jonathan D. Zuegel. Fiber Front End With Multiple Phase Modulations and High-Bandwidth Pulse Shaping for High-Energy Laser-Beam Smoothing. *IEEE Journal of Selected Topics in Quantum Electronics*, 19(6):219–230, November 2013. Conference Name: IEEE Journal of Selected Topics in Quantum Electronics. 3.4.1

[37] R. A. Meijer, A. S. Stodolna, K. S. E. Eikema, and S. Witte. High-energy Nd:YAG laser system with arbitrary sub-nanosecond pulse shaping capability. *Optics Letters*, 42(14):2758–2761, July 2017. Publisher: Optica Publishing Group. 3.4.1

[38] Raphaël Humblot, Loïc Meignien, Joanna De Sousa, Cyril Rapenaud, Sophie Baton, Frédéric Druon, and Patrick Audebert. Semiconductor optical amplifier used as fibered arbitrary waveform generator for high energy applications. In *High-Brightness Sources and Light-Driven Interactions Congress (2024), paper JTu4A.9*, page JTu4A.9. Optica Publishing Group, March 2024. 3.4.1

[39] Jerome M. Auerbach and Victor P. Karpenko. Serrated-aperture apodizers for high-energy laser systems. *Applied Optics*, 33(15):3179–3183, May 1994. Publisher: Optica Publishing Group. 3.4.2, 4.16

[40] Raphaël Humblot, Joanna De Sousa, Cyril Rapeneau, Sophie Baton, Patrick Audebert, Frédéric Druon, and Loïc Meignien. Semiconductor optical amplifiers as an optical arbitrary waveform generator for high-energy laser systems. *Optics Express*, 32(22):37959–37967, October 2024. Publisher: Optica Publishing Group. 3.4.3, 5.1

4 - SBS-PCM characterisation at the joule energy level

4.1 . Introduction

In the previous chapters, the theoretical description of the SBS effect was presented. We then developed simulation models for in-depth studies of the dynamics of the nonlinear effect and used the results for the first designs of the experimental setups. The performances reached in the literature were then analysed under the scope of those theoretical studies, and allowed to properly assess our own objectives for this thesis. We then described the experimental realisation of an SBS cell, specifically describing the preparation and purity validation of our nonlinear medium.

In this chapter, the first experimental studies on an SBS-PCM are performed. We use the custom laser source built at *Amplitude* described in 3.4.2, with $6\ \mathrm{J}$ output energy, and $5\ \mathrm{Hz}$ repetition rate, to acquire the first experimental data on SBS reflection. The aim of these studies are:

- The experimental demonstration of SBS reflection with our newly designed cells.
- The measurements of high SBS efficiencies (reflectivity $> 90\%$).
- The characterisation of spatial fidelity (the conservation of the near field spatial profile during reflection).
- The characterisation of wavefront reversal and wavefront correction.
- The characterisation of the SBS reflection effects on temporal profile.
- The experimental demonstration of temporal fidelity for diverse temporal shapes of interest.
- The stability of all those parameters over several hundreds of thousands of shots.

For this last point, the particular interest is the absence of a *rogue wave*, an aberrant behaviour of the PCM, changing the properties of the input pulse in such a way that the reflected Stokes wave damages the optical components during the backward amplification.

In the following, we present the (almost) chronological experimental studies using this laser source. We started by studying the reflectivity of our SBS cell to compare our results to the state of the art and identify any residual design errors. To this aim, we first started building and aligning an experimental bench for metrology purposes.

4.2 . Experimental optical layout

We start by comparing our SBS cell in configuration similar to the ones of state of the art. The most documented property of SBS-PCMs being their reflectivity, we also start by this measurement. To this aim, we look for a way to change the energy of our laser and measure the reflectivity against input energy on cell.

To change the laser energy, several methods are accessible. The first and most used is to change the pumping level of the amplifiers. In our case, this also means changing the thermal lensing level of our amplifiers. Hence, the laser output changes size and becomes convergent. Thus, this solution was rejected. Changing the delay of the pump current relative to the beam allows to shift the timing of the amplified pulse away from the gain maximal value. Therefore, the laser pulse is less amplified, reducing the output pulse energy. However, this method also changes the saturation level of the amplifiers [1] and thus, the output temporal profile (and the beam profile to some extent). As described previously, this temporal profile is a key parameter for SBS reflection. Thus, changing the delay of the seed pulse compared to the pump current would change all the parameters of the system and prevent proper characterisation.

The method chosen is therefore to attenuate the output pulse using several halfwave plates and polarisers to switch a part of the pulse energy on an orthogonal polarisation and eject it in a beam dump. One couple of wave-plate and polariser is used to filter out all the depolarisation component and two additional couples are used to attenuate the laser signal. The maximum attenuation by couple is chosen equal to 10% to avoid a dominant contribution of the residual deplorisation component in the transmitted pulse. This allows the tuning of the output energy over two orders of magnitude. However, the introduction of the seven polarisers and the Faraday isolator means that the maximum energy accessible at cell input was reduced to $5\ \mathrm{J}$.

After the attenuation part of the experimental optical layout, the optical isolation between the laser source and the PCM is performed using a Faraday isolator. This allows to ensure no Stokes signal could propagate backward inside the laser source and damage its optical components.

Then, a polariser is placed in the beam path. If the polarisation leaving the isolator is unchanged, the laser beam passes though this polariser and travels toward the metrology bench. If a halfwave plate is placed inside the beam path and switches the polarisation by $90°$, the beam instead goes inside the SBS cell. A quarterwave plate placed before the cell allowed the polarisation to be switched again during the double pass, thus the Stokes beam coming back from the cell is reflected by the polariser on the way back and propagates on the metrology bench as well. This setup allows very quick switching between

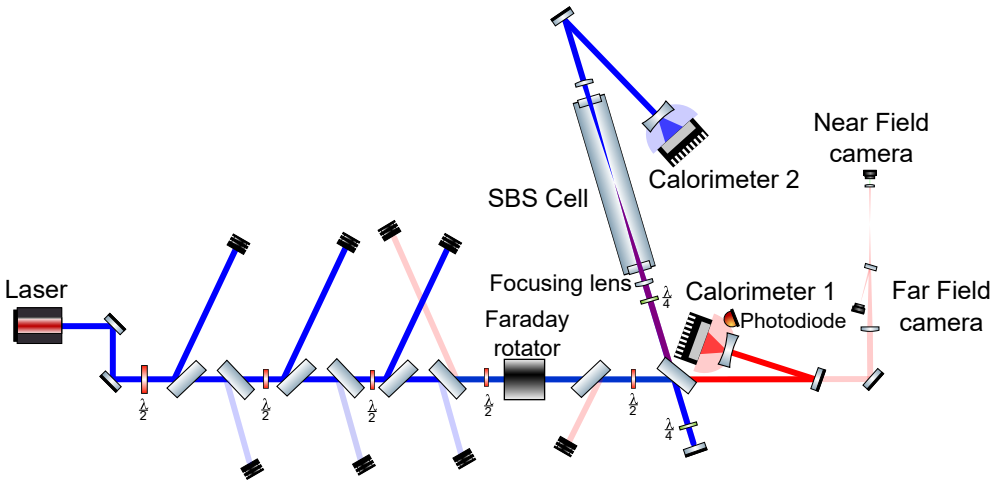

Figure 4.1: Optical layout of the experimental bench for the SBS characterisation on the *Amplitude* laser chain.

pump and Stokes analysis.

The metrology bench is composed of a calorimeter measuring the energy of either the input pump pulse or the output Stokes pulse. In addition, a photodiode detects the light scattered by this calorimeter and analyses the corresponding temporal profile of the measured pulse. A part of the signal leaking from a mirror is sent into a beam reducer and the splitting polariser is imaged on a camera to analyse the near field. A wedge extracts an additional part of the signal inside the imaging system and a camera is placed at focus point to analyse the beam far field. With this setup, simultaneous measurements of the energy, the temporal profile and the near field and far fields of either the pump beam or the Stokes beam are accessible. Furthermore, an additional calorimeter is placed in transmission to observe the stability of the transmitted signal through the cell. The full optical layout is presented in Fig.4.1.

As one can see on this figure, the return signal from the cell inside the laser can be analysed by placing a calorimeter on the leaking signal from the polariser placed just after the back propagation in the Faraday rotator. This backward energy is monitored, and the detected signal is $< 30\ \mathrm{mJ}$ mostly composed of parasitic reflection on the optical components of the system. The return energy inside the laser is therefore not considered as a major issue in this setup.

4.3 . First experimental results

We now describe the first reflectivity measurements on the system. For the evaluation of the reflectivity near Brillouin threshold, we had to delay the

seed energy compared to the maximum gain of the amplifier heads to reach energy level below $50\ \mathrm{mJ}$. The comparison of the pump and Stokes energies was also performed taking into account the losses for every reflection and transmission as well as the leaking of the pump wave through the polariser. On this first experiment, the pump pulse is a gaussian pulse with rise time $3.3\ \mathrm{ns}$ and FWHM duration of $5\ \mathrm{ns}$. The input pump energy is increased by rotating the halfwave plates of the attenuators and varied from $10\ \mathrm{mJ}$ to $1\ \mathrm{J}$. The results are presented Fig.4.2.

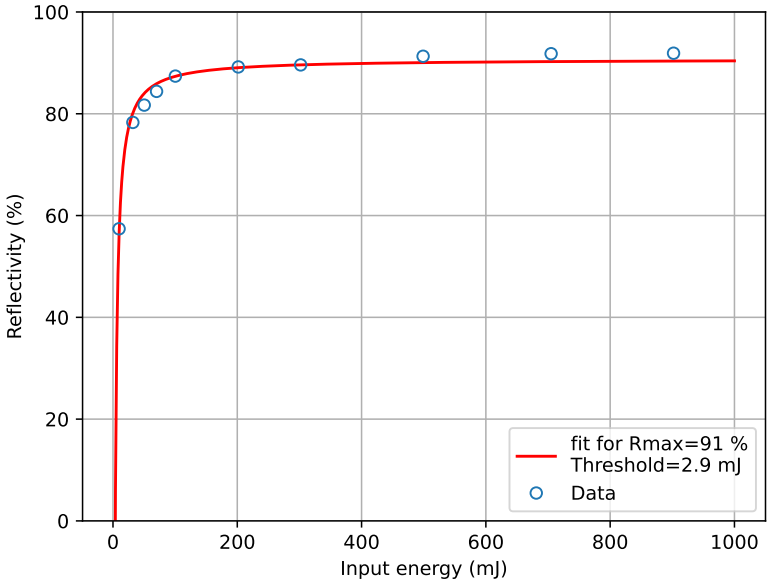

Figure 4.2: Reflectivity measurements and corresponding fit using Eq.1.56.

In this figure, the corresponding fit curve is obtained by fitting the data with the simple reflectivity model given by Eq.1.56. To account for the initiation time, the maximum reflectivity was introduced as a fit parameter. We remind the reader that this model doesn't take into account the focusing geometry, thus explaining the slight inaccuracies of the fitting curve. The energy threshold is estimated at $2.9\ \mathrm{mJ}$, and the maximum reflectivity obtained is > 92 %, close but slightly below state-of-the-art values. This can also be explained by our short pulse duration, as presented Sec.3.1.

When performing the reflectivity measurement at higher energies, the delay between the amplifiers gain and the seed pulse is optimized and the maximum energy can be brought to $5\ \mathrm{J}$. This further reduces the pulse duration down to $4.2\ \mathrm{ns}$. During the energy increase, this leads to observation of plasma formation at the focus point in the cell. This was the first observation of the manifestation of *Optical Breakdown* as defined including all parasitic effects that can affect SBS reflection. In the following section, we describe the effects observed as a consequence of breakdown.

4.3.1 . Optical Breakdown

The optical breakdown effect is mostly known in the literature as being caused by the impurities of the nonlinear medium [2]. In our observation, the liquid purity at the start of the experiments indicates that, although the particle presence can facilitate avalanche ionization, other physical effects can lead to breakdown. Among those, Stimulated Raman Scattering, self focusing or direct ionization of the molecules of the medium [3]. In our case, this breakdown lead to the following observable effects:

- The apparition of a spark inside the medium near the focus point.
- Bubbles' apparition in the liquid, rising to the top of the cell.
- A sudden drop of transmitted energy.
- A sudden drop of transmitted energy stability.
- A very slight drop of the Stokes energy stability.

It is remarkable that in our case, no drop of reflected energy can be observed, even with breakdown occurrence. However, as indicated, the apparition of bubbles means that the chemical composition of the cell changes due to erratic recombination of the ionized molecules inside the medium. This was further confirmed when, turning down the energy, sparks could still be observed down to few tens of millijoules, way below the first breakdown apparition level. The breakdown *changes the chemical composition of the cell and lowers further breakdown threshold*.

This proved to be a regular issue in our experiments, in particular when exploring the behaviour of SBS cell in unusual operation regimes. Once breakdown appears, The experiments are either continued with regular breakdown occurrence or an additional filtration cycle has to be performed. During those additional filtration cycles, macroscopic particles could be seen directly in suspension in the liquid or stopped by the filters, as shown in Fig.4.3.

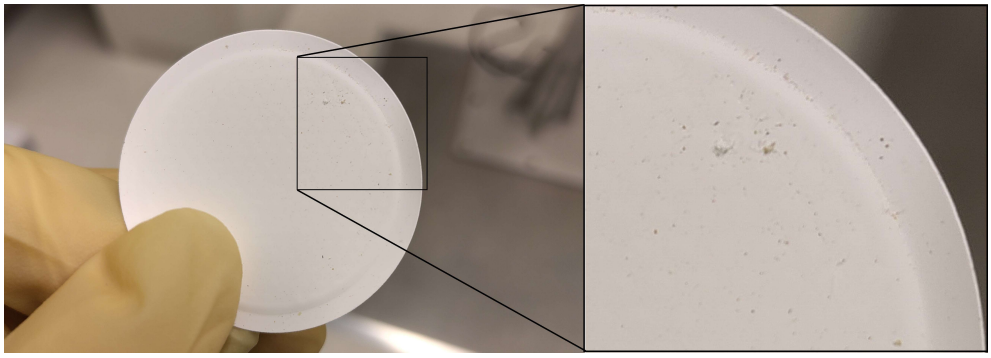

Figure 4.3: Filter of pore size $220\ \mathrm{nm}$, picture taken after filtration of a liquid presenting impurities from optical breakdown. Picture taken in LULI2000 clean room.

4.3.2 . High energy reflectivity

After an additional filtration step of the liquid, the analysis of the reflectivity of the cell was pursued. The breakdown occurrence is identified to be caused by the short pulse duration and the high energy density at focus point before the liquid initiation. To solve this issue, we use the temporal shaping capabilities of our SOA (Sec.3.4.2) to compensate for energy saturation inside the amplifiers, to increase the pulse duration and, especially, to lengthen the rise time.

The new rise time obtained was about $7\ \mathrm{ns}$ for a pulse duration of $5\ \mathrm{ns}$ at half maximum. The temporal profile of the pulse used is given Fig.4.4

Using this new pulse shape, the peak reflectivity and maximum energy sent inside the cell before breakdown drastically increased. The results are shown Fig.4.5.

The result reflectivity is greatly increased and reaches $95\ \%$ superior to state-of-the-art results for this pulse duration. This is due to the relatively long rise time compared to FWHM pulse duration. In our case, the transparency time corresponding to SBS effect initiation represent a negligible part of the energy and the reflectivity integrated along the full pulse energy is maximized. The reflectivity limit in this case is above 95% for input energy level above $3\ \mathrm{J}$.

Furthermore, the short term stability (over 1000 pulse) of this reflectivity is excellent and improves with energy (shown in Fig.4.6). The instability of the reflected wave is due to the fundamentally stochastic behaviour of SBS initiation, on thermal noise. This behaviour makes SBS initiate with slightly different coupling strength and delay and is therefore visible on the energy stability. The higher the input energy, the earlier SBS threshold is reached, and the less energy is transmitted. The less energetic part triggering SBS means that the total uncertainty introduced by the PCM decreases.

Overall, we demonstrate that an SBS cell can operate with outstanding

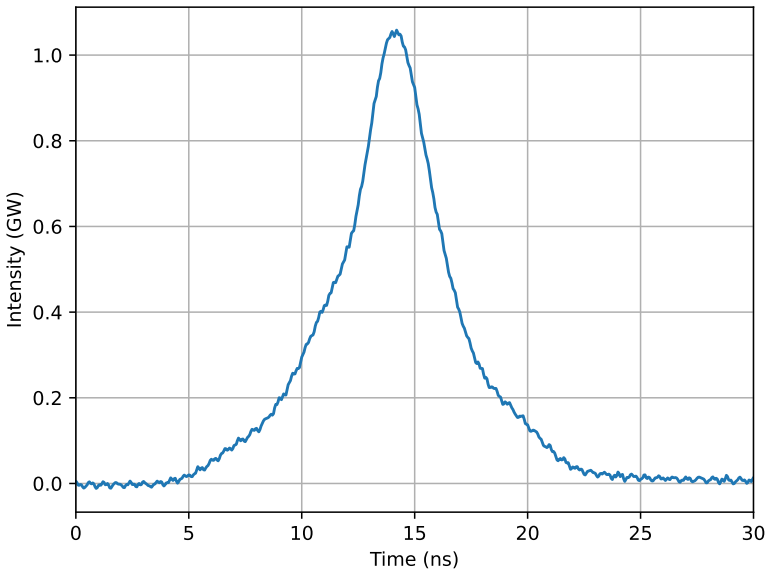

Figure 4.4: Input temporal profile used for the reflectivity measurements. Rise time: 7 ns, FWHM duration: 5 ns.

energy stability < 0.3 %RMS at high energy when the rising edge of the pump pulse is slow enough to guarantee initiation using a minimal amount of pump energy. In this case, Stokes energy stability can become comparable to pump energy stability.

In both Fig.4.5 and Fig.4.6, the point corresponding to an input energy of 5.7 J clearly presents aberrant behaviour. This point corresponds to optical damage on the polariser due to strong near-field modulations. In the following section, we study the causes of this degradation of the near field spatial profile.

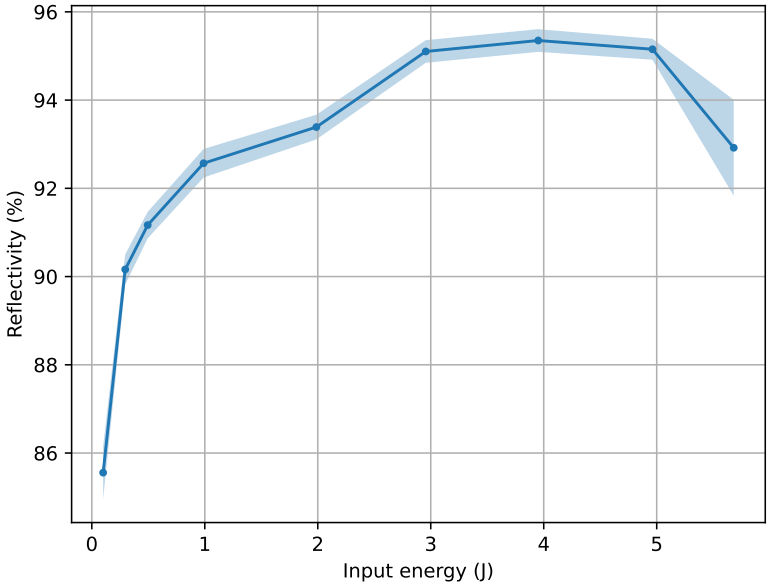

Figure 4.5: SBS cell reflectivity as a function of input energy. The light blue area around the curve represents the reflectivity standard deviation around the average measurement. Input temporal profile shown Fig.4.4. The drop in reflectivity for point at 5.7 J corresponds to optical damage on the polariser.

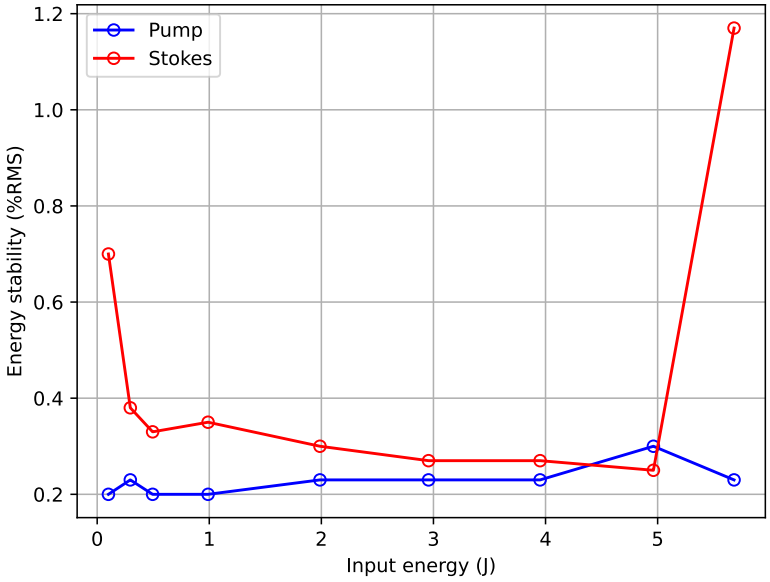

Figure 4.6: Energy stability for pump and Stokes pulses as a function of energy. The sudden increase in instability for the 5.7 J point corresponds to optical damage on the polariser. Short term stability measurements over 1000 pulses.

4.4 . Spatial fidelity

The drop in spatial fidelity in near and intermediate fields is probably one of the most concerning aspect of an SBS mirror as it can quickly lead to optical damages of the components of the laser system when placed in double pass configuration. Many mentions of this drop of spatial fidelity can be found in the literature [4–7] and the offered explanations imply that several effects can create those perturbations:

- A strong aberration level can decrease the fidelity when the aberrated far field intensity becomes comparable to SBS threshold [4]. This effect is characterised by a large drop in fidelity and reflectivity as well as an unstable behaviour of the PCM. In our case, the aberration level was low and the power at focus spot was enough to ionize the medium $\mathrm{I} \approx 10^{11}\ \mathrm{W/cm^2}$ hence confirming that the intensity is orders of magnitude greater than the SBS threshold $\approx 100\ \mathrm{MW/cm^2}$. In our experiments, no drop of reflectivity is observed and no particular instability of the reflectivity can be measured as shown in Fig.4.6. Hence, the degradation of the spatial fidelity is not associated with strong aberrations in our case.

- Thermal effects inside the cell can deteriorate fidelity [5, 6], yet this phenomenon has mostly been observed either for nonlinear medium with relatively high absorption values or for laser sources with high average power (few tens of watts for PCFs). This effect is characterised by a quasi-deterministic change of shape of the reflected Stokes beam (ellipticity, introduction of several lobes, ...). Although our laser source can start reaching the critical power level, no significant improvement of the spatial quality was observed when decreasing the energy (and therefore the average optical power inside the cell) and the spatial profile is still extremely unstable in this case.

- Fast initiation of SBS effect with power greatly above the SBS threshold can also generate drops in fidelity [7]. Large amounts of power are indeed capable of initiating several spatial modes (and not only the phase conjugated Stokes mode), including higher order modes that are usually discriminated against by gain selection. That effect has been considered in our case, but no improvement in spatial fidelity is ever observed when tweaking the temporal profile to reduce optical power density during SBS initiation.

To properly identify the cause of our issue, we perform analysis of the near field description of the beam. Because of the stochastic behaviour, this analysis is mostly statistical.

4.4.1 . Statistical description of near field

The drop of spatial fidelity mentioned previously is described in depth. First, we present the stochastic character of the beam.

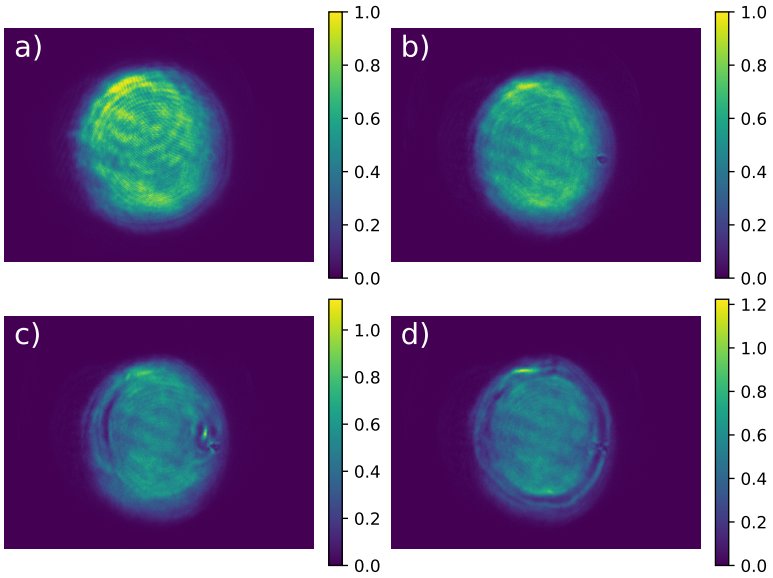

Figure 4.7: Examples of normalized near-field spatial profiles for the preliminary measurements. a) Pump beam (stable). b) Example of Stokes beam without degradation - good spatial fidelity. c) Example of Stokes beam with degradation (cold and hot spots). d) Example of Stokes beam with degradation (cold and hot spots). a) and b) are normalised independently whereas c) and d) are normalised compared to the high fidelity stokes beam presented in b). The hot spots presented in c) and d) therefore correspond to a fluence increase of about 20%.

In Fig.4.7 are displayed 4 near-field beam profiles. The typical pump beam is very stable whereas the Stokes beam is unstable. Fig.4.7.b to Fig.4.7.d are examples of Stokes beams acquired on camera. The spatial fidelity drop is characterised by local cold spots and hot spots in the reflected beam. Those spots can change shape, localisation and intensity.

In particular, the apparition of punctual hot spots in the beam as shown in Fig.4.7.c can damage optical components during the backward propagation.

Since the reflected spatial profile randomly changes for every shot, we performed a statistical analysis of the properties of the beam. In particular, the local average and local stability of the beam were analysed.

In Fig.4.8, those statistical properties are analysed. The pump beam is shown to be very stable with local amplitude stability below 10% except on the very edges (due to noise being dominant at this point). The Stokes beam is shown to be clean *on average* but the stability analysis shows a clear

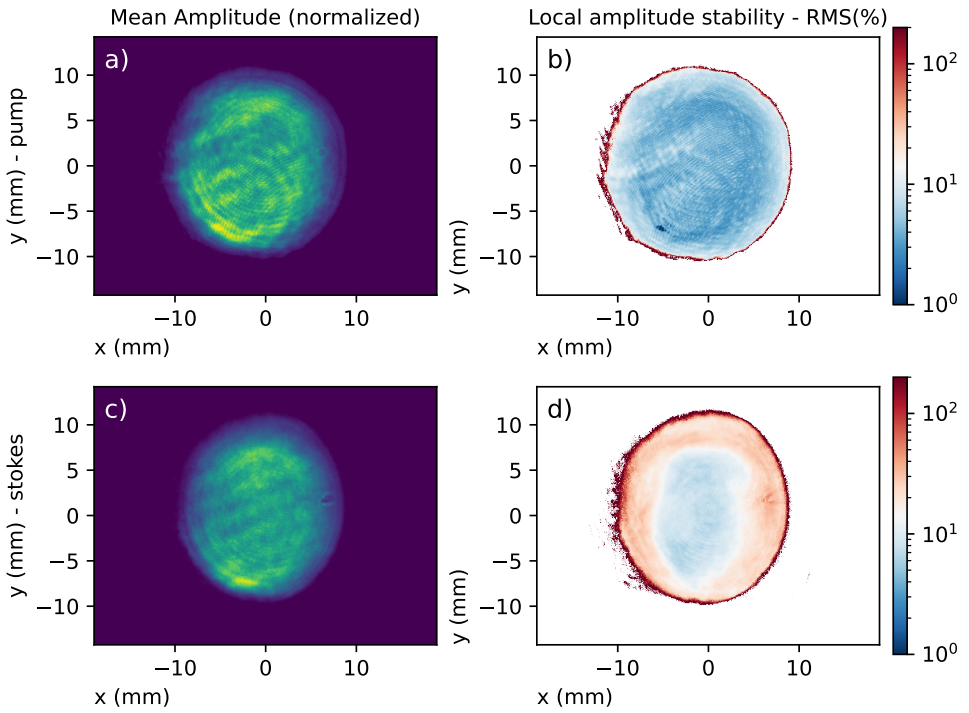

Figure 4.8: Comparison of the statistical properties of the near fields of pump and Stokes beams. a) Average pump beam. b) Pixel per pixel local pump amplitude stability (% RMS). c) Average Stokes beam. d) Pixel per pixel local Stokes amplitude stability (% RMS). Statistical analysis over 500-pulse samples.

degradation of the stability to values above 30% RMS on the edges of the beam. The localisation of those instabilities is of great interest: The SBS reflection introduces instabilities only at the edges of the beams. Therefore, we firstly tried to eliminate those instabilities by clipping the edges of the beam with an hard aperture of variable diameter. We present in Fig.4.9 the stability characterisation for a hard aperture of $10\ \mathrm{mm}$ diameter.

The clipped beam spatial profile stability is greatly increased. In particular, the number and intensity of hot spots is decreased. This study confirms that it is indeed the edges of the beam that generate those instabilities. The remainder of the study focuses on the characterisation of these hot spots since they represent the main concern for a laser chain, should the SBS mirror be placed inside a double pass amplification scheme.

In the following, we measure the hot spots by locating the maximum value on a pixel and comparing it with the average value of the pixels over the beam. This is the *Peak to mean ratio* for a particular beam. The results of this measurement for the initial configuration (same as Fig.4.8 and Fig.4.9) are given Fig.4.10.

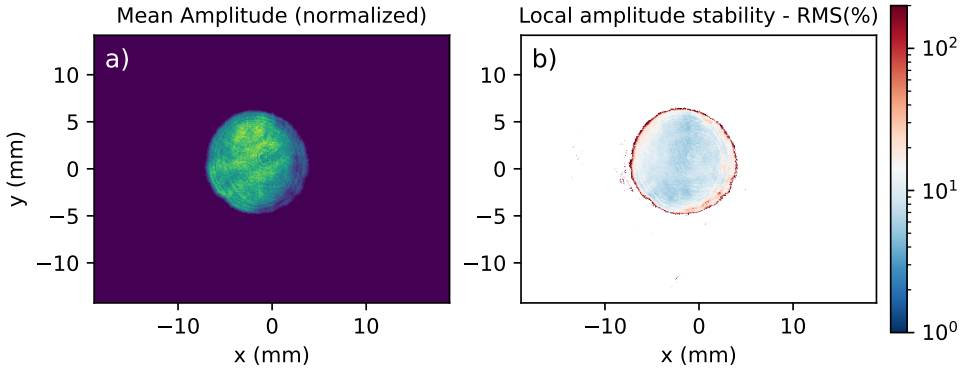

Figure 4.9: Mean amplitude and amplitude stability of the Stokes beam after SBS reflection. The initial $20\ \mathrm{mm}$ diameter beam is clipped using a hard aperture of diameter $10\ \mathrm{mm}$.

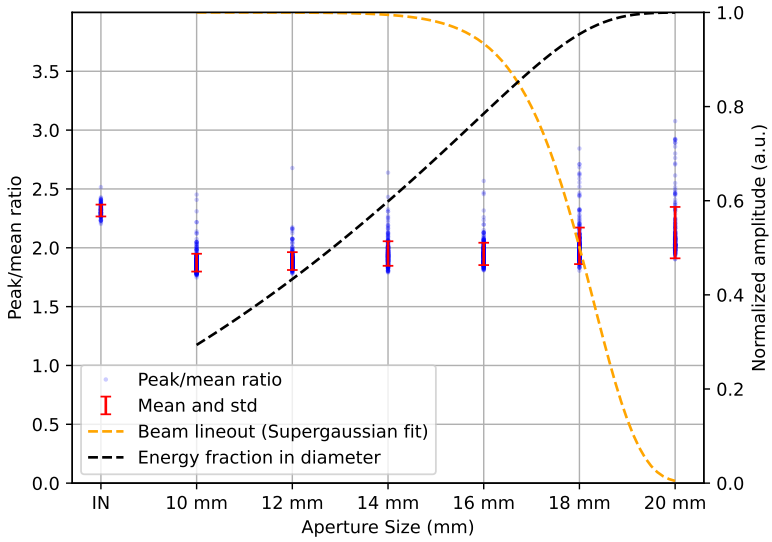

Figure 4.10: Characterisation of the Stokes beam local surintensity as a function of the diameter of the hard aperture placed before the cell. Every point of a dataset is plotted as a blue dot. The mean and standard deviation is represented in red for every dataset. A supergaussian fit of the beam is also presented in dashed yellow.

On this figure, several observations can be made

- As stated previously, the presence of the edges of the beam increases the probability of hot spot apparition.
- The larger the input beam, the more frequent and more intense the hot spots are.

- The edges of the beams greatly increase the probability of hot spot occurrence despite not representing a major energy contribution.

This representation is used in the following to characterise the improvements of the configurations studied.

4.4.2 . Spatiotemporal effects

Since the observed phenomenon has never, to the best of our knowledge, been identified in the state of the art, the spatial profile instabilities are clearly characteristic of an issue either on our laser source or our optical configuration of the SBS cell (propagation length, focusing, ...).

Several analyses are performed to find the root cause of this phenomenon. The pump beam wavefront is measured, the depolarisation component is found insignificant, the focusing length inside the cell is changed and no clear instability or particular contribution of the edges of the beam is found.

We then tried to analyse the temporal profile over the beam aperture. Because the initial temporal measurement is performed on the diffusion from the calorimeter, an average of the temporal profile over the beam aperture is effectively performed. A photodiode with small optical aperture (< 1 mm) is translated across the beam to measure the temporal profile of every radial component. This measurement is performed over the horizontal axis only and the results are shown Fig.4.11.

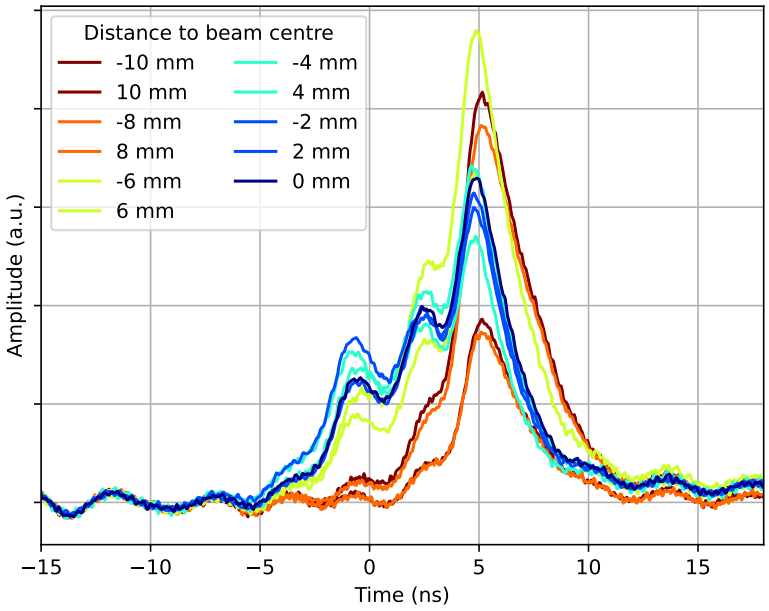

Figure 4.11: Comparison of the temporal profiles of the pump beam for several distances from the near-field centre.

Besides the strong noise perceived by the photodiode (oscillations of period ≈ 5 ns) we can directly see the existence of a dependence of the temporal profile on the radial position. In particular, the slow rise time to properly initiate SBS effect described Sec4.3.2 is not present on the edges of the beams.

Because the developed numerical simulations do not allow to properly simulate an arbitrary spatial profile (and even less a temporal profile changing as a function of a position in the beam), we cannot theoretically describe how this spatiotemporal effect takes place. Hence, we cannot confirm with just this measurement that the spatiotemporal is the cause of the modulations in the spatial profile. To confirm our new hypothesis, we reduce the temporal profile discrepancies in the beam and analyse its influence on the spatial quality of the reflected beam experimentally.

Spatiotemporal reduction To reduce the spatiotemporal effects in the pump beam profile, modifications to the laser chain are performed. Firstly, the root cause of the spatiotemporal effects is identified to be inhomogeneous temporal saturation along the beam [1]. As presented in Sec.3.4.2, the seed beam is initially gaussian and is amplified successively in a regenerative amplifier then cut using a serrated aperture then amplified again in single or double pass in high gain, flash pumped, Nd:YAG rods. The most likely origin of the spatiotemporal effects are the different regime of amplification along the beam:

- When an initially gaussian beam travels inside a gain medium, the small-signal gain (assumed initially constant along the radial axis) amplifies the beam homogeneously. Because the intensity is higher at the centre of the beam, the energy extraction is higher and the residual gain after the amplification is higher on the edges of the amplifiers.
- In a regenerative amplifier, this extraction discrepancy accumulates passes after passes and the complete saturation of the extraction of the energy is reached in a lower amount of passes for the center than on the edges. An example of the spatio-temporal distortion for a temporally square pulse is given in Fig.4.12
- Then, the beam is turned into a high order supergaussian due to gain saturation in the single pass amplifiers. This additional saturation step generates further discrepancies between the edges and the centre of the pump beam.

To reduce the amount of spatiotemporal effects, we first start by mitigating the spatiotemporal effects in the regen. To this aim, several solutions are available.

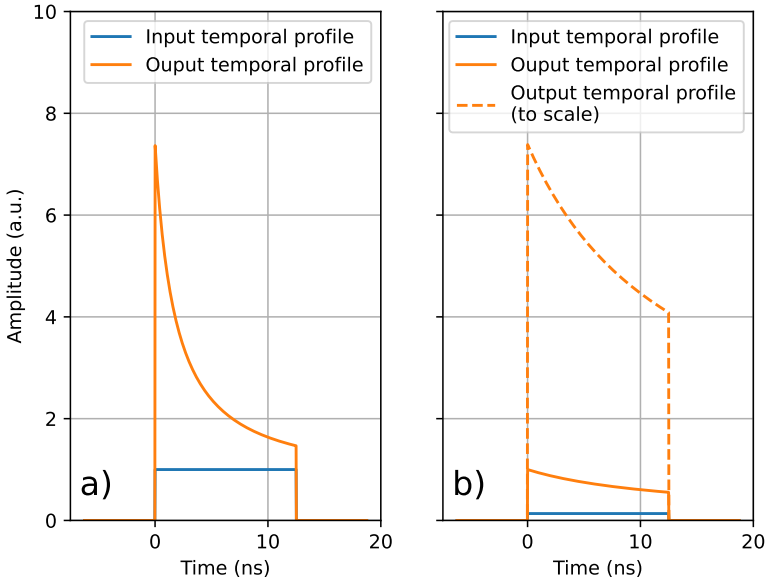

Figure 4.12: Spatio-temporal distortion caused by energy saturation inside a typical amplifier. a) For beam centre with input fluence $F_{In-centre} = 4F_{sat}$ b) For beam edge with input power $F_{In-outer} = F_{In-centre}/\exp 2 \approx 0.54F_{sat}$. Flat gain distribution in the amplifiers.

- It is possible to design a regen with top-hat propagation mode [8, 9]. Applying this solution in our case would have required a complete re-design of our regen module and was therefore rejected.
- It is possible to add a beam expander before the serrated aperture to not only *cut out the edges of the beam* but instead *keep only the centre*. This way, the only part that is allowed to be amplified is the quasi-homogeneously-saturated beam centre. This solution is easily implemented by simply changing the focal length of the magnifying telescope after the pockels pulse cleaner. This obviously comes at the cost of reduced energy since most of the pulse is cropped by the serrated. An illustration of that solution is presented in Fig.4.13

This second solution is directly put into place by simply changing the values of the convergent and divergent lens from our regen amplifier module. Under this new optical configuration, the energy at regen output drops significantly down to ≈ 1 mJ. The spatiotemporal measurements are then performed once again and compared with the original configuration. The spatiotemporal measurements figure and the *peak to mean* distribution figures are shown in Fig.4.14-Fig4.15.

Several observations can be made with this new configuration. On the spatiotemporal measurements (Fig.4.14), we can see a clear improvement on

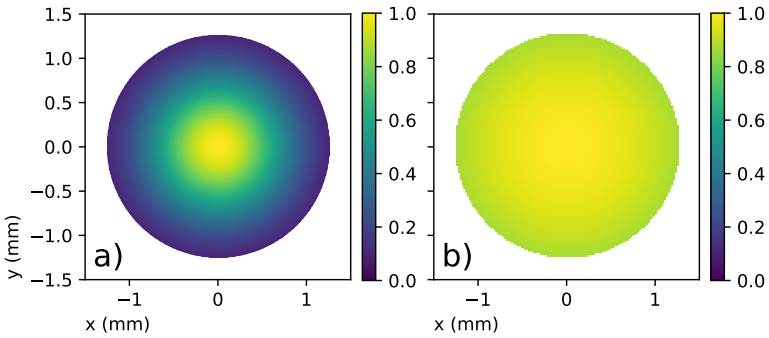

Figure 4.13: Example of the resultant spatial profile for a) The output beam of the regen clipped by an aperture of size $2.3\ \mathrm{mm}$ b) The output of the same regen and the same aperture but with a x4 beam magnifier before the aperture. Only the centre of the beam is kept with an almost flat-top beam at output. On this second configuration, the temporal saturation is almost homogeneous on the beam area.

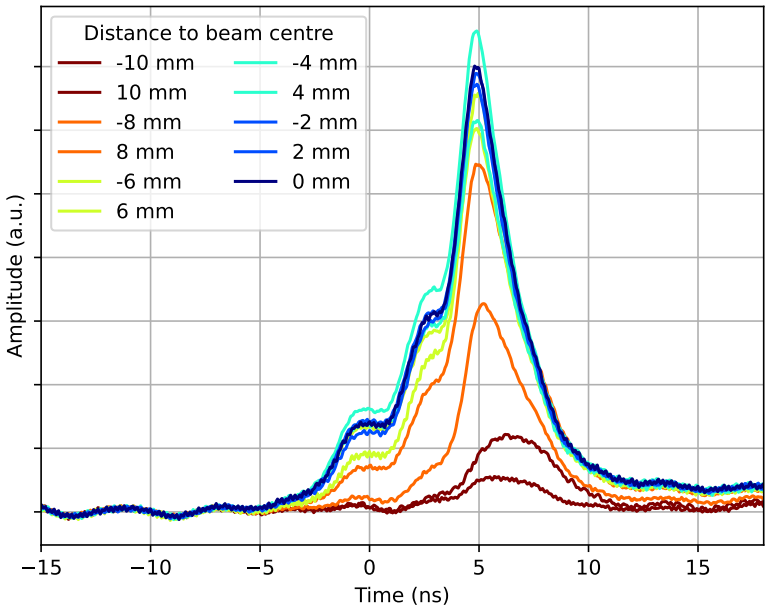

Figure 4.14: Comparison of the temporal profiles of the pump beam for several distances from the center. Configuration with the output beam from the regenerative amplifier is magnified before the serrated aperture to keep only the center.

the temporal profile homogeneity across the beam. The global shape is preserved on almost the full surface on the beam except the very edges for distance to centre $> 8\ \mathrm{mm}$ corresponding to aperture values of $> 16\ \mathrm{mm}$. This measurement presents a good correlation with the overshoot

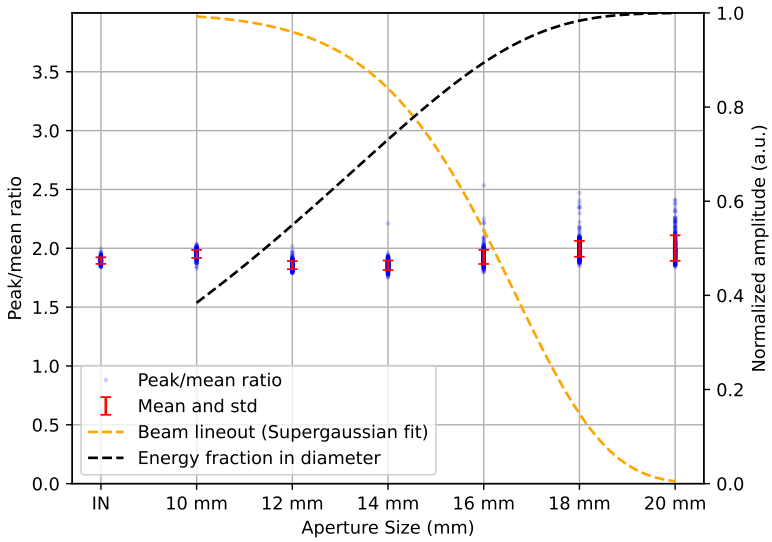

Figure 4.15: Characterisation of the Stokes beam local surintensity as a function of the diameter of the har aperture placed before the cell. Every point of a dataset is plotted as a blue dot. The mean and standard deviation are representd in ted for every dataset. A supergaussian fit of the beam is also presented in dashed yellow.

measurements of Fig.4.15 where the degradation of the beam quality is observed for beam diameters above $14\ \mathrm{mm}$. Even for aperture diameters above this threshold value, the instabilities observed are far weaker than the typical overshoots observed in the previous configuration (Fig.4.10). The reduction of the temporal profile inhomogeneities along the beam clearly influences the quality of the reflection.

The residual instabilities are observed for aperture diameters above $16\ \mathrm{mm}$ corresponding to the residual temporal profile inhomogeneities. Those are most likely caused by the amplification in the double and single pass amplifiers placed after the regen. Because we use a serrated aperture and a spatial filter to clip out the edges of the beam without introducing high order spatial frequencies, the edges of the beam present a smooth decrease of power down to zero at the amplifiers input (as seen in Fig.4.16). By the same phenomenon as described previously, this leads to a more pronounced saturation effect for the centre of the beam than on the edges and once again introduce temporal profile inhomogeneities on the beam.

The diameter on which those inhomogeneities are introduced corresponds to the relative depth of the serrated teeth compared to the serrated centre part. In our case, the internal diameter of the serrated is $2.6\ \mathrm{mm}$ and the outer diameter is $3.2\ \mathrm{mm}$. After beam magnification to an outer diameter of $20\ \mathrm{mm}$, this corresponds to an inner diameter of $16.2\ \mathrm{mm}$

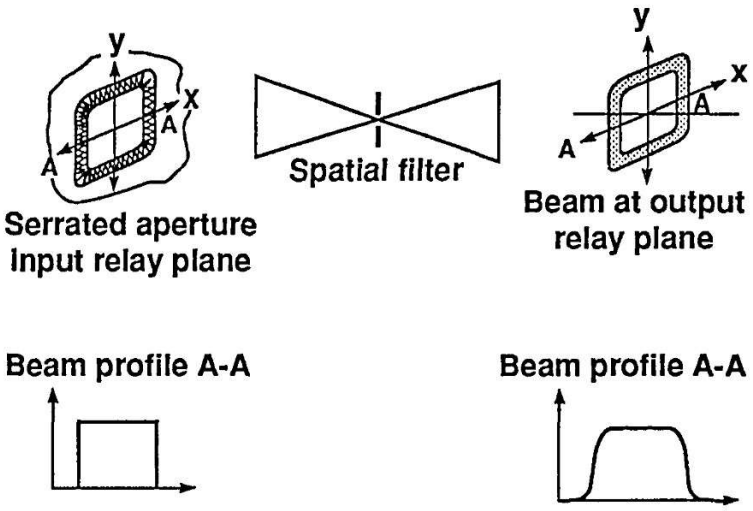

Figure 4.16: Effect of the introduction of a serrated aperture and a spatial filter for spatial beam shaping. Source: [10].

close to the experimental value observed for instabilities apparition. Further improvements in stability are then expected if the relative serrated aperture inner to outer diameter is increased. Yet to maintain a proper spatial filtering of the teeth only, the number of teeth of the serrated should also be increased accordingly. An experimental attempt was made to place two serrated apertures with opposite tooth pattern to reduce the teeth length and increase the teeth number by a factor of 2 which lead to marginal improvement, partly due to the precision required for proper alignment. In the following, the laser configuration used is the configuration with only a magnification of the beam before a single serrated aperture for stability measurements presented in Fig.4.15.

4.4.3 . Spatiotemporal effects suppression

To perform further characterisation of the SBS cell, complete suppression of all the residual instability was performed. To this aim, a hard aperture of diameter $10\ \mathrm{mm}$ is introduced to clip out the edges of the beam and keep only the very stable centre. Because the introduction of a hard aperture introduces high spatial frequencies and disturbs the spatial profile at cell entrance, the aperture is directly imaged at cell entrance by the mean of an afocal imaging system with twofold magnification. This allows one to conserve the input beam diameter of $20\ \mathrm{mm}$ and demonstrates that the input diameter has no influence on the stability of the reflection. The focal spot is placed inside a vacuum tube to avoid air ionization and the beam is then sent either on a fold mirror placed before the cell or directly on the SBS cell. The measurements comparing the pump and Stokes beam are this time

performed in parallel to study shot by shot the spatial and temporal fidelity and insure no missed shot occurrence. To this aim, a glass window AR coated on only one face is introduced in the beam path. It samples 4% of the input energy and 4% of the output energy and send those samples to two symmetric metrology benches, each composed of a photodiode and a near field camera.

The new optical configuration is presented in Fig.4.17

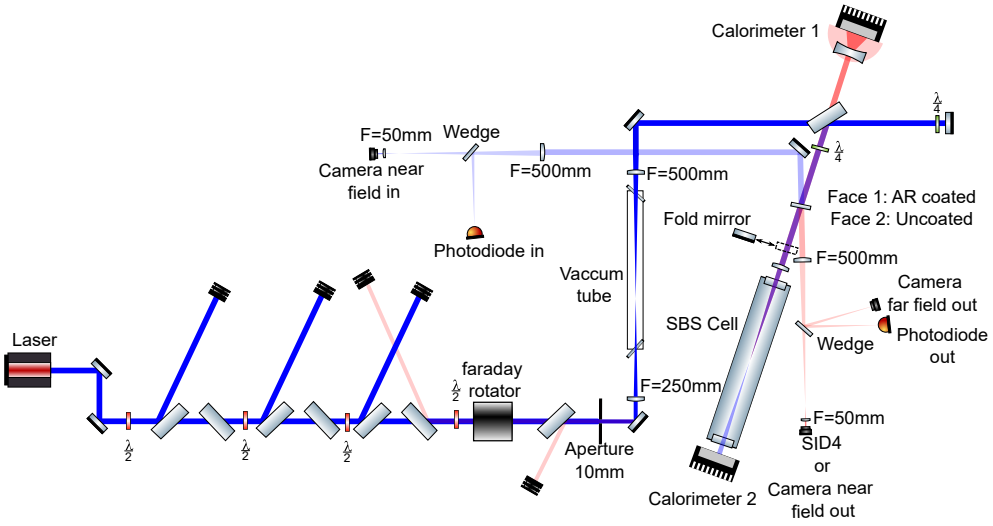

Figure 4.17: Optical layout of the characterisation bench of the medium energy SBS cell.

The introduction of the hard aperture clipped out a large part of the beam and reduced the overall energy accessible at cell input down to 1 J.

This setup allows not only to minimize the hot spot apparition and hence maximize spatial fidelity but also to compare shot by shot the input and output spatial and temporal profile. The introduction of the fold mirror allows to compare the wavefront and far field of either the pump or the Stokes beam. This setup was used to complete the parametric study of the SBS cell in all the next experiments.

4.4.4 . Conclusion

In this section, we have for the first time demonstrated the influence of inhomogeneous temporal profile on the quality of SBS phase conjugation. The present study shows that an inhomogeneous temporal profile can cause the apparition of stochastic hot and cold spots in the near field spatial profile during reflection. Those hot and cold spots have been shown to be able to cause optical damage on the backward propagation (see Fig.4.5) and thus represent a concerning issue for high energy phase conjugation.

Those spatiotemporal phenomena do not induce a reflectivity loss or any

particular drop in stability (excellent energy stability performances -down to 0.3% RMS - were reached before the removal of the spatiotemporal effects) or in the wavefront reversal correction and are only noticeable on the near field spatial profile of the reflected pulse.

This phenomenon, although concerning, is also largely caused by the configuration selected for the experiments. The laser source is a Nd:YAG laser chain with low saturation fluence ($\mathrm{F_{sat}} = 0.6\ \mathrm{J/cm^2}$) and is operated in highly saturated regime ($F_{laser} > 2F_{sat}$ for several amplifier passes). Furthermore, since the SBS reflection is performed at the output of the laser chain, the input laser on SBS cell undergo a significant amount of amplification (and therefore potential saturation) compared to the usual SBS cell placed in the middle of a double pass. We can therefore assume that the spatiotemporal issue is less concerning for typical laser architecture with SBS cells placed at the middle of a double pass as most of the spatiotemporal coupling due to saturation is performed during the last amplification stages.

Despite all of this, we show that the initial regenerative amplification stage can already be critical for SBS reflection. We demonstrate that the saturation in the first stage of amplification can generate temporal profile instabilities that are converted to spatial profile hot spots during the SBS reflection. This work demonstrates that when employing an SBS mirror, it is required to suppress residual temporal profile inhomogeneities across the beam by either adequate design of the regenerative cavity (flat mode regen) or by using a hard aperture at the regen output (and thus losing a large amount of energy). This last solution is employed in the following, leading to maximum input energy on cell of about $1\ \mathrm{J}$.

In the following, we use this new, single shot complete optical configuration to analyse the wavefront correction capabilities of the cell.

4.5 . Wavefront reversal

In a double pass scheme, the SBS cell can be used at the middle of the double pass to invert the wavefront, making all aberration sources self correct during the backward propagation. As seen previously, this aberration correction should present a limit (may it be only because the intensity at waist become too low to trigger SBS effect [4]).

In the following, we look into the wavefront correction capacities of the SBS cell. Several aberrations of interest are tested and parametric studies on the wavefront reversal are presented. Since, in the following, we will be talking about wavefront analysis and switching between the classical aberration description (Seidel and Zernike basis), we firstly succinctly present the formalism used in this section. In particular the Seidel and Zernike aberration basis are presented and the notion of analysis either in

Peak-to-Valley PV or Root-Mean-Square RMS are recalled.

4.5.1 . Wavefront analysis

A laser beam wavefront Σ is defined as the set of points in space of constant phase:

$$\Sigma_A = \{(x, y, z)/\phi(x, y, z) = A\} \tag{4.1}$$

In geometrical optics, punctual objects emit light rays in all direction. The corresponding wavefronts emitted by these objects are thus spheres centred around the emitting objects. If we consider a perfect imaging system, the image of a point is also a point. Hence, perfect imaging systems or optical components are capable of transforming a sphere wavefront in another sphere wavefront. It is then natural to characterise the *imperfections* of an imaging system (or simply an optical component) by the deviation it introduces *compared to the reference wavefront*: a sphere. This deviation Δ is, in the general case, a function of three variables: the field variable y (height of the object or angle of the beam compared to the optical axis), and the impact coordinates (h, φ) of the optical component aperture.

The Seidel decomposition develop this deviation as a sum of terms y^2, h^2 and $\cos(\varphi)$. The decomposition is:

$$\Delta(y, h, \varphi) = \sum_{(p,q,m)\in\mathbb{N}^3} a_{p,q,m} h^{2p+m} y^{2q+m} cos(m\varphi) \tag{4.2}$$

with $a_{p,q,m}$ the relative amplitude of each term. For a collimated laser beam, the dependence along y is very weak (same angle for the whole field) and usually placed inside the amplitude term. For clarity, the h variable is also often normalised as the ratio of the height on aperture divided by the full aperture: $u = h/h_{max}$.

Some of these terms corresponds to classical wavefront aberrations such as: the defocus term ($p = 1, m = 0$), the spherical aberration ($p = 2, m = 0$), the comas ($p = 1, m = 1$), the astigmatisms ($p = 0, m = 2$)...

Using this formalism, it is possible to describe the amplitude of the aberrations studied using one of the following two description:

- The *Peak-to-Valley* or PV describes the difference between the maximum and minimum of the deviation from the ideal wavefront. It is often used to describe a wavefront were only one aberration is dominant or to characterise the presence of strong localised wavefront deviation.

  $$PV_\Delta = \max(\Delta)_{u,\varphi} - \min(\delta)_{u,v\phi} \tag{4.3}$$

  Furthermore, when correcting the aberrations using a deformable mirror, the PV aberration value represent the difference in optical

path required for correction and therefore are directly linked to the strain on the actuators of the deformable mirror.

- The *Root-Mean-Square* or RMS describes the variance of the wavefront deviation over the aperture. It is mostly used to characterise the beam quality during focusing. A significant RMS wavefront aberration degrades the Strehl ratio of the beam.

$$RMS_\Delta = \sigma_\Delta^2 = \frac{1}{\pi}\int_0^1 \int_0^{2\pi} |\Delta(u,\varphi)|^2 u du d\varphi \tag{4.4}$$

Zernike basis Although the Seidel basis offers a natural analysis tool for the study of wavefront aberration, it cannot describe a wavefront as a unique sum of wavefront aberration. For instance, the introduction of spherical aberration ($\Delta = a_{AS}u^4$) also shifts the best focus position ($\Delta = a_{Defocus}u^2$). The Zernike basis is an alternative basis on which the aberration polynomials have been orthogonalized and normalised. It is then possible to describe a wavefront as a unique sum of amplitude c_{nm} over the basis polynomials Z_n^m.

$$\Delta(u,\varphi) = \sum_{(n,m)\in\mathbb{N}} c_{nm} Z_n^m(u,\varphi) \tag{4.5}$$

Furthermore, the polynomials of the basis have been normalised such that $c_{nm} = 1$ corresponds to an RMS value of the polynomial of 1. This means that the amplitude of an aberration on the Zernike basis is not the same as the value of the same aberration on the Seidel basis and that the amplitude RMS of the full wavefront can be simply calculated as the sum of all the amplitude aberrations:

$$\sigma_\Delta^2 = \sum_{(n,m)\neq(0,0)} c_{nm}^2 \tag{4.6}$$

The first few polynomials of the basis corresponding to the aberrations of interest are given Tab.4.1.

The polynomials formulas allow us to explicitly calculate the difference between the PV amplitude and RMS amplitude for the aberrations of interest. For example, a spherical aberration of amplitude c_{mn} on the Zernike basis corresponds to:

- An RMS aberration level of $s_\Delta = c_{mn}$
- A PV aberration level of $\frac{3\sqrt{5}}{2}c_{mn}$ on the Zernike basis (about 3.35 times the RMS value).

n	m	$Z_n^m(u, \varphi)$	Name
0	0	1	Piston
1	1	$2u\cos(\varphi)$	$0°$ Tilt
1	-1	$2u\sin(\varphi)$	$90°$ Tilt
2	0	$\sqrt{3}(2u^2 - 1)$	Focus
2	2	$\sqrt{6}u^2\cos(2\varphi)$	$0°$ Astigmatism
2	-2	$\sqrt{6}u^2\sin(2\varphi)$	$45°$ Astigmatism
3	1	$\sqrt{8}(3u^3 - 2u)\cos(\varphi)$	$0°$ Coma
3	-1	$\sqrt{8}(3u^3 - 2u)\sin(\varphi)$	$90°$ Coma
4	0	$\sqrt{5}(6u^4 - 6u^2 + 1)$	Spherical aberration

Table 4.1: Zernike polynomial basis. Aberrations of interest, up to third order.

- By isolating the u^4 component, the Seidel equivalent of this Zernike aberration has amplitude of $6\sqrt{5}c_{mn} \approx 13.4c_{mn}$. More than 13 times higher than the RMS value on Zernike basis. This conversion will be used frequently in the following.

The amplitudes of the aberrations are usually given in waves: the number of wavelength corresponding to the optical path difference.

The need for this conversion rises from the following: The Zernike basis is very useful for independent decomposition of the polynomials' basis. It also characterises the far field properties of a laser beam and thus permit the description of the beam usability on focused applications. If an SBS cell were to be used for plasma physics experiments with a tight focusing on target, the RMS description allows us to directly access to the size of the focused beam on target.

Conversely, the PV amplitude along Seidel basis is the usual "amount of aberration to be corrected" by a deformable mirror. During the comparison of the performances of the SBS mirror and typical deformable mirrors, the PV value will be used. For reference, a typical deformable mirror is able to correct a few waves (2-3 waves) of PV optical path difference (OPD) (for spherical aberration).

In the following, we introduce only one kind of optical aberration and perform the measurements of the wavefront reversal capacities of the cell. The aberration correction and its stability are measured using a wavefront sensor SID4 from the company *Phasics*.

4.5.2 . Spherical aberration

To characterise the SBS performances when aberration is introduced, we study the aberration inversion and aberration self correction of known, calibrated aberration. To the best of our capabilities, aberrations of interest are added independently.

The first aberration of interest is the spherical aberration, that generally represents the first limiting optical aberration in an optical system, especially in the case of side-pumping geometry. In particular, it cannot be easily corrected by simple optical arrangement (on the contrary to defocus or astigmatism for example) and, is also the hardest third order aberration to compensate for with a deformable mirror. This aberration depends on u^4 and is therefore extremely localised on the edges of the aperture. Hence putting on a large strain on deformable mirrors, limiting the maximum correctable aberration.

To introduce calibrated spherical aberration, spherical aberration plates were purchased (*Edmunds optics - 66-759*) introducing $1\ \lambda$ PV of Seidel spherical aberration for $\lambda = 587\ \mathrm{nm}$, over $21.1\ \mathrm{mm}$. Our beam having a $20\ \mathrm{mm}$ diameter, at $1064\ \mathrm{nm}$, the actual aberration level introduced is $0.4\ \lambda$ PV per plate. Since 5 plates are accessible, the maximum aberration level accessible in single pass is $2\ \lambda$ PV. The aberration plates are placed in front of the cell and the residual spherical aberration after the double pass is analysed.

The optical layout used for the spherical aberration measurements is shown Fig.4.18.

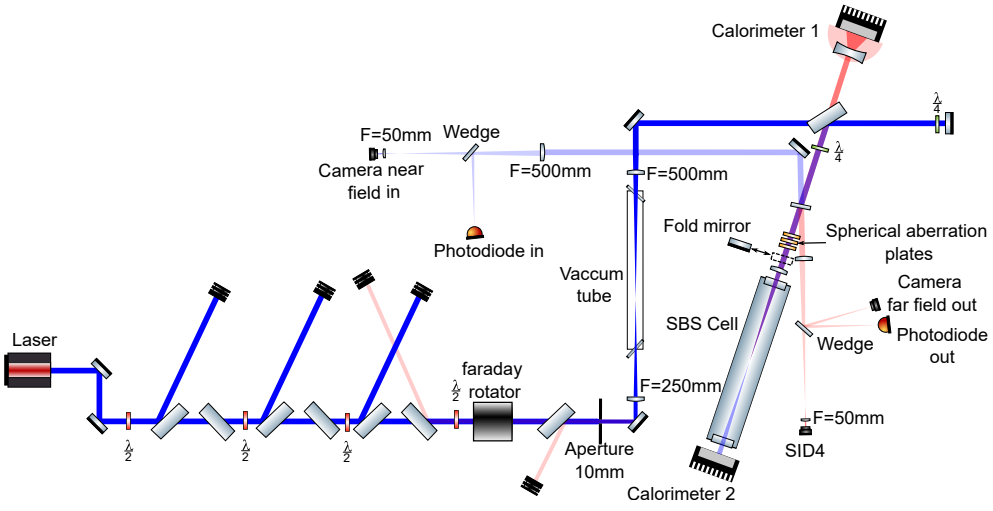

Figure 4.18: Optical layout used for the spherical aberration measurements.

Because the aberration plates are placed in the middle of the double pass, the cell should effectively correct all the spherical aberration and the residual spherical aberration measured on the SID4 should be close to 0, the

only residual aberration being the laser source aberrations, with sign reversal. Conversely, if the cell does not properly invert the wavefront, the residual spherical aberration level measured is expected to be twice the level at cell input. This input reference wavefront is measured using the fold mirror in place of the cell and no aberration plate and is shown Fig.4.19. Residual astigmatism can be observed due to the window of the vacuum tube (shown Fig.4.18) placed at Brewster angle inside the magnifying afocal optical system.

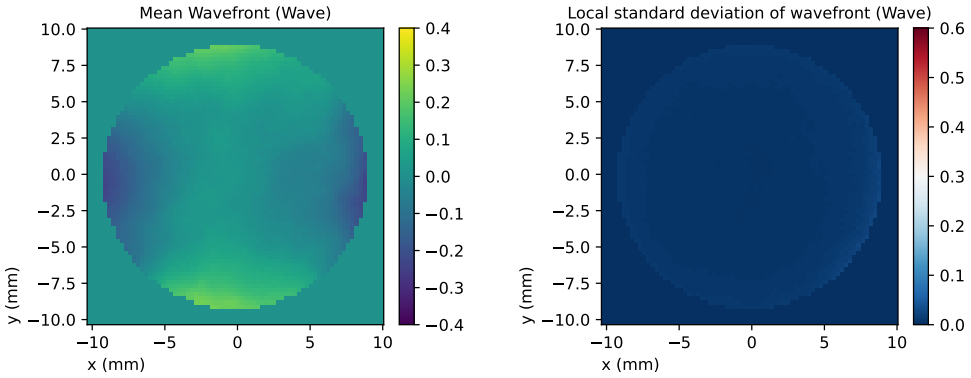

Figure 4.19: Wavefront measurements of the pump beam. Measurement performed with 0 aberration plates and the fold mirror in place of the cell.

To study not only the mean correction but also the stability of the wavefront correction, 200 Sid4 measurements were performed for every configuration (ranging from 0 to 5 aberration plates). The results of the measurements including the mean level of spherical aberration, the standard deviation and the extremal values are displayed Fig.4.20. On this figure, the initial spherical aberration has been used as a reference and subtracted for all the other datasets.

The residual spherical aberration is extremely low (< 0.05 waves PV), comparable to the SID4 resolution ($\approx 0.01\ \lambda$ RMS). The stability was also excellent with standard deviation below $0.1\ \lambda$ PV. Several of those datasets' stability are presented Fig.4.21-Fig.4.23

As observed on the previous figures, although the input spherical aberration does not impact the level of the output spherical aberration a slight wavefront reversal error can be seen in the Stokes beam. Furthermore, the stability of the Stokes wavefront is degraded compared to the stability of the pump. The degradation of the stability is particularly visible toward the centre of the beam.

This study was performed for several energy values ranging from $500\ \mathrm{mJ}$ to $1\ \mathrm{J}$ and no significant variation of the correction properties were observed.

Although a numerical simulation of this phenomenon is impossible with

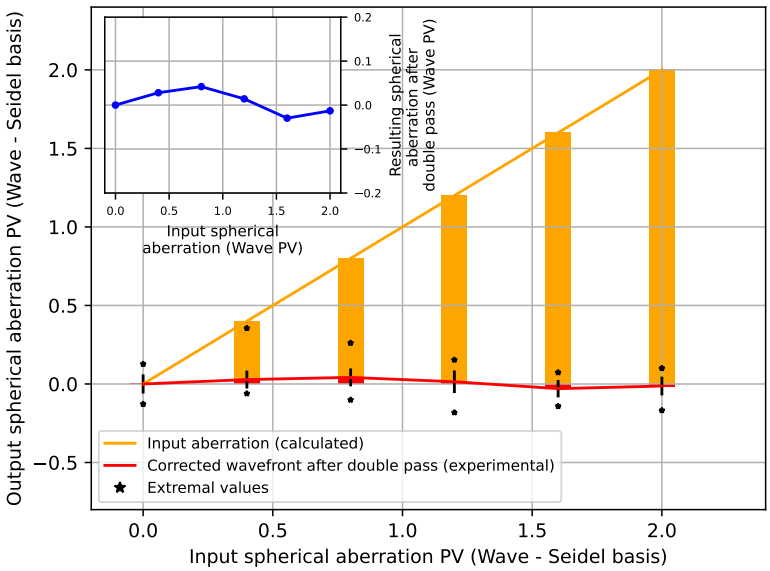

Figure 4.20: Output spherical aberration level as a function of input spherical aberration. The standard deviation is plotted as a line and the extremal values are plotted as a star. 200 wavefronts taken for every input aberration level. Spherical aberration value for input aberration of $0\ \lambda$ used as a reference. Inset: zoom on the mean residual aberration as a function of input aberration

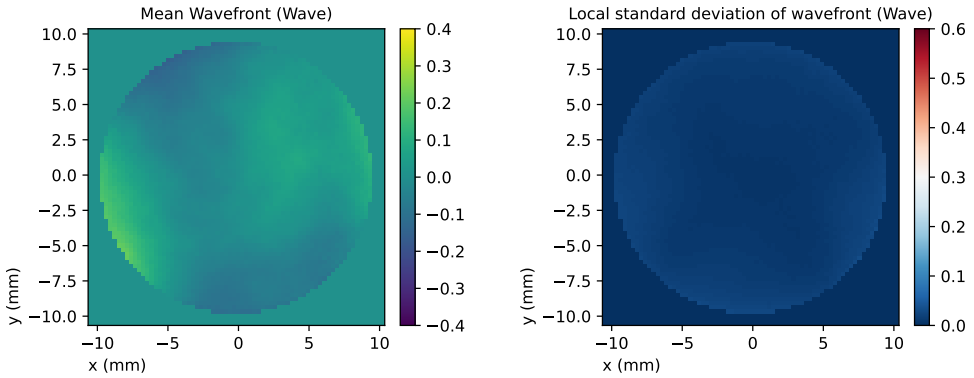

Figure 4.21: Wavefront measurements of the Stokes beam. Measurement performed without aberration plates in double pass.

the tools at hands (the *split-step model* is theoretically able to simulate the spatial profile but is currently limited to low focusing), the degradation of the stability can be attributed to the difference between the marginal and paraxial rays. The marginal rays focus closer to the cell entrance window due to the spherical aberration. This secondary focus point is able to generate an acoustic wave that disturbs the paraxial rays, focusing farther from cell entrance.

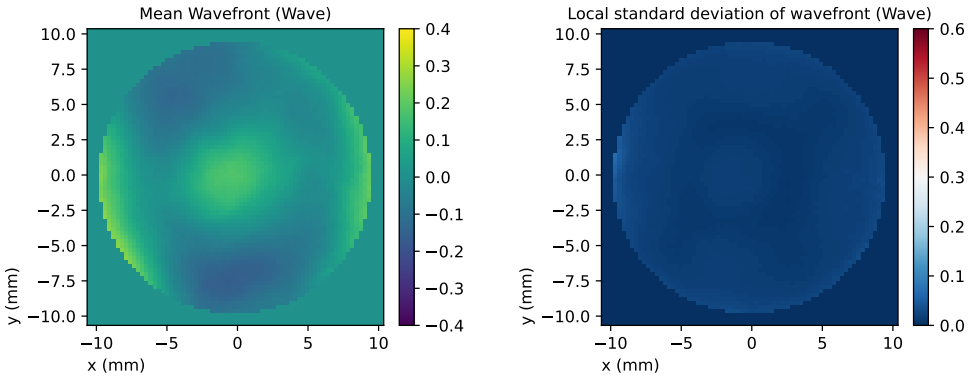

Figure 4.22: Wavefront measurements of the Stokes beam. Measurement performed with 3 aberration plates in double pass. ($\approx 1.2\ \lambda\mathrm{PV}$)

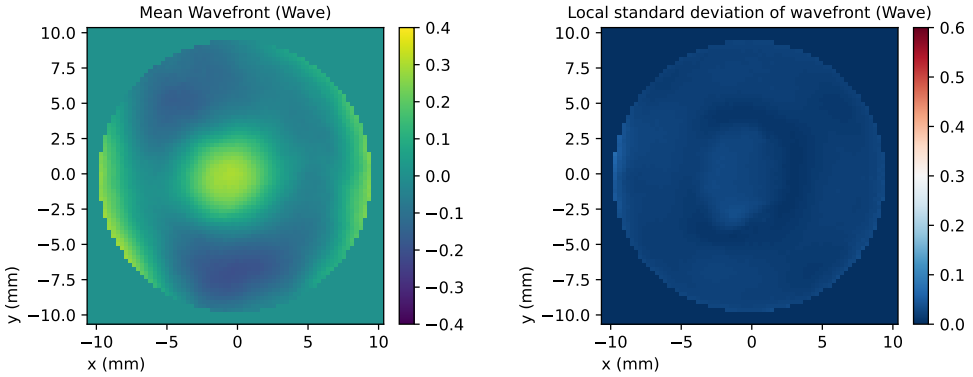

Figure 4.23: Wavefront measurements of the Stokes beam. Measurement performed with 5 aberration plates in double pass.($\approx 2\ \lambda\mathrm{PV}$)

Further studies are required to confirm or infirm this hypothesis. Yet, this result is the first demonstration of local wavefront instabilities introduced in the beam due to wavefront aberration.

4.5.3 . Astigmatism

The second aberration of interest studied in this chapter is the astigmatism. This aberration is generally the dominant aberration in laser chains, although it is usually relatively easily corrected.

Astigmatism characterises a curvature defect only present on one axis (contrary to defocus). It can appear when a laser beam passes through a tilted beam, or when mechanical constraint on an optical component deform it along one axis only. The corresponding Zernike polynomials according to Tab.4.1 are:

$$\sqrt{6}u^2\cos(2\varphi) \tag{4.7}$$

for $0°$ Astigmatism and

$$\sqrt{6}u^2 \sin(2\varphi) \tag{4.8}$$

for $45°$ Astigmatism.

Those formulas directly gives the conversion factor PV-RMS on Zernike basis: $1\ \lambda\mathrm{RMS} = 2\sqrt{6}\ \lambda\mathrm{PV}$. Contrarily to the spherical aberration, the introduction of a large PV astigmatism also corresponds to a high value of the RMS and can then lead to a degradation of the focus spot.

Astigmatism introduction To introduce astigmatism, we need to introduce a curvature defect on one axis only. This is simply done using a titled lens of focal distance f with rotation angle θ on one axis (here X) only. In this case, the beam rays on the X axis focus at a distance $f/\cos(\theta)$ of the lens and the beam along the Y axis focus at the usual distance f. This is illustrated by the schematics in Fig.4.24.

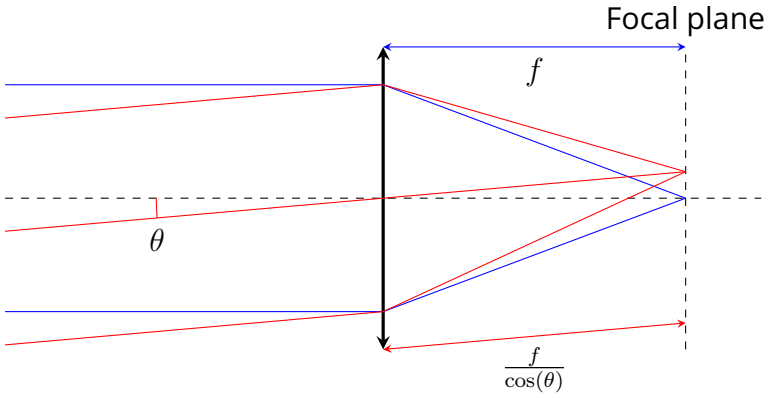

Figure 4.24: Representation of the difference in curvature between rays impacting the lens with normal incidence (blue) and rays impacting the lens with an angle θ (red).

In the general case, the introduction of a curvature of radius R introduce a OPD compared to the reference sphere of:

$$\Delta(r) = r^2/2R \tag{4.9}$$

Thus, with a tilted lens, the curvature difference between the vertical (normal) and horizontal (tilted) axis can be written as:

$$\Delta_X(r) - \Delta_Y(r) = \frac{r^2}{2f}\left(\frac{1}{\cos(\theta)} - 1\right) \tag{4.10}$$

And the PV of the astigmatism aberration Δ_{PV} is then:

$$\Delta_{PV} = |\Delta_X(r_{max}) - \Delta_Y(r_{max})| = \left| \frac{r_{max}^2}{2f} \left(\frac{1}{\cos(\theta)} - 1 \right) \right| \tag{4.11}$$

In our case, the easiest way to introduce astigmatism is then to tilt the focusing lens place just before the cell. We present the calculated PV values of aberration for different tilt angle in Tab.4.2

Focusing lens (220 mm) angle	Astigmatism value (PV-Zernike, in waves)
$0°$	0
$3°$	0.29
$5°$	0.81
$7°$	1.60
$10°$	3.30

Table 4.2: Astigmatism (PV-Zernike) induced as a function of the focusing lens tilt angle.

The introduction of astigmatism this way allows us to reach large amount of aberration, way above what is typically present in a laser chain ($> 3\ \lambda\mathrm{RMS}$ in single pass) and thus study the cell behaviour at this aberration level. As mentionned previously, the pump beam still presents some astigmatism caused by the tilted windows of the vacuum tube in the magnification afocal system (as seen in Fig.4.19). Thus, the measurements will be presenting an offset since the cell also reverses this contribution to astigmatism coming from the imaging system. The results of the cell wavefront inversion are given Fig.4.25.

Once again we see almost perfect correction of the induced aberrations in the middle of the double pass as the average value. However, we see that the uncertainty (standard deviation and extremal values) are greatly increased, especially for large level of aberration. This confirms the observation first made for the spherical aberration: The greater the aberration corrected, the less stable the wavefront correction is.

We present Fig.4.26-Fig.4.28 the average wavefront and wavefront stability for several datasets.

On the contrary to the spherical aberration presented before, the wavefront instabilities seem less localised. The typical shape of the wavefront instability seems to depend on the structure of the energy repartition near focus inside the cell and should vary widely depending on the aberration type observed. However, the mean wavefront remains almost constant no matter the amount of input aberration introduced.

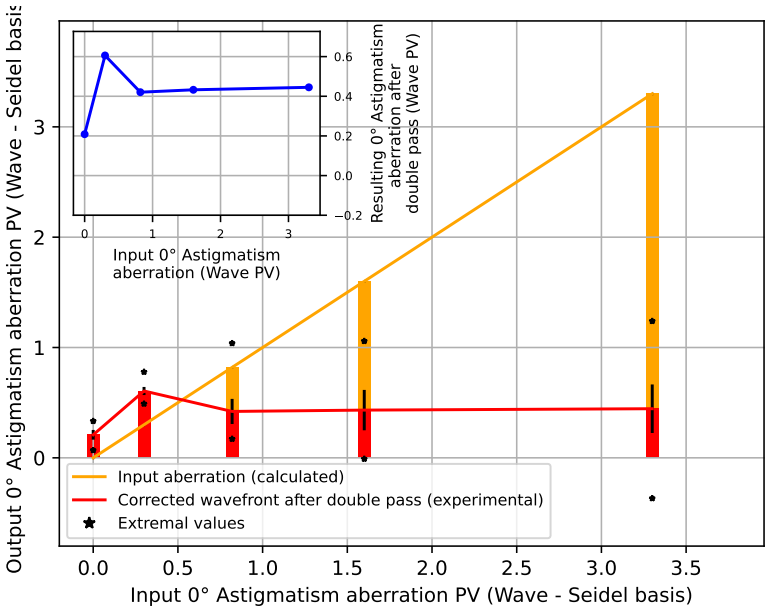

Figure 4.25: Output 0° astigmatism level as a function of induced astigmatism by the tilt of the lens. The standard deviation of the measurements is plotted as a line and the extremal values are plotted as stars. 200 wavefronts measurements are taken for every dataset.

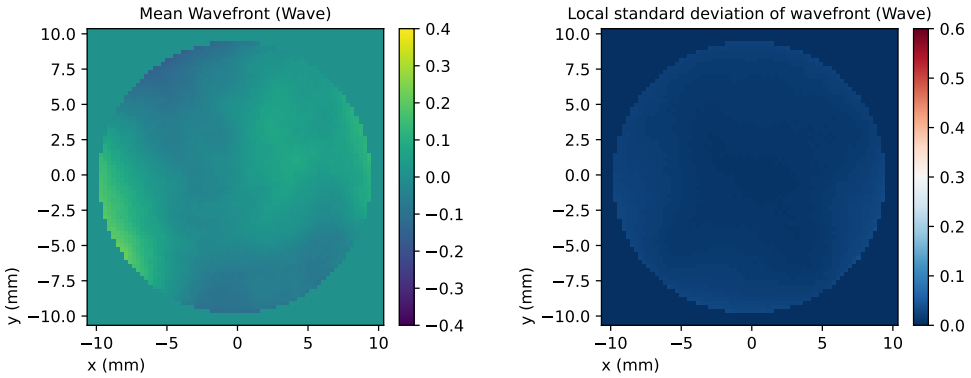

Figure 4.26: Wavefront measurements of the Stokes beam. Measurements performed with lens untilted.

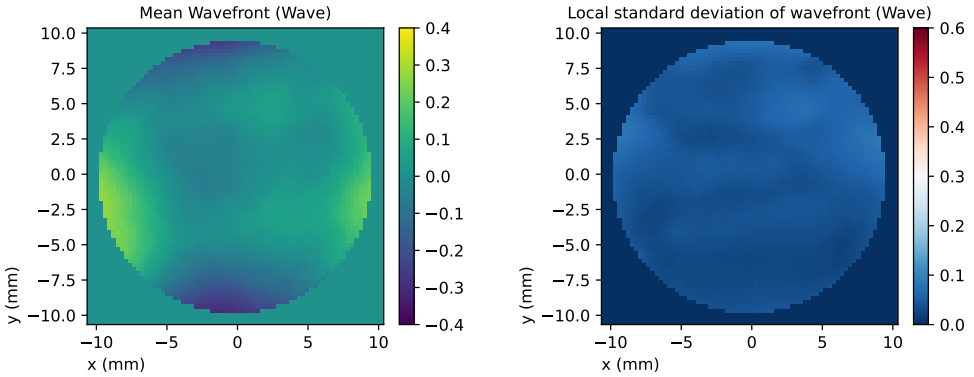

Figure 4.27: Wavefront measurements of the Stokes beam. Measurements performed with lens tilted at $5°$. Corresponding to $0.81\ \lambda\mathrm{PV}$.

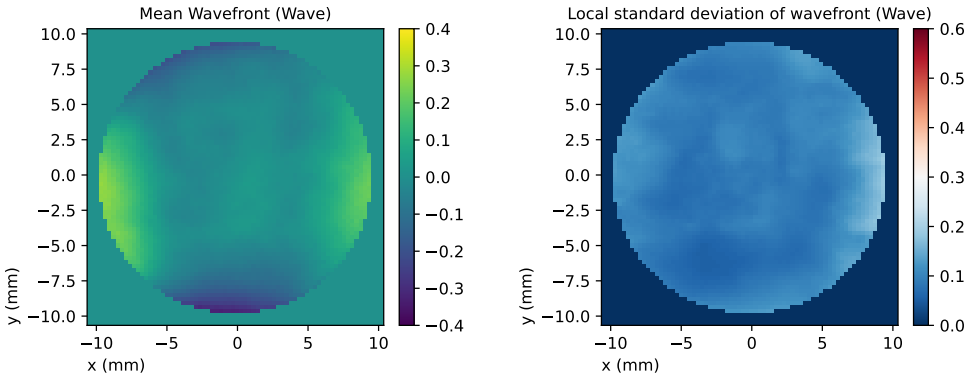

Figure 4.28: Wavefront measurements of the Stokes beam. Measurements performed with lens tilted at $10°$. Corresponding to $3.3\ \lambda\mathrm{PV}$.

4.5.4 . Aberration correction limits

Reflectivity When plotting the reflectivity curve for several different values of lens tilt (up to $45°$), we can observe an increase of the SBS threshold as well as the overall reflectivity. The corresponding curves are shown in Fig.4.29.

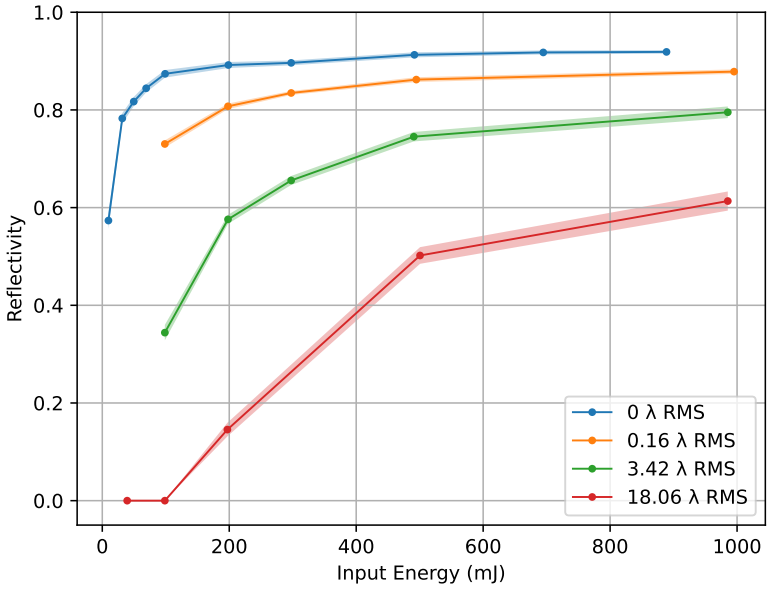

Figure 4.29: Reflectivity curves for several values of astigmatism aberration level.

As expected and theoretically predicted in Chap.2.5.3, the reflectivity drops when the aberration level increases and the maximum energy density inside the cell is subsequently reduced. The absolute quantification of the decrease of maximum energy density depends on the kind of aberration introduced and therefore, the reflectivity curves might be different reflectivity measurements with other kind of aberrations.

Spatial profile artefacts In the scope of this work, we were unable to reach an input aberration level that made the cell unable to properly invert the wavefront. However, as stated before, the stability of the reflected wavefront drops with the input aberration level. Furthermore, another parasitic effect was detected when increasing the astigmatism level above $10\ \lambda$, with tilt angles above $20°$. In this case, the reflected beam spatial profile was distorted and presented "fringe-like" patterns with contrast increasing with lens angle. The position and shape of those fringes were stochastic. An example of such a beam is shown in Fig.4.30.

When looking at the far field energy distribution, the apparition of those

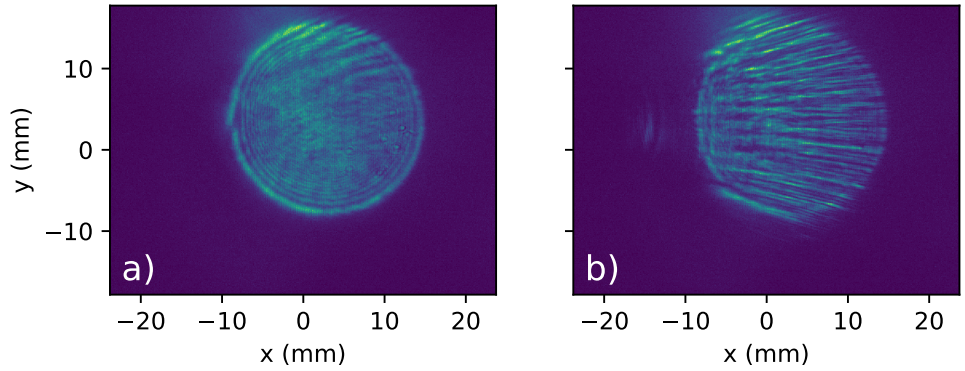

Figure 4.30: Near field spatial profile of the Stokes beam when correcting large amount of astigmatism. a) Focusing lens tilted at $20°$ corresponding to $3.5\ \lambda\mathrm{RMS}$ of Zernike astigmatism. b) Focusing lens tilted at $45°$ corresponding to $18\ \lambda\mathrm{RMS}$ of Zernike astigmatism.

modulations in the spatial profile corresponded to several spots along one axis (in our case, the y-axis). This behaviour is shown Fig.4.31

If we consider the far field energy distribution as the re-imaging of the energy distribution inside the cell near the focus point, what we see on Fig.4.31 can be assimilated to the source term of the Stokes field inside the cell (although disturbed by the lens aberration during the back-propagation inside the aberrant lens). The multiplicity of the source points may indicate that several acoustic waves are created in parallel inside the nonlinear medium then mix and interfere, hence creating those fringes pattern in the output near field. This parallel initiation is obviously possible only when the spatial extension in farfield inside the cell allows for interaction with different acoustic waves and is therefore more likely to happen for extended focus spots (and thus large amount of RMS wavefront aberration). Confirmation of this process through simulation is impossible using the *2D* or the *modal-decomposition* simulation model but might be accessible with a more elaborated *split-step* model.

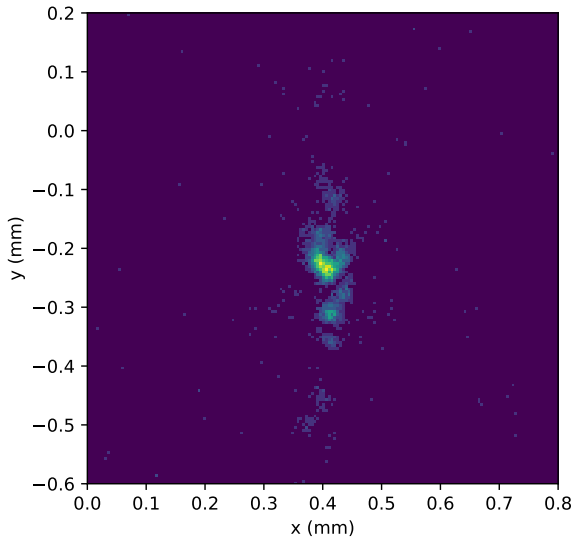

Figure 4.31: Far field distribution of energy of the Stokes beam when correcting large amount of astigmatism. Focusing lens tilted at $45°$ corresponding to $18\ \lambda\mathrm{RMS}$ of Zernike astigmatism. Several spots in the far field, each corresponding to a potential Stokes wave source term are visible.

4.5.5 . Conclusion

The study of the wavefront reversal capacities of the cell has been conducted and presented. The cell is found to be able to compensate for large amount of aberration in the double pass ($> 4\ \lambda\mathrm{PV}$ for the spherical aberration, $> 7\ \lambda\mathrm{PV}$ for astigmatism) at the cost of a slight degradation of the reflected wavefront stability.

When increasing the input aberration,the wavefront stability degrades, either locally (spherical aberration) or on the full wavefront (astigmatism). This degradation is found to depend on both the aberration kind and its corresponding amplitude. In the case of strong astigmatism aberration, the cell is found to generate detrimental artefacts in the spatial profile. Those artefacts are also assumed to depend on the kind of aberration observed, although the maximum amount of spherical aberration accessible did not allow to observe degradation on the near field spatial profile.

When the wavefront is disturbed enough to generate a significant increase of beam size at focus spot, the reflectivity is found to drop, as predicted by the numerical simulations. This degradation in reflectivity is not found to be detrimental up until aberration level exceeding several waves RMS.

4.6 . Temporal fidelity

We now study the influence of the SBS reflection on the temporal profile. The extensive theoretical and numerical studies of Chap.1-2 have confirmed that the displacement of the acoustic wave from focus point to entrance window, as well as the cell transparency before initiation is capable of changing the pump pulse temporal profile. To mitigate those effects, we designed our SBS cell (usage of a liquid for fast initiation) and our focusing condition (short propagation distance inside the cell).

Our aim in this section is the experimental confirmation that the conservation of a temporal profile through SBS reflection is possible. To this aim, we study the temporal profiles of the pump and Stokes pulse and compare them under several operating conditions. Because of the intended target applications, several temporal shapes of interest have been identified for these studies. They include gaussian and ramp temporal shapes as well as a two-step temporal shape, referred to in the following as *fusion-shape*. This last denomination is somewhat inaccurate as this might not be the exact shape used in fusion experiments, but it is in this chapter used as a demonstration that actual fusion temporal shape are accessible using the SBS-PCM.

4.6.1 . Requirements

Firstly we remind the reader of the requirements for the temporal shapes.

- The goal is to obtain arbitrary temporal profile at SBS cell output. To this aim, the *conservation of the pump pulse temporal pulse shape* has been targeted but is actually even more challenging. It would be acceptable if the output temporal shape were of the required shape after a deformation by SBS reflection. For this reason, the disappearance of the leading edge of the pump pulse due to SBS initiation does not present a problem for our application.

- The reflection on the SBS cell should not introduce detrimental effects such as jitter or rogue waves.

- The different parameters influencing the SBS mirror reflectivity should be identified and their relative influence characterised.

To this aim, we introduce an analysis tool that will be used in the following: the *reflectivity along time*. It is simply the ratio of Stokes pulse over pump pulse along time, given by:

$$R(t) = \frac{I_s(t+\tau)}{I_P(t)} \tag{4.12}$$

In this equation, note that the Stokes pulse is delayed by a time τ representing the propagation time of the pulse inside the cell (and include in experiments the delay of propagation to measurements line). Because the temporal shape of the Stokes pulse might differ compared to the pump pulse, this delay τ is not always easily found (i.e. In the compression case, the definition of τ becomes ambiguous). Hence, in the following, τ is found numerically by *maximizing the mathematical correlation between pump and Stokes pulse*. An example of reflectivity along time measurement is presented Fig.4.32.

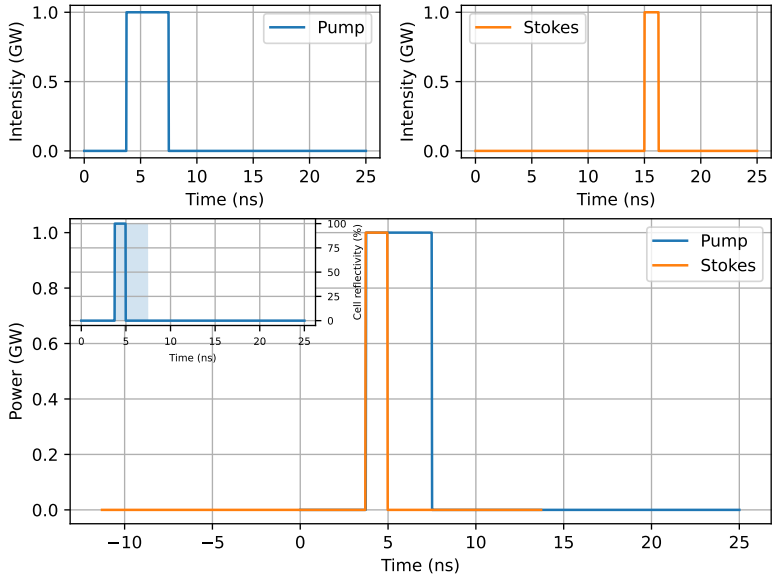

Figure 4.32: Reflectivity along time for an SBS interaction. Pump pulse:7 ns square pulse, Stokes pulse: 2 ns square pulse. The bottom graph represents the two pulses delayed to maximize their correlation. Inset is the reflectivity along time. On this inset, the reflectivity is plotted as a blue line and the shape of the pump pulse is displayed as a blue area.

On this kind of graph, a compression is represented as an overshoot with the reflectivity curve (in inset) goes above 100%.

In the case of real pulses, the detection will be performed with photodiodes and their corresponding measurement noise will be introduced. This noise can make the pump intensity reach values close to 0. In this case, the calculation of the reflectivity along time presents aberrant values and therefore has to be manually set to 0. In the following, we put this threshold for pump intensity below 5% of their maximum value. A comparison of the effect of noisy temporal profiles on this representation with and without these thresholds is presented in Fig.4.33-Fig.4.34

A perfect temporal profile conservation would mean a reflectivity along

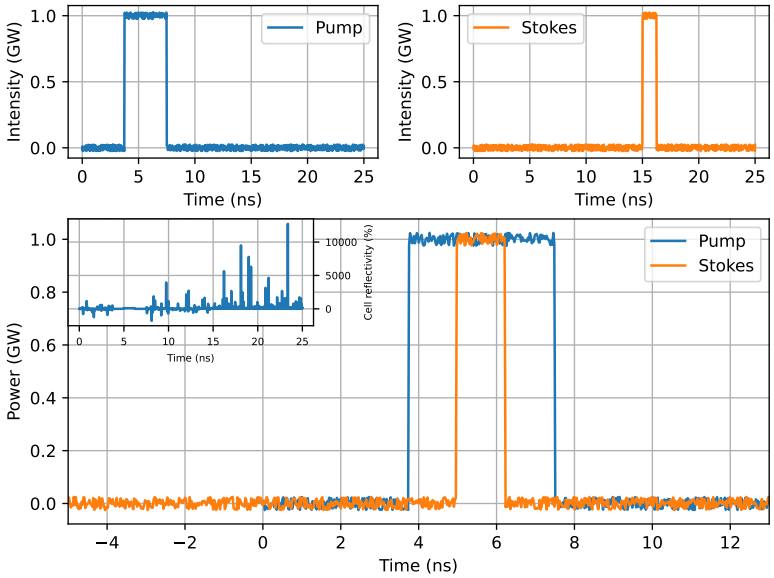

Figure 4.33: Inset of the bottom graph: Reflectivity along time for an SBS interaction with noisy temporal profiles (noise set at 5% of peak). Without threshold to set the reflectivity at 0 for low signal pump pulses. The included graph presents aberrant values and the meaningful part curve of interest (the reflectivity along time during the duration of the pump pulse) is invisible.

time constant over the whole duration of the pump pulse. Conversely, a compression scheme is characterised by an overshoot, with reflectivity over 100% followed by a sudden drop.

Firstly, a typical quasi-gaussian pulse shape was used with a mirror in place of the cell to calibrate the metrology measurement setup. The obtained temporal fidelity is given Fig.4.35.

Using a mirror, a good temporal fidelity is obviously reached. We can however notice some differences of photodiode signal before the main part of the pulse (dark current) and a different response to higher signal (characterised by a reflectivity drop at highest input power). This last point a characteristic of the photodiode, loosing linearity at higher input optical power, and is present despite the photodiode used being identical.

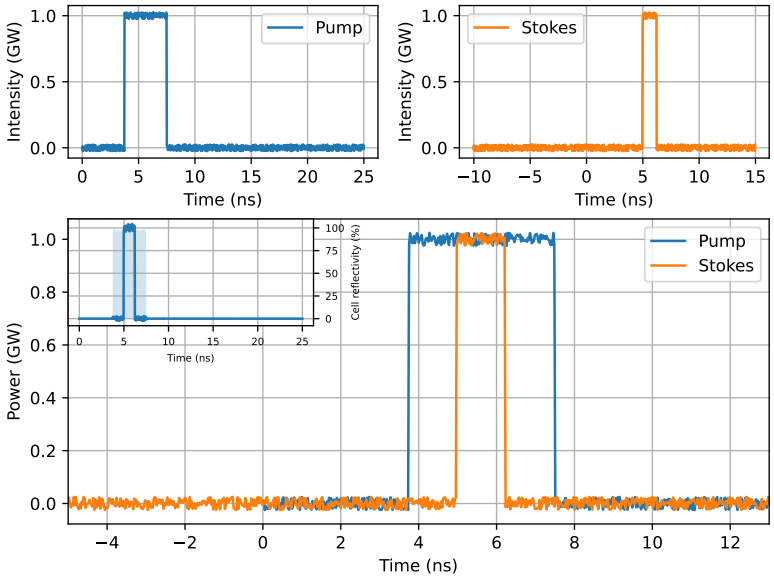

Figure 4.34: Inset of the bottom graph: Reflectivity along time for an SBS interaction and noisy temporal profiles. With threshold to set the reflectivity at 0 for low signal pump pulses (below 5%). On the contrary to Fig.4.33, the included graph this time represent the real reflectivity along time for the duration of the pump pulse, and 0 elsewhere.

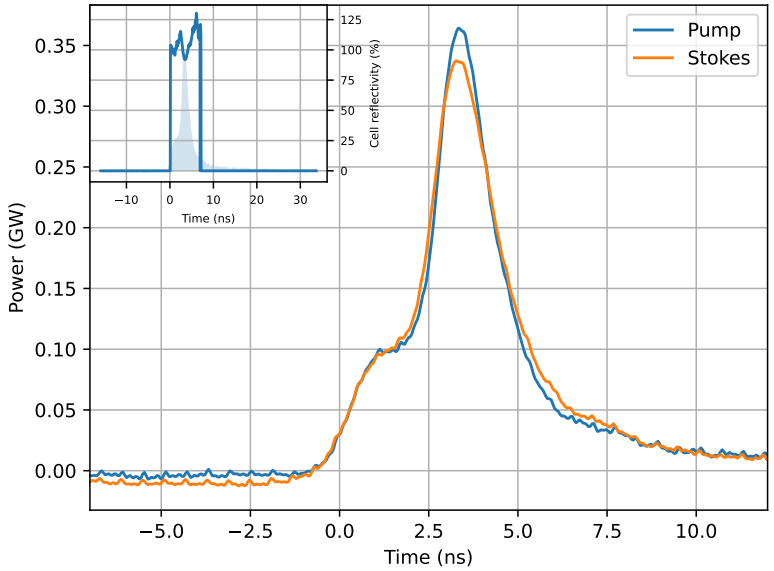

Figure 4.35: Experimental temporal fidelity measurement for a mirror.

4.6.2 . Interaction length dependence

The numerical simulation developed in Chap.2 showed a clear dependence of the temporal fidelity with the interaction length. A long interaction distance allows for long displacement of the acoustic wave maxima and hence of the reflecting zone. This displacement being able to compress the input temporal pulse into a shorter Stokes wave. In this section, we investigate this behaviour experimentally by choosing different focal length values for the focusing lens in the liquid, thereby changing the interaction distance. Although typical simulations results were already performed in Sec.2.3, we show in Fig.4.36 some additional simulations results, with simulation input corresponding to our experimental temporal shape and focusing condition.

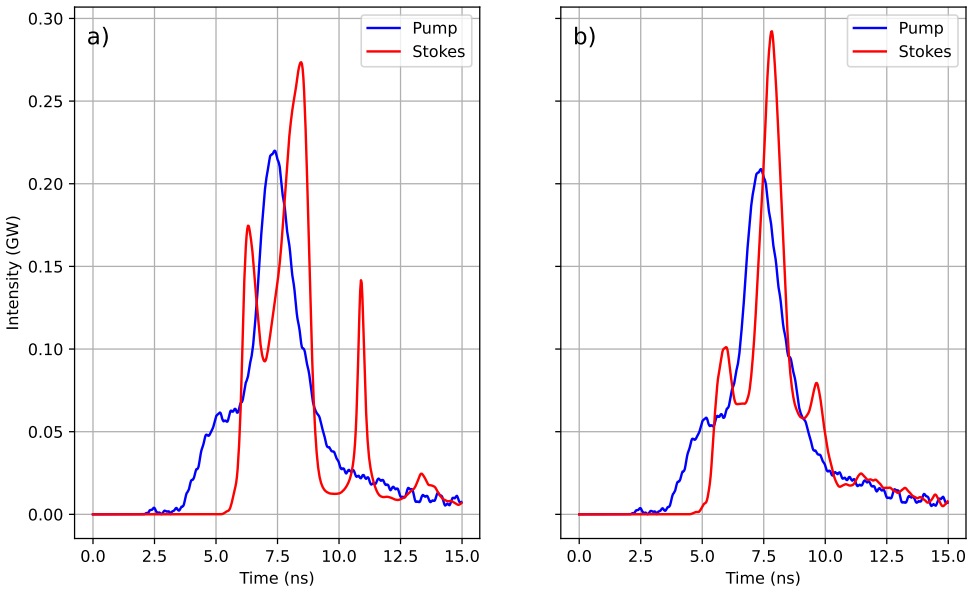

Figure 4.36: Simulation results for an SBS interation using as input parameters the experimental parameters. Nonlinear medium: HT70, input beam diameter: $20\ \mathrm{mm}$, input energy: $700\ \mathrm{mJ}$ focal length used: a) $220\ \mathrm{mm}$ b) $180\ \mathrm{mm}$. Simulation results obtained using the 2D model.

As expected after the initial studies of the simulations, in the case of the use of a liquid with response time of the order of the nanosecond (Sec.2.3.5, Fig.2.16), the compression start to appear for focal length of the order of $200\ \mathrm{mm}$. The simulations for our experimental case allows us to refine this study and shows that using a $180\ \mathrm{mm}$ focusing lens instead of a $220\ \mathrm{mm}$ provides a clear improvement of the Stokes temporal profile conservation. Those simulations were then compared with experimental results.

Firstly, a focusing length with focal length $220\ \mathrm{mm}$, corresponding to an interaction distance inside the cell of $280\ \mathrm{mm}$ was used. The comparison between input and output temporal profiles is shown in Fig.4.37

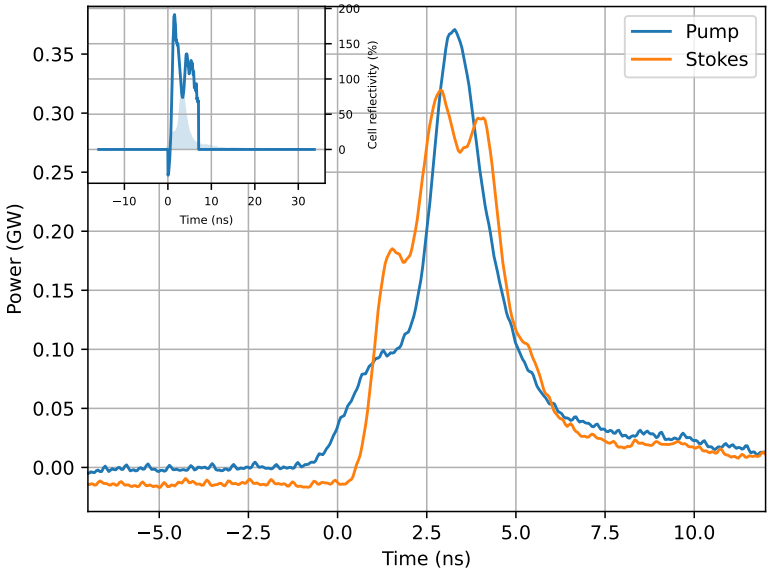

Figure 4.37: Experimental temporal fidelity. Interaction in HT70 with an input energy of $700\ \mathrm{mJ}$, with input diameter of $20\ \mathrm{mm}$ and a focusing lens of $220\ \mathrm{mm}$ focal, corresponding to an interaction distance of $280\ \mathrm{mm}$.

This experimental curve shows similar behaviour with the predicted shape in Fig.4.36.a. In particular, the modulations in the Stokes temporal profile corresponding to relaxation oscillation are present. Perfect accuracy with the simulated temporal profile has yet to be reached, and is assumed to be caused by the lack of proper spatial profile simulations.

To characterise the improvement numerically predicted in Fig.4.36, the same experiment was performed using a $180\ \mathrm{mm}$ focusing lens, all the other parameters remaining unchanged. The corresponding temporal fidelity curve is shown in Fig.4.38

The usage of this shorter focusing lens allows a much better conservation of the pump temporal profile. Although the leading edge is slightly compressed, and a residual short amplitude compression spike is still visible, the relaxation oscillation numerically predicted and seen in the reflected temporal profile in Fig.4.37 with the $220\ \mathrm{mm}$ focal lens are suppressed. Only a small overshoot is present in the reflected temporal profile.

Those results confirm several points of interest of the thesis so far:

- It is possible to accurately predict the behaviour of the SBS interaction using the numerical simulations developed in Chap.2, albeit limited by the spatial profile description.

- It is possible to choose the focusing lens to be used in the experiments

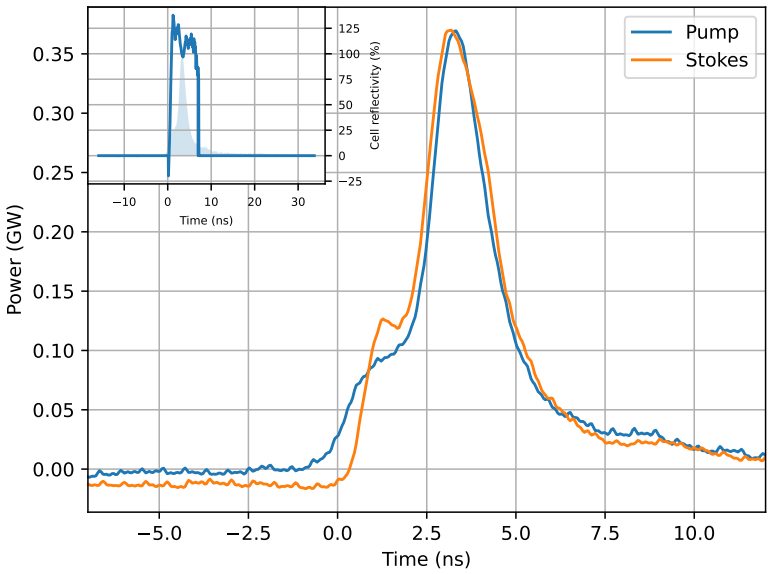

Figure 4.38: Experimental temporal fidelity. Interaction in HT70 with an input energy of $700\ \mathrm{mJ}$, with input diameter of $20\ \mathrm{mm}$ and a focusing lens of $180\ \mathrm{mm}$ focal, corresponding to an interaction distance of $230\ \mathrm{mm}$.

and therefore design a cell for a particular application.

- It is possible to experimentally reach a proper temporal fidelity for at least some shapes of interest.

Despite those points, the results are limited by the quality of our laser source, with significant spatiotemporal coupling limiting the rise in energy. Furthermore, the beam used in those experiments has an extremely clean wavefront. An actual pump beam for a cell operating in a proper laser system will be harder to properly simulate due to the spatial profile and wavefront description not accurately represented here.

In the following, we study the jitter introduced by the SBS reflection in the laser system for the gaussian temporal profile.

4.6.3 . Jitter

The jitter of a high energy laser chain is an important parameter for a large range of applications, in particular for synchronisation of the output pulse with secondary sources such as in the case of pump-probe experiments or OPCPA pumping. Because the SBS interaction is capable of modifying the input temporal profile, it is natural to assume it is also capable of adding a random delay to the reflected Stokes pulse compared to the pump pulse, hereby inducing jitter.

If the SBS mirror were to be put in a laser system with strict jitter

requirements, this jitter introduced by the SBS cell can become the limiting factor of the full laser system. Typically, the jitter of a high energy laser following the MOPA architecture is limited by its seeder. Standard TTL based clock technology present jitter values between the trigger signal and the output laser pulse of $1\ \mathrm{ns}$ without locking the clocks of the seeder and down to $60\ \mathrm{ps}$ with clock locking. More complex systems used in high energy lasers manage jitter values of about $20\ \mathrm{ps}$. If the jitter between the pump and Stokes pulse is above those values, the cell becomes the dominant source of jitter in the laser system.

Because of the initiation of the Stokes wave by thermal noise, the start of the SBS interaction intrinsically present a random behaviour. The rising edge of the Stokes pulse can shift randomly, introducing jitter. Once the acoustic wave has grown and stabilized near the cell entrance, the jitter of the cell should intuitively be largely reduced or even disappear. Yet this behaviour might change depending on the input pulse temporal shape and has to be confirmed experimentally.

Methodology of Jitter measurement The measurement of the jitter can also be technical. To measure the intrinsic jitter of the cell, we measure the *delay* between the input and output pulse inside the cell. Then, the statistics of this delay gives the jitter. Because the temporal shape between pump and Stokes pulses are changed by the reflection, the *delay* is calculated for a specific *power threshold*. The delay τ for a power threshold of 10% is noted $\tau_{0.1}$ the jitter is then the standard deviation $\sigma_{0.1}$ of this delay. Note that this definition requires independent normalization of pump and Stokes pulse and therefore looses its physical meaning for widely different pulses shape.

Assuming identical pulse shapes with random delay, the main limitation during the experimental measurements becomes the electronic noise of the measurements. The photodiode and oscilloscope present large amount of noise (about 7%, no matter the oscilloscope range used - minimized by taking a moving average over $500\ \mathrm{ps}$ of every pulse). This significant amplitude noise is converted into delay noise with a factor proportional to the *first order derivative* of the temporal profile: for an arbitrary temporal shape, the jitter measured for a particular threshold level depends on the slope of the temporal profile when crossing this level.

To minimize the electronic noise, degrading the jitter measurements, a moving average over $500\ \mathrm{ps}$ is performed for every curve before the threshold detection. Although this value might seem high for the detection of delay variations about an order of magnitude below those $500\ \mathrm{ps}$, we remind the reader that a moving average does not impact the jitter for noise-free monotonously increasing slopes. In our case, as shown in

Fig.4.38, the curve is mostly monotonous, except for the residual compression spike visible on the Stokes curve at about $1\,\mathrm{ns}$ delay, corresponding to a threshold about 30%. The validity of this calculation is further confirmed by the capacity to observe jitter increase for the fast structures of both the pump and Stokes waves as seen in Fig.4.39.

In all cases, in the following, all the jitter measurements are performed for the SBS cell and for a mirror in place of the cell under the exact same configuration. The obtained results are then compared in the figures in the following. Because a mirror introduce a very low amount of jitter, it is used as a reference. The inherent jitter of the cell would thus be observed for a jitter curve of the cell significantly higher than the mirror curve.

Jitter measurements The jitter measurements were performed for the same temporal shape as previously shown in Sec.4.6.2, with the $180\,\mathrm{mm}$ focal length to keep good temporal fidelity as presented in Fig.4.38. The jitter measurements are given in Fig.4.39.

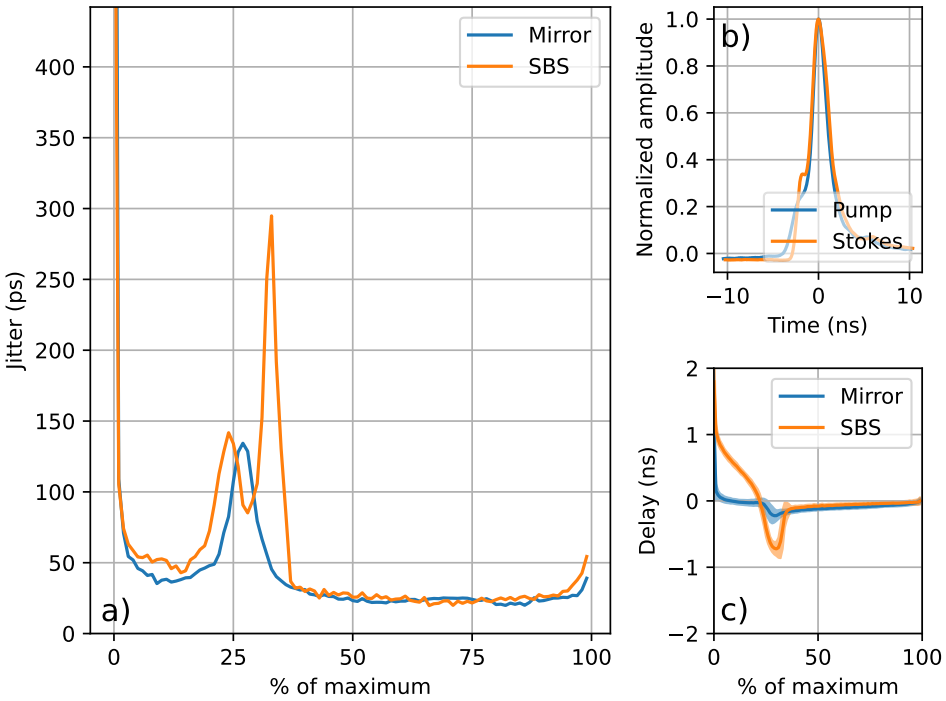

Figure 4.39: Jitter measurement of the SBS interaction for a quasi-gaussian temporal profile. a) Jitter of the rising edge plotted against the threshold taken $\sigma_a(a)$ b) Average input and output temporal shape c) Average delay between pump and Stokes for reaching every value on the rising edge $\tau_a(a)$.

This figure has been obtained following the methodology previously

described and a significant amount of information can be extracted from it:

- The curve presented in Fig.4.39.b is the comparison of the average pump and stokes temporal profile as presented in Fig.4.38.
- From this curve, we can extract the timing at which the pump and Stokes wave exceed threshold for the first time, and plot the *average delay* as a function of the threshold. Because the temporal shape changes during the SBS reflection, this delay is not necessarily a constant line. In our particular case, this is shown in Fig.4.39.c. For the case of the SBS mirror, we can see that the Stokes pulse is delayed compared to the pump for low threshold intensities (characteristic of a leading edge sharpening) then gets ahead for thresholds about 25% of maximum intensity (characteristic of a compression) before stabilising. This stabilisation for delays of $0\ \mathrm{ns}$ being characteristic of a good conservation of the temporal shape.
- Lastly, we can evaluate the deviation compared to this average behaviour. The deviation of the delay for a particular threshold is what we call the *jitter* for this particular threshold. It is shown in Fig.4.39. The definition of the jitter in this particular case is highly dependent on the measurement amplitude noise that gets converted into delay noise. Furthermore, as mentioned earlier, this conversion is also dependent on the temporal shape.

With this, the following informations can be extracted.

- The jitter for very low threshold value is important ($> 400\ \mathrm{ps}$) and caused by electronic noise.
- The large jitter increase for threshold value of 0.2 to 0.35 is caused by the plateau that can be seen on the temporal shapes. Because this plateau reduces the slope, the conversion from electronic noise to delay noise is increased and the jitter value also increase. Because the deformation of the temporal profile generates a flatter plateau of the Stokes temporal shape, the jitter value for the Stokes pulse is increased even further than when using a mirror.
- Despite all those considerations, the timing of the compression spike seems to be the most uncertain part of the pulse. *When observing a residual compression effect, the SBS reflection adds jitter for the leading edge of the pulse*
- for low threshold value < 0.2 , the SBS interaction increases the jitter, despite the Stokes pulse having a sharper slope. *At least some of the* $50\ \mathrm{ps}$ *jitter value is due to a jitter increased caused by the SBS interaction*.

- For higher threshold values $> 35\%$, the jitter of the *mirror* configuration is equal to the jitter of the *SBS* configuration. The SBS does not add jitter after initiation and is indistinguishable from a mirror after the initial compression spike.

In all cases, the jitter value caused by the SBS reflection is below 60 ps (except for the top of the compression spike) no matter the threshold value chosen. And the mirror curve indicates that this measurement is at least partly limited by electronic noise and the real value should be even lower.

4.6.4 . Arbitrary temporal shapes

To evaluate the capacity of the SBS interaction to conserve arbitrary temporal shapes, another shape of interest was studied. Because of the high saturation level of the laser source, the generation of precise and arbitrary temporal shape was arduous. In this section, only preliminary studies are performed to show the feasibility of temporal fidelity. More details and more shapes of interest will be studied in further experiments on a different, Nd:Glass, laser source operating in lower saturation regime and presented in Chap.5. Here, we studied the so-called *fusion-shape* with two successive steps. The temporal fidelity for this shape of interest is shown in Fig.4.40.

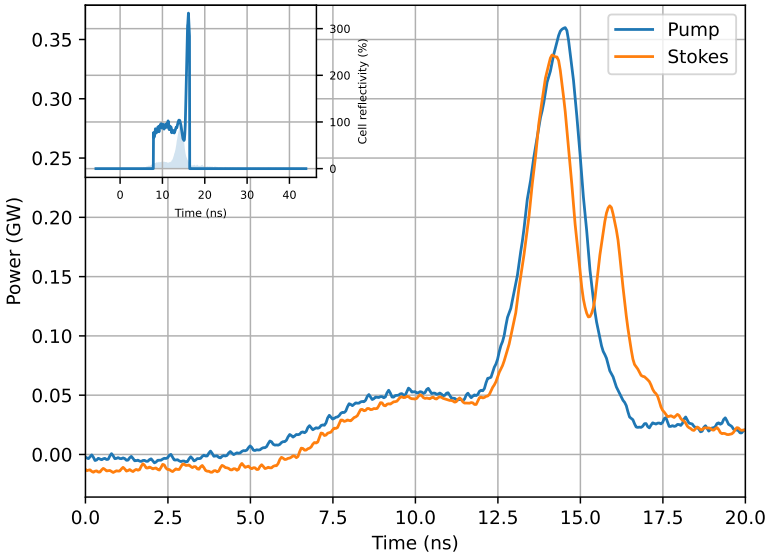

Figure 4.40: Experimental temporal fidelity measurements. Fusion shape with input energy 700 mJ using the 180 mm focusing lens.

This figure shows a good conservation of the main part of the temporal shape but the trailing edge present a sharp spike, characterised by a reflectivity above 300%. Simulations performed for the input temporal shape and the experimental condition and no appearance of this trailing

spike was never observed (see, Fig.4.41), whereas the experimental appearance of the spike was observed with high stability over several hundreds of pulses.

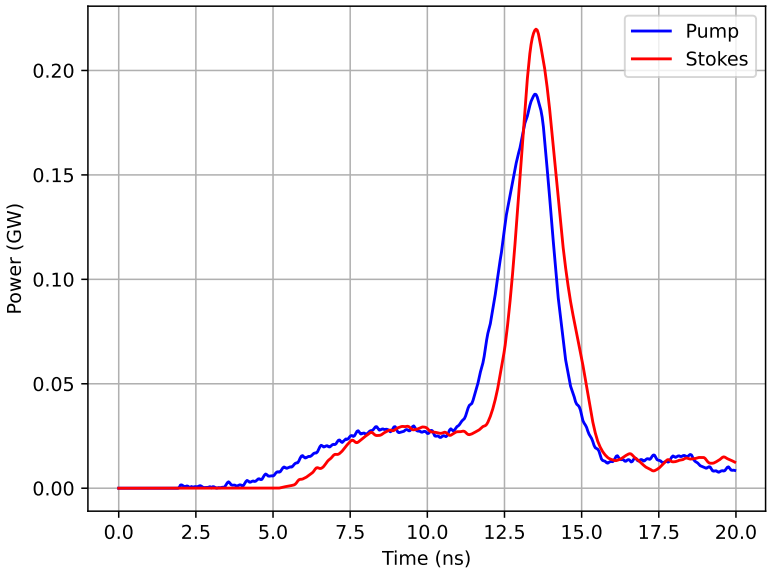

Figure 4.41: Simulation results for an SBS inteaction using as input parameters the experimental parameters of the temporal fidelity with the fusion shape. Nonlinear medium: HT70, input beam diameter: $20\ \mathrm{mm}$, input energy: $700\ \mathrm{mJ}$, focal length used: $180\ \mathrm{mm}$. Simulation results obtained using the 2D model.

One hypothesis regarding the lack of correlation between the simulation results and the experimental results concerns the spectral properties of the pump beam. The simulation models described in Chap.2, derived from the fundamentals SBS equations derived in Chap.1, do not take into account the linewidth of the optical pulses, assuming infinitely narrow-linewidth pulses. The experimental conditions, however, present a short spike of duration FWHM $\approx 2\ \mathrm{ns}$. The typical variation time of this pulse is therefore close to the Brillouin lifetime for the nonlinear medium used ($0.9\ \mathrm{ns}$ for the HT70 liquid used here), and the corresponding linewidth can then approach the Brillouin linewidth. This could then cause a reflectivity drop in the area close to cell entrance and a rebound, generating a compression spike as follow:

- When the SBS cell reaches steady state, the reflecting zone is located close to cell entrance window. Most of the pump signal is therefore reflected in the first few millimeters of liquid. The rest of the cell is hence effectively screened from pump light and the acoustic wave fades.
- When reflectivity drops, due to the linewidth broadening or another

process, the pump is allowed to propagate further inside the liquid and because the acoustic wave has mostly faded, reaches the area near focus point.

- Another cycle of SBS initiation, capable of generating compression, is therefore triggered, and a reflectivity rebound can be seen on the Stokes temporal profile.

This rebound was found to be highly dependent on the input pulse temporal shape (it is completely absent for the gaussian temporal pulse shape). Because of the high saturation of the present system, adapting this temporal shape in this setup was arduous. Finer studies of the feasibility of arbitrary temporal profile conservation will therefore be performed and presented on the setup described in Chap.5.

4.6.5 . Temporal shapes stability

In the previous section, we detailed the measurements of the temporal shape conservation during an SBS interaction. We proved it was possible to conserve arbitrary temporal shapes. In this section, we study the stability of this temporal shape over time. The aim of this section is to ensure no high temporal shape instability is introduced by the component during reflection.

To this aim, about a thousand temporal profiles were acquired for both the input pump beam inside the cell and the output Stokes beam. Statistical analysis was performed to extract the mean temporal profiles and standard deviation of each dataset. Comparison of the mean curves and standard deviation between the pump and Stokes beam are shown for the temporal pulse shapes of interest, for the gaussian pulse shape in Fig.4.42 and for the fusion-like temporal pulse shape in Fig.4.43.

For both temporal pulse shapes, no significant instability increase was identified, although a slight increase can be observed for the residual compression overshoots present inside the Stokes pulses: the SBS interaction does not degrade the temporal pulse shape stability.

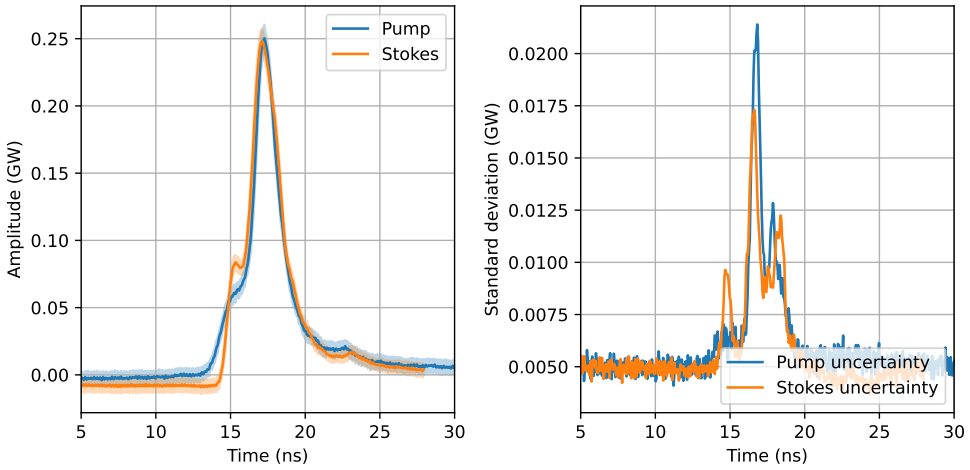

Figure 4.42: Comparison of the stability of the pump and Stokes beam for the SBS interaction. Input pulse: Gaussian pulse shape with input energy $700\ \mathrm{mJ}$ and focusing length of focal length $180\ \mathrm{mm}$.

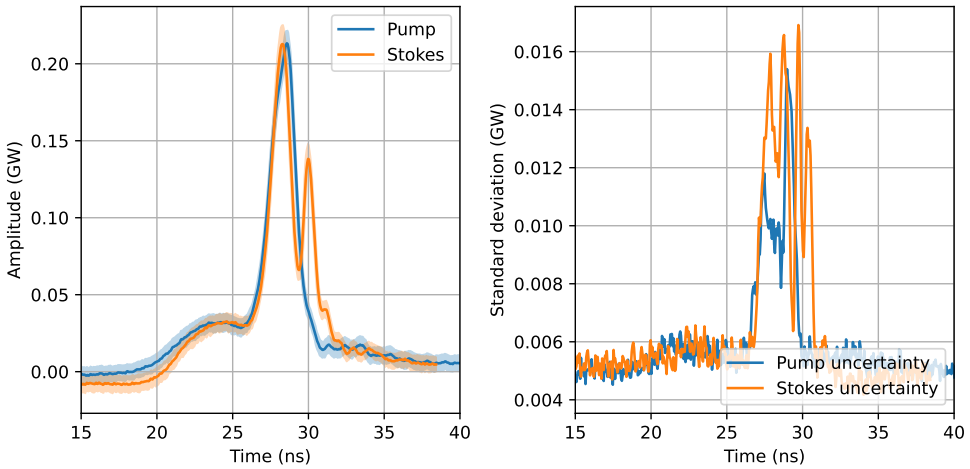

Figure 4.43: Comparison of the stability of the pump and Stokes beam for the SBS interaction. Input pulse: fusion-like pulse shape with input energy $700\ \mathrm{mJ}$ and focusing length of focal length $180\ \mathrm{mm}$.

4.7 . Long term stability measurements

During all the experiments described in this Chap.4, we experimentally demonstrated a good behaviour of the SBS cell over a limited number of shots. Short term stability was demonstrated, and the phenomenon was found not to introduce a significant amount of instability.

In this section, we experimentally investigate the behaviour of the SBS cell over long period of time to confirm the lack of *rogue waves*, or periodical

failure of the SBS interaction. This investigation aimed to identify the presence (or lack thereof) of punctual erratic behaviour by storing and analysing data of at least 100 000 shots. During those experiments, procedural data acquisition was developed and post-processing of the data was performed using a custom python code.

The following datasets are separated day by day to minimize external perturbations caused by temperature and humidity variation inside the lab. About 100 000 shots were performed every day for over 3 weeks leading to more than a million shots over the whole experiment.

Errors on the laser side As mentioned in Sec.3.4.2, the laser source presents occasional failure caused by the low current in the flashlamps of the regenerative section. Those failures do not cause any issues on their own (happening on average once every 2000 shots) but perturb the long-term stability measurement by generating some errors unrelated to SBS failure. To prevent this, simultaneous measurements and acquisition of every input and output pump and Stokes properties are performed. The failures of SBS were in every case correlated to a failure in the pump laser. Points corresponding to aberrant values were isolated to be able to be analysed by hand to assert the absence of erratic behaviour by the SBS cell. In the following, some of the properties of interest are demonstrated.

4.7.1 . Reflectivity

The first property that was analysed was the reflectivity. The goal of this study was to insure the lack of SBS failure where all the input signal was transmitted and ionized the cell, destroying the liquid purity and potentially the components in transmission. This measure was performed using the near-field cameras, analysing the pump and Stokes beams as shown in Fig.4.17. The average reflectivity value was first calibrated using the calorimeter and the fold mirror and reflectivity drops were measured using the comparison of the two cameras.

Using the cameras instead of calorimeters was a choice made to avoid a lack of trigger on one side and de-synchronisation of the calorimeters leading to flawed measurements datasets.

Fig.4.44 shows an example of a reflectivity curve for a single day, using a Gaussian temporal pulse shape and a focusing length of $180\ \mathrm{mm}$.

On this figure can be observed large scale variations on both the input and output signal, due to airflow perturbations inside the room as well as the chiller cycles inside the laser. The simultaneous measurements allow us to measure the individual contribution of the cell. The stability of the cell over a whole day is $< 1\ \%\mathrm{RMS}$. In particular, none of the contribution of the experimental environment (airflow perturbations, chiller cycle) can be

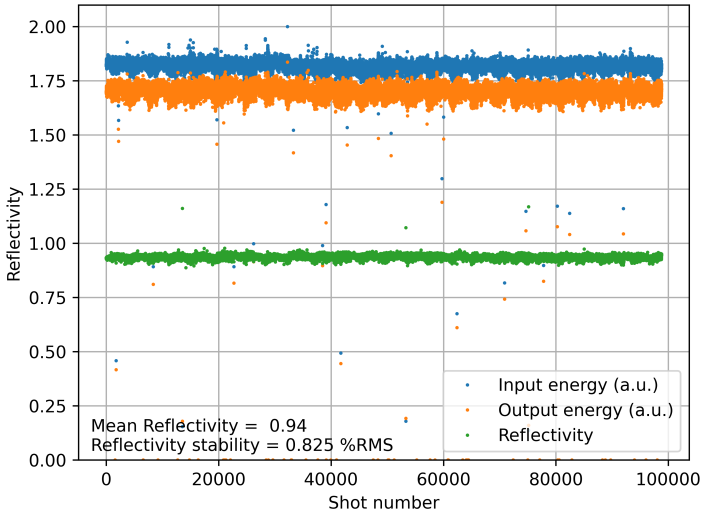

Figure 4.44: Long term reflectivity curve for SBS interaction with gaussian temporal pulse shape, an input energy of 1 J, and a focusing length of 180 mm.

observed. No missed shots were observed during this dataset, as well as in none others. By removing all the point corresponding to a failure on the pump laser, we can correct the measurement. This corrected reflectivity measurement is presented in Fig.4.45.

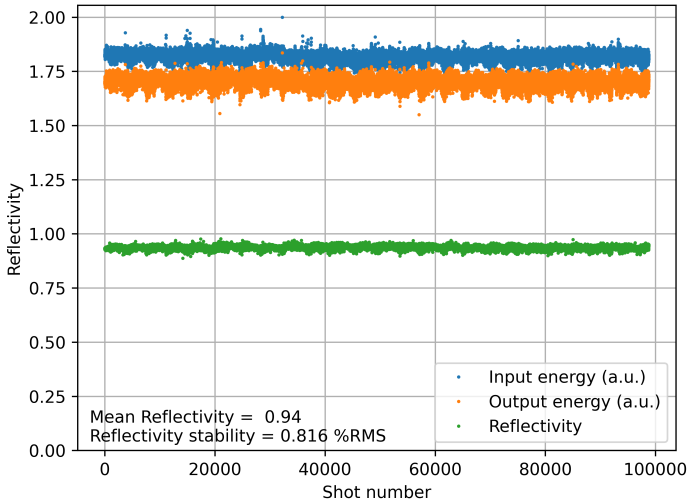

Figure 4.45: Long term reflectivity curve for SBS interaction with gaussian temporal pulse shape, an input energy of 1 J, and a focusing length of 180 mm.

On this graph is presented the long-term reflectivity stability of about 0.8 % RMS, sufficient for most applications. This stability is believed to increase with

input energy, following the results of the short-term stability measurements presented in 4.6.

4.7.2 . Transmitted energy

Calorimeter measurements were also performed, one analysing the reflected energy and the other the transmitted energy. The calorimeters' measurement over 700 000 shots are shown in Fig.4.46 with dashed red lines indicating a day change.

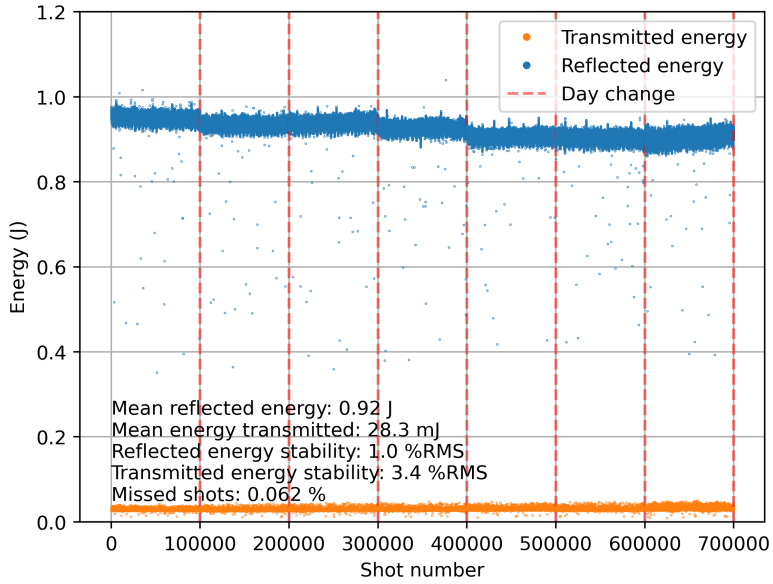

Figure 4.46: Long term calorimeters measurements over 2 weeks of operation in nominal condition.

The instabilities dues to airflow perturbations are this time visible in the energy measurements and slightly degrade the reflectivity values that we observed previously. This measurement shows in particular no transmitted energy increase in 700 000 shots. This confirms the complete lack of SBS failure in the presented operating condition.

4.7.3 . Wavefront

We also study the wavefront stability over a few thousand shots. As stated previously in Sec.4.5.4, the SBS interaction corrects effectively the wavefront but tends to introduce some low-amplitude instabilities in the output wavefront. In this section, we use a *Phasics Sid4* and acquire about 10 000 shots per dataset to compare the input and output wavefront stability. The number of measurements are this time limited by the SID4 memory consumption and analysis speed.

Furthermore, to measure the farfield correction capacities, we use a standard camera placed near best focus and analyse the farfield distribution extension and stability. In those experiments, SBS measurements are correlated with the same measurements using a mirror in place of the cell.

Wavefront stability First, the laser output beam is reflected using either a mirror or the SBS cell and sent on the *SID4* wavefront sensor. The beam aberration contains a small astigmatism because of the added afocal system and the imaging system of the *SID4*. The SBS interaction inverts the wavefront leading to slight differences in *average values* between mirror measurements and cell measurements. In this paragraph, we therefore only consider the *dispersion* of the wavefront information: that is to say, we compare the stability of the reflected Stokes wavefront to the input wavefront stability to evaluate the stability of the reflection itself. Three values of interest are studied: The PV value of the wavefront aberration, the RMS value and the spherical aberration value.

- The RMS wavefront characterises the farfield properties and can be directly linked to the Strehl ratio. This last value corresponding to the actual peak intensity on a potential target at laser chain output. We investigate the wavefront RMS statistic to observe if the SBS reflection introduce inherently stochastic increases of the beam size at focus spot on a potential target.

- The PV wavefront corresponds to the maximum phase difference in the beam. A high PV value can correspond to high spatial frequencies and local beam deformation in propagation. The investigation on the wavefront PV distribution is performed to identify stochastic local increase in high spatial frequencies inside the beam that could therefore generate near field modulation after propagation. It has to be performed separately to the RMS measurements because a very localised high amplitude wavefront aberration would be invisible in the RMS measurements.

- The spherical aberration is, in our case of study, the aberration of interest that will be added to quantify the cell statistical correction capacities. Spherical aberration and RMS wavefront measurements are performed without and with aberration introduction in the middle of the double pass and the statistics of the SBS reflection are compared depending on the input aberration level.

The comparison of those three values between pump (with a mirror in place of the cell) and Stokes (after reflection in the SBS cell) datasets are shown in Fig.4.47-Fig.4.49. Because only one *SID4* is accessible, those

measurements were not performed in parallel. Hence, no correlation or aberrant shot analysis can be performed.

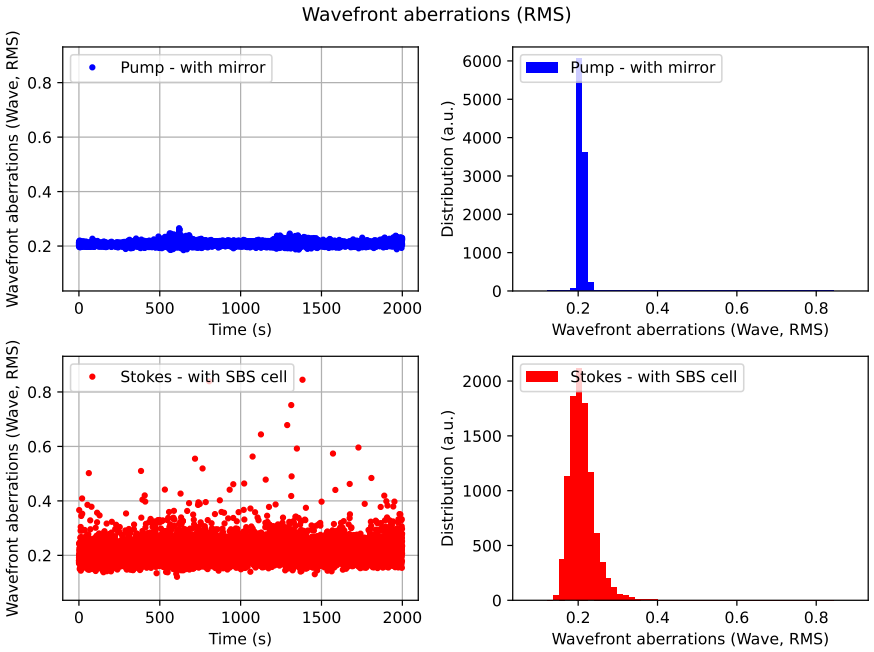

Figure 4.47: Comparison of the long term stability of the pump and Stokes RMS value of the wavefront as measured with the SID4 (Phasics). The average wavefront RMS dispersion is equal for the cell configuration and the mirror configuration, yet the cell induces some additional wavefront instabilities.

As expected, no clear degradation of the wavefront properties can be observed in those three datasets on average. Yet the dispersion of the data shows yet again that the SBS reflection introduces some low amplitude instabilities during reflection.

The same measurements are then performed a second time with the introduction of $1\,\lambda\mathrm{PV}$ of Seidel spherical aberration (approximately $0.08\,\lambda\mathrm{RMS}$ Zernike aberration) in front of the cell or mirror. The corresponding results for RMS and spherical aberration are shown in Fig.4.50-Fig.4.51. The PV measurements were also performed and no clear change was observed.

As expected, the aberrations wavefront measurement are shifted to higher aberration values (for both RMS and spherical aberration) equal to twice the aberration level introduced, because of the double pass: $0.16\,\lambda\mathrm{RMS}$ of pure spherical aberration. On the contrary, the SBS curves stay constant on average (thanks to the double pass wavefront correction). No significant instability increase is observed during this second experiment. The quality of correction obtained by using the SBS cell is further confirmed

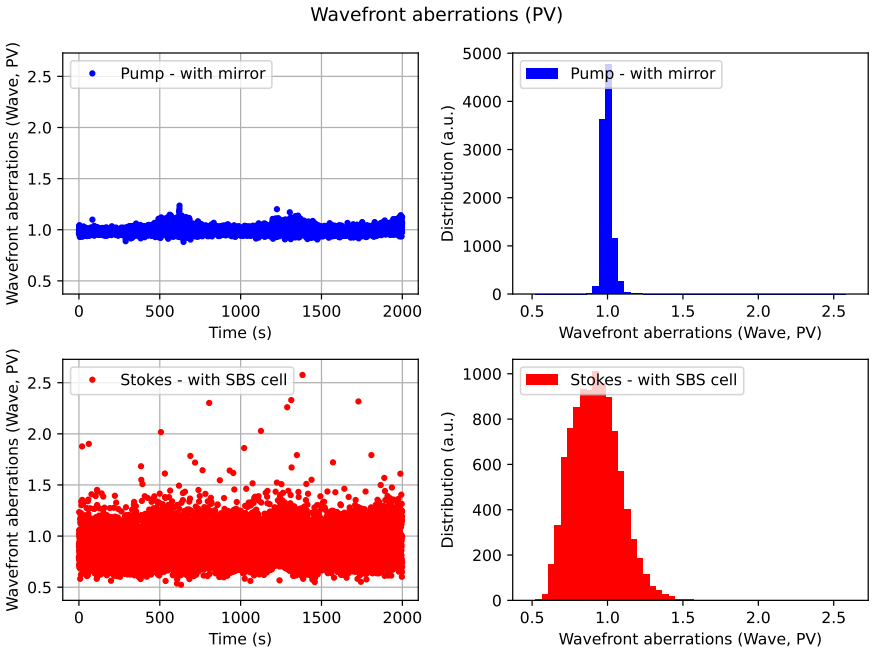

Figure 4.48: Comparison of the long term stability of the pump and Stokes PV value of the wavefront as measured with the SID4 (Phasics). As in the RMS wavefront measurements, the average PV value measured is equal for the mirror and cell configuration but some instabilities are added by the SBS reflection. Those instabilities are of higher amplitude in the PV case because of the inherent averaging across the aperture performed during the RMS calculation. However, no highly aberrant PV value, that could characterise beam deformation in propagation, can be observed.

by using the far-field camera and measuring the diameter of encircled energy as shown Fig.4.52.

Under the unaberrated configuration, measurements of the focus spot size for a mirror and an SBS cell are similar and the SBS cell do not degrade good farfield properties. However the introduction of aberration causes a clear increase of the pump focus spot size but the Stokes focus spot size stays constant no matter the aberration level introduced. The farfield analysis shows that a good correction of the wavefront aberration is effectively performed by the SBS cell.

Once again, the wavefront correction capacities of the cell are confirmed, guaranteeing good farfield quality after a double pass in wavefront aberration source at the cost of a low amplitude wavefront instability. No significant circled energy drop were observed during the experiments over 10 000 shots.

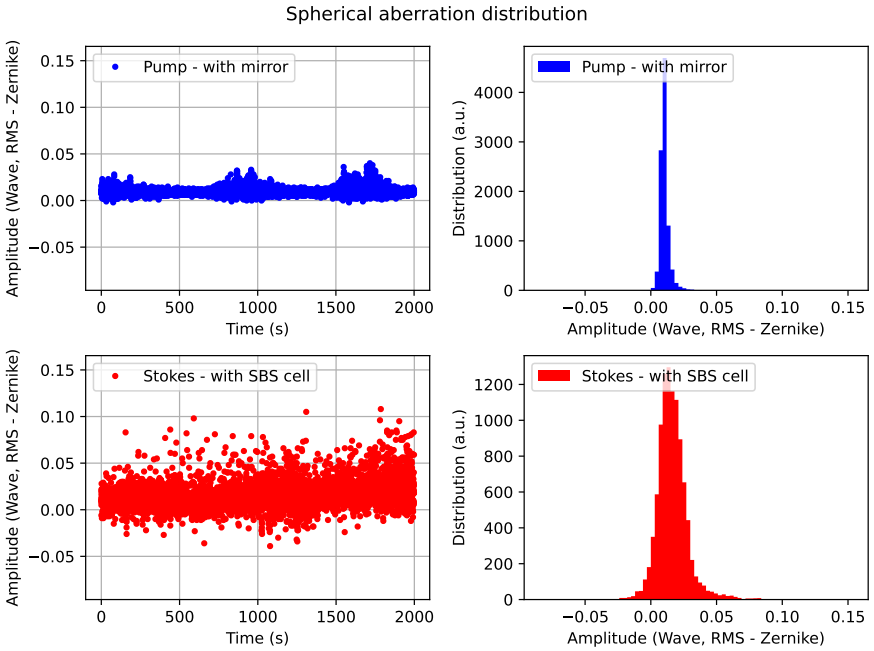

Figure 4.49: Comparison of the long term stability of the pump and Stokes spherical aberration value as measured with the SID4 (Phasics). Once again, the average spherical aberration value measured with and without the SBS reflection is equal but the SBS reflection adds a small amplitude instability.

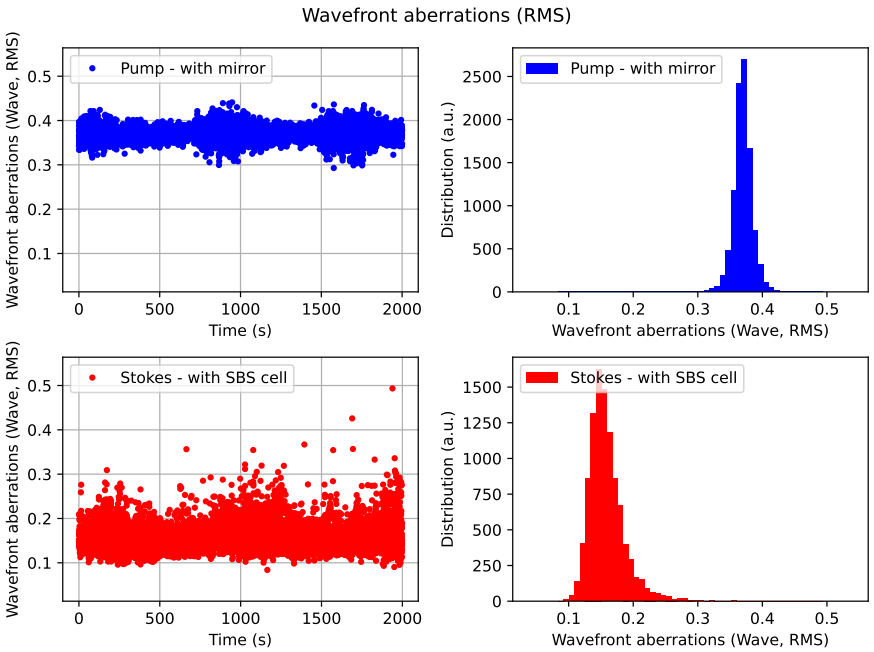

Figure 4.50: Comparison of the long term stability of the pump and Stokes RMS value of the wavefront as measured by *Phasics - SID4*. $0.08\ \lambda\mathrm{RMS}$ of spherical aberration added in the middle of the double pass. Compared to the data obtained with the aberration plates given Fig.4.47, the pump RMS wavefront aberration are shifted towards higher values by twice the introduced amount in the middle of the double pass $0.16\ \lambda\mathrm{RMS}$. The data obtained under the SBS configuration stay of the same average aberration and same dispersion than without the aberration plates: the SBS reflection effectively corrects all the aberrations present in the middle of the double pass.

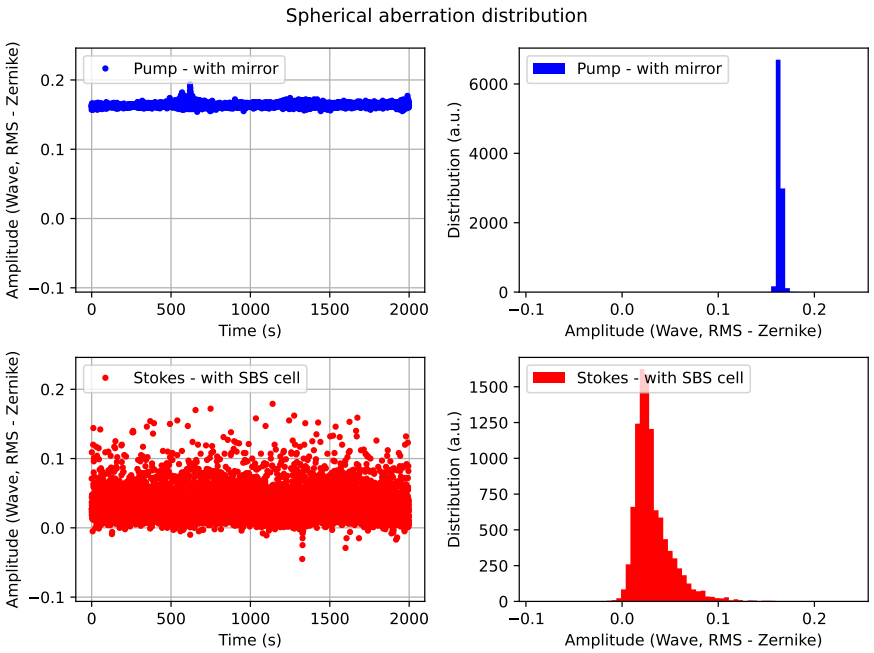

Figure 4.51: Comparison of the long term stability of the pump and Stokes spherical aberration amplitude as measured by *Phasics - SID4*. $0.08\ \lambda\mathrm{RMS}$ of spherical aberration added in the middle of the double pass. As described previously, the average spherical aberration shifts only for the configuration with a mirror in place of the cell. Once again, the SBS reflection corrects all the aberration in the middle of the double pass, at the cost of a small amplitude stability degradation.

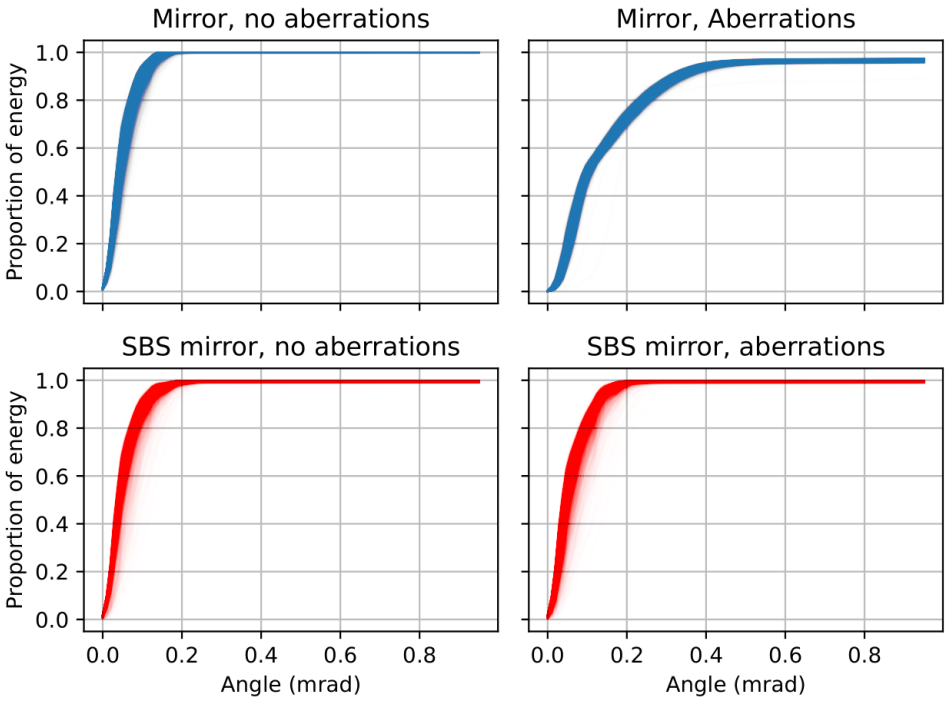

Figure 4.52: Accumulation of the encircled energy as a function of ray angle for 9000 shots. Focal lens used for the farfield focusing: $500\ \mathrm{mm}$. When no aberration is introduced in the middle of the double pass, the mirror and the cell present similar average circled energy value. The SBS cell introduces low-amplitude instabilities that can be seen when observing the width of the circled energy curves. When introducing aberrations in the middle of the double pass, the mirror circled energy curve shifts and the focus spot broadens, whereas the SBS mirror curve stays identical to the unaberrated one.

4.8 . Conclusion

In this chapter, we investigated the behaviour of a phase conjugate mirror placed outside the laser. The individual contribution of the cell were investigated at medium energy and proper operation conditions were identified. The cell proved to be an efficient tool to correct aberration and was additionally shown to be able to conserve properly temporal profiles. Some detrimental effects that could perturb the good operation were identified:

- A sharp rise time, of the time scale of the SBS phonon lifetime, was shown to generate plasma inside the cell, thereby changing the chemical composition of the fluid and potentially degrading good cell long-term operation (Sec.4.3.1). Ionization proved to be a challenging issue to eliminate without proper SBS cell initiation.

- The presence of spatiotemporal coupling inside the beam (temporal profile shape dependency with position inside the beam) were shown to disturb the homogeneous SBS initiation and to generate stochastic hot spots inside the reflected beam.

- The presence of high amplitude aberration was shown to degrade the quality of the SBS reflection, generating in order of increasing amplitude: 1. A drop in wavefront stability. 2. A drop in reflectivity as the focus spot size (and hence peak intensity inside the cell) decreases. 3. The apparition of spatial profile artefacts. Further development of the numerical models taking into account the transverse description of the beam will be required to quantitatively understand this last phenomenon.

However, it is possible to get rid of all those limitations by adequately adjusting the parameters of the pump beam. This requires a particular design of the laser source, including temporal shaping capabilities and the limitation of the saturation during the first stages of amplification.

Eliminating all those inadequate properties from the pump beam allowed us to reach excellent reflectivity (up to 95%), excellent wavefront compensation capabilities and to demonstrate the first temporal profile conservation properties ever in an SBS cell. Our experimental setup consisting of several Nd:YAG amplifiers operating in highly saturated regime, made the arbitrary generation of temporal shapes arduous. And in our case limited the quality of the experiments regarding temporal profile.

In addition to this, long term stability measurements were performed over several hundreds of thousands of shots and no particular erratic SBS behaviour was ever identified. Those experiments confirmed the usability of

SBS at low risk in industrial laser system and highlighted some of the requirement of the laser sources for good operation.

In the following, the first technological locks removed by those preliminary studies will allow us to design experiments on high energy SBS mirrors operating at extremely high energy level, on the order of 100 J.

Bibliography

The following bibliography contains all the references cited in this chapter. A full bibliography of the thesis is given after the general conclusion. In addition, every bibliography entry is associated with every paragraph it has been referenced in. The corresponding section numbers are indicated at the very end of the entry.

[1] Lee M. Frantz and John S. Nodvik. Theory of Pulse Propagation in a Laser Amplifier. *Journal of Applied Physics*, 34(8):2346–2349, August 1963. 3.2, 3.4.1, 4.2, 4.4.2

[2] H. Yoshida, V. Kmetik, H. Fujita, K. Yoshida, T. Yamanaka, and S. Nakai. High performance of phase conjugated stimulated Brillouin scattering mirror based on high purity liquid heavy fluorocarbons. *AIP Conference Proceedings*, 369(1):1004–1008, May 1996. 3.1, 3.1, 3.2, 3.3, 3.1.3, 3.4, 3.3.2, 3.3.2, 4.3.1

[3] Nikolay Andreev, Oleg P. Kulagin, Oleg V. Palashov, Guerman A. Pasmanik, and Vladimir Rodchenkov. SBS of repetitively pulsed radiation and possibility of increasing the pump average power. In *Solid State Lasers for Application to Inertial Confinement Fusion (ICF)*, volume 2633, pages 476–493. SPIE, December 1995. 3.1, 3.3.2, 4.3.1

[4] L. P. Schelonka and C. M. Clayton. Effect of focal intensity on stimulated-Brillouin-scattering reflectivity and fidelity. *Optics Letters*, 13(1):42–44, January 1988. Publisher: Optica Publishing Group. 4.4, 4.5

[5] John J. Ottusch and David A. Rockwell. Stimulated Brillouin scattering phase conjugation fidelity fluctuations. In *Conference on Lasers and Electro-Optics (1991), paper CTuW23*, page CTuW23. Optica Publishing Group, May 1991. 4.4

[6] Yifu Chen, Bowen Tan, Duo Jin, Bin Chen, Zhenxu Bai, Kun Wang, Yulei Wang, and Zhiwei Lü. Characteristics and suppression of beam distortion in a high repetition rate nanosecond stimulated Brillouin scattering phase conjugation mirror. *High Power Laser Science and Engineering*, 12:e20, January 2024. 3.2, 3.3.1, 4.4

[7] C. Brent Dane, William A. Neuman, and Lloyd A. Hackel. Pulse-shape dependence of stimulated-Brillouin-scattering phase-conjugation fidelity for high input energies. *Optics Letters*, 17(18):1271–1273, September 1992. Publisher: Optica Publishing Group. 3.1.2, 4.4, 5.4.2

[8] James R. Leger, Diana Chen, and Kevin Dai. High modal discrimination in a Nd:YAG laser resonator with internal phase gratings. *Optics Letters*, 19(23):1976–1978, December 1994. Publisher: Optica Publishing Group. 4.4.2

[9] Jacques Luce, Gerard Deschaseaux, and Claude Rouyer. Wide square flat top mode discrimination in a regenerative amplifier. In *2006 Conference on Lasers and Electro-Optics and 2006 Quantum Electronics and Laser Science Conference*, pages 1–2, May 2006. ISSN: 2160-9004. 4.4.2

[10] Jerome M. Auerbach and Victor P. Karpenko. Serrated-aperture apodizers for high-energy laser systems. *Applied Optics*, 33(15):3179–3183, May 1994. Publisher: Optica Publishing Group. 3.4.2, 4.16

5 - High energy characterisation

5.1 . Introduction

In the previous chapters, the SBS effect was introduced theoretically, simulated numerically, then subsequently demonstrated and characterized experimentally on a custom laser source developed for the thesis. Those studies allowed for a wide range of parametric measurements, understanding of the SBS effects and gave us insightful feedback for the energy scale-up.

In this chapter, we perform SBS reflection experiments on a high energy laser system at LULI's HERA facility up to $122\ \mathrm{J}$. The experimental setup is similar to the one in the previous chapter with the SBS cell placed outside the laser to study its individual contribution and measure its spatial and temporal fidelity.

In the scope of this thesis, one of the goals is to develop an SBS cell compatible with multi-kilojoule laser systems. The cell being placed at the middle of the double pass inside the amplifiers, this corresponds, under particular laser architectures, to about $100\ \mathrm{J}$ input energy on the cell. The cell should thus operate at this energy level while keeping a good temporal and spatial fidelity. Because the laser source developed in the precedent part of the thesis was limited to about $5\ \mathrm{J}$, a second test laser source is required. The experiments are then performed at the HERA laser facility [1], providing up to $200\ \mathrm{J}$ per shot, with a repetition rate of $1\ \mathrm{shot}$ per $20\ \mathrm{min}$ and temporal profile shaping capabilities.

In the present chapter, we first use the numerical simulation to design an SBS cell optimised for the required energy levels. We then present the experimental optical layout used and the first tests at reduced energy. Last, the present the experimental results on these high energy experiments up to input energy level of $122\ \mathrm{J}$, corresponding to the maximum energy ever reported inside a phase conjugate mirror.

5.2 . Experiment design

5.2.1 . Focusing conditions

As described in the numerical simulation chapter (Sec.2.3.5 as well as in the preliminary experiments 4.6.2), the choice of focusing lens has a large influence on the pump temporal profile conservation during the SBS reflection. This effect is particularly concerning in the case of high-energy operation as the compression effect on high-energy pulses can generate

high intensity spikes and hence damage large aperture optical components. For this reason, simulations of the SBS interaction as a function of the focal lens of our system is performed with the parameters of the laser chain. In particular, an input energy of 50 J, the nonlinear medium selected for this experiment *FC770* and the beam diameter at laser chain output of 93 mm were set as simulation input. The simulations results are shown in Fig.5.1

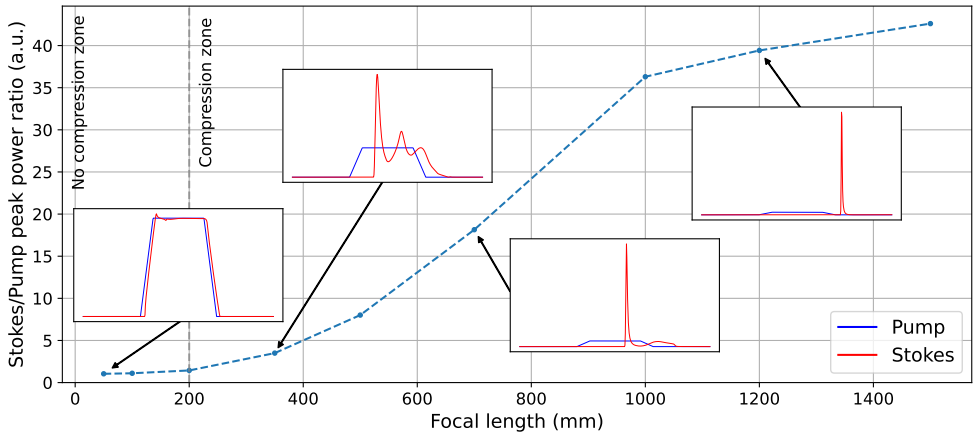

Figure 5.1: Simulations of the peak power increase during SBS reflection as a function of the focusing lens used. Simulation based on the 2D model for a pump energy of 50 J, an input beam diameter of 93 mm and a square input temporal profile of duration 10 ns.

The simulation results clearly show an increase in compression ratio for focusing lens of focal length > 200 mm corresponding to interaction distances inside the fluid of > 250 mm. As such a short focal lens is chosen. However, on the contrary to the preliminary studies presented in Chap.4, this focal length distance is now non-negligible compared to the full aperture of the beam. A 200 mm focal lens is opened at $F/2.15$, and is therefore hard to manufacture and introduces a significant wavefront aberration. Furthermore, at that energy level, the ghost focus created by the lens can start to ionize the air and hence perturb the propagation of the incident beam or, in the worst case, damage the other optical components. To answer those difficulties, two different focusing lenses were used during the experiments.

5.2.2 . Focusing lens design

First, a focal lens is designed to be used as the input window of the cell, focusing the input beam at a propagation depth of 300 mm and using the air-glass as well as the glass-liquid interfaces for the focusing. This design also prevents all ghost foci on the air side of the lens, hence guaranteeing no plasma formation in the pump beam path. This design comes at the cost of a

high aberration level: $30\ \lambda\mathrm{PV}$ on the Zernike basis, corresponding to $9\ \lambda\mathrm{RMS}$ or $100\ \lambda\mathrm{PV}$ on the usual Seidel basis. The optical layout as given by the optical simulation software *ZEMAX* is given in Fig.5.2 and the resulting wavefront is given in Fig.5.3 In the following, this focusing lens is called L_1.

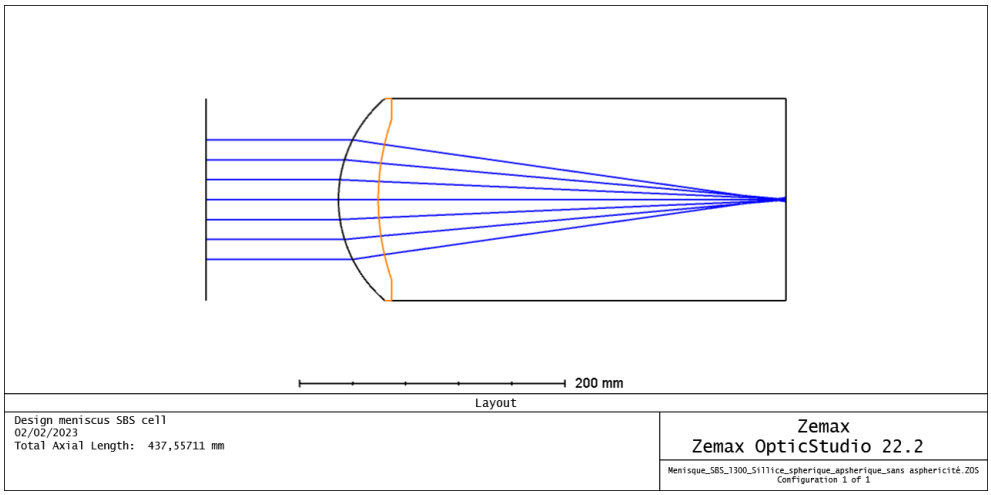

Figure 5.2: Optical layout and beam tracing of the pump beam focused by the L_1 focusing lens. Figure obtained by the *ZEMAX* software

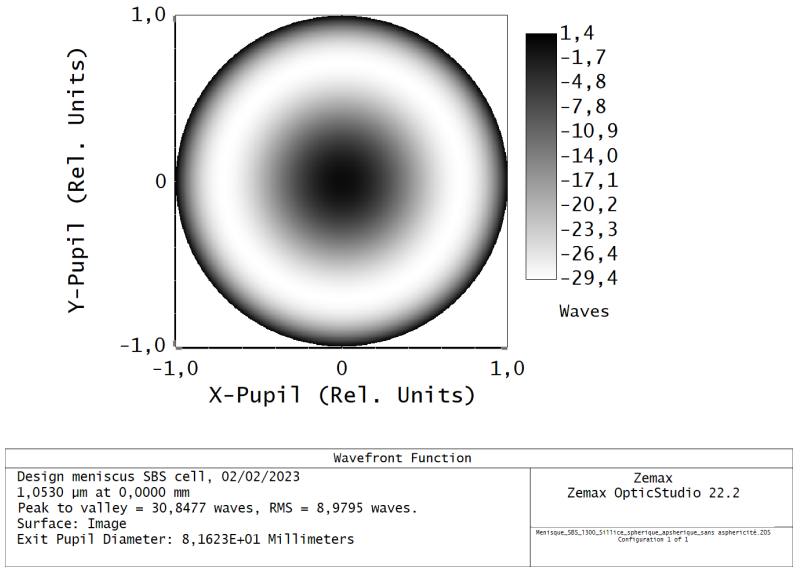

Figure 5.3: Simulated wavefront after a single pass in the L1 lens as calculated by the ZEMAX software.

The second window of the high energy SBS cell is plane and offers the freedom to choose a standard focusing lens to be placed before the cell.

During the experiments, a second lens L_2 is used and is constituted of a $340\ \mathrm{mm}$ doublet lens placed before the cell in such a way that the interaction distance of $300\ \mathrm{mm}$ was unchanged compared to L_1. This lens presents several glass-air interfaces and hence generates ghost foci. The operation with the L_2 lens then requires placing all the other components of the systems away from the parasitic focus points. The optical layout and resulting wavefront are given in Fig.5.4-5.5.

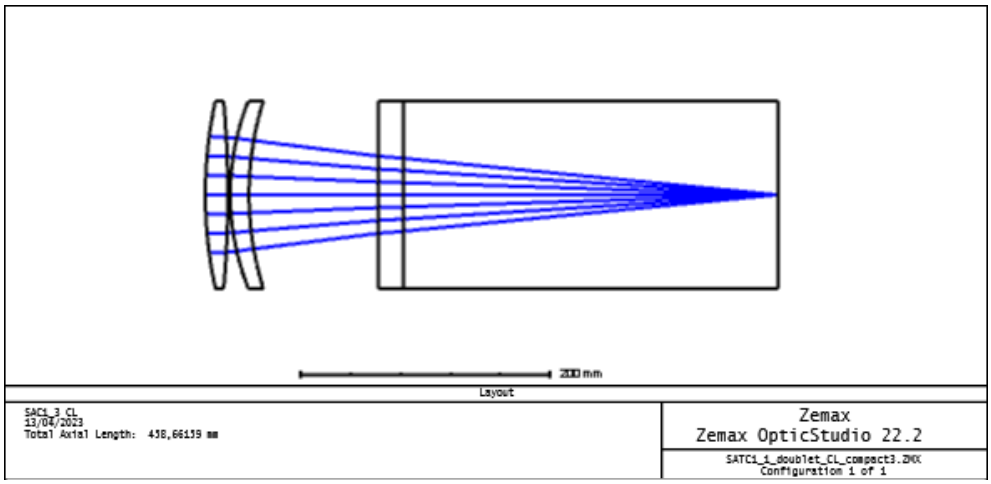

Figure 5.4: Optical layout and beam tracing of the pump beam focused by the L2 focusing lens. Figure obtained by the *ZEMAX* software

A summary comparing the properties of the two lenses is presented in Tab.5.1.

	L_1	L_2
Focal length	$236\ \mathrm{mm}$	$340\ \mathrm{mm}$
Effective interaction length	$300\ \mathrm{mm}$	$300\ \mathrm{mm}$
Spherical aberration introduced (Zernike RMS)	$8.9\ \lambda\mathrm{RMS}$	$1.0\ \lambda\mathrm{RMS}$
Spherical aberration introduced (Seidel PV)	$119.4\ \lambda\mathrm{PV}$	$13.8\ \lambda\mathrm{PV}$

Table 5.1: Summary of the properties of the two lenses used in the experiments

In the following, those two lenses are used and compared in the experiments by using the optical layout presented.

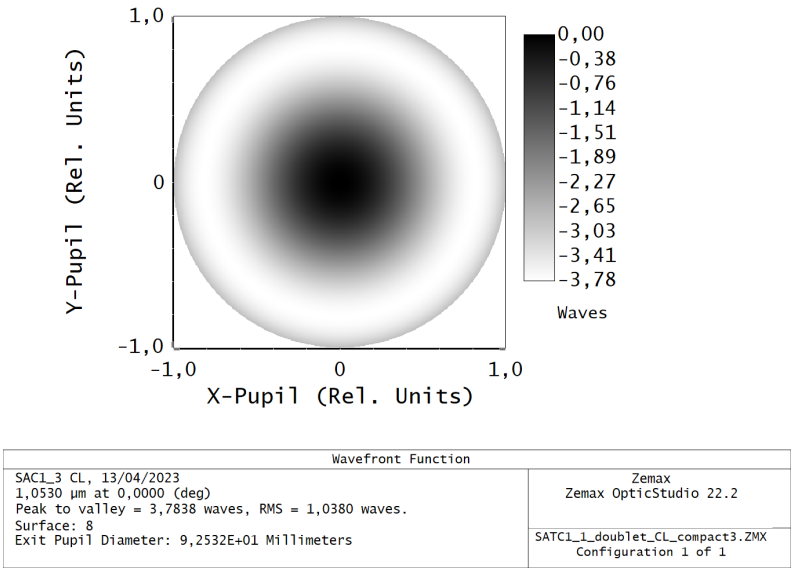

Figure 5.5: Simulated wavefront after a single pass in the L2 lens as calculated by the ZEMAX software.

5.2.3 . Experimental layout

Besides these 2 focusing lenses, a setup comparable to the one described in Chap4 is built for the high energy experiments. As previously, the SBS cell is placed outside the amplifier section. The isolation between the laser and the cell is performed through polarisation isolation. A glass plate AR coated on only one side is introduced on the beam path and extracts about 4% of the input energy and 4% of the output energy to be sent on the two metrology optical lines analysing the properties of the pump and Stokes beams. The pump and Stokes beam metrology lines both contains:

- QE-95 calorimeters measuring the input (output) energy of the pump (Stokes) beam.
- An EOT-3000 photodiode analysing the pump (Stokes) temporal profile with a rise time of $175\ \mathrm{ps}$, fast enough to measure potential compression spikes or modulation in the reflected pulse.

In addition to that, the Stokes beam metrology line contains an imaging system redirecting the beam to either a camera or a wavefront sensor (*Sid4 V - Phasics*). This imaging system is constituted of two plano-convex lenses of focal length respectively $1200\ \mathrm{mm}$ and $25\ \mathrm{mm}$. The second lens in particular is arduous to align properly, and the full system introduces a significant amount of aberration. More information on that particular aspect is presented in the wavefront reversal section (Sec.5.4.3). During the experiment, the calibration

for the reflectivity as well as the reference wavefront are acquired by placing a 0° *fold* mirror in place of the cell. For most of the shots, a beam profile control is simultaneously performed with burn papers attached to the beam dump after reflection by the isolation polariser. A full representation of the optical layout used in the experiments is presented in Fig.5.6.

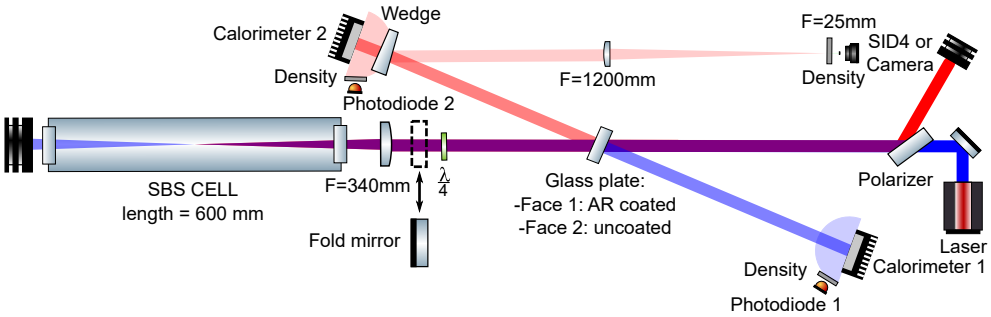

Figure 5.6: Optical layout of the high-energy SBS experiments

In the following, we present the experiments performed with those two lenses and this experimental setup.

5.3 . Low-energy experiments

To avoid optical damage on the components of the system at high energy, we first start the experiment at low pump energy (about $1\ \mathrm{J}$) and test the good operation using the L_1 focusing lens. Those first experiments lead to an unexpected cell behaviour: the occurrence of a highly peaked hot spot in the centre of the Stokes beam. The investigation of this hot spot occurrence is presented in the following.

5.3.1 . Hot spot

The hot spot in the reflected beam is first identified using the burn paper placed on the beam dump after the polariser. A scan of this burn paper is presented in Fig.5.7.

First, we investigate whether this hot spot on the burn paper can correspond to a high order focus spot. Several subsequent shots are thus performed, moving the paper over $10\ \mathrm{m}$ in both directions. The spot shape, location in the beam, and intensity remain constant. Furthermore, when performing several shots on the same burn paper, the spot properties stayed perfectly identical. Hence, the physical process in action is clearly deterministic.

We consider the fact that the hot spot can be caused by parasitic reflections on the inner interface of the L_1 lens, generating a focal spot inside the liquid. We thus slightly tilt the cell. The hot spot is still present and

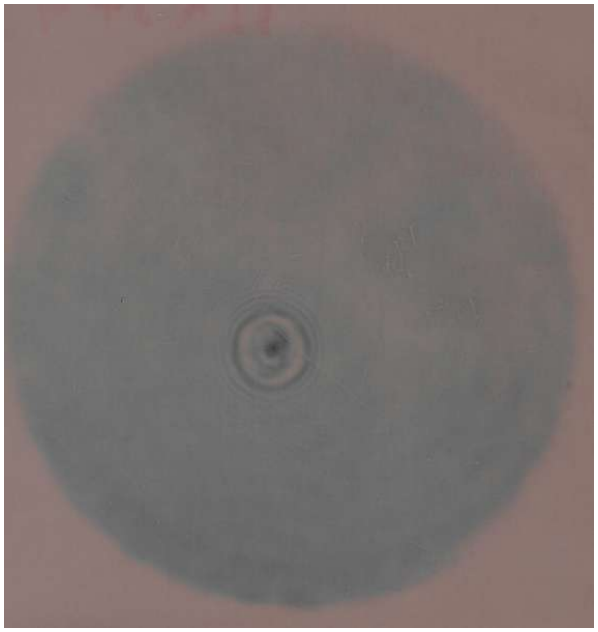

Figure 5.7: Burn paper of the Stokes beam for a low energy shot using focusing lens L_1.

its shape is barely affected by the operation. Since the parasitic reflection should have been removed from the beam path with the tilting, the hot spot was found to not correspond to this ghost focus effect inside the liquid.

The fact that the shape of the hot spot changes shape when tilting the lens, as well as the overall shape of the spot makes us think about a parasitic effect of the high spherical aberration introduced by L_1. In the following, we reduce the spherical aberration by placing a hard aperture in the pump beam path.

5.3.2 . Hot spot mitigation

The introduction of a hard aperture drastically decreases the hot spot intensity until its complete mitigation for aperture diameters $< 60\ \mathrm{mm}$. The wavefront sensor is, at this stage, replaced with a camera to better characterise the hot spot relative intensity compared to the rest of the beam and quantify the aperture reduction effect. Several beam profiles acquired with this camera for smaller apertures are presented in Fig.5.8.

The spherical aberration level being strongly linked to the diameter (Seidel spherical aberration level is $\Delta_{spherical} = w^4$), the reduced hot spot value with aperture decrease thus confirms our hypothesis: The hot spot occurrence is caused by the high spherical aberration level. When translating the aperture, un-centring it compared to the optical axis of the L_1 lens, we introduce aberration again. In this case, the hot spot appears

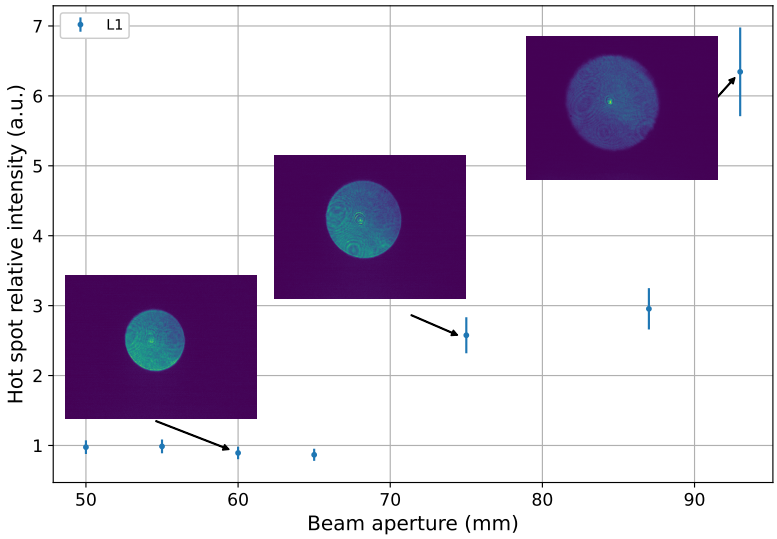

Figure 5.8: Hot spot relative intensity compared to the rest of the beam as a function of pump aperture (diameter).

again but changes shape. This change can be attributed to the aberration type change and the lack of axisymmetry. The corresponding burn paper is shown in Fig.5.9.

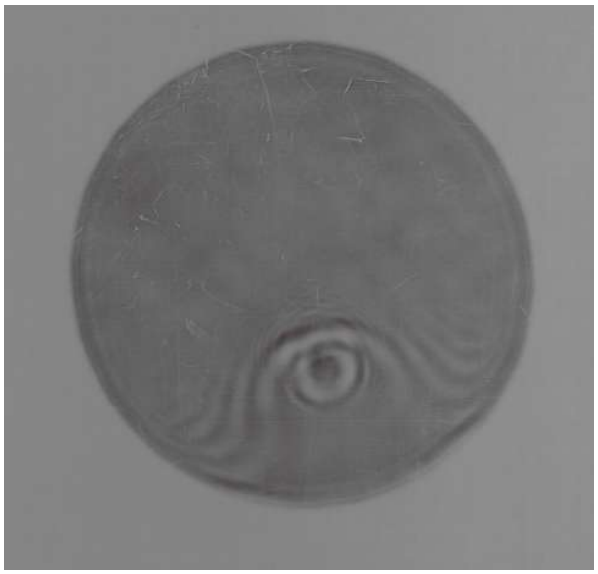

Figure 5.9: Spatial profile of the Stokes beam measured by a burn paper. Hard aperture of diameter $50\ \mathrm{mm}$ placed in the pump beam and uncentered. The hot spot location remains centered on the optical axis of the L_1 focusing lens.

To further confirm that experimentally, we make sure that the edges of the beam cause the hot spot occurrence. To this aim, we place several

optical densities of increasing attenuation value inside the beam, partially shielding the hot spot location from pump light, before the glass plate. The Stokes beam is then observed using the camera and the hot spot is still present with comparable intensity (shown in Fig.5.10).

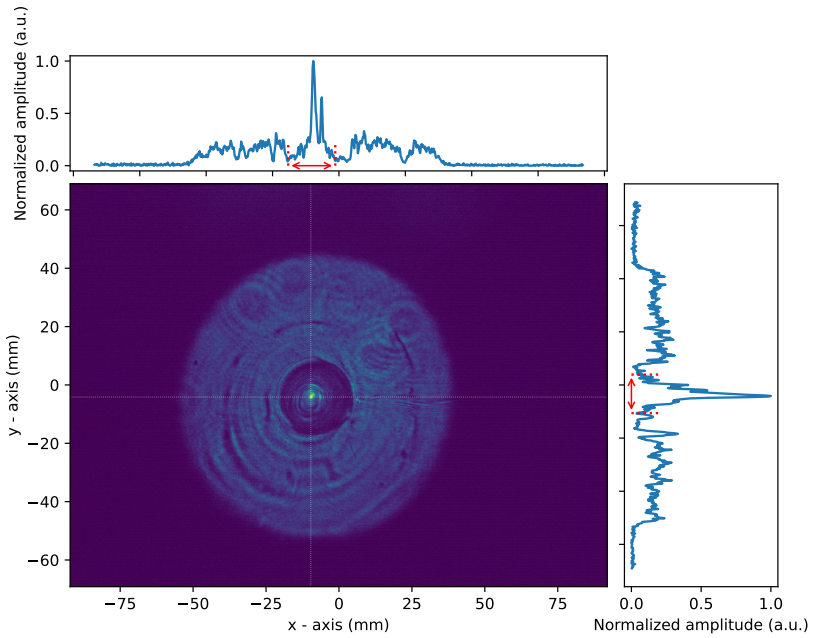

Figure 5.10: Spatial profile of the Stokes beam as measured by the camera. OD1 density placed in the pump beam path at the location of the hot spot.

This confirms the fact that *the edges of the beam cause the hot spot occurrence*, and validate our hypothesis of the spherical aberration influence on our experiments. It is to be noted that no significant aberration excess is measured on the reflected beam by the SID4 analysis, demonstrating the full correction of the lens spherical aberration (more than $200\ \lambda\mathrm{PV}$ of Seidel aberration in the double pass), even during the operation with a hot spot inside the beam.

We also try to study the influence of input energy on the hot spot contrast as shown in Fig.5.11. The hot spot visibility is found to strongly depend on the input energy, being more peaked for lower input energy. Hence, we believe that increasing the input energy could decrease the hot spot intensity. In the scope of our experiments, it was decided not to risk damaging the optical components of the system by testing this hypothesis.

The hot spot occurrence is then solved by replacing the focusing lens L_1 by L_2, usable at full aperture and inducing aberration corresponding to a spherical aberration level of L_1 with aperture $60\ \mathrm{mm}$. Using the corresponding hot spot intensity vs aperture given Fig.5.8, the hot spot

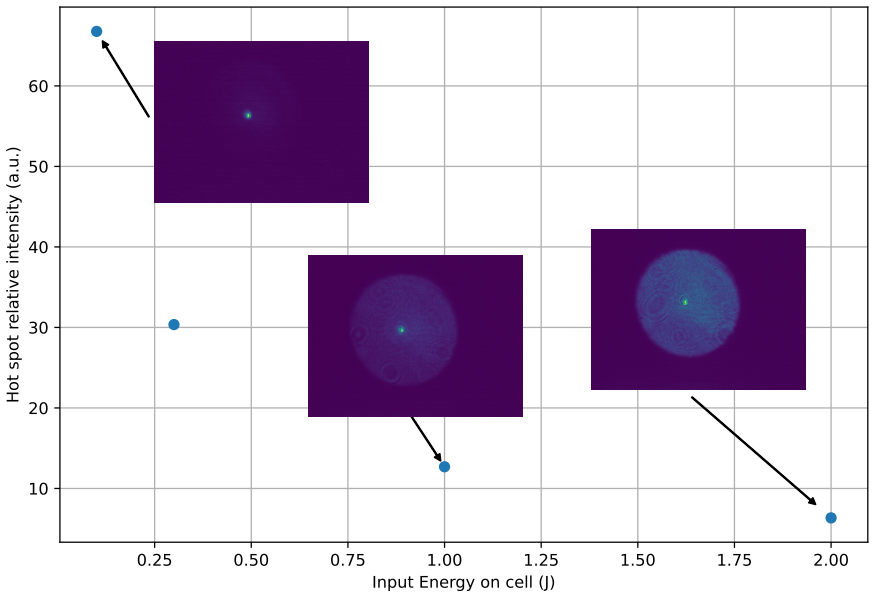

Figure 5.11: Hot spot visibility as a function of input energy.

should therefore completely disappear when using L_2. We confirmed this experimentally as shown in the beam profile obtained at full aperture at an input energy level of 2 J presented in Fig.5.12.

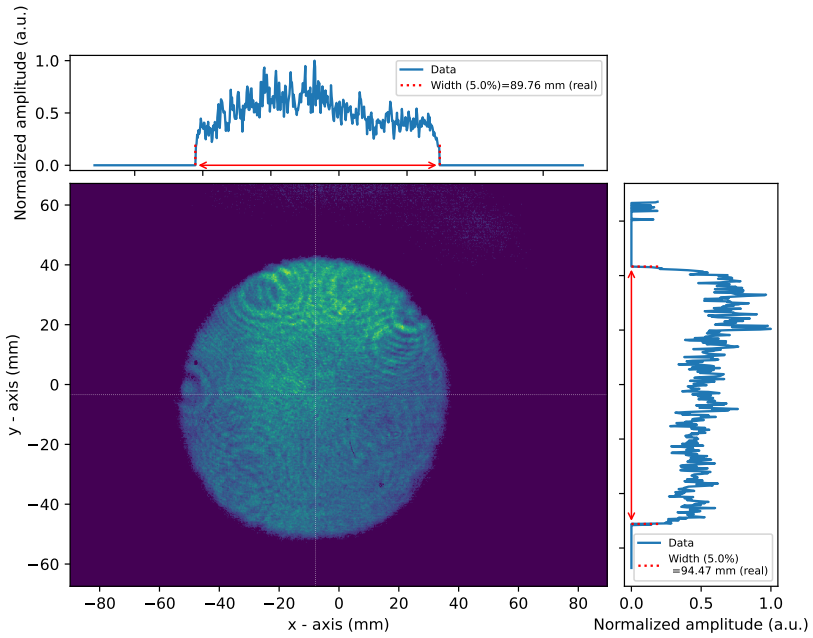

Figure 5.12: Spatial profile of the Stokes beam measured with the camera using the L_2 focusing lens at full aperture and an input energy of 2 J

5.4 . High-energy experiments

In the following, we describe the results of the 120 shots performed during the high energy experiments using the L_2 focusing lens.

5.4.1 . Reflectivity

During the experiments, several temporal shapes are used with energy ranging from $100\ \mathrm{mJ}$ up to $122\ \mathrm{J}$. For every shot, a very high reflectivity is observed. Because the calorimeters present a significant uncertainty and the energy stability of the laser chain is limited, the reflectivity measurements are limited to about 7% precision. To increase this precision, a second calorimeter is placed behind the cell in order to detect potential significant transmitted energy increases characteristic of a reflectivity drop. This second calorimeter has an energy detection threshold of $100\ \mathrm{mJ}$ and did not detect any laser signal during the experiments. Hence, the real reflectivity for input energy $> 100\ \mathrm{J}$ is $> 99\%$, limited by the residual liquid absorption and parasitic reflection on the cell windows interfaces. The complete reflectivity curve is given in Fig.5.13.

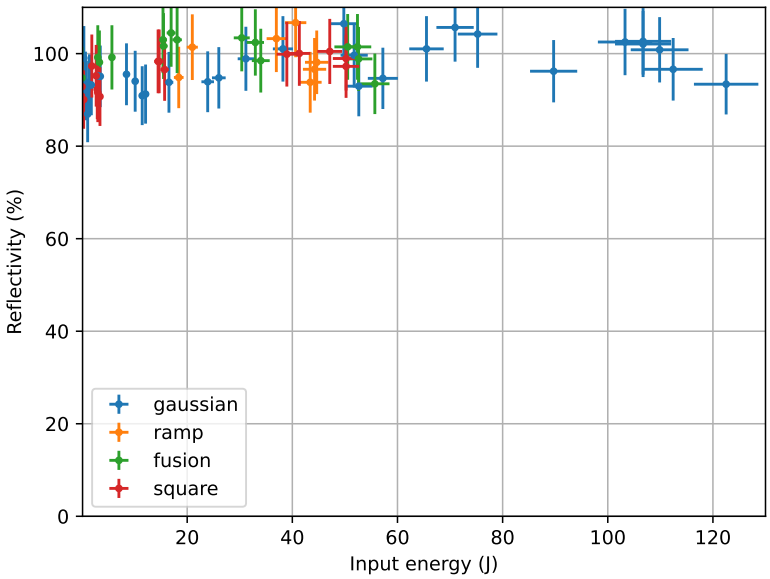

Figure 5.13: Refletivity as a function of input energy for the high energy experiments on the SBS cells.

In this figure, the different temporal profiles present a similarly high reflectivity. The good reflectivity performance demonstrated in Sec.4.3 is maintained over 3 orders of magnitude of energy.

To the best of our knowledge, those results represent the highest energy ever reflected on a phase conjugate mirror [2]. In particular, more than 10

shots were performed at energy levels over 100 J (7 displayed Fig.5.13 due to calorimeters energy range issues) guaranteeing a good stability even in those extreme operation regimes.

5.4.2 . Spatial fidelity

During the experiments, another effect limiting the spatial fidelity is identified in addition to the hot spot occurrence when using L_1. When initiating the SBS effect with a sharp leading edge (or with any temporal pulse shapes that leads to SBS initiation with peak power density near focus spot much higher than SBS threshold power density), the SBS effect can be initiated on several spatial modes [3]. This leads to hot and cold spots appearing in the reflected Stokes beam. One (especially concerning) example is shown in Fig.5.14.

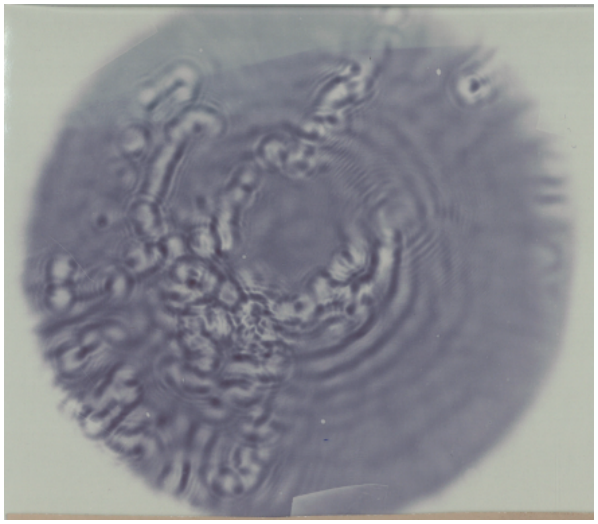

Figure 5.14: Example of a burn paper corresponding to the spatial profiles modulations appearing when initiating the SBS effect with high power density near the waist.

Those modulations were stochastic in their shapes or intensities but the presence or absence of modulations was relatively stable. A configuration with spatial modulations would always lead to spatial modulations in the Stokes beam, whereas a configuration with a clean spatial profile always led to a clean reflected Stokes beam. It was possible to completely eliminate the spatial modulations by reducing the input power at the very start of the pump pulse through temporal shaping. Experimentally this is done by generating a *pedestal* of low energy (< 100 mJ) at the start of the pump temporal profile and lowering this pedestal energy until modulations mitigation.

When increasing the energy, the energy level of this pedestal rises and

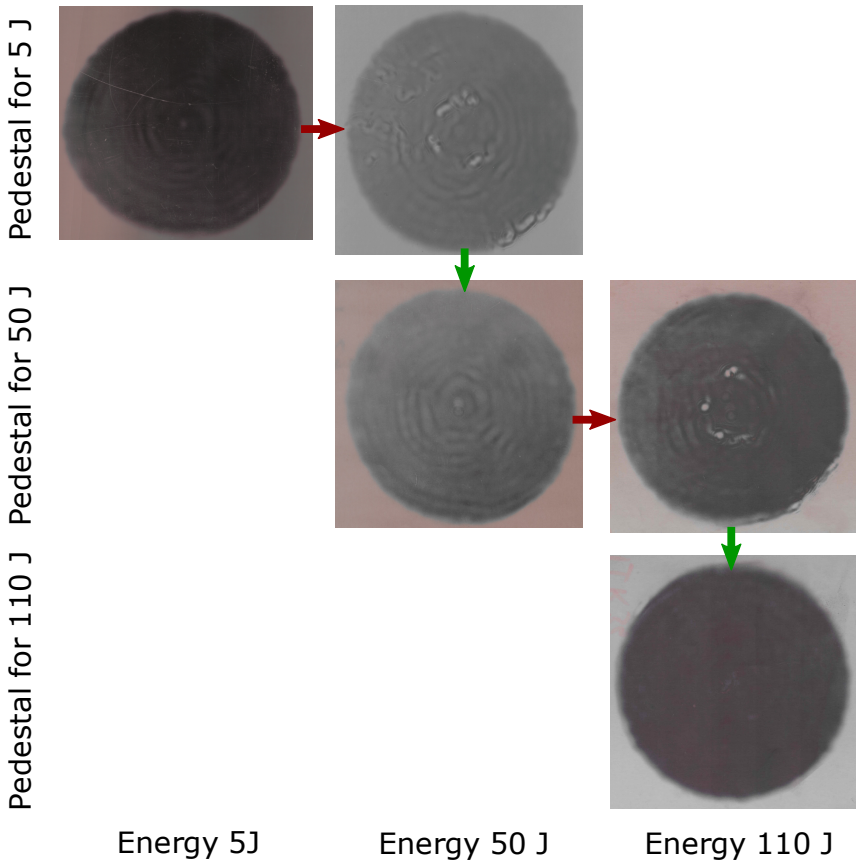

Figure 5.15: Spatial fidelity of SBS reflection as a function of energy and pedestal optimisation. Several burn papers corresponding to different shots are shown. Increasing the input energy up to a certain level without changing the pedestal contrast (red arrows) deteriorates the reflected near field beam quality and requires an adaptation of the pedestal level to near SBS threshold (green arrows) to retrieve good spatial fidelity.

requires being manually decreased again by changing the pulse shape at the SOA seeder's output. An illustration of this process for a gaussian temporal profile with successive energy increases and pedestal optimisations is shown in Fig.5.15. Several optimisation steps have to be done to reach the energy level of 100 J.

Experimentally, the good spatial fidelity is harder to reach with pump pulse shape presenting sharp rise time (in particular the square pulse temporal shape proved to be a challenge to optimise) but is stable from shot to shot once reached. Furthermore, a pedestal for a particular pulse shape can be transferred to another with relative ease for similar energy levels.

Overall, we demonstrate a good spatial fidelity for all temporal pulse shapes and all energy levels, by optimising the pedestal energy level. Thus,

we experimentally confirm that temporal shaping can solve one of the issues regarding spatial fidelity identified in the state of the art.

5.4.3 . Wavefront reversal

To evaluate the performance of the wavefront reversal, we compare the input and reflected beam wavefront. First, the Stokes beam is perfectly retro-reflected and collimated after its second pass in the focusing lens, demonstrating perfect correction of tilts and focus aberrations.

In the usual setups of the state of the art, the compensation capacities of the cell are measured by comparing the beam quality (through the M^2 or, less frequently the Strehl ratio) at laser output, at the end of the double pass, with either the cell or a conventional plano mirror in place of the cell. In our case, since we do not place our beam in the middle of a round-trip amplification, the aberration source is actually the focusing lens L_2. The correction capacities of the cell are measured by comparing the wavefront of the pump and Stokes beam as seen by a wavefront sensor (Phasics, SID4-V). Because of the large beam aperture, the beams have to be reduced by an imaging system. The space constraints and the material available make this imaging system induce a large amount of aberrations that has to be taken into account for the wavefront measurements.

Furthermore, in our case, the pump laser wavefront is unknown and can typically present some low-amplitude aberrations due to slight misalignments, thermal effects or airflow. For the measurements, these aberrations are measured positively for the pump beam (with the fold mirror in place of the cell) and negatively for the Stokes beam. The reliability of our measurement lies in the fact that the dominant spherical aberration source was the focusing lens L_2 and hence the WFE (WaveFront Error) for this particular aberration can be measured with relatively high confidence.

In the setup, the measurement of the wavefront of the pump beam ϕ_{pump} is the sum of the laser wavefront ϕ_{laser} and the imaging system aberrations $\phi_{imaging}$.

$$\phi_{pump} = \phi_{laser} + \phi_{imaging} \tag{5.1}$$

Conversely, the measurement of the Stokes, phase conjugated wavefront is the reversed laser wavefront $-\phi_{laser}$ plus the imaging system aberration $\phi_{imaging}$ plus the WFE of the cell Δ_{cell}.

$$\phi_{Stokes} = -\phi_{laser} + \phi_{imaging} + \Delta_{cell} \tag{5.2}$$

It is convenient to use the pump wavefront as a reference to suppress the contribution of the imaging system. In this case, the residual wavefront measured after reference subtraction is

$$\phi_{residual} = \phi_{Stokes} - \phi_{pump} = -2\phi_{laser} + \Delta_{cell} \tag{5.3}$$

Because the wavefront of the input laser is unknown, but no significant amount of aberration should be present (low repetition rate and low beam spatial modulations in propagation), the dominant aberration at cell entrance is the spherical aberration of the lens L_2. Therefore, this particular aberration coefficient is used to validate the cell correction efficiency. It is also the only component whose contribution is effectively corrected by the double pass and whose aberrations can thus be corrected by the SBS reflection. The WFE is then evaluated only using the residual spherical aberration and comparing it to the theoretical calculated aberrations assuming a complete lack of wavefront reversal. The results are shown in Fig.5.16 where ϕ_{pump}, ϕ_{Stokes}, and $\phi_{residual}$ are shown respectively in blue, red and pink and the expected spherical aberration level is displayed with a dashed line. The WFE for the spherical aberration is found to be extremely low, and the lens aberrations are fully corrected.

It has to be noted that this same experiment when performed with L_1 at low energy gives similar results. The SBS cell is thus able to fully correct extremely high level of spherical aberration wavefront distortion ($18\ \lambda\mathrm{RMS}$ of Zernike spherical aberration using L_1). In the experiments, up to $2\ \lambda\mathrm{RMS}$ of this same aberration were corrected at high energy to guarantee an absence of hot spot occurrence, as detailed previously. This last value corresponds to about $28\ \lambda\mathrm{PV}$ of Seidel spherical aberration and hence to about an order of magnitude above the deformable mirrors operating at this energy level.

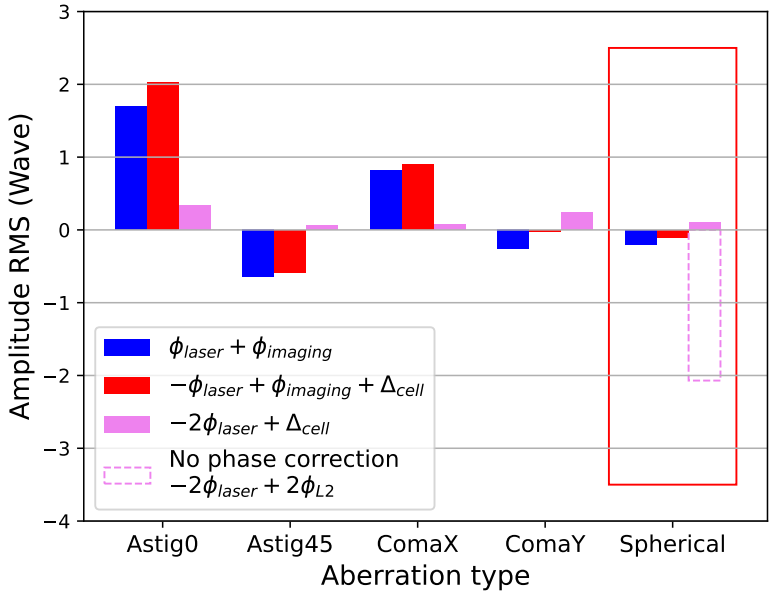

Figure 5.16: Main aberrations amplitude values for: pump beam using the fold mirror instead of the cell (blue), Stokes beam (red) and the residual phase calculated using Eq.5.3. The expected spherical aberration value after a double pass in the L2 lens and without phase reversal is displayed in dashed pink. The first 4 aberration coefficients only show that no significant wavefront perturbations are introduced by the cell during the reflection. The correction capacities of the cell are only visible on the spherical aberration part (red rectangle) where the cell effectively corrects more than $2\ \lambda\mathrm{RMS}$ ($\approx 7\ \lambda$ PV) of Zernike's spherical aberration, corresponding to $\approx 28\ \lambda\mathrm{PV}$ of Seidel spherical aberration.

5.4.4 . Temporal fidelity

As mentioned previously in the reflectivity paragraph, several temporal pulse shapes of interest are investigated to confirm the capacity of the SBS cell to properly conserve arbitrary temporal shapes, even at very high energy level. To this aim, we use the temporal shaping properties of the laser chain to generate arbitrary temporal shapes to be reflected. The development of the temporal shaping scheme for this high energy laser is presented in an article given in AppendixA. As stated previously, all the studied temporal shapes have to be preceded by a pedestal for SBS initiation close to SBS threshold and avoid spatial fidelity degradation.

It is found that initiation at low power was not always enough. Despite a good fidelity being reached, initiation with a single low power pedestal generated an acoustic wave not contrasted enough to reflect the sudden increase once the main part of the pulse reaches the cell. In particular, for the square pulse shape, we had to shape the pump pulse through two

successive pedestals, the first guaranteeing good spatial fidelity and the other avoiding compression. This particular shape was found to be the most difficult to optimise due to the sharp rise time.

The duration and relative intensities of those pedestals depends on both the input temporal shape and the focusing condition (since the aberration level influences the power density inside the cell) and have then to be found experimentally. In Fig.5.17 is shown the effect of the duration of the second pedestal: a pedestal too short leads a residual compression spike, while a pedestal too long leads to the conservation of the pedestal on the reflected temporal shape. On the contrary, a pedestal shaped with the right duration leads to proper conservation of the temporal pulse shape of interest.

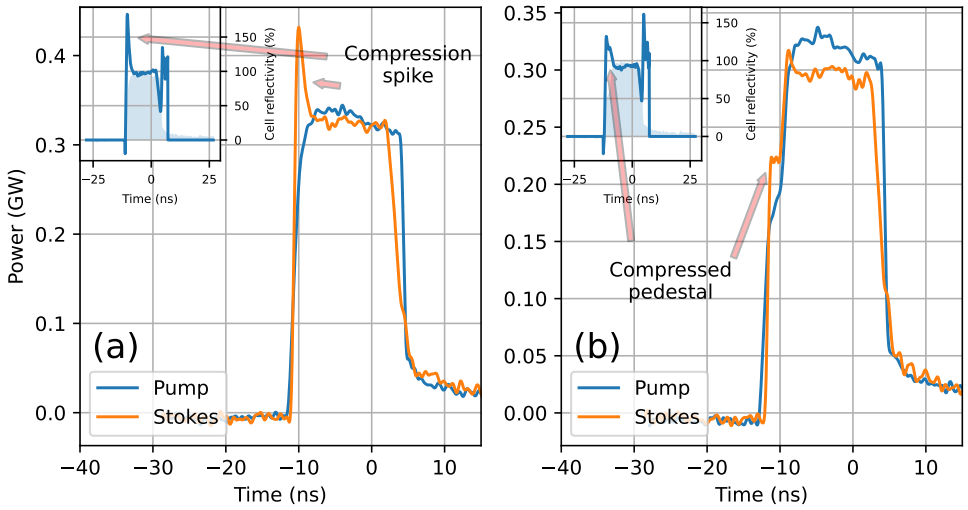

Figure 5.17: Comparison of the temporal fidelity of the SBS cell for square pulses of 5 J energy and unoptimised pedestal duration. a) Too short pedestal duration of 1 ns, the acoustic grating doesn't have time to build-up properly and the main part of the impulsion can penetrate inside the liquid and be compressed during backward propagation. b) Too long pedestal duration (here of 5 ns). This time, the pedestal is so long that its shape is properly conserved (although a residual compression tend to shorten the pedestal duration and increase its intensity). The pedestal can thus be seen in the reflected Stokes pulse.

In the scope of the thesis, two shapes of interest besides the gaussian shape are investigated. The square pulse is chosen since it is the shape most adapted to high-efficiency SHG. In addition, this pulse is the most challenging to reflect using the SBS mirror since it presents a sharp rise time and hence is susceptible to breakdown and ionisation. The second pulse shape chosen is the fusion-like pulse already studied in Chap4. For both of these shapes, the maximum energy sent inside the cell is reduced to about

40 J to avoid any damages to the optical components in case of residual compression spike generated during the SBS reflection. During the experiments, no particular effects that could prevent the energy scale up have been identified. Efficient temporal fidelities for both of these shaped are reached after pedestal optimisation as shown in Fig.5.18.

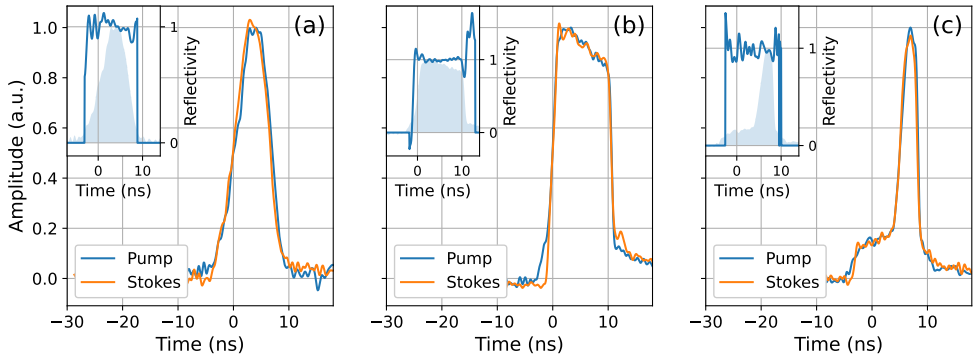

Figure 5.18: Temporal fidelity during high energy SBS reflection. Main graph: comparison of the input (Pump) and output (Stokes) temporal pulse shapes during SBS reflection. The included graphs represent the reflectivity of the PCM along time plotted for pump value above 10% of peak and are all flat over the whole pulse duration. a) Gaussian pulse for input energy of 122 J. b) Square pulse for input energy of 40 J. c) two step "fusion-like" shape for input energy of 40 J. In all of these curve, no sudden increase of the reflectivity along time can be observed, contrary to Fig.5.17

Compared to the low energy first tests performed on the low-energy chain and presented in Sec.4.6.4, no high-intensity rebounds are measured in those high-energy experiments, confirming the hypothesis that the rebounds are caused by the former configuration used and did not correspond to limitations of the nonlinear effect.

Although no long term stability measurements can be performed due to the laser chain repetition limitations, several shots (≈ 5 per configuration) were performed for every temporal shapes without any clear change of behaviour. In addition, it was possible to obtain simultaneously and with good stability proper temporal and spatial fidelity together with high reflectivity and wavefront compensation for every pulse shape studied.

5.5 . Conclusion

The previous theoretical and experimental studies allowed us to design high energy experiments with high confidence. The key points found in the previous experiments: a short focal lens to avoid compression, together with the pedestal introduction to avoid ionisation allowed us to reach the highest input energies ever demonstrated in an SBS cell. In addition to this, we identified during the experiments several detrimental effects not mentioned in the literature:

- A high level of spherical aberration can generate a highly peaked hot spot in the reflected beam. The parametric study of this process would require simulation tools compatible with arbitrary spatial profile description (As the one presented in Sec.2.5). This aberration correction limit was found to be about an order of magnitude above the competing solutions. Further studies are needed to establish a limit for different optical configurations.

- Decreasing the power density inside the cell during SBS initiation through the use of temporal shaping allowed us to avoid the spatial fidelity degradation during the input energy increase.

Using this information, it was possible to reflect energies of $122\ \mathrm{J}$ on the cell, with excellent spatial and temporal fidelity. More than 10 shots were performed with energy above $100\ \mathrm{J}$ and no failed shot was identified. The reflected wavefront was properly phase conjugated and corrected the full aberration of the focusing lens used.

Furthermore, the temporal modulation capacities of the laser chain used allowed us to experimentally confirm the capabilities of the SBS PCM to properly reflect arbitrary temporal pulse shapes, at the cost of having to introduce a sacrificial pedestal before the leading edge of the main part of the impulsion.

No fundamental limits on the input energy were identified other than the input fluence on the cell input window. We now confidently believe phase conjugation to be compatible with multi-kilojoule class lasers and with temporal shaping. The fundamental limit remains the spectrum properties as the SBS effect is still limited to extremely narrow linewidth $\approx 100\ \mathrm{MHz}$ and hence to rise and fall time on the nanosecond time-scale. This restrains the potential uses of SBS for application where sharp rise times are needed such as some experiments of dynamic shock compression. However, the overall performance of the component make its use particularly relevant and convenient for the wavefront correction of high energy laser chains.

Bibliography

The following bibliography contains all the references cited in this chapter. A full bibliography of the thesis is given after the general conclusion. In addition, every bibliography entry is associated with every paragraph it has been referenced in. The corresponding section numbers are indicated at the very end of the entry.

[1] Raphaël Humblot, Joanna De Sousa, Cyril Rapeneau, Sophie Baton, Patrick Audebert, Frédéric Druon, and Loïc Meignien. Semiconductor optical amplifiers as an optical arbitrary waveform generator for high-energy laser systems. *Optics Express*, 32(22):37959–37967, October 2024. Publisher: Optica Publishing Group. 3.4.3, 5.1

[2] Viliam Kmetik, Hidetsugu Yoshida, Hisanori Fujita, Masahiro Nakatsuka, and Tatsuhiko Yamanaka. Very high energy SBS phase conjugation and pulse compression in fluorocarbon liquids. In *Advanced High-Power Lasers*, volume 3889, pages 818–826. SPIE, April 2000. 3.1, 3.1, 3.2, 3.3, 3.1.3, 3.4, 3.3.1, 5.4.1

[3] C. Brent Dane, William A. Neuman, and Lloyd A. Hackel. Pulse-shape dependence of stimulated-Brillouin-scattering phase-conjugation fidelity for high input energies. *Optics Letters*, 17(18):1271–1273, September 1992. Publisher: Optica Publishing Group. 3.1.2, 4.4, 5.4.2

[4] Raphaël Humblot, Loïc Meignien, Joanna De Sousa, Cyril Rapenaud, Sophie Baton, Frédéric Druon, and Patrick Audebert. Semiconductor optical amplifier used as fibered arbitrary waveform generator for high energy applications. In *High-Brightness Sources and Light-Driven Interactions Congress (2024), paper JTu4A.9*, page JTu4A.9. Optica Publishing Group, March 2024. 3.4.1

Conclusion

This thesis is the synthesis of a research work performed conjointly between *LULI*, *Laboratoires Charles Fabry* and Amplitude laser group. The studies aimed to develop and make compatible SBS mirrors with high-average power, high-energy laser sources. In particular, two kinds of lasers were identified that could benefit from the development of SBS-PCM. Firstly, "high-energy, high-repetition-rate" lasers with energy $> 10\,\mathrm{J}$ and average power $> 1\,\mathrm{kW}$, and secondly "very high energy" lasers of the kilojoule class and above.

To this aim, we first studied the theory of the SBS effect and presented the formalism of the nonlinear effect. In the second part, several numerical models of increasing complexity (and accuracy) were developed and used to understand the dynamics of the nonlinear interaction. Those simulation results were used to find optical configurations that offered good fidelity during reflection. In particular, the interaction distance inside the liquid, dependent on the focal length, was identified as a crucial property that could deform the temporal pulse shape. A long focal length can in certain cases lead to compression of the pump pulse and optical damage to the components of the setup.

In a third part, we described the state of the art of existing SBS-PCM. We found that because of the temporal compression phenomenon presented above, the focal lens used in phase conjugation experiments were always relatively short ($150\,\mathrm{mm}$ to $300\,\mathrm{mm}$). This led to major issues during the energy increase as the power density near the focus point before SBS initiation led to ionization of the liquid used for the experiments. To this aim, we offer the innovative solution of using temporal shaping to reduce the input power before reaching SBS steady state. This additional step prevents liquid ionization even for higher input energy as the main part of the pulse cannot propagate to the tightly focused region, near focus spot. The study of the state of the art as well as the numerical simulations allowed the different entities involved in the thesis to establish experimental goals for the research that are reminded here:

- Investigate the limits of the SBS-PCM in terms of aberration correction capacities.
- Investigate the capacity for the SBS cell to become compatible with arbitrary temporal shaping solutions, required for a large range of applications.
- Confirm the fidelity of the reflection properties over long period of

time, and in particular asses the complete absence of *rogue waves* over several hundreds of thousands of shots.

- Improve the energy load of the components to make SBS-PCMs compatible with kilojoule class lasers.

To this aim, we developed and presented two separate test-beds to investigate the mirror properties. On the contrary to state-of-the-art studies, we investigated the cells' behaviour while placed at the output of a laser system to better control and understand the individual contribution of the SBS reflection. Each of the test beds was adapted to particular objectives: a relatively low energy laser (≈ 5 J) with high repetition rate was developed for the preliminary studies and the stability objectives while experiments at LULI's HERA laser chain were dedicated to the energy scale-up. Then, the experiments on the two setups were performed and presented.

The first experiments were performed on the low-energy high repetition rate laser source at *Amplitude laser* on a custom laser source built and dedicated to those experiments. This study confirmed the significant influence of the input pulse temporal profile on the quality of the reflection. A too sharp rise time lead to ionization and degradation of the nonlinear medium, and to a reflectivity drop. Furthermore, a detrimental effect never mentioned in the state of the art was identified: when the temporal profile was not homogeneous over the beam aperture, a stochastic degradation of the spatial fidelity of the PCM was observed, with cold and hot spots appearing in the reflected beam spatial profile. This effect was particularly visible in our setup, at the end of the laser chain, where saturation-induced spatiotemporal inhomogeneities were present. Suppressing this issue led to a reduction of the available energy down to 1 J.

This updated laser chain was then used to confirm all the other properties of the beam. The SBS-PCM was shown able to reflect laser pulses with high efficiencies $> 93\ \%$ and high stability. The spatial profile was properly conserved during the reflection, and it was shown that arbitrary temporal profile conservation was possible, although highly dependent on the focal length used. Spherical aberration and astigmatism were artificially introduced inside the beam to evaluate the cell correction capacities and the cell was able to perfectly correct all the introduced aberrations. Two detrimental effects were identified: Firstly, the higher the input aberration introduced, the lower the wavefront shot to shot stability was, although the resultant stabilities were always within acceptable ranges. Secondly, when introducing very high aberration amount (namely, astigmatism in our case), the spatial fidelity dropped and patterns were visible on the reflected beam. The physical processes in action that lead to the apparition of this second phenomenon is to this day not perfectly understood and requires further

developments on advanced numerical simulation models.

Stability measurements were performed over a million shots and the reflection properties were found to be stable in time, barely reducing the laser stability. In particular, no missed shots were ever identified, and no significant hot spots appeared in the reflected beam. The main difficulty identified was the ionization of the liquid when SBS initiation was performed with too high and too steep pump intensity. In this case, the chemical constitution of the liquid changed, and the ionization threshold was irreversibly reduced, therefore inducing more frequent occurrences of further ionization. Integration of an SBS cell inside a laser within a laser therefore has to be done with care to never ionize the liquid.

This first successful experiments gave us insights for the energy scale-up. We therefore designed the second experimental layout accordingly, with short focal lens and high contrast temporal shaping capability. The high energy led to high beam diameter and hence large aperture, the focusing lens exhibited a high numerical aperture ($F/3$) and induced a large amount of spherical aberration ($\approx 9\ \lambda\mathrm{RMS}$ of spherical aberration). The high spherical aberration level was found to cause the apparition of a hot spot in the centre of the beam. This highlighted, once more, one of the limits of aberration correction of the SBS-PCM: the degradation of spatial fidelity when the input aberration (here, spherical) level is too high. Although this limit is found to be about an order of magnitude above competing wavefront correction systems. To the best of our knowledge, this is the first mention of such phenomenon in the state of the art.

The hot spot was eliminated by changing the focusing lens. This allowed one to increase the energy up to an unprecedented level of $122\ \mathrm{J}$ while conserving the high reflectivity, spatial and temporal fidelity. Several pulse shapes of interest were also properly conserved for the first time, even at very high energy level. This demonstrated the good understanding and design capacity of the physical process in action and unlocked high energy SBS conjugation. Those high energy results increased the maximum energy sent inside the cell by an order of magnitude compared to the state of the art and no fundamental limit on the energy scale up was identified.

Those two experiments removed most of the technical locks preventing the use of SBS-PCMs for high-energy laser systems. Several prospects for better understanding of the remaining parasitic phenomenons are proposed, including the development of simulation models taking into account the full transverse dimension. Next experimental studies should also address the behaviour of such a component under high-power load and the mitigation of the thermal accumulation inside the cell due to the residual absorption of the liquid used. However, some of the solutions developed in this work (low propagation distance, SBS initiation with minimal power with

temporal shaping) already reduce the overall absorbed energy by the cell and hence minimize the thermal load on the cell for a fixed power load. We thus believe that significant improvements compared to state of the art solutions can already be reached by employing the developed solutions. In the scope of the work, no laser source compatible with high energy and high repetition rate was accessible, and those studies could not be performed.

A significant effort of development and industrialization remains to be done to implement the component in a commercial laser system. The requirements for high quality SBS reflection (beam quality, temporal shaping for proper nonlinear initiation, lack of temporal profile inhomogeneities across the beams, ...) indicate that a phase conjugate mirror is not an easy solution to implement and that a system making use of this solution should be properly designed for it. In particular, the nonlinear effects dynamics in action should be understood by the laser designers prior to its implementation.

Furthermore, a whole range of laser systems are unable to make use of SBS phase conjugation because of its intrinsic limitations. Broadening the acceptable linewidth to make use of SBS for shorter pulses seems to this date to represent a difficult challenge. Some studies of the accessible nonlinear medium could possibly improve the current limits by an order of magnitude (at most), but the application of SBS to proper pico-second class lasers would require extensive research. Furthermore, making a laser utilizing SBS for phase conjugation inherently makes the laser inoperable for experiments where SBS is an issue for the laser application (laser plasma instabilities, transverse SBS in large optics,...), hence, reducing the application range of the component.

However, a laser system implementing a proper phase conjugation mirror definitely has an edge over competing solutions as the simplicity of the alignment, the overall cost, and the reliability of the component over unusual operating condition (varying repetition rate) remains unmatched. Industrial laser systems requiring one-demand shots at high (but varying) repetition rate, or over-cadencing without warm-up time, can definitely drastically improve their performances making use of it.

In conclusion, SBS-PCMs are found to be an excellent alternative to deformable mirrors for a large range of nanosecond laser systems, albeit requiring narrow bandwidth and relatively slow rise time (of about $1\ \mathrm{ns}$) to properly function. They particularly shine for systems that require varying repetition rate and provide an ease of alignment, maintenance and reduced cost compared to deformable mirrors, making them an attractive solution for industrials and laboratories alike.

Bibliography

The following bibliography contains all the references cited in this chapter. A full bibliography of the thesis is given after the general conclusion. In addition, every bibliography entry is associated with every paragraph it has been referenced in. The corresponding section numbers are indicated at the very end of the entry.

[1] Masahiro Nakatsuka and Hidetugu Yoshida. Wavefront compensator by SBS-PCM in power photonics. *Journal of the Communications Reasearch Laboratory*, 46(3):471–478, 1999. 3.1, 3.1, 3.2, 3.3, 3.4

[2] Vladimyros Devrelis. *Fidelity of optical phase conjugation using stimulated brillouin scattering*. PhD Thesis, The University of Adelaide, 1997.

[3] Amnon Yariv. *Quantum electronics*. Wiley, New York, 1989. 1.2

[4] F T Arecchi and E O Schulz-Dubois. *Laser Handbook. Volume 2*. January 1972.

[5] Robert W. Boyd. *Nonlinear Optics, Third Edition*. Academic Press, Inc., USA, 3rd edition, 2008. 1.1

[6] Anthony Scopatz and Kathryn Huff. *Effective Computation in Physics*. O'reilly media inc edition, June 2015. ISBN: 9781491901533.

[7] Govind P. Agrawal. *Nonlinear Fiber Optics*. Academic Press, 2013. 1.1, 1.2.1

[8] Léon Brillouin. Diffusion de la lumière et des rayons X par un corps transparent homogène - Influence de l'agitation thermique. *Annales de Physique*, 9(17):88–122, 1922. Number: 17 Publisher: EDP Sciences. 1.2

[9] Gil Bashan, H. Hagai Diamandi, Elad Zehavi, Kavita Sharma, Yosef London, and Avi Zadok. A forward Brillouin fibre laser. *Nature Communications*, 13(1):3554, June 2022. Number: 1 Publisher: Nature Publishing Group.

[10] Toshio Kurashima, Tsuneo Horiguchi, and Mitsuhiro Tateda. Distributed-temperature sensing using stimulated Brillouin scattering in optical silica fibers. *Optics Letters*, 15(18):1038–1040, September 1990. Publisher: Optica Publishing Group. 1.6

[11] D. W. Forslund, J. M. Kindel, and E. L. Lindman. Theory of stimulated scattering processes in laser irradiated-plasmas. *The Physics of Fluids*, 18(8):1002–1016, August 1975. 1.6

[12] E. Wolf and W. H. Carter. Comments on the theory of phase-conjugated waves. *Optics Communications*, 40(6):397–400, February 1982.

[13] Raphaël Humblot, Loïc Meignien, Joanna De Sousa, Cyril Rapenaud, Sophie Baton, Frédéric Druon, and Patrick Audebert. Semiconductor optical amplifier used as fibered arbitrary waveform generator for high energy applications. In *High-Brightness Sources and Light-Driven Interactions Congress (2024), paper JTu4A.9*, page JTu4A.9. Optica Publishing Group, March 2024. 3.4.1

[14] Tadashi Ikegawa, Takashi Sekine, and Ryo Yasuhara. Upgrade of Nd:glass zigzag slab laser by a wavefront compensation and second harmonic generation. *Annual progress report*, 2007, February 2008. 3.1, 3.1, 3.2, 3.3, 3.4

[15] B. Zel'Dovich, V.I. Popovichev, and V.V. Ragul'skii. Connection Between the Wave Fronts of the Reflected and Exciting Light in Stimulated Mandel'shtem-Brillouin Scattering. *JETP Letters*, 15:109–112, January 1972. 3.1

[16] Raphaël Humblot, Joanna De Sousa, Cyril Rapeneau, Sophie Baton, Patrick Audebert, Frédéric Druon, and Loïc Meignien. Semiconductor optical amplifiers as an optical arbitrary waveform generator for high-energy laser systems. *Optics Express*, 32(22):37959–37967, October 2024. Publisher: Optica Publishing Group. 3.4.3, 5.1

[17] Hang Yuan, Yulei Wang, Chengyu Zhu, Zhenxing Zheng, and Zhiwei Lu. Investigation of sub-phonon lifetime pulse amplification in active frequency matching stimulated Brillouin scattering. *Optics Express*, 27(12):16661–16670, June 2019. Publisher: Optica Publishing Group.

[18] Hongli Wang, Seongwoo Cha, Hong Jin Kong, Yulei Wang, and Zhiwei Lu. Sub-nanosecond stimulated Brillouin scattering pulse compression using HT270 for kHz repetition rate operation. *Optics Express*, 27(21):29789–29802, October 2019. Publisher: Optica Publishing Group. 3.3.1

[19] Hongli Wang, Seongwoo Cha, Hong Jin Kong, Yulei Wang, and Zhiwei Lu. Rotating off-centered lens in SBS phase conjugation mirror for high-repetition-rate operation. *Optics Express*, 27(7):9895–9905, April 2019. Publisher: Optica Publishing Group. 3.2

[20] Zhaohong Liu, Yulei Wang, Zhenxu Bai, Yirui Wang, Duo Jin, Hongli Wang, Hang Yuan, Dianyang Lin, and Zhiwei Lu. Pulse compression to one-tenth of phonon lifetime using quasi-steady-state stimulated Brillouin scattering. *Optics Express*, 26(18):23051–23060, September 2018. Publisher: Optica Publishing Group.

[21] Zhijun Kang, Zhongwei Fan, Yutao Huang, Hongbo Zhang, Wenqi Ge, Mingshan Li, Xiaochao Yan, and Guoxin Zhang. High-repetition-rate, high-pulse-energy, and high-beam-quality laser system using an ultraclean closed-type SBS-PCM. *Optics Express*, 26(6):6560–6571, March 2018. Publisher: Optica Publishing Group. 3.1, 3.1, 3.2, 3.3, 3.4, 3.2, 3.3.2, 3.3.3

[22] C. Brent Dane, William A. Neuman, and Lloyd A. Hackel. Pulse-shape dependence of stimulated-Brillouin-scattering phase-conjugation fidelity for high input energies. *Optics Letters*, 17(18):1271–1273, September 1992. Publisher: Optica Publishing Group. 3.1.2, 4.4, 5.4.2

[23] Viliam Kmetik, Henryk Fiedorowicz, Alexander A. Andreev, Klaus J. Witte, Hiroyuki Daido, Hisanori Fujita, Masahiro Nakatsuka, and Tatsuhiko Yamanaka. Reliable stimulated Brillouin scattering compression of Nd:YAG laser pulses with liquid fluorocarbon for long-time operation at 10 Hz. *Applied Optics*, 37(30):7085–7090, October 1998. Publisher: Optica Publishing Group. 2.3.4

[24] A. A. Kuzmin, E. A. Khazanov, O. V. Kulagin, and A. A. Shaykin. Neodymium glass laser with a phase conjugate mirror producing 220 J pulses at 0.02 Hz repetition rate. *Optics Express*, 22(17):20842–20855, August 2014. Publisher: Optica Publishing Group. 3.1, 3.1, 3.2, 3.3, 3.1.3, 3.4

[25] L. P. Schelonka and C. M. Clayton. Effect of focal intensity on stimulated-Brillouin-scattering reflectivity and fidelity. *Optics Letters*, 13(1):42–44, January 1988. Publisher: Optica Publishing Group. 4.4, 4.5

[26] Xiaozhen Xu, Chengyong Feng, and Jean-Claude Diels. Optimizing sub-ns pulse compression for high energy application. *Optics Express*, 22(11):13904–13915, June 2014. Publisher: Optica Publishing Group. 3.2

[27] Hidetsugu Yoshida, Takaki Hatae, Hisanori Fujita, Masahiro Nakatsuka, and Shigeru Kitamura. A high-energy 160-ps pulse generation by stimulated Brillouin scattering from heavy fluorocarbon liquid at 1064 nm wavelength. *Optics Express*, 17(16):13654–13662, August 2009. Publisher: Optica Publishing Group. 2.3.4

[28] Hidetsugu Yoshida, Villiam Kmetik, Hisanori Fujita, Masahiro Nakatsuka, Tatsuhiko Yamanaka, and Kunio Yoshida. Heavy fluorocarbon liquids for a phase-conjugated stimulated Brillouin scattering mirror. *Applied Optics*, 36(16):3739–3744, June 1997. Publisher: Optica Publishing Group.

[29] Jisi Qiu, Xiongxin Tang, Zhongwei Fan, and Haocheng Wang. 200 Hz repetition frequency joule-level high beam quality Nd:YAG nanosecond

laser. *Optics Communications*, 368:68–72, June 2016. 3.1, 3.1, 3.2, 3.3, 3.4, 3.3.1

[30] Zhenxu Bai, Hang Yuan, Zhaohong Liu, Pengbai Xu, Qilin Gao, Robert J. Williams, Ondrej Kitzler, Richard P. Mildren, Yulei Wang, and Zhiwei Lu. Stimulated Brillouin scattering materials, experimental design and applications: A review. *Optical Materials*, 75:626–645, January 2018. 3.3.1, 3.4.1

[31] Xiongxin Tang, Jisi Qiu, Zhongwei Fan, Haocheng Wang, Hao Liu, Yueliang Liu, and Zhijun Kang. Experimental study on SBS-PCM at 200 Hz repetition rate pumped with joule-level energy. *Optical Materials*, 67:64–69, May 2017. 3.1, 3.1, 3.1.1, 3.2, 3.3, 3.4

[32] Jacques Luce, Gerard Deschaseaux, and Claude Rouyer. Wide square flat top mode discrimination in a regenerative amplifier. In *2006 Conference on Lasers and Electro-Optics and 2006 Quantum Electronics and Laser Science Conference*, pages 1–2, May 2006. ISSN: 2160-9004. 4.4.2

[33] H. Yoshida, V. Kmetik, H. Fujita, K. Yoshida, T. Yamanaka, and S. Nakai. High performance of phase conjugated stimulated Brillouin scattering mirror based on high purity liquid heavy fluorocarbons. *AIP Conference Proceedings*, 369(1):1004–1008, May 1996. 3.1, 3.1, 3.2, 3.3, 3.1.3, 3.4, 3.3.2, 3.3.2, 4.3.1

[34] T. Hatae, O. Naito, M. Nakatsuka, and H. Yoshida. Applications of phase conjugate mirror to Thomson scattering diagnostics (invited). *Review of Scientific Instruments*, 77(10):10E508, September 2006. 3.1, 3.1, 3.2, 3.3, 3.4

[35] Lee M. Frantz and John S. Nodvik. Theory of Pulse Propagation in a Laser Amplifier. *Journal of Applied Physics*, 34(8):2346–2349, August 1963. 3.2, 3.4.1, 4.2, 4.4.2

[36] R. Y. Chiao, C. H. Townes, and B. P. Stoicheff. Stimulated Brillouin Scattering and Coherent Generation of Intense Hypersonic Waves. *Physical Review Letters*, 12(21):592–595, May 1964. Publisher: American Physical Society. 1.2, 3.1

[37] E. Garmire and C. H. Townes. Stimulated Brillouin Scattering in liquids. *Applied Physics Letters*, 5(4):84–86, August 1964. 3.1

[38] M. Maier, W. Rother, and W. Kaiser. Time-resolved measurements of Stimulated Brillouin Scattering. *Applied Physics Letters*, 10(3):80–82, February 1967. 1.3.4

[39] D. Pohl, M. Maier, and W. Kaiser. Phonon Lifetimes Measured in Amplifiers for Brillouin Radiation. *Physical Review Letters*, 20(8):366–368, February 1968. Publisher: American Physical Society.

[40] D. Pohl and W. Kaiser. Time-Resolved Investigations of Stimulated Brillouin Scattering in Transparent and Absorbing Media: Determination of Phonon Lifetimes. *Physical Review B*, 1(1):31–43, January 1970. Publisher: American Physical Society.

[41] K. O. Hill, B. S. Kawasaki, and D. C. Johnson. CW Brillouin laser. *Optics Communications*, 18(1):52–53, July 1976.

[42] David T. Hon. Pulse compression by stimulated Brillouin scattering. *Optics Letters*, 5(12):516–518, December 1980. Publisher: Optica Publishing Group.

[43] Boris Ya. Zel'dovich, Nikolai F. Pilipetsky, and Vladimir V. Shkunov. Introduction to Optical Phase Conjugation. In Boris Ya. Zel'dovich, Nikolai F. Pilipetsky, and Vladimir V. Shkunov, editors, *Principles of Phase Conjugation*, pages 1–24. Springer, Berlin, Heidelberg, 1985. 1.3.2

[44] G. Valley. A review of stimulated Brillouin scattering excited with a broad-band pump laser. *IEEE Journal of Quantum Electronics*, 22(5):704–712, May 1986. Conference Name: IEEE Journal of Quantum Electronics.

[45] J. M. Eggleston and M. J. Kushner. Stimulated Brillouin scattering parasitics in large optical windows. *Optics Letters*, 12(6):410–412, June 1987. Publisher: Optica Publishing Group.

[46] J. R. Murray, J. Ray Smith, R. B. Ehrlich, D. T. Kyrazis, C. E. Thompson, T. L. Weiland, and R. B. Wilcox. Experimental observation and suppression of transverse stimulated Brillouin scattering in large optical components. *JOSA B*, 6(12):2402–2411, December 1989. Publisher: Optica Publishing Group. 1.6

[47] J. R. Smith, J. R. Murray, D. T. Kyrazis, R. B. Wilcox, T. L. Weiland, R. B. Ehrlich, C. E. Thompson, R. B. Engle, and A. E. Brown. Acoustic Damage To Large-Aperture Optics. In *Mirrors and Windows for High Power/High Energy Laser Systems*, volume 1047, pages 219–225. SPIE, July 1989.

[48] Robert W. Boyd, Kazimierz Rzaewski, and Paul Narum. Noise initiation of stimulated Brillouin scattering. *Physical Review A*, 42(9):5514–5521, November 1990. Publisher: American Physical Society. 1.2.3

[49] John J. Ottusch and David A. Rockwell. Stimulated Brillouin scattering phase conjugation fidelity fluctuations. In *Conference on Lasers and*

Electro-Optics (1991), paper CTuW23, page CTuW23. Optica Publishing Group, May 1991. 4.4

[50] S. P. Smith, F. Zarinetchi, and S. Ezekiel. Narrow-linewidth stimulated Brillouin fiber laser and applications. *Optics Letters*, 16(6):393–395, March 1991. Publisher: Optica Publishing Group. 1.6

[51] Raijun Chu, Morton Kanefsky, and Joel Falk. Numerical study of transient stimulated Brillouin scattering. *Journal of Applied Physics*, 71(10):4653–4658, May 1992.

[52] Metin S. Mangir and David A. Rockwell. 4.5-J Brillouin phase-conjugate mirror producing excellent near- and far-field fidelity. *JOSA B*, 10(8):1396–1400, August 1993. Publisher: Optica Publishing Group. 3.1, 3.1, 3.2, 3.3, 3.4

[53] Jerome M. Auerbach and Victor P. Karpenko. Serrated-aperture apodizers for high-energy laser systems. *Applied Optics*, 33(15):3179–3183, May 1994. Publisher: Optica Publishing Group. 3.4.2, 4.16

[54] James R. Leger, Diana Chen, and Kevin Dai. High modal discrimination in a Nd:YAG laser resonator with internal phase gratings. *Optics Letters*, 19(23):1976–1978, December 1994. Publisher: Optica Publishing Group. 4.4.2

[55] Nikolay Andreev, Oleg P. Kulagin, Oleg V. Palashov, Guerman A. Pasmanik, and Vladimir Rodchenkov. SBS of repetitively pulsed radiation and possibility of increasing the pump average power. In *Solid State Lasers for Application to Inertial Confinement Fusion (ICF)*, volume 2633, pages 476–493. SPIE, December 1995. 3.1, 3.3.2, 4.3.1

[56] C.B. Dane, L.E. Zapata, W.A. Neuman, M.A. Norton, and L.A. Hackel. Design and operation of a 150 W near diffraction-limited laser amplifier with SBS wavefront correction. *IEEE Journal of Quantum Electronics*, 31(1):148–163, January 1995. Conference Name: IEEE Journal of Quantum Electronics. 3.1, 3.1, 3.2, 3.3, 3.1.2, 3.4

[57] R.J. St. Pierre, D.W. Mordaunt, H. Injeyan, J.G. Berg, R.C. Hilyard, M.E. Weber, M.G. Wickham, G.M. Harpole, and R. Senn. Diode array pumped kilowatt laser. *IEEE Journal of Selected Topics in Quantum Electronics*, 3(1):53–58, February 1997. Conference Name: IEEE Journal of Selected Topics in Quantum Electronics. 3.1, 3.1, 3.2, 3.3, 3.4

[58] Shahraam Afshaarvahid, Vladimyros Devrelis, and Jesper Munch. Nature of intensity and phase modulations in stimulated Brillouin scattering. *Physical Review A*, 57(5):3961–3971, May 1998. Publisher: American Physical Society. 2.3.4

[59] Andrew J. Schmitt and Bedros B. Afeyan. Time-dependent filamentation and stimulated Brillouin forward scattering in inertial confinement fusion plasmas. *Physics of Plasmas*, 5(2):503–517, February 1998. 1.6

[60] Li Yu, Meichun Huang, Mouzhi Chen, Wenzhong Chen, Wenda Huang, and Zhizhong Zhu. Quasi-discrete Hankel transform. *Optics Letters*, 23(6):409–411, March 1998. Publisher: Optica Publishing Group.

[61] Viliam Kmetik, Hidetsugu Yoshida, Hisanori Fujita, Masahiro Nakatsuka, and Tatsuhiko Yamanaka. Very high energy SBS phase conjugation and pulse compression in fluorocarbon liquids. In *Advanced High-Power Lasers*, volume 3889, pages 818–826. SPIE, April 2000. 3.1, 3.1, 3.2, 3.3, 3.1.3, 3.4, 3.3.1, 5.4.1

[62] Shahraam Afshaarvahid and Jesper Munch. A transient, three-dimensional model of stimulated brillouin scattering. *Journal of Nonlinear Optical Physics & Materials*, 10(01):1–27, March 2001. Publisher: World Scientific Publishing Co. 2.1

[63] C. Brent Dane and Lloyd A. Hackel. High-Pulse-Energy Phase Conjugated Laser System. In *Phase Conjugate Laser Optics*, pages 147–204. John Wiley & Sons, Ltd, john wiley & sons edition, 2003.

[64] Axel Heuer and Ralf Menzel. Principles of Phase Conjugating Brillouin Mirrors. In *Phase Conjugate Laser Optics*, pages 19–62. John Wiley & Sons, Ltd, john wiley & sons, ltd edition, 2003. 2.1, 2.3.2, 2.7

[65] Manuel Guizar-Sicairos and Julio C. Gutiérrez-Vega. Computation of quasi-discrete Hankel transforms of integer order for propagating optical wave fields. *JOSA A*, 21(1):53–58, January 2004. Publisher: Optica Publishing Group. 2.5.2, 2.5.2

[66] Takaki Hatae, Masahiro Nakatsuka, and Hidetsugu Yoshida. Improvement of Thomson Scattering Diagnostics Using Stimulated-Brillouin-Scattering-Based Phase Conjugate Mirrors. *Journal of Plasma and Fusion Research*, 80(10):870–882, 2004. 3.1, 3.1, 3.2, 3.3, 3.4, 3.3.1

[67] A. Einstein. Zur Elektrodynamik bewegter Körper [AdP 17, 891 (1905)]. *Annalen der Physik*, 517(S1):194–224, 2005. 3.3.3

[68] Hidetsugu Yoshida, Hisanori Fujita, Masahiro Nakatsuka, Tetsuji Ueda, and Akira Fujinoki. Compact Temporal-Pulse-Compressor Used in Fused-Silica Glass at 1064 nm Wavelength. *Japanese Journal of Applied Physics*, 46(1L):L80, January 2007. Publisher: IOP Publishing. 3.3.1

[69] W. L. J. Hasi, Z. W. Lu, S. Gong, S. J. Liu, Q. Li, and W. M. He. Investigation of stimulated Brillouin scattering media perfluoro-compound and perfluoropolyether with a low absorption coefficient and high power-load ability. *Applied Optics*, 47(7):1010–1014, March 2008. Publisher: Optica Publishing Group. 3.3.1

[70] M. Ostermeyer, H. J. Kong, V. I. Kovalev, R. G. Harrison, A. A. Fotiadi, P. Mégret, M. Kalal, O. Slezak, J. W. Yoon, J. S. Shin, D. H. Beak, S. K. Lee, Z. Lü, S. Wang, D. Lin, J. C. Knight, N. E. Kotova, A. Sträßer, A. Scheikh-Obeid, T. Riesbeck, S. Meister, H. J. Eichler, Y. Wang, W. He, H. Yoshida, H. Fujita, M. Nakatsuka, T. Hatae, H. Park, C. Lim, T. Omatsu, K. Nawata, N. Shiba, O. L. Antipov, M. S. Kuznetsov, and N. G. Zakharov. Trends in stimulated Brillouin scattering and optical phase conjugation. *Laser and Particle Beams*, 26(3):297–362, September 2008. 2.3.4

[71] Frank Wu, Anatoliy Khizhnyak, and Vladimir Markov. High-reflectivity SBS phase conjugate mirror. In *Nonlinear Frequency Generation and Conversion: Materials, Devices, and Applications VIII*, volume 7197, pages 317–323. SPIE, February 2009. 3.1, 3.1, 3.2, 3.3, 3.4

[72] Hong Jin Kong, Seong Ku Lee, Jin Woo Yoon, Jae Sung Shin, Sangwoo Park, Hong Jin Kong, Seong Ku Lee, Jin Woo Yoon, Jae Sung Shin, and Sangwoo Park. Stimulated Brillouin Scattering Phase Conjugate Mirror and its Application to Coherent Beam Combined Laser System Producing a High Energy, High Power, High Beam Quality, and High Repetition Rate Output. In *Advances in Lasers and Electro Optics*. IntechOpen, intechopen edition, April 2010. 3.1, 3.1, 3.2, 3.3, 3.1.2, 3.4, 3.2, 3.5

[73] Y. L. Wang, Z. W. Lu, Y. Li, P. Wu, X. M. Fan, Z. X. Zheng, and W. M. He. Investigation on high power phase compensation of strong aberrations via stimulated Brillouin scattering. *Applied Physics B*, 99(1):257–261, April 2010. 3.1, 3.1, 3.2, 3.3, 3.4, 3.2

[74] Stefan Behnel, Robert Bradshaw, Craig Citro, Lisandro Dalcin, Dag Sverre Seljebotn, and Kurt Smith. Cython: The Best of Both Worlds. *Computing in Science & Engineering*, 13(2):31–39, March 2011. Conference Name: Computing in Science & Engineering. 2.4.2

[75] A. Couairon, E. Brambilla, T. Corti, D. Majus, O. de J. Ramírez-Góngora, and M. Kolesik. Practitioner's guide to laser pulse propagation models and simulation. *The European Physical Journal Special Topics*, 199(1):5–76, November 2011. 2.5

[76] Christophe Dorrer, Richard Roides, Robert Cuffney, Andrey V. Okishev, Wade A. Bittle, Gregory Balonek, Albert Consentino, Elizabeth Hill, and

Jonathan D. Zuegel. Fiber Front End With Multiple Phase Modulations and High-Bandwidth Pulse Shaping for High-Energy Laser-Beam Smoothing. *IEEE Journal of Selected Topics in Quantum Electronics*, 19(6):219–230, November 2013. Conference Name: IEEE Journal of Selected Topics in Quantum Electronics. 3.4.1

[77] Benjamin J. Eggleton, Christopher G. Poulton, and Ravi Pant. Inducing and harnessing stimulated Brillouin scattering in photonic integrated circuits. *Advances in Optics and Photonics*, 5(4):536–587, December 2013. Publisher: Optica Publishing Group. 1.6

[78] W. L. J. Hasi, Z. Qiao, S. X. Cheng, X. Y. Wang, Z. M. Zhong, Z. X. Zheng, D. Y. Lin, W. M. He, and Z. W. Lu. Characteristics of SBS hundreds picosecond pulse compression and influence of energy on pulse stability in FC-770. *Optics Communications*, 311:375–379, January 2013. 2.3.4

[79] W. L. J. Hasi, X. Y. Wang, S. X. Cheng, Z. M. Zhong, Z. Qiao, Z. X. Zheng, D. Y. Lin, W. M. He, and Z. W. Lu. Research on the compression properties of FC-3283 and FC-770 for generating pulse of hundreds picoseconds. *Laser and Particle Beams*, 31(2):301–305, June 2013.

[80] Erika Eiser. Dynamic Light Scattering. In *Multi Length-Scale Characterisation*, pages 233–282. John Wiley & Sons, Ltd, john wiley & sons, ltd edition, 2014. 3.6, 3.3.3

[81] Yulei Wang, Xuehua Zhu, Zhiwei Lu, and Hengkang Zhang. Self-pumped SBS effect of high-power super-Gaussian-shaped laser pulses. *Laser and Particle Beams*, 34(1):72–79, March 2016.

[82] Zhenxu Bai, Yulei Wang, Zhiwei Lu, Hang Yuan, Zhenxing Zheng, Sensen Li, Yi Chen, Zhaohong Liu, Can Cui, Hongli Wang, and Rui Liu. High Compact, High Quality Single Longitudinal Mode Hundred Picoseconds Laser Based on Stimulated Brillouin Scattering Pulse Compression. *Applied Sciences*, 6(1):29, January 2016. Number: 1 Publisher: Multidisciplinary Digital Publishing Institute. 3.3.2

[83] Yue Gao, Yanjie Wang, Amy Chan, Murray Dawson, and Ben Greene. High average power diode pumped solid state laser. *Laser Physics Letters*, 14(3):035803, February 2017. Publisher: IOP Publishing. 3.1, 3.1, 3.1.1, 3.2, 3.3, 3.4

[84] R. A. Meijer, A. S. Stodolna, K. S. E. Eikema, and S. Witte. High-energy Nd:YAG laser system with arbitrary sub-nanosecond pulse shaping capability. *Optics Letters*, 42(14):2758–2761, July 2017. Publisher: Optica Publishing Group. 3.4.1

[85] Qingsong Feng, Lihua Cao, Zhanjun Liu, Chunyang Zheng, and Xiantu He. Stimulated Brillouin scattering of backward stimulated Raman scattering. *Scientific Reports*, 10(1):3492, February 2020. Publisher: Nature Publishing Group.

[86] Indirect Drive ICF Collaboration. Lawson Criterion for Ignition Exceeded in an Inertial Fusion Experiment. *Physical Review Letters*, 129(7):075001, August 2022. Publisher: American Physical Society. 1.6

[87] Bin Chen, Zhenxu Bai, Yifu Chen, Kun Wang, Can Cui, Yaoyao Qi, Jie Ding, Bingzheng Yan, Yulei Wang, and Zhiwei Lu. Influence of a longitudinal-mode on stimulated Brillouin scattering characteristics in fused silica. *Optics Express*, 31(19):30030–30039, September 2023. Publisher: Optica Publishing Group. 3.3.1

[88] Bin Chen, Zhenxu Bai, Xuanning Hun, Jianping Wang, Can Cui, Yaoyao Qi, Bingzheng Yan, Jie Ding, Kun Wang, Yulei Wang, and Zhiwei Lu. Gain characteristics of stimulated Brillouin scattering in fused silica. *Optics Express*, 31(4):5699–5707, February 2023. Publisher: Optica Publishing Group. 3.3.1

[89] S. Depierreux, D. Pesme, R. Wrobel, D. T. Michel, P.-E. Masson-Laborde, G. Riazuelo, E. Alozy, N. Borisenko, A. Orekhov, M. Casanova, A. Casner, M. Grech, A. Heron, S. Huller, P. Loiseau, C. Meyer, P. Nicolaï, C. Riconda, V. Tikhonchuk, and C. Labaune. Experimental investigation of the interplay between optical and plasma smoothing induced on a laser megajoule beamline. *Physical Review Research*, 5(4):043060, October 2023. Publisher: American Physical Society. 1.6

[90] Yifu Chen, Bowen Tan, Duo Jin, Bin Chen, Zhenxu Bai, Kun Wang, Yulei Wang, and Zhiwei Lü. Characteristics and suppression of beam distortion in a high repetition rate nanosecond stimulated Brillouin scattering phase conjugation mirror. *High Power Laser Science and Engineering*, 12:e20, January 2024. 3.2, 3.3.1, 4.4

[91] Immanuil L. Fabelinskii. *Molecular Scattering of Light*. Springer New York, Boston, MA, 1968. 1.2.3

[92] Norman M. Kroll. Excitation of Hypersonic Vibrations by Means of Photoelastic Coupling of High-Intensity Light Waves to Elastic Waves. *Journal of Applied Physics*, 36(1):34–43, January 1965. 1.2.3, 1.4

[93] Eyal Feigenbaum, Richard A. Sacks, Kathleen P. McCandless, and Brian J. MacGowan. Algorithm for Fourier propagation through the near-focal region. *Applied Optics*, 52(20):5030–5035, July 2013. Publisher: Optica Publishing Group. 2.5.3, 2.5.4

[94] V. I. Talanov. Focusing of Light in Cubic Media. *JETP Letters*, 11(6):303, 1970. 2.5.3, 2.5.4

[95] W. Simmons, J. Hunt, and W. Warren. Light propagation through large laser systems. *IEEE Journal of Quantum Electronics*, 17(9):1727–1744, September 1981. Conference Name: IEEE Journal of Quantum Electronics. 2.5.3, 2.5.4

A - Scientific publications associated with the thesis

Research Article | Vol. 32, No. 22 / 21 Oct 2024 / Optics Express 37959
Optics EXPRESS

Semiconductor optical amplifiers as an optical arbitrary waveform generator for high-energy laser systems

RAPHAËL HUMBLOT,[1,2] JOANNA DE SOUSA,[1] CYRIL RAPENEAU,[1] SOPHIE BATON,[1] PATRICK AUDEBERT,[1] FRÉDÉRIC DRUON,[2] AND LOÏC MEIGNIEN[1,*]

[1] *LULI, CNRS, École Polytechnique, CEA, Sorbonne Université, Institut Polytechnique de Paris, 91128 Palaiseau CEDEX, France*
[2] *Université Paris-Saclay, Institut d'Optique Graduate School, CNRS, Laboratoire Charles Fabry, 91127 Palaiseau, France*
[*] *loic.meignien@ploytechnique.edu*

Abstract: A simple and straightforward technique is presented as a novel temporally controllable front-end for nanosecond very-high energy laser systems. It is based on an original utilization of a semiconductor optical amplifier (SOA) used as an intensity modulator. The essential characteristics of the component are analyzed in order to evaluate potential limitations. Various parameters of interest for standard operation are displayed, demonstrating its usability and its effectiveness. We demonstrate arbitrary and controllable pulse temporal profiles with duration ranging from 1 nanosecond to 100 nanoseconds and a temporal precision of 1.1 ns. A high extinction ratio is also achieved ensuring a modulation contrast up to 53 dB. The SOA is then integrated into an existing operating system in an ultra-compact, reliable all-fibered system. It is used to seed a 2*200 J laser system, exhibiting excellent performance, and validating its usability under operation conditions without any detrimental effects.

1. Introduction

The development of high-energy lasers in the nanosecond regime is a subject of significant interest for numerous scientific and industrial applications. These lasers enable precise energy deposition on targets with high temporal and spatial concentration. Lasers ranging from the 100s of mJ energy level and beyond are used for material treatment processes [1], enhancing metal resistance to deformation and corrosion. Additionally, they are also the most widely used pump source for Ti:Sa femtosecond [2,3] and OPCPA [4,5] laser amplifiers. Laser sources with energy levels ranging from the joule level up to several kilojoules find application in plasma physics and shock physics experiments, as they allow generation of extreme pressure and temperature conditions during short amount of time [6,7]. Recent advancements have shown that combining hundreds of kilojoule class lasers is one of the most promising ways for achieving controllable nuclear fusion by inertial confinement fusion [8].

Laser sources for the aforementioned applications are mainly based on a moderate-energy front end followed by increasing amplifiers (in size and in energy). The temporal properties of the entire chain are usually imposed by its front end. Two classical front-end architectures are typically used: energetic Q-switch lasers or low-energy modulated seeder. Q-switched lasers are the easiest way of achieving high energies with a simple optical configuration and good extraction efficiency. However, the properties of the output laser beam can be hard to control. In particular, the temporal profile of the laser, and with that, the energy deposition through time on target, is largely determined by the cavity geometry, the pumping power, and the gain medium. Several temporal profiles of interest are therefore inaccessible with this kind of design. On the other hand,

#530119 https://doi.org/10.1364/OE.530119
Journal © 2024 Received 14 May 2024; revised 5 Jul 2024; accepted 8 Jul 2024; published 7 Oct 2024

Optics EXPRESS

a low-energy laser impulsion (seed) with tailored properties can be subsequently amplified to reach the desired energy. Most of the properties of the output high energy pulses are then mainly dependent on the seeders and are easily controllable at low energy. In particular, it is possible to control the output pulse temporal profile using several modulation techniques while taking into account the gain saturation compensation in the amplifiers [9]. Despite a higher complexity, the controllable seeders offer more versatility than Q-switched lasers and are often required or preferred for several applications such as dynamic shock compression [10], damage threshold testing [11], laser material processing [12] or diverse parametric study of laser matter interaction and nonlinear effects in the transient regime. Several components and techniques are available in the literature to perform temporal modulation [13–21]. The main characteristics of interest sough after each of these components are the following: The modulation speed of a component defines the pulse shape accuracy and the minimal rise and fall time of the generated temporal shapes. For some applications, the requirements range from a few nanoseconds down to a hundred picosecond. The modulation contrast characterizes the difference between the minimal and maximal power achievable and should be maximized. The components spectral properties are also significant and to be considered since applications can demand either narrow spectrum properties [16], or broader bandwidth. To date, the solution used in most high energy laser facilities consists of acousto-optic modulators (AOM) and electro-optics modulators (EOM) placed in series. AOMs present high contrast (70 dB) with slow modulation time (10 ns) [17,18], while EOMs are able to modulate light in the range of 35 dB with fast modulation time (100 ps). A typical oscillator using those components consists of a CW laser gated by an AOM, generating flat-top pulses of desired duration and high contrast. The light is then further modulated by one or several EOMs to reach the desired temporal shape with high modulation speed and significant contrast. Such systems have been experimentally demonstrated and present outstanding performances in many high-energy laser facilities albeit relatively high complexity and costs [19,20].

Here, we present a novel modulation technique for high energy lasers based on a Semiconductor Optical Amplifier (SOA) [22]. This component is composed of a semiconductor gain medium with anti-reflection coating at both ends. By placing it at the output of a CW laser system, the SOA acts as an amplifier when driven with current above semiconductor threshold and as a high-extinction-ratio absorber when not alimented. Combining those two modes of operation (amplifier and absorber) allows to generate arbitrary temporal pulse shapes with high contrast and address all the described applications with a cost several times lower than state-of-the-art solutions and easy implementation.

2. SOA for gain modulation

In order to use an SOA as seeder in a high energy master oscillator power amplifier system (MOPA), its properties are checked to ensure the absence of detrimental effects during the propagation of the laser pulse in the amplifiers. In this work, the SOA and driver used are a PPL512-SOA-1064 from PicoQuant which integrates an SOA-1060-90-PM-30 DB from Innolume. A schematic of the system as well as a picture of the fiber part of the system is shown in Fig. 1.

Firstly, the spectral properties are checked. In particular, two properties are deemed of significant importance: the spectral bandwidth accessibility of the component and the conservation of spectral purity. On the one hand, a large gain spectral bandwidth is crucial for broad spectrum amplification used for plasma smoothing in fusion experiments [23] or to avoid transversal stimulated Brillouin scattering in large scale optical components [24]. Large spectral bandwidth also allows for amplification of incoherent amplified stimulated emission (ASE) without spectral narrowing or FM-AM conversion. In the case of the SOA, the amplification spectrum bandwidth is measured by direct observation of the unseeded SOA's ASE in an optical spectrum analyzer (MS9740A from Anristu with 0.03 nm resolution bandwidth).

Optics EXPRESS

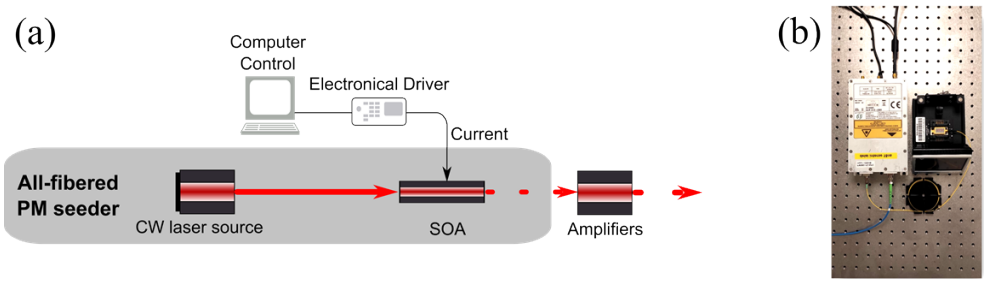

Fig. 1. (a) Schematics of an SOA used as an all-fibered temporal-shaper MOPA seeder. (b) Picture of the compact, integrated all-fibered optical arbitrary waveform generator SOA system used in this experiment. On the right, a distributed feedback narrow-linewidth (DFB) laser diode with 100 kHz linewidth and an SMSR of 45 dB, on the left, an SOA modulator. The optical signal in the seeder system is transmitted by PM980-fibers to be simply injected at the input of the chain (free space injection not shown in the picture)

The spectrum bandwidth is found to be extremely large with a FWHM of 39.2 nm as shown in Fig. 2(a). In particular, the component is compatible with the 1030 nm, 1053 nm and 1064 nm lines and is able to amplify broadband signals with an optical bandwidth well above alternative solutions. This is experimentally confirmed using a pulsed diode generating square pulses with 0.4 nm bandwidth and further modulating it using an SOA. In this case, the output spectrum shows great fidelity with the input (Fig. 2(b)). The SOA is thus able to temporally shape light with conservation of the spectrum across the pulse. While the modulation by the SOA induces dispersion, no particular artifacts in the temporal profile are measured after the shaping of this broadband pulse.

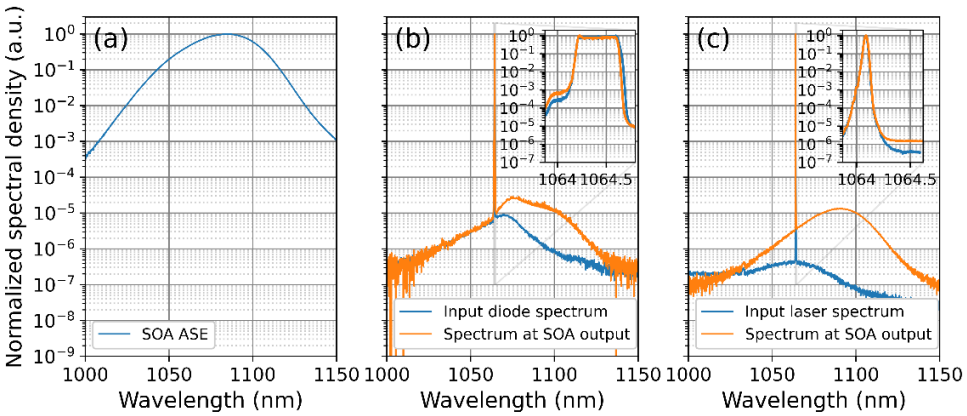

Fig. 2. Normalized spectrum measurements of (a) ASE of the SOA alimented with current of 300 mA. The shift in central wavelength versus current is negligeable (<1 nm over the full current dynamic) compared to the bandwidth of the ASE (b) Pulsed laser diode with a spectrum width of 0.42 nm FWHM at the SOA input and at the SOA output after temporal modulation (c) of the DFB laser at the SOA input and at the SOA output after temporal modulation. Both spectrum widths are below the OSA resolution of 0.03 nm

On the other hand, the conservation of the spectral purity of narrow linewidth cw injection is also important for some applications requiring interferometry. This property is measured using both a RPMC R1064SB0300 PA laser diode with side mode suppression ratio (SMSR) of 45 dB

Optics EXPRESS

and a NP Photonics fiber laser with 66 dB SMSR (shown in Fig. 2(c)). In both cases, the spectrum is measured before and after temporal modulation by the SOA. Albeit a slight degradation of the SMSR ratio of 6 dB, the spectrum remains pure, limited by the spectrometer resolution as shown in Fig. 2(c). The coherence length of the signal at system output is also tested using a custom-build Michelson interferometer and the fringes visibility stayed above 0.95 even with 1 m of optical path difference, making the SOA system compatible with most interferometric applications.

The maximum output power of the seeders is also an important consideration for high energy laser chains seeders. In particular, more input power at the seeder level allows to reduce the total gain needed in the further amplifying stages and generally improves the signal to ASE ratio of the full system. This maximum output power is determined by both the maximum input power and the maximum gain.

Firstly, the input power is limited by the saturation of the absorption of the semiconductor energy bands. While absorption-induced heating in the semiconductor medium could lead to a power acceptance of the order of few hundreds of milliwatts or more, too much input power also leads to the saturation of the absorption and a behavior close to transparency resulting in a loss of modulation contrast, as shown in Fig. 3(a). In this case, a part of the continuous wave (cw) signal starts to leak through the component and the total modulation contrast is drastically reduced. Typical input peak powers are therefore in practice limited to a few milliwatts (10 mW in our use case). Under those conditions, the absorption of the un-alimented SOA reaches 53 dB and the output power at maximum current reaches 20 mW (3 dB gain). In particular, Fig. 3(b) shows that the amplitude of the modulation capacities of the system (from maximum absorption to maximum gain) decrease with input power. The user should therefore make a compromise between the total contrast of the system and the output peak power. On the system presented in this work, an emphasis is placed on the nominal temporal profiling capacities to avoid the amplification of temporal profile artifacts.

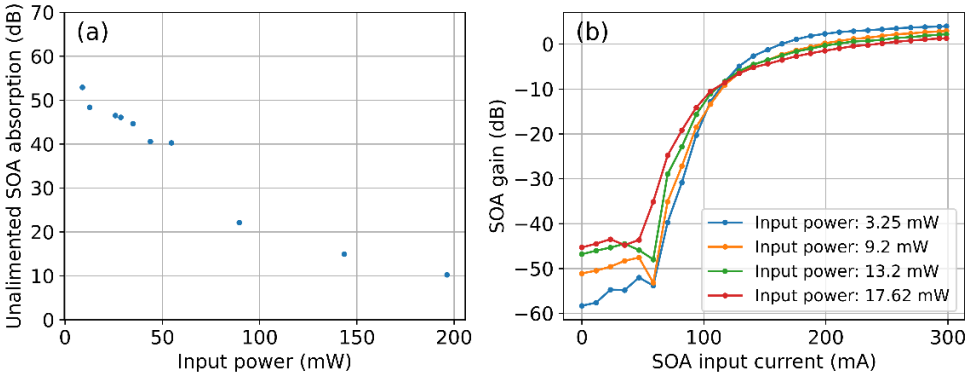

Fig. 3. (a) Maximum absorption of our SOA system. Measurements of the difference between input and output power spectra (absorption) achieved using the OSA with a span of 1 nm and a 30 pm resolution (b) Normalized output power of the SOA as a function of the driving current. The modulation capacity is above 50 dB for input powers below 10 mW and is reduced for higher input power. Input signal: CW-DFB laser diode.

The maximum available gain of the SOA also shows a trade-of. Indeed, to guaranty temporal profile purity the maximum driving current and therefore the maximum gain accessible has to be reduced. This is mainly due to the capacities of the electronic current drivers accessible that presents higher temporal accuracy for lower currents. Figure 4 shows some examples of pulse shaping in this regime with electronic driver limited to peak current of 300 mA corresponding to

Optics EXPRESS

a maximum gain of 3 dB. For alternative priority, higher output peak power using SOA (up to few hundreds of milliwatts) with good conservation of the absorption are also demonstrated by increasing the driving current as shown in Fig. 5, with another SOA and driver system. The total gain is improved to values up to 20 dB and output powers above 300 mW with peak current of 1 A, leading to 60 dB full modulation capacity (absorption + gain) corresponding to the point of the green curve Fig. 5(a). for lowest input power. This increase in gain is done at the expense of artefacts in the temporal profile (Fig. 5(b) and Fig. 5(c)). The total output power can be further improved by increasing the input power, at the cost of the total modulation capacity, both due to a gain discrepancy and absorption discrepancy.

The SOA is capable of acting either as an attenuator or an amplifier depending on the current applied. This can be useful for high-contrast pulse shaping by modulating the current. Its modulation capacities are analyzed, and several typical arbitrary temporal shapes are demonstrated. The jitter between the optical output of the component and an external asynchronous square trigger signal was limited by the electronical driver and measured to be below 66 ps RMS. The temporal resolution of the component is below 1 ns with rise and fall time as low as 1.1 ns in case of square pulses. Shapes such as square, triangle and offseted-exponential are shown in Fig. 4. The main drawback of the system is its low modulation speed compared to EOMs. This limitation is for now caused by the existing electronic drivers, which struggle to provide sharp current rise time with good temporal shape accuracy, but no measurements to find the intrinsic limitation of the SOA have been performed. However, literature from the telecommunication industry let us think going well below this limitation will prove to be difficult [25]. If needed, SOAs could be used conjointly with EOMs for easy access to high contrast and high-speed temporal shaping. The component used in this article is limited to 100 ns by the electronic driver, yet SOAs can generate modulated pulses up to tens of microsecond with nanosecond resolution. In this last case, the main limitation is the heating caused by the average current sent inside the component and the capacities of the electronic driver.

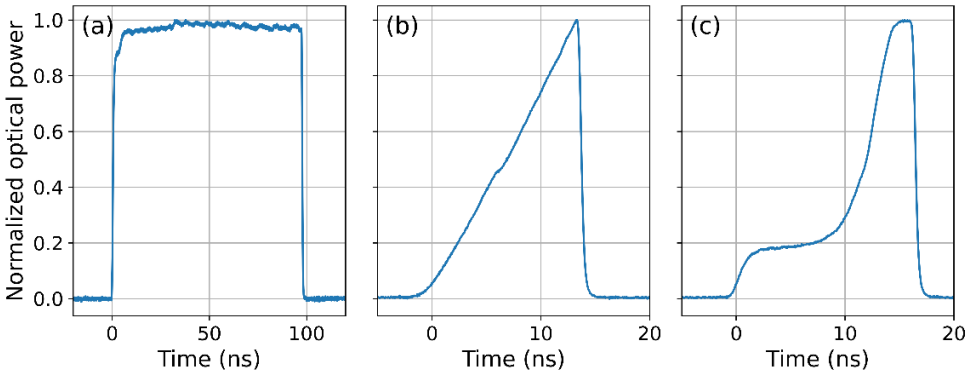

Fig. 4. Examples of temporal shapes generated with SOA modulation system with peak current limited to 100 mW. (a) 100 ns square pulse, (b) 17 ns ramp-shaped pulse and (c) 17 ns offseted-exponential pulse. Temporal shapes averaged over 4 pulses to reduce electronic noise, acquired with a 25 GHz fibered photodiode and a 20 GHz oscilloscope. Small periodic ripple oscillations are visible every 7 ns in the top of the square pulse and the ramp pulse due to residual imperfections in the driver electronical signal.

Considering the spectral properties, temporal shaping capabilities and the peak power accessible, the component is shown to be adapted to high energy laser seeding. We will then present in detail experimental outcomes of a 200 J laser chain employing an SOA as waveform-generator seeder.

Optics EXPRESS

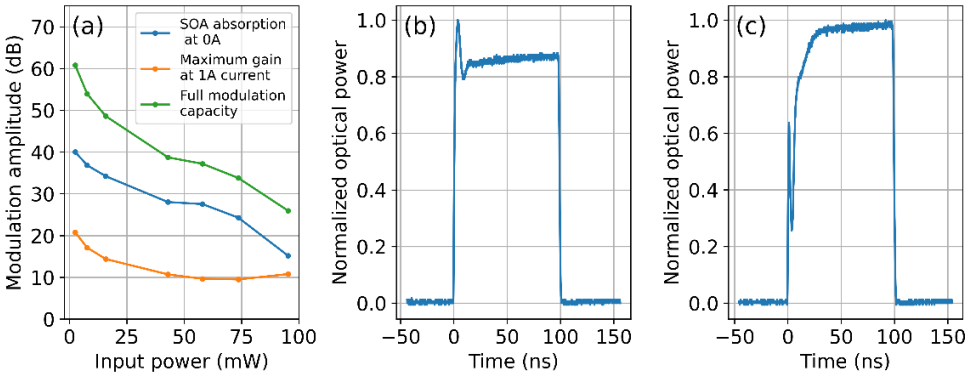

Fig. 5. Results for an SOA driven by a high current square pulse. (a) SOA isolation and gain for high current operation of 1 A. More than 300 mW of output peak power was achieved with 60 dB modulation capacity using an input power of 3 mW. The blue curve represents the same information as shown in Fig. 3(a) for a different SOA component and present the same general shape of the saturation of the absorption (b) Output temporal shape obtained at SOA output for a driving current of 500 mA of 100 ns duration. The optical pulse shape follows the current pulse shape. Command sent to the driver was square (c) Output temporal shape obtained at SOA output for a driving current of 1 A of 100 ns duration. The optical pulse shape follows the current pulse shape.

3. SOA as arbitrary waveform generator seeder in a high-energy laser system

The laser chain on which this apparatus is implemented is a 2*200 J, single-shot shot every 20 min - 1053 nm Nd:Glass laser system. This laser chain, called HERA, is currently operational at the LULI facility in Ecole Polytechnique for conducting high-energy experiments primarily for shock applications. It typically provides squared-shape laser pulses with arbitrary duration from 3 ns to 15 ns and tunable energy. Following the MOPA classical architecture, we simply modified the laser system by replacing the standard seeder by the SOA-based arbitrary waveform generator seeder. As shown in Fig. 6, it is used to inject with low energy the amplifiers of the MOPA chain. The seed pulse is then amplified to millijoule level in a Nd:YLF diode-pumped regenerative amplifier. The amplified pulse then passes through a series of additional single and double pass amplifiers of increasing size to reach the desired level of energy. The laser pulse is split at the middle of the amplification process to generate 2 separate lasers pulses that can be delayed using a delay line placed before the target chamber.

In this laser chain, the SOA is used for both temporal gating and temporal shaping. It is injected by the aforementioned laser diode providing narrow linewidth cw laser radiation. Because of the contrast properties of the SOA, the actual power of the diode is limited to 10 mW to guarantee a good optical contrast before and after the pulse. The output peak power of the fiber system after SOA amplification is therefore 20 mW. The seed pulse is then sent into a regenerative amplifier using a fiber to free space coupler. Because of the cavity length of 8 m, the maximum duration of the input pulses is limited to 17 ns (taking into account the Pockels cell rise and fall time). Since the peak power of the pulses injected in the regenerative amplifier is limited around 20 mW, the maximum seed energy is in our configuration 340 pJ. The regenerative amplifier allows to guarantee and stabilize the output energy at millijoule level without constrain on the input energy and whatever the pulse duration and shape by simply changing the number of passes in the cavity. After extraction, the contrast of the amplifier is further increased by a pulse cleaner Pockels cell removing all the ASE, pre-pulses and post-pulses leaking from the cavity with a 30 dB contrast

Optics EXPRESS

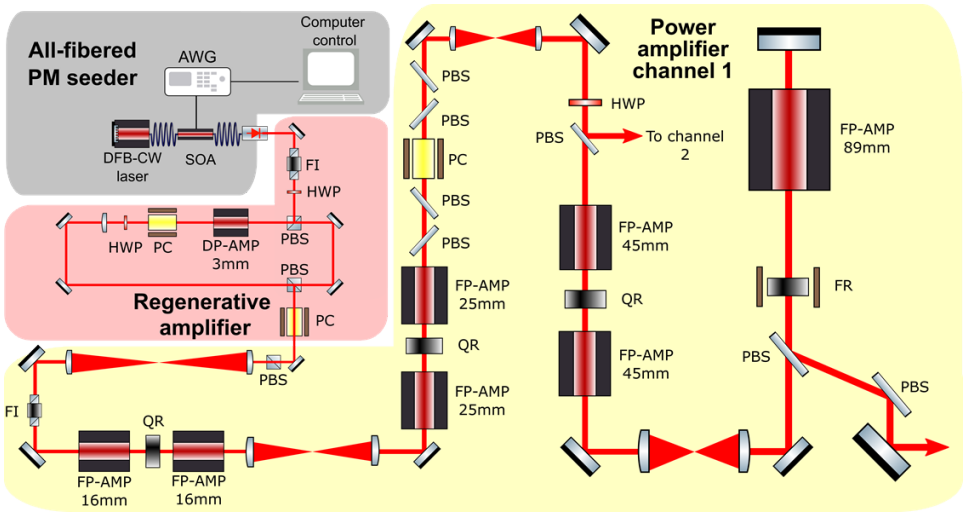

Fig. 6. Schematics of the HERA laser. AWG: Arbitrary current Waveform Generator, DFB-CW laser: DFB laser diode, SOA: Semiconductor Optical Amplifier, FI: Faraday Isolator, HWP: Half-waveplate, PBS: Polarizing Beam Splitter, DP-AMP: Diode-pumped Amplifier, PC: Pockels cell, FP-AMP: Flash-pumped Amplifier, QR: Quartz Rotator, FR: Faraday Rotator

ratio. The pulse energy after extraction and the pulse cleaner reaches 1 mJ with energy stability of 0.7% RMS before injection in the amplifying stages.

The full system reached energies above 2*200 J. The low thermal conductivity of glasses as well as the use of flash pumping reduces the repetition rate to 1 shot per 20 min at laser output. Despite the high saturation fluence of the amplifiers, the temporal saturation in the amplifier is still high. The full square pulse distortion of the system is above 70% and required pre-compensation at seeder level to reach a square pulse at output. A comparison of the input temporal profile and laser chain output is shown in Fig. 7. Output rise time is experimentally

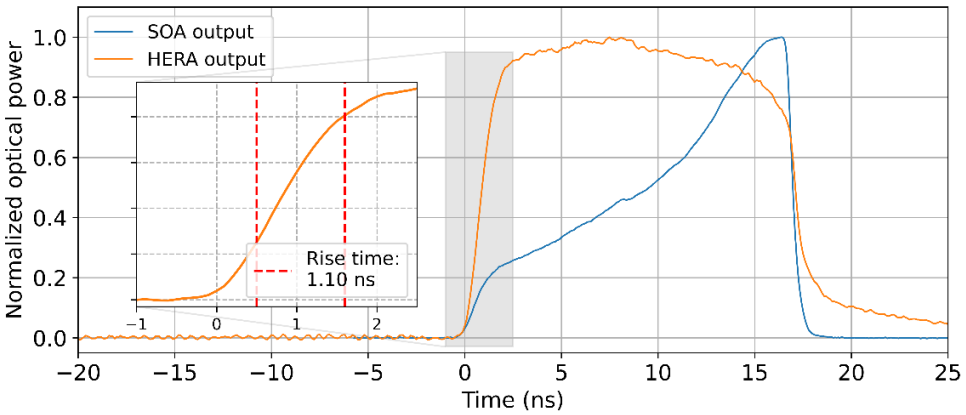

Fig. 7. Comparison of the temporal shape at the seeder level and at the laser chain output. Measures taken with an EOT-3500 photodiode and a 2 GHz bandwidth oscilloscope. Typical operation mode of the HERA laser chain producing 2*200 J square pulses.

Optics EXPRESS

measured to be 1.1 ns compatible with most shock experiments. The pulse shaping capabilities of the seeder system allow to easily tune the pulse duration from 1.5 ns (quasi-gaussian-shaped due to the limited rise and fall time) to 17 ns. Furthermore, ramp shapes and other non-standard temporal shapes are accessible with high modulation contrast. Some examples are presented Fig. 8.

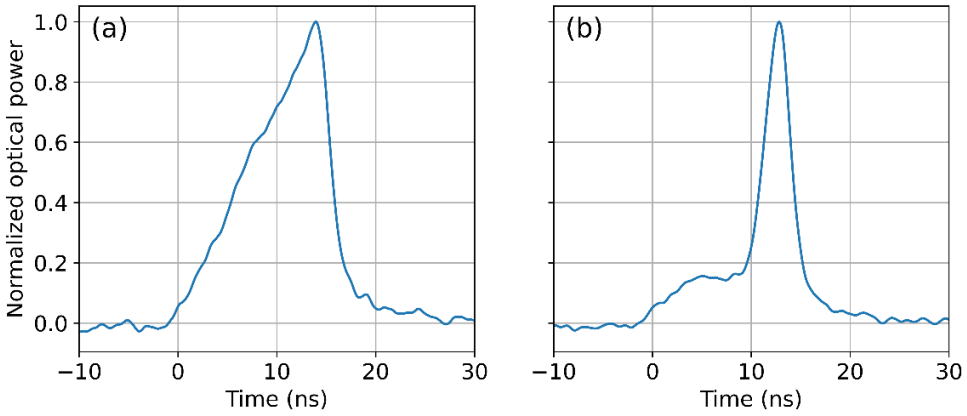

Fig. 8. Temporal shapes generated at the laser chain output using SOA temporal modulation. In those figures, 13 dB of the 53 dB of modulation dynamics have been exploited. (a) Linearly increasing ramp for shock experiments (50 J) (b) Two step temporal shape (50 J). Measures acquired using EOT-3000 photodiodes and a 2 GHz bandwidth oscilloscope.

The introduction of the beam splitting, and the 2 channels make this laser chain very flexible. The total system capabilities of 2*200 J synchronized with arbitrary temporal profiling make this laser chain compatible with a wide range of shock experiments. The SOA represents a good add-on for reaching arbitrary temporal profiles with state-of-the-art contrast as long as the rise-time requirements stays above the nanosecond time scale.

4. Conclusion and prospects

We investigated and experimentally validated the capability of the SOA component to be used as a temporal shaper seeder for high-energy laser systems employing MOPA architecture. This system is compact, user-friendly, offering over 50 dB modulation dynamic with moderate modulation speed. We demonstrate that the SOA system operates nominally with clean temporal shapes in the 10 mW peak-power range. We were able to generate arbitrary shapes from standard square to exponentially increasing peaks that presents a great interest for the plasma community. The SOA arbitrary waveform generator is ultra-compact and reliable thanks to an all-fibered architecture. Moreover, it can be easily implemented into existing laser chains as its fiber output can be injected into the laser chain without drastic modifications. We demonstrate its application on a 2×200 J system and highlight its potential. The system truly shines through its wide gain bandwidth, making it a promising choice for ICF systems requiring bandwidth in the range of several tens of nanometers. However, the main limitations of the system lie in its modulation speed and restricted peak power accessibility. Those limitations could potentially be addressed by developing new electronic drivers with higher modulation speed, higher peak current, lower jitter and cleaner temporal shapes.

Funding. Bpifrance (DOS0153842/00, DOS0153845/00); Centre National de la Recherche Scientifique.

Acknowledgments. The authors thank PicoQuant GmbH for the conjoint development of the SOAs applied to high energy laser chain seeding. The authors would like to thank all the technical teams at LULI for their valuable assistance, especially Sandra Dorard from the mechanical group.

Optics EXPRESS

Disclosures. The authors declare no conflicts of interest.

Data availability. Data underlying the results presented in this paper are not publicly available at this time but may be obtained from the authors upon reasonable request.

References

1. M. Munther, T. Martin, A. Tajyar, *et al.*, "Laser shock peening and its effects on microstructure and properties of additively manufactured metal alloys: a review," Eng. Res. Express **2**(2), 022001 (2020).
2. R. S. Nagymihály, F. Falcoz, B. Bussiere, *et al.*, "The petawatt laser of ELI ALPS: reaching the 700 TW level at 10 Hz repetition rate," Opt. Express **31**(26), 44160–44176 (2023).
3. U. Schramm, M. Bussmann, A. Irman, *et al.*, "First results with the novel petawatt laser acceleration facility in Dresden," J. Phys.: Conf. Ser. **874**, 012028 (2017).
4. N. Ekanayake, M. Spilatro, A. Bolognesi, *et al.*, "Design and optimization of a high-energy optical parametric amplifier for broadband, spectrally incoherent pulses," Opt. Express **31**(11), 17848–17860 (2023).
5. A. Wang, P. Xue, X. Liu, *et al.*, "Characteristics of broadband OPCPA based on DKDP crystals with different deuterations for the SEL-100 PW laser system," Opt. Express **32**(3), 3597–3605 (2024).
6. J. Lütgert, J. Vorberger, N. J. Hartley, *et al.*, "Measuring the structure and equation of state of polyethylene terephthalate at megabar pressures," Sci. Rep. **11**(1), 12883 (2021).
7. Y. Raffray, B. Jodar, J.-C. Sangleboeuf, *et al.*, "Zr-based metallic glasses Hugoniot under laser shock compression and spall strength evolution with the strain rate (> 107 s-1)," International Journal of Impact Engineering **181**, 104755 (2023).
8. A. B. Zylstra, O. A. Hurricane, D. A. Callahan, *et al.*, "Burning plasma achieved in inertial fusion," Nature **601**(7894), 542–548 (2022).
9. L. M. Frantz and J. S. Nodvik, "Theory of Pulse Propagation in a Laser Amplifier," J. Appl. Phys. **34**(8), 2346–2349 (1963).
10. J.-A. Hernandez, N. Sévelin-Radiguet, R. Torchio, *et al.*, "The high power laser facility at beamline ID24-ED at the ESRF," High Pressure Res. **1**, 1–28 (2024).
11. M. Veinhard, O. Bonville, S. Bouillet, *et al.*, "Parametric study of laser-induced damage growth in fused silica optics with large beams at 351 nm. Part 1: stochastic approach," Appl. Opt. **59**(31), 9643–9651 (2020).
12. A. Cournoyer, D. Gay, P. Turbis, *et al.*, "Maximizing laser ablation efficiency of silicon through optimization of the temporal pulse shape," in *Laser Applications in Microelectronic and Optoelectronic Manufacturing (LAMOM) XIX* (SPIE, 2014), Vol. 8967, pp. 125–136.
13. R. M. Malone, J. R. Bower, D. K. Bradley, *et al.*, "Imaging VISAR diagnostic for the National Ignition Facility (NIF)," in *26th International Congress on High-Speed Photography and Photonics* (SPIE, 2005), Vol. 5580, pp. 505–516.
14. K. T. Vu, A. Malinowski, D. J. Richardson, *et al.*, "Adaptive pulse shape control in a diode-seeded nanosecond fiber MOPA system," Opt. Express **14**(23), 10996–11001 (2006).
15. S. Hocquet, D. Penninckx, E. Bordenave, *et al.*, "FM-to-AM conversion in high-power lasers," Appl. Opt. **47**(18), 3338–3349 (2008).
16. R. Zhang, M. Li, J. Wang, *et al.*, "Experimental research on an arbitrary pulse generation system for imaging VISAR," Opt. Laser Technol. **43**(1), 179–182 (2011).
17. M. Beyer, J. C. Roth, E. Edwards, *et al.*, "Frequency-doubled Nd:YAG MOPA laser system with programmable rectangular pulses up to 200 microseconds," Opt. Express **29**(13), 20370–20378 (2021).
18. Q. Xiao, X. Pan, J. Guo, *et al.*, "High-stability, high-beam-quality, and pulse-width-tunable 1319 nm laser system for VISAR applications in high-power laser facilities," Appl. Opt. **59**(20), 6070–6075 (2020).
19. R. A. Meijer, A. S. Stodolna, K. S. E. Eikema, *et al.*, "High-energy Nd:YAG laser system with arbitrary sub-nanosecond pulse shaping capability," Opt. Lett. **42**(14), 2758–2761 (2017).
20. C. Dorrer, R. Roides, R. Cuffney, *et al.*, "Fiber Front End With Multiple Phase Modulations and High-Bandwidth Pulse Shaping for High-Energy Laser-Beam Smoothing," IEEE J. Sel. Top. Quantum Electron. **19**(6), 219–230 (2013).
21. A. Malinowski, K. T. Vu, K. K. Chen, *et al.*, "High power pulsed fiber MOPA system incorporating electro-optic modulator based adaptive pulse shaping," Opt. Express **17**(23), 20927–20937 (2009).
22. H. Tang, C. Yang, L. Qin, *et al.*, "A Review of High-Power Semiconductor Optical Amplifiers in the 1550 nm Band," Sensors **23**(17), 7326 (2023).
23. S. Skupsky and R. S. Craxton, "Irradiation uniformity for high-compression laser-fusion experiments," Phys. Plasmas **6**(5), 2157–2163 (1999).
24. J. R. Murray, J. R. Smith, R. B. Ehrlich, *et al.*, "Experimental observation and suppression of transverse stimulated Brillouin scattering in large optical components," J. Opt. Soc. Am. B **6**(12), 2402–2411 (1989).
25. A. Assadihaghi, H. Teimoori, and T. J. Hall, "6 - SOA-based optical switches," in *Optical Switches*, B. Li and S. J. Chua, eds., Woodhead Publishing Series in Electronic and Optical Materials (Woodhead Publishing, 2010), pp. 158–180.

Research Article | Vol. 32, No. 26 / 16 Dec 2024 / Optics Express 47347
Optics EXPRESS

High fidelity phase conjugation in a stimulated Brillouin scattering cell at 122 J

RAPHAËL HUMBLOT,[1,2,3,*] BRANLY STÉPHANE,[2] MEIGNIEN LOÏC,[3] AUDEBERT PATRICK,[3] AND DRUON FRÉDÉRIC[1]

[1] *Université Paris-Saclay, Institut d'Optique Graduate School, CNRS, Laboratoire Charles Fabry, 91127 Palaiseau, France*
[2] *Amplitude Laser Group, 2 rue du bois Chaland, 91090 Lisses, France*
[3] *LULI, CNRS, Ecole Polytechnique, CEA, Universite Sorbonne, Institut Polytechnique de Paris, 91128 Palaiseau CEDEX, France*
[*] *raphael.humblot@institutoptique.fr*

Abstract: We demonstrate a passive and automatic correction of high-energy laser wavefront using stimulated Brillouin scattering (SBS) based phase conjugating mirror (PCM) establishing a new record in terms of input energy level of 122 J together with an extremely high reflectivity, leading to efficiencies of 99 % with both high temporal fidelity and good spatial profile conservation. For this achievement, we developed an innovative design of high-energy SBS-PCM based on high numerical aperture focusing and on the temporal shaping of the input pulse, guaranteeing good SBS initiation before the arrival of the main part of the pulse. An original approach was introduced compared to previous works where the temporal fidelity was a limitation for energy scale-up. This approach allows, for the first time in an SBS cell, perfect conservation of the input pulse temporal profile, demonstrated for several temporal pulse shapes of interest. Pulsed laser sources with nanosecond duration and energy levels above the kilojoule represent a crucial tool for a wide range of plasma and shock physics experiments. This work will unlock a crucial bottleneck by addressing the correction of the wavefront distortions due to the accumulating thermal load in these lasers and opens the way to higher repetition rate kilojoule systems.

1. Introduction

High energy laser sources have been a topic of interest for the past 50 years, allowing to reach outstanding temporal and spatial concentration of energy. Several laser systems have since been built and gave insightful results on the behavior of matter under high pressure and temperature conditions. Now a wide range of plasma physics and dynamic-shock-compression experiments [1–3] is being performed at the several high-energy laser facilities available to the community. In particular, significant advances have recently been performed at the National Ignition Facility on the generation of controllable inertial confinement fusion [4]. High energy lasers also find applications in the industry for material treatment processes [5], or as pumping source for high-energy optical parametric amplifiers [6,7] and for Titanium:Sapphire amplifiers lasers [8] that are in turned used for several scientific experiments including electron and proton acceleration [9,10]. In all these diverse application domains, one limiting factor is the repetition rate of the laser sources, currently limited to a few shots per second down to few shots a day, depending on the energy level it operates at and the technology used. Increasing this repetition is now a major work axis for the community.

This repetition rate limitation for high-energy lasers in the nanosecond regime is mostly caused by heat accumulation inside the active laser medium shot after shot. Imperfect and inhomogeneous energy deposition and heat removal between shots create temperature gradients inside the amplifiers and therefore generates wavefront distortions [11]. For large beam size, these

#538542 https://doi.org/10.1364/OE.538542
Journal © 2024 Received 5 Aug 2024; revised 14 Nov 2024; accepted 20 Nov 2024; published 12 Dec 2024

Optics EXPRESS

inhomogeneous distortions can lead to deleterious hot spots damaging the optical components of the laser source. Several work axis are currently being tackled by the different laboratories and companies of the field, including uses of new gain media and new cooling architectures [12–14] to extract the stored heat more efficiently.

Correction of the residual aberrations is usually done by using a wavefront sensor controlling a deformable mirror but this approach is expensive and often limited in the total correction amplitude to a few waves PV [15], especially for very localized aberration such as spherical aberrations. Furthermore, the fast feedback loop required to properly compensate for airflow perturbation is still in development phase [16]. Therefore, an alternative way of correcting aberration using stimulated Brillouin scattering based phase conjugating mirror (SBS-PCM) has been investigated. This component is able to reflect narrow-linewidth nanosecond laser pulses with high efficiency, reversing the wavefront in the process. All the aberrations introduced in the middle of a round-trip multi-pass amplifying scheme can therefore be automatically self-corrected using this component. SBS-PCM mirrors operating at significant energy level have been reported previously [17,18] but little information on the quality, the recurrence of the results and the stability of the reflection fo the component is available for SBS systems working at very high energy. In particular, SBS-PCMs are known to introduce deformations of the input pulse's temporal profile during the reflection and the only input temporal pulse shapes used to date were Gaussian. The components was therefore thought-of as not adapted to all the range of experiment requiring arbitrary temporal profiles.

In this paper, high-energy SBS-PCM is carried out for the first time using a laser system above 100 Joules. The study focuses on the precise and extensive characterization of the fidelity of the SBS-PCM by characterizing it independently. To this aim, the component is placed at the laser system output and not in the middle of the round-trip of the multi-pass amplifier as usually done to take advantage of the phase conjugation. The optical configuration used is optimized to maximize spatial and temporal fidelity. An innovative optical design based on a high numerical aperture focusing in the PCM as well as SBS effect initiation with high-dynamic temporal shaping at the seeder level is implemented. The effect of this new configuration on spatial and temporal fidelity is demonstrated. In particular we demonstrate proper conservation of several temporal profiles of interest. An SBS-PCM operating at this energy level in an actual laser system would be compatible with high repetition rate, aberration free, several-kilojoule laser with kilowatt class average power by being inserted in the middle of a round-trip kJ-amplification system for intermediate wavefront corrections.

2. Innovative design of an SBS-PCM for high energy operation

2.1. Theoretical and numerical model

Phase conjugation by SBS is a widely documented topic [19] and can be described by the interaction between the Pump (incident) beam, the Stokes (reflected) beam, and a Phonon (an acoustic wave). The relative amplitude and coupling between those three waves can be described using the standard SBS equations [20] with temporal, and 3D spatial dependence.

$$\left(\frac{n}{c}\frac{\partial}{\partial t}+\frac{\partial}{\partial z}+\frac{i}{2k}\nabla_{\perp}^{2}\right)A_P=\frac{i\omega\gamma_e}{2nc\rho_0}\rho A_S \tag{1}$$

$$\left(\frac{n}{c}\frac{\partial}{\partial t}-\frac{\partial}{\partial z}+\frac{i}{2k}\nabla_{\perp}^{2}\right)A_S=\frac{i\omega\gamma_e}{2nc\rho_0}\rho^{*}A_P \tag{2}$$

$$\left(\frac{\partial}{\partial t}+\Gamma_B/2\right)\rho=\frac{i\epsilon_0\gamma_e k_B^2}{\Omega}A_P A_S^{*}+f \tag{3}$$

Optics EXPRESS

with A_P, A_S and ρ the complex envelope amplitude of the pump, stokes and acoustic waves respectively. n, γ_e, ρ_0 and Γ_B diverse parameters of the nonlinear medium. ω and Ω the frequency of the optical and sound waves and f the thermal noise term in the medium.

Those equations are typically not solvable in the general case and even numerical simulations struggle to provide results in the full 4D (x, y, z, t) case, taking into account the transverse dimension. Most of the numerical models available therefore chose to only treat the 2D case (z, t) [21,22] thereby neglecting the transverse derivative in the left-hand side of Eqs. (1) and (2). Some models implement a modal decomposition to simulate a quasi-3D (r, z, t) description of the effect [23]. In this work, the input beam is a high-order nearly-flattop supergaussian beam. Hence, the optimal approach consists in utilizing the 2D modal (and adapting the intensity versus beam size at every longitudinal position to simulate the focusing). Indeed, nearly flattop beam are relatively consistent with the 2D model away from focus and the number of transverse modes necessary to accurately represent the transverse distribution of the energy is deemed too high to be properly simulated.

The first goal in this model development was to find an optical configuration guaranteeing the lack of temporal compression. Because the initiation of the SBS effect happens at focus, the reflecting zone appears at a certain depth inside the PCM and the reflected Stokes light subsequently stimulates acoustic waves to the entire area in the medium between the entrance window and the focus spot. The reflecting zone therefore moves at relativistic speed from focus to PCM entrance during the initiation of the SBS effect and this movement is able to compress the pump pulse. This effect, widely used in the literature [24–27], would lead to immediate damage of the optical components in case of a high-energy pulse compression.

The SBS mirror's longitudinal contra-propagating displacement tends to temporally compress all the energy present in the cell between entrance window and the focus point during SBS initiation. Therefore, two parameters have the potential to mitigate this compression: the volume of the interaction zone and the fraction of the pump energy present before SBS initiation should both be minimized. The interaction volume can be minimized by reducing the focal length of the focusing system placed before the PCM, therefore reducing the propagation distance between cell entrance and focus. And the pump energy sent in the PCM before SBS initiation can be reduced by adequate temporal shaping of the pump pulse with a high dynamic range.

A study was first conducted on the focal length of the focusing system placed before the PCM. Numerical simulations were run to find the Stokes and pump peak power ratio (compression ratio) as a function of focal length and are presented Fig. 1. Results show a clear dependence of the Stokes-pulse temporal profile with the focal length used. Reducing the focal length decrease the interaction-zone length and leaves a smaller margin for compression. Conversely, choosing a propagation distance long enough for the entire pump pulse to be present in the cell before the Stokes wave has time to exit through the entrance window, allows for the compression of the entire duration of the pump pulse. In our case, this is achieved for focal lengths above 1.5 m and led to compression ratio above 40. In the case of high energy reflection, this should be avoided, and the focusing lens should be chosen as small as possible, ideally guaranteeing insertion depth < 250 mm for our nonlinear medium.

2.2. Nonlinear effect initiation

Because the compression effect can not be completely suppressed by only reducing the volume of the interaction zone (by adapting the focal length) and that a too-short focal length would lead to peak intensity inside the PCM much higher than ionization threshold, it is also necessary to diminish the amount of energy compressed by shaping the pump temporal profile in order to initiate the SBS-mirror with a sufficiently-low-power seeder before the arrival of the main energetic part of the pump pulse. This approach was studied at low-energy by the geometric separation through polarization of the beam into a main pulse and a prepulse [28]. In this article,

Optics EXPRESS

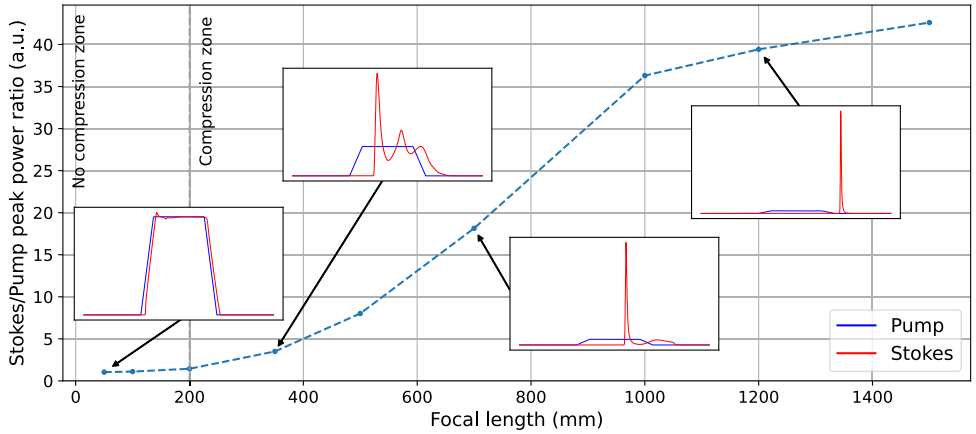

Fig. 1. Simulation of Stokes/Pump peak power ratio as a function of the focusing-lens focal length. Simulations based on a 2D model for a pump energy of 50 J, with a diameter of 93 mm at cell entrance. Input temporal profile is a 10 ns square temporal shape with 1 ns rise time.

the solution is simplified and applied for the first time to high energy SBS phase conjugation. The prepulse is included directly into the main part of the pulse through a temporal shaping at the oscillator level, therefore being easily tunable with high contrast, and becoming independent to the temporal pulse shape.

Because typical SBS threshold effect starts at the millijoule level, reflection of 100 J can be properly initiated using less than 0.1% of the available input energy, as long as the temporal modulation capacities of the laser system permit it, especially in terms of dynamic range. This preparation is done by adding an additional low-energy background in front of the pulse, that we call *pedestal* in the following. This pedestal serves only for SBS initiation purposes and should be intense enough to properly initiate SBS effect and long enough that the acoustic wave have time to reach back the entrance of the cell (from the focus), thereby allowing SBS stationary operation for the main energetic pulse. Overall, the introduction of this pedestal presents five advantages compared to classical solutions reported up to now in the literature:

1. The sharpening of the front edge due to cell transparency before the response time of the SBS medium does not impact the main and useful part of the pump pulse. 2. The residual compression applies only on the pedestal and is thus completely invisible on the reflected temporal pulse shape no matter the actual focal length used. 3. The first few ns usually transmitted by the SBS mirror only contains a minimal amount of energy and the overall reflectivity of the mirror is maximized. 4. As the nonlinear effect is already initiated when the majority of the pulse energy arrives in the cell, the acoustic field has already propagated toward cell entrance and the reflecting zone is well before focus (with a large area). The power density inside the cell is thus minimized and parasitic nonlinear effects (self-focusing, ionization,. . .) do not occur. 5. Because the main part of the pump pulse is reflected very close to cell entrance, the overall absorbed energy in the SBS-medium is also minimized and we believe this could largely increase SBS-PCM average power load in the future high repetition rate experiments.

Thus, carefully controlling the pedestal contrast allows for an arbitrary rise time (between pedestal and main impulsion) without degradation of the spatial fidelity [29,30], as long as it stays above response time of the liquid.

Numerical simulations comparing temporal fidelity of SBS reflection for 100 J pulses, with and without pedestal are shown Fig. 2 and demonstrate the increase of temporal fidelity for

Optics EXPRESS

several temporal pulse shape with the introduction of the pedestal. Those simulations have been made under the 2D model and therefore simulate perfects un-aberrated beams, confined on diameters calculated for TEM00 beams. In particular, this leads to smaller focal spots compared to corresponding experiments. Therefore the simulated SBS mirror efficiency near focus is so strong that it can be numerically considered as perfect in the simulation model. This condition leads to coupling strength way above experimental values and create those oscillations seen in the reflected pulse after the initial compression spike [31] by regular extinction of the pump pulse seen at focus just after a compression spike. Those parasitic low-intense and fast oscillations have never been observed in experiments and can considered as numerical artifacts.

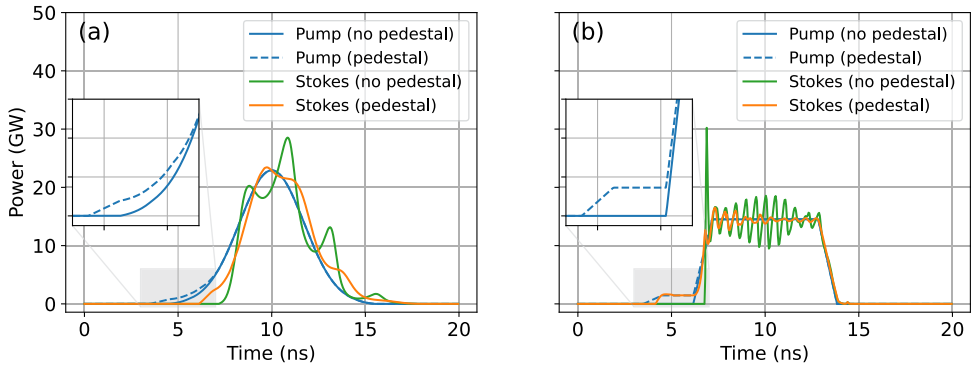

Fig. 2. Numerical simulations for SBS reflection of an input pump pulse with and without pedestal. The pedestal influences and smooths the leading edge of the reflected pulse. The Stokes overshoot is also significantly reduced. a) Gaussian pulse, 100 J input energy b) Square pulse shape, 100 J input energy.

In conclusion, the theoretical framework described in the paper allows to identify proper working operation of a high energy SBS cell. The numerical simulation demonstrates that the focusing optical component must be chosen to minimize the insertion depth of the focus spot inside the cell to prevent compression. For the configuration chosen, significant compression started to appear for focusing lens of focal length 200 mm corresponding to interaction distance of 254 mm (considering the optical index of the liquid used). Additionally, the simulations show that compression can be further reduced to an insignificant part of the pulse by introducing a pedestal before the leading edge of the main pulse. This pedestal also simultaneously helps mitigating ionization inside the liquid hence solving the main issue of tight focusing of high energy pulses inside the nonlinear medium.

2.3. Experimental optical setup

Following the simulation results, completely avoiding compression would require a distance, between the cell entrance and the beam focus, of 100 mm. The 100 J input beam having a 93 mm diameter, this nominal regime would require a lens aperture about $F/1$, thus hard to manufacture and introducing a high level of aberrations. Subsequently, the propagation distance is chosen as a compromise between lens aperture and minimization of temporal deformation during reflection. And a final propagation distance of 300 mm is chosen. Two focusing lenses with similar focal length but introducing different aberrations levels (mainly spherical aberration) are used during the experiments to study the effect of the apparatus aberrations on the quality of phase conjugation. At full aperture, the two lenses L_1 and L_2 induce respectively $\Delta_1 = 30\lambda$ PV and $\Delta_2 = 4\lambda$ PV of Zernike's spherical aberration (our main aberration of interest beside defocus

Optics EXPRESS

since the hardest to compensate for in typical laser systems) per pass. Both lenses lead to a focus spot at 300 mm propagation depth in liquid.

The laser source used to perform the experiments is a Nd:Glass laser system based on the Master Oscillator Power Amplifier (MOPA) architecture capable of delivering pulses up to 200 J at 1053 nm with arbitrary temporal profile in the nanosecond time-scale [32]. It is seeded by a CW laser diode with narrow spectrum, temporally shaped by a high-dynamic Semiconductor Optical Amplifier (SOA) pulse-shaper and subsequently amplified to high energy. The high dynamic-range capacities of the oscillator (above 50 dB) as well as the high saturation fluence of the gain medium used allows for precise and highly contrasted control of the pump temporal shape. In particular, it is possible to generate pedestals of very low power and arbitrary duration. The already-operating laser system is such that the output pulse is spatially and temporally filtered to insure good beam quality.

The cell itself is 600 mm long and filled in class-100 clean room with ultra-filtered Fluorinert FC770 [33]. Since an SBS-PCM in a kilojoule class laser system would typically be used in the middle of multipass amplifier round trip (with typically at the 100-J level of amplification at this point), we aim to identify and measure the individual contribution of the PCM in the following. It is therefore placed at the one-trip output of the laser chain and the Stokes beam are analyzed directly after reflection, without being subsequently amplified backward.

Experimental data acquisition is performed for every shot for input and output pulses simultaneously. For this matter, a plano glass plate AR-coated on only one face is placed inside the optical path of the input beam and is used to extract 4 % of the input beam energy and of reflected beam energy, as shown in Fig. 3. A fold mirror is initially placed before the cell to calibrate the 100 % reflectivity for both gentec QE95LP-S-MB-D0 calorimeters 1 and 2 (Fig. 3). The photodiodes (EOT ET-3000 rise time 175 ps) allow for simultaneous measurement of input and reflected pulses and thus temporal pulse shape comparison.

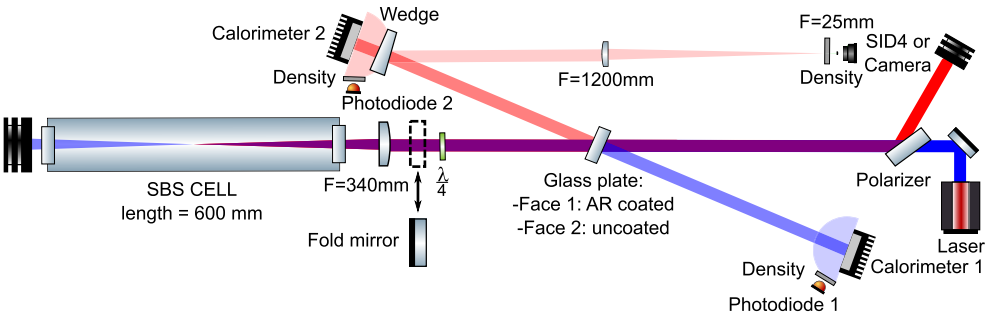

Fig. 3. Optical layout of the experiment and the associated metrology. In the preparatory phase, a "fold mirror" is used to either analyze pump pulse aberrations and calibrate calorimeters. It is removed after qualification to send pump beam into the SBS cell.

3. Experimental results

3.1. Overcoming critical spatial issues

For cell operation with L_1 (the lens with the most spherical aberration), a high intensity hot spot is observed at the center of the reflected Stokes beam spatial profile as shown in Fig. 4. The position, shape and relative intensity (visibility) of the hot spot remains constant along propagation axis over 10 m and thus does not correspond to a parasitic ghost focus spot. Moreover, the visibility of this hot spot is strongly dependent on the beam aperture as shown in Fig. 4(a). It is therefore correlated to the spherical aberration level of the beam sent into the cell. To

Optics EXPRESS

validate this hypothesis, we perform an additional experiment: when operating with L_1 at small aperture but with a translation offset compared to the optical axis of L_1, the aberration level is increased again and the hot spot re-appears still on the optical axis but slightly changes shape (due to symmetry breaking) as shown in Fig. 4(b). The strong dependence on aperture as well as the hot spot spatial shape indicates the influence of the spherical aberration on the near field spatial profile conservation. While the simulation model would require a precise description of the transverse component of the optical and acoustic waves to quantitatively describe this phenomenon, we propose the following explanation: The high amplitude spherical aberration makes the marginal rays focus at shorter insertion depth than the rest of the rays. They then generate a parasitic deleterious acoustic grating inside the cell, interacting with the paraxial rays and creating this spatial hot spot in the reflected beam profile. Although the visibility of the hot spot is found to decrease with input energy, our experimental configuration prevented us to investigate further on the influence of other kind of aberrations and on the dependence of other parameters such as input beam diameter or focusing conditions. Reducing spherical aberration of the apparatus is then a key point in this experiments : it allows to drastically reduce the hot spot visibility. Its complete disappearance appears for spherical aberrations below 14λ PV on Zernike basis. For safety considerations, no high energy experiments (> 3 J) has been done with L_1 to avoid any damages in the experimental setup.

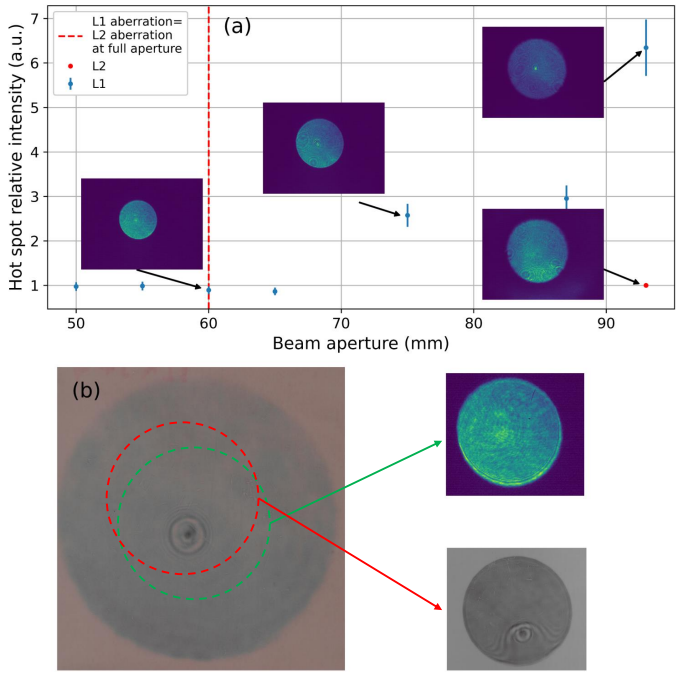

Fig. 4. a) Hot spot visibility as a function beam aperture on focusing optic for L_1 and L_2. Camera images are given for several points of interest. b) Burn paper for reflected beams using L_1 at full aperture and corresponding spatial profiles for a 50 mm aperture centered and uncentered.

It is interesting to note that, despite those strong near-field hot-spot due to the spherical aberration inside the cell, no significant increase in WaveFront reversal Error (WFE) is detected during the experiments and the resultant at the cell output is still clean, devoid of spherical aberrations. The PCM in a double pass is thus capable of correcting more than $2\Delta_1 = 60\lambda$ PV (Zernike basis) of spherical aberration at the cost of near field spatial profile perturbation and

Optics EXPRESS

14λ PV without any detrimental effects. This limit is about an order of magnitude above classical wavefront correction solutions in high-energy laser chains [15].

In the following, all the high-energy experimental results presented will be for the L_2 focusing length, with aberration level below the hot-spot-apparition threshold and therefore presenting high spatial-quality Stokes beam. A typical reflected beam profile at low energy and full aperture for the L_2 focusing lens is shown included in Fig. 4(a).

A secondary detrimental effect on the reflected spatial profile appears when increasing the energy. As stated in the literature [34], initiation of the SBS effect with intensity much higher than the threshold intensity allows for large cell volume to act as a stokes wave source terms. Hence several noise modes can be amplified, sometimes competing with the perfectly phase conjugated mode. The output spatial profile can therefore be distorted. This leads to energy structures with local cold and hot spots appearing in the reflected Stokes beam. We demonstrate here that this effect can be efficiently eliminated by an appropriate shaping of the input pulse temporal profile, by optimally adapting the pedestal level to just above SBS threshold. Experimentally, this optimization is done by progressively reducing the pedestal level shots after shots down to the disappearance of the patterns on the reflected beams. In our optical configuration, the duration of the pedestal was at 3 ns, and its total energy was 100 mJ, independent of the temporal shape and total energy of the main pulse. This value represents less than 1% of the energy for input pulses > 10 J, and down to 0.1% for the > 100 J pulses. The pedestals are therefore not visible in the pulse temporal pulse shapes measured with photodiodes. Once the correct pedestal level found, more than 10 shots at high energy are performed without any degradation of spatial fidelity.

Burns patterns relative to pedestal contrast for different energies are shown in Fig. 5 showing the importance of controlling the contrast of the pedestal on the quality of the output spatial profile.

We demonstrated with those experiments that SBS phase conjugation can lead to degradation of the spatial fidelity if not designed properly. The maximum aberration level sent inside the cell have to be monitored and is, in our experimental setup, limited to $\approx 7\lambda$ PV (for spherical aberration on Zernike basis). The input temporal profile, and in particular, the pulse power during SBS initiation also have to be properly monitored and are found to lead to spatial fidelity degradation (hot and cold spots apparition) in case of SBS initiation with power density much high than SBS threshold. Conversely, proper management of this power density though temporal profile control leads to excellent beam profile conservation no matter the input energy in the cell as long as the pedestal is optimized in this matter. In the following, we will describe the other properties of the SBS conjugation at high energy under optimal operating conditions.

3.2. High energy operation

The maximum output energy of the laser is 200 J but the temporal shaping as well as the limited size on the cell input window 65 mm limits the input energy to ≈ 120 J. During the experiment, more than 120 shots were fired with energy ranging between 350 J and 122 J including over ten shots at energy above 100 J. The reflectivity data for all shots performed with Gaussian temporal profile is shown in Fig. 6(a). The low repetition rate leads to a high incertitude on the absolute reflectivity of the cell. The calorimeters are frequently calibrated during the experiment using the fold mirror in place of the cell. However, there is still a notable degree of uncertainty associated with the joule-meters, typical for this kind of high-energy single-shot measurements. This explains the seemingly aberrant measurement points with > 100 % reflectivity. For all input energy, the measured reflectivity is > 95 %. A calorimeter with trigger level of 300 J is placed to detect input energy going through the cell and no energy was ever detected even for input energy level > 100 J. Taking into account the liquid absorption and the parasitic reflections at optical surfaces, the reflectivity is then > 99 % at high energy.

Optics EXPRESS

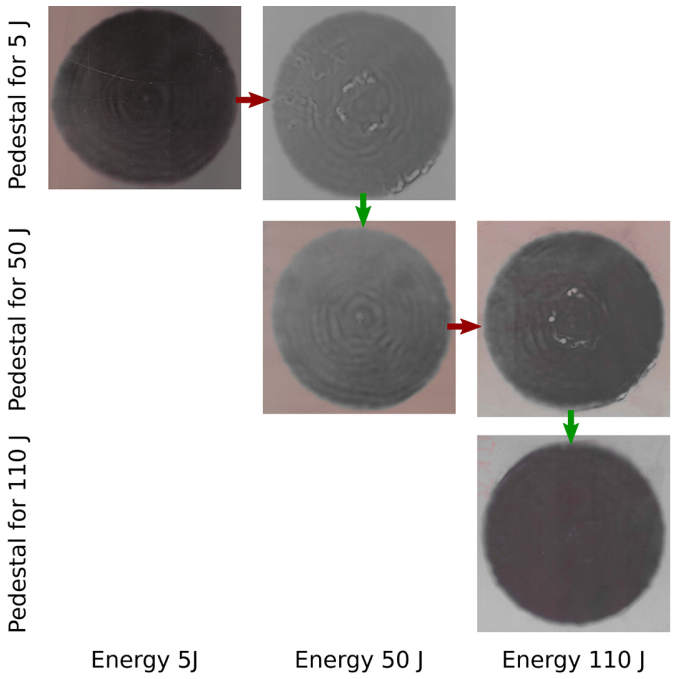

Fig. 5. Spatial fidelity of SBS reflection as a function of energy and pedestal optimization. Spatial profiles acquired by directing the reflected beam toward burn papers. Increasing the input energy without changing the pedestal contrast (red arrows) deteriorates the reflected near field beam quality and requires a reduction of the pedestal level to near SBS threshold (green arrows) to retrieve good spatial fidelity.

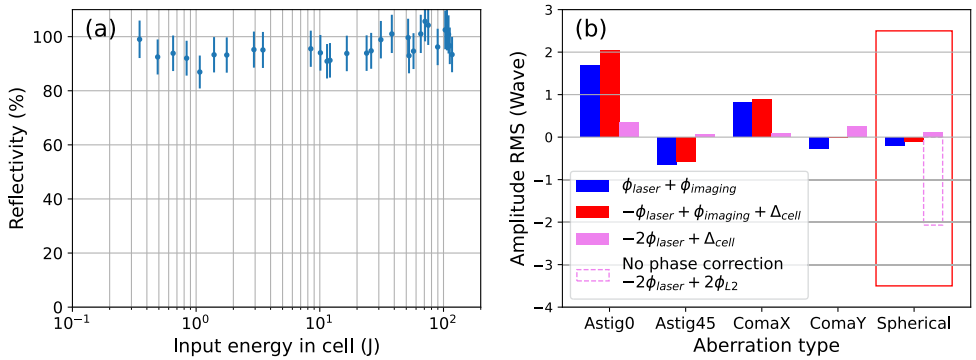

Fig. 6. Experimental results for high energy SBS phase conjugation using L2 focusing lens. a) Reflectivity of the cell versus input energy for Gaussian pulse shape. b) Main aberrations coefficients values for pump beam using a classical mirror instead of the cell (blue), Stokes beam (red) and the residual phase calculated using Eq. (6). The expected spherical aberration value after a double pass in the L_2 lens and without phase reversal is displayed in dashed pink. The first 4 aberrations coefficients only shows that no significant aberration is introduced by the cell during the reflection. The correction capacities of the cell are only visible on the spherical aberration part (red rectangle) where the cell effectively corrects more than 2λ RMS ($\approx 7\lambda$ PV) of Zernike's spherical aberration.

Optics EXPRESS

To the best of our knowledge, this input energy and this reflectivity are the highest recorded for any SBS mirror. This particularly-high reflectivity is mainly attributed to the accurate temporal shaping limiting the transmitted part of the pulse to the pedestal only and therefore containing minimal energy.

To evaluate the performance of the wavefront reversal, we compare the input and reflected beam wavefront. Firstly, the Stokes beam is perfectly retro-reflected and collimated after its second pass in the focusing lens, demonstrating perfect correction of tilts and focus aberrations. To measure the higher order aberration, the Pump beam is imaged, after its reflection by a conventional plano-mirror, by a convergent-convergent-lens telescope and sent on a wavefront sensor (Phasics, SID4-V) imaging the glass plate.

This experimental layout slightly differs from most of the state of the art setups where a clean beam wavefront is observed before and after reflection, with some aberrations placed in the double pass. Here, the initial wavefront coming from the laser is unknown and typically present some low amplitude aberrations that will be measured positively for input wave and negatively for output wave. Furthermore, since the high energy beam has large diameter, an imaging system has to be introduced before the wavefront sensor, and the experimental conditions and available optical components make this system highly aberrant. The reliability of our measurement lies in the fact that the dominant spherical aberration source was the focusing lens L_2 and hence the WFE for this particular aberration can be measured.

In this setup, the measurement of the wavefront of the pump beam ϕ_{pump} is the sum of the laser wavefront ϕ_{laser} and the imaging system aberrations $\phi_{imaging}$.

$$\phi_{pump} = \phi_{laser} + \phi_{imaging} \tag{4}$$

Conversely, the measurement of the stokes, phase conjugated wavefront was the reversed laser wavefront $-\phi_{laser}$ plus the imaging system aberration $\phi_{imaging}$ plus the WFE of the cell Δ_{cell}.

$$\phi_{stokes} = -\phi_{laser} + \phi_{imaging} + \Delta_{cell} \tag{5}$$

It is convenient to use the pump wavefront as a reference to suppress the contribution of the imaging system. In this case, the residual wavefront measured after reference subtraction is

$$\phi_{residual} = -2\phi_{laser} + \Delta_{cell} \tag{6}$$

However, the strong aberration level of the imaging system prevents validation of the reversal efficiency of the SBS cell. Because the wavefront of the input laser is unknown, but no significant amount of aberration should be present (low repetition rate and low beam spatial modulations in propagation), the dominant aberration at cell entrance is the spherical aberration of the lens L_2. Therefore this particular aberration coefficient is used to validate the cell correction efficiency. It is also the only component that effectively perceive the double pass and whose aberration can be corrected by SBS reflection. The WFE is then evaluated only using the residual spherical aberration and comparing it to the theoretical calculated aberration assuming a complete lack of wavefront reversal. The results are shown in Fig. 6(b) where ϕ_{pump}, ϕ_{stokes}, and $\phi_{residual}$ are shown respectively in blue, red and pink and the expected spherical aberration level is displayed in dashed line. The WFE for the spherical aberration is found to be extremely low and the lens aberration is fully corrected.

Finally, we study the conservation of the temporal profile of the reflected pulse. The two photodiodes analyze the temporal fidelity of the PCM on-shot and the reflectivity of the PCM along time is calculated such as $I_S(t)/I_P(t)$, ideally constant equal to 1. Because of the low repetition rate and low energy stability of the laser chain, no averaging of the pulse shapes is possible and the electronic noise is clearly visible on the temporal profile measurements, hence limiting the precision of the measurement and calculation of the reflectivity of very low signal

Optics EXPRESS

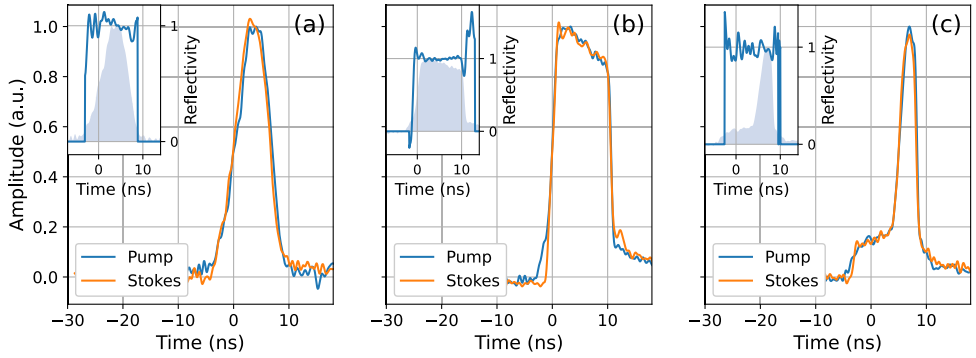

Fig. 7. Temporal fidelity during high energy SBS reflection. Main graph: comparison of the input (Pump) and output (Stokes) temporal pulse shapes during SBS reflection. Inset graphs represent the pump temporal pulse shape in solid blue as well as the reflectivity of the PCM along time plotted for pump value above 10% of peak. A straight line over the pump pulse duration means a perfect conservation of the temporal shape during reflection a) Gaussian pulse for input energy of 122 J . b) Square pulse for input energy of 40 J c) two step "fusion-like" shape for input energy of 40 J.

(I_P<10%I_{Pmax}). Temporal fidelity of the PCM is analysed for several pulse shapes (Gaussian, square, fusion-shape,. . .) and is shown in Fig. 7.

In all cases, no overshot and no compression spikes are observed. The reflectivity along time is almost constant for the whole duration of the pulse, limited -especially on the edges where the intensities are very low- by the electronic noise of the photodiodes. The reflectivity curve is manually set to 0 outside of the pulse for better visibility. The SBS mirror can effectively reflect any pulse shape if the rise and fall time do not exceed the SBS frequency bandwidth and are not sharper than the response time of the nonlinear medium (≈ 1 *ns* for the classical liquids used). Those results remain true over the whole energy range studied, down to about 1 J where the pedestal's energy becomes comparable with the main pulse's energy and is visible in the temporal profiles measurements.

4. Conclusion

We demonstrate the usability of SBS-PCMs systems for ultra-high energy laser systems. Operating points with good spatial and temporal fidelities were achieved with input energy on the PCM as high as 122 J. In a multi-pass laser system, this energy at the middle of the round-trip could lead to several kilojoules of energy at laser output after backward amplification. Those results were obtained due to an innovative design of the PCM geometry. The choice of a focusing lens with very high aperture, as well as the introduction of an optimal pedestal for SBS initiation before the arrival of the main part of the pulse removed the energy limit at the SBS-PCM input. We originally demonstrated that limiting the intrinsic spherical aberrations and optimizing the pedestal level allows for efficiently removing the deleterious hot-spot and opening a route to SBS cells operating at higher energy. In the apparatus, this input energy is now limited by the LIDT (Laser-Induced Damage Threshold) of the input cell window and, consequently, by the transverse size of our cell, even though we did not observe any damage during the entire demonstration. This LIDT, for a glass window, is of the same order of magnitude than the LIDT of the typical optical components of the laser chain and, thus, does not represent an additional limitation for the full laser system. The energy limitation for SBS cell operation is then effectively removed. Additionally, the nonlinear effect initiation allowed to reflect for the first time arbitrary temporal

Optics EXPRESS

pulse shapes with minimal distortion. This system now represents a simpler, cheaper, and more powerful alternative to deformable mirrors applicable for narrow-linewidth high energy lasers.

Funding. Association Nationale de la Recherche et de la Technologie (Cifre 2021/1470).

Acknowledgements. The authors thank LULI's HERA staff. In particular Joanna De Sousa, Cyril Rapeneau for their valuable assistance during the experiment weeks and Sandra Dorard from LULI's mechanical group for her contribution to the laser chain adaptation for the experiment. We also thank Ivan Delgado from Amplitude laser group for the cell design.

Disclosures. Raphaël Humblot: Amplitude laser (F,E,P). Stéphane Branly: Amplitude laser (F,E,P). Loic Meignien: LULI-CNRS (P). Frédéric Druon: Laboratoire Charles Fabry (P)

Data Availability. Data underlying the results presented in this paper are not publicly available at this time but may be obtained from the authors upon reasonable request.

References

1. R. J. Trainor, J. W. Shaner, J. M. Auerbach, *et al.*, "Ultrahigh-pressure laser-driven shock-wave experiments in aluminum," Phys. Rev. Lett. **42**(17), 1154–1157 (1979).
2. P. M. Celliers, G. W. Collins, L. B. Da Silva, *et al.*, "Accurate measurement of laser-driven shock trajectories with velocity interferometry," Appl. Phys. Lett. **73**(10), 1320–1322 (1998).
3. J. K. Wicks, R. F. Smith, D. E. Fratanduono, *et al.*, "Crystal structure and equation of state of Fe-Si alloys at super-Earth core conditions," Sci. Adv. **4**(4), eaao5864 (2018).
4. H. Abu-Shawareb, R. Acree, P. Adams, *et al.*, "Lawson criterion for ignition exceeded in an inertial fusion experiment," Phys. Rev. Lett. **129**(7), 075001 (2022).
5. C. B. Dane, L. A. Hackel, J. Halpin, *et al.*, "High-throughput laser peening of metals using a high-average-power Nd: glass laser system," U.S. Department of Energy Office of Scientific and Technical Information (1999).
6. I. N. Ross, P. Matousek, G. H. C. New, *et al.*, "Analysis and optimization of optical parametric chirped pulse amplification," J. Opt. Soc. Am. B **19**(12), 2945–2956 (2002).
7. S.-W. Bahk, I. A. Begishev, R. Roides, *et al.*, "Effect of the pump beam profile and wavefront on the amplified signal wavefront in optical parametric amplifiers," Opt. Express **30**(8), 12995–13008 (2022).
8. J. P. Zou, C. L. Blanc, D. N. Papadopoulos, *et al.*, "Design and current progress of the Apollon 10 PW project," High Power Laser Sci. Eng. **3**, e2 (2015).
9. R. Assmann, M. Weikum, T. Akhter, *et al.*, "EuPRAXIA Conceptual Design Report," Eur. Phys. J. Spec. Top. **229**(24), 3675–4284 (2020).
10. F. Kroll, F.-E. Brack, C. Bernert, *et al.*, "Tumour irradiation in mice with a laser-accelerated proton beam," Nat. Phys. **18**(3), 316–322 (2022).
11. V. Sazegari, M. R. J. Milani, and A. K. Jafari, "Structural and optical behavior due to thermal effects in end-pumped Yb:YAG disk lasers," Appl. Opt. **49**(36), 6910–6916 (2010).
12. J. Yi, B. Tu, X. An, *et al.*, "9 kilowatt-level direct-liquid-cooled Nd:YAG multi-module QCW laser," Opt. Express **26**(11), 13915–13926 (2018).
13. M. D. Vido, G. Quinn, D. Clarke, *et al.*, "Demonstration of stable, long-term operation of a nanosecond pulsed DPSSL at 10 J, 100 Hz," Opt. Express **32**(7), 11907–11915 (2024).
14. R. S. Nagymihály, F. Falcoz, B. Bussiere, *et al.*, "The petawatt laser of ELI ALPS: reaching the 700 TW level at 10 Hz repetition rate," Opt. Express **31**(26), 44160–44176 (2023).
15. P. Mason, S. Banerjee, J. Smith, *et al.*, "Development of a 100 J, 10 Hz laser for compression experiments at the High Energy Density instrument at the European XFEL," High Power Laser Sci. Eng. **6**, e65 (2018).
16. J. B. Ohland, N. Lebas, V. Deo, *et al.*, "From Astronomy to Laser-Labs: Real-Time Wavefront Stabilization at Apollon," in *High-Brightness Sources and Light-Driven Interactions Congress* (2024), paper HTh3B.5, (Optica Publishing Group, 2024), p. HTh3B.5.
17. H. Yoshida, V. Kmetik, H. Fujita, *et al.*, "Heavy fluorocarbon liquids for a phase-conjugated stimulated Brillouin scattering mirror," Appl. Opt. **36**(16), 3739–3744 (1997).
18. V. Kmetik, H. Yoshida, H. Fujita, *et al.*, "Very high energy SBS phase conjugation and pulse compression in fluorocarbon liquids," in *SPIE*, M. Osinski, H. T. Powell, and K. Toyoda, eds. (2000).
19. R. W. Boyd, *Nonlinear Optics, Third Edition* (Academic Press, Inc., USA, 2008), 3rd ed.
20. A. Heuer and R. Menzel, *Principles of Phase Conjugating Brillouin Mirrors* (John Wiley and Sons, Ltd, 2003). Publication Title: Phase Conjugate Laser Optics Section: 2.
21. R. Chu, M. Kanefsky, and J. Falk, "Numerical study of transient stimulated Brillouin scattering," J. Appl. Phys. **71**(10), 4653–4658 (1992).
22. X. Xu, C. Feng, and J.-C. Diels, "Optimizing sub-ns pulse compression for high energy application," Opt. Express **22**(11), 13904–13915 (2014).
23. S. Afshaarvahid and J. Munch, "A Transient, Three-Dimensional Model of Stimulated Brillouin Scattering," J. Nonlinear Opt. Phys. Mater. **10**(01), 1–27 (2001).
24. D. T. Hon, "Pulse compression by stimulated Brillouin scattering," Opt. Lett. **5**(12), 516–518 (1980).

Optics EXPRESS

25. H. Yoshida, T. Hatae, H. Fujita, *et al.*, "A high-energy 160-ps pulse generation by stimulated Brillouin scattering from heavy fluorocarbon liquid at 1064 nm wavelength," Opt. Express **17**(16), 13654–13662 (2009).
26. C. Feng, X. Xu, and J.-C. Diels, "Spatio-temporal characterization of pulses obtained from a high-energy sub-nanosecond laser system," Appl. Opt. **55**(7), 1603–1612 (2016).
27. H. Yuan, Y. Wang, C. Zhu, *et al.*, "Investigation of sub-phonon lifetime pulse amplification in active frequency matching stimulated Brillouin scattering," Opt. Express **27**(12), 16661–16670 (2019).
28. J. W. Yoon, J. S. Shin, H. J. Kong, *et al.*, "Investigation of the relationship between the prepulse energy and the delay time in the waveform preservation of a stimulated Brillouin scattering wave by prepulse injection," J. Opt. Soc. Am. B **26**(11), 2167–2170 (2009).
29. C. B. Dane and L. A. Hackel, "High-pulse-energy phase conjugated laser system," in *Phase Conjugate Laser Optics*, (John Wiley and Sons, Ltd, 2003), pp.147–204.
30. M. Ostermeyer, H. J. Kong, V. I. Kovalev, *et al.*, "Trends in stimulated Brillouin scattering and optical phase conjugation," Laser Part. Beams **26**(3), 297–362 (2008).
31. R. V. Johnson and J. H. Marburger, "Relaxation oscillations in stimulated Raman and Brillouin scattering," Phys. Rev. A **4**(3), 1175–1182 (1971).
32. R. Humblot, L. Meignien, J. D. Sousa, *et al.*, "Semiconductor optical amplifier used as fibered arbitrary waveform generator for high energy applications," in *High-Brightness Sources and Light-Driven Interactions Congress (2024)*, paper JTu4A.9, (Optica Publishing Group, 2024), pp.JTu4A.9.
33. H. Yoshida, V. Kmetik, H. Fujita, *et al.*, *High Performance of Phase Conjugated Stimulated Brillouin Scattering Mirror Based on High Purity Liquid Heavy Fluorocarbons* (AIP, 1996).
34. C. B. Dane, W. A. Neuman, and L. A. Hackel, "Pulse-shape dependence of stimulated-Brillouin-scattering phase-conjugation fidelity for high input energies," Opt. Lett. **17**(18), 1271–1273 (1992).